



HAL
open science

Raman modes in index-identified individual single-walled and multi-walled carbon nanotubes

Dmitry Levshov

► **To cite this version:**

Dmitry Levshov. Raman modes in index-identified individual single-walled and multi-walled carbon nanotubes. Physics [physics]. Université Montpellier II - Sciences et Techniques du Languedoc; Rostovskij gosudarstvennyj universitet, 2013. English. NNT : 2013MON20116 . tel-01023001

HAL Id: tel-01023001

<https://theses.hal.science/tel-01023001>

Submitted on 11 Jul 2014

HAL is a multi-disciplinary open access archive for the deposit and dissemination of scientific research documents, whether they are published or not. The documents may come from teaching and research institutions in France or abroad, or from public or private research centers.

L'archive ouverte pluridisciplinaire **HAL**, est destinée au dépôt et à la diffusion de documents scientifiques de niveau recherche, publiés ou non, émanant des établissements d'enseignement et de recherche français ou étrangers, des laboratoires publics ou privés.

THÈSE

Pour obtenir le grade de
Docteur

Délivré par **Université Montpellier 2**

Préparée au sein de l'école doctorale: **I2S**
Et de l'unité de recherche: **Laboratoire Charles Coulomb**
Et en cotutelle avec **Southern Federal University**
Spécialité : **Physique**

Présentée par **Dmitry Levshov**

**Raman modes in index-identified individual
single-walled and multi-walled carbon nanotubes**

Soutenue le 16 décembre 2013 devant le jury composé de

Dr Stéphane BERCIAUD, Université de Strasbourg

Pr Luc HENRARD, Université de Namur

Dr Raul ARENAL, Université de Saragosse

Pr Vladimir LORMAN, Université Montpellier 2

Pr Christophe VOISIN, Université Paris Diderot

Pr Yuri YUZYUK, SFU, Rostov-on-Don

Dr Jean-Louis SAUVAJOL, CNRS-Université Montpellier 2

Dr Thierry MICHEL, Université Montpellier 2

Rapporteur

Rapporteur

Examineur

Examineur

Invité

Directeur de thèse

Directeur de thèse

Co-directeur de thèse

Abstract

The main objective of this work is the fundamental physical study of individual isolated carbon nanostructures in order to address their intrinsic vibrational and optical properties and also to estimate and quantify the environmental effects. For these purposes, we synthesized individual single- and multi-walled carbon nanotubes by chemical vapour deposition method on dedicated substrates. The main aspect of the work involves the combined use of different experimental probes on the same individual nanostructures. We performed a complete structure analysis by electron diffraction and high-resolution electron microscopy and the measurement of the Raman spectra on these individual nanostructures. Several important environmental effects were evidenced for the first time, e.g. the effect of mechanical coupling (van-der-Waals interaction) between the layers of double-walled carbon nanotubes leading to the change in the low-frequency Raman modes and the optical resonance conditions. Moreover the behaviour of high-frequency modes of double-walled tubes was also analysed and described. As a result of this work several experimental criteria for structure diagnostics of multi-walled carbon nanotubes were proposed.

Keywords: Carbon nanotubes, Raman spectroscopy, Electron diffraction, Coupling

Résumé

L'objectif principal de ce travail est l'étude fondamentale de nanostructures à base de carbone individuelles dans le but d'améliorer la compréhension de leurs propriétés vibrationnelles et optiques intrinsèques ainsi que d'estimer et de quantifier les effets d'environnement. Dans ce but, nous avons synthétisé des nanotubes de carbone mono- et multi-feuillets par décomposition catalytique en phase vapeur sur des substrats dédiés. L'aspect principal du travail est basé sur l'utilisation combinée de plusieurs sondes expérimentales sur la même nanostructure carbonée individuelle. Nous avons effectué une analyse structurale complète par diffraction électronique et microscopie électronique haute résolution et mesuré les spectres Raman de ces nanostructures individuelles. Plusieurs effets environnementaux importants ont été mis en évidence pour la première fois, comme par exemple l'effet d'un couplage mécanique (due à l'interaction de van-der-Waals) entre les parois des nanotubes bi-feuillets conduisant à une modification des modes Raman de basse fréquence et des conditions de résonances optiques. De plus, le comportement des modes de haute fréquence des nanotubes bi-feuillets a été analysé. Suite à ce travail plusieurs critères expérimentaux permettant un diagnostic de la structure des nanotubes multi-feuillets ont été proposés.

Mots clés : nanotubes de carbone, spectroscopie Raman, diffraction électronique, couplage

Acknowledgement

This work was carried out during the years 2010-2013 in the heart of Laboratoire Charles Coulomb of the University Montpellier 2 in France and at the Physics Faculty of the Southern Federal University in Russia. Such a “co-tutelle” format of the thesis has brought me an invaluable research and personal experience and it is a pleasure to thank those who made it possible.

I owe sincere and earnest thankfulness to my Russian mentor Prof. Yuri Yuzyuk who guided me since my early days at the Physics Faculty. I am grateful for his continuous support of my study and research, for his patience and enthusiasm. In 2007, long before the PhD thesis, it is with the help of Yuri I met my future French mentor Dr. Jean-Louis Sauvajol. Jean-Louis kindly agreed to guide my first steps in the field of carbon nanotubes and that determined the next 6 years of my scientific career. I cannot even express how greatly the work with Jean-Louis motivated me, but for sure without his immense knowledge and his constant support, this thesis would not be possible.

I would like to thank my jury members Dr. Stéphane Berciaud, Prof. Luc Henrard, Prof. Vladimir Lorman, Dr. Raul Arenal, Prof. Christophe Voisin who agreed to revise my manuscript and for their insightful comments and hard questions. I also express my gratitude to Ahmed Zahab for being my committee member during all three years of the thesis.

I would like to show my gratitude to Dr. Raul Arenal who kindly received me in the Institute of Advanced Nanoscience of Aragon and helped me to develop the expertise in the electron microscopy and electron diffraction. Besides, I am also obliged to many of my French colleagues, namely: Dr. Laurent Alvarez, David Maurin, Jean-Christophe Art, Adoration Gabillard and other members of Laboratoire Charles Coulomb who were always kind and helped me one way or another during my work in France. Especially, I want to thank Dr. Matthieu Paillet for fruitful discussions and for his readiness to assist in my work even to the detriment of his own scientific experiments.

I would like to thank the French Embassy in Moscow for the financial support of my PhD work.

I am also indebted to the many of my Russian friends and colleagues for the support during my stay in Russia: Andrei Anokhin, Alexey Mikheykin, Nicolai Lyanguzov, Anna Razumnaya and Olga Konevstova. Our convivial meetings inside and outside the university always encouraged and kept me positive.

I cannot find words to express the gratitude to my parents Igor Levshov and Larisa Levshova and to my grandparents. They were those I could always rely on and this work would not be possible without them. I'm also very glad to realize that I found a new family in Montpellier: my friends Tatyana Sotnikova, Ksenia Zhirova and Denis Chepaykin. I will always remember your cordial welcome, your readiness to help, your smiles and our cheerful meetings during my days in France. I hope that our friendship will last for a long time.

Finalement, je voudrais écrire ce dernier paragraphe en français pour signifier ce que la France, sa culture et sa langue sont devenus pour moi après ces 3 années d'études. Depuis 2010, j'ai appris beaucoup des choses mais je reste toujours convaincu que ce n'est que le début. Je suis maintenant passionné de la culture française et j'aimerais en savoir plus. Sans nul doute, la personne qui m'a le plus apporté en cette matière c'est mon co-directeur de thèse et ami, le Dr. Thierry Michel. Il n'était pas seulement celui qui passait le plus de temps avec moi en laboratoire en faisant des manipulations et en dépouillant des données, mais aussi la personne avec qui je me sentais toujours à l'aise. Je dois le remercier pour sa bonne volonté de répondre à mes questions et de m'aider dans n'importe quelle situation. Je me souviens, avec sourire, nos voyages en Espagne, des soirées non-scientifiques et la dégustation de vin à la campagne. J'espère qu'un jour on se reverra et ça sera alors à mon tour de lui recommander du bon vin au restaurant. Merci d'avoir su développer l'engouement que j'ai pour la culture française.

Dmitry Levshov

Contents

General introduction	1
Chapter 1: Introduction to carbon nanotubes	3
1.1 Single-walled carbon nanotubes	4
1.1.1 Atomic structure.....	4
1.1.2 Electronic Properties	6
1.1.3 Types of single-walled carbon nanotubes	9
1.1.4 The “Kataura plot” and excitons in single-walled carbon nanotubes	10
1.1.5 Raman spectroscopy of single-walled carbon nanotubes.....	12
1.2 Double-walled carbon nanotubes	23
1.2.1 Structure and configurations	23
1.2.2 Electronic properties of DWNTs	23
1.2.3 Raman spectroscopy of DWNTs.....	25
1.3 Triple-walled carbon nanotubes	30
Summary.....	32
References of Chapter 1	33
Chapter 2: Synthesis and structural identification of individual carbon nanotubes	40
2.1 The synthesis of ultra-long individual nanotubes	41
2.2 Localization of as-grown individual carbon nanotubes.....	47
Summary.....	50
2.3 Structure identification of individual carbon nanotubes.	51
2.3.1 Introduction and experimental section.....	51
2.3.2 Electron diffraction of carbon nanotubes	52
Summary.....	64
2.4 Results. Index-assignment. Data treatment and existing problems.	65
2.4.1 Single-walled carbon nanotubes	65
2.4.2 Double-walled carbon nanotubes	70
2.4.3 Triple- and multi-walled nanotubes.....	77
2.5 Conclusion.....	78
References of Chapter 2.	79
Chapter 3: The study of vibrational and optical properties of individual single-walled carbon nanotubes.	82

3.1 Raman spectroscopy of individual single-walled carbon nanotubes.	83
3.1.1 Radial Breathing Modes. The nature of ω_{RBM} vs d relations.	83
3.1.2 Experimental measurements of diameter dependence of RBM frequencies.	84
Summary.....	88
3.2 Additional experimental results on the index-identified individual SWNTs.....	89
3.3 The presence of strains or external pressure.....	93
3.4 The nature of environmental effects in ω_{RBM} vs d relations	96
3.4.1. The change of elastic constants	98
3.4.2. The change of mass density ρ due to contamination (chemical doping or adsorption).....	98
3.4.3. The presence of environmental interaction.....	100
Summary.....	106
3.5 The G-modes (or Tangential modes)	107
3.6 Optical transitions of individual free-standing SWNTs from the measurements of the excitation profile of the RBM and G-modes	112
3.7 Raman spectroscopy of bundles of single-walled nanotubes.	115
3.8 Conclusion.....	121
Reference of Chapter 3	122
Chapter 4: Raman spectroscopy of individual free-standing double-walled carbon nanotubes.....	125
4.1 Raman spectroscopy of (12,8)@(16,14) DWNT. First direct evidence of mechanical coupling in a DWNT	126
4.1.1 Structural information.....	127
4.1.2 The Radial breathing-like modes	128
Summary.....	136
4.1.3 Discussion and comparison with other experimental and theoretical studies.	138
4.2 G-modes of DWNTs.	147
4.3 Sensitivity of individual DWNTs to environment.	158
Summary.....	162
4.4 Understanding of Raman data measured on non-index identified DWNTs.	163
4.5 Optical transitions of individual free-standing DWNTs from the measurements of the excitation profile of the RBM and G-modes	165
4.6 Conclusion.....	167
Reference of Chapter 4	168

Chapter 5: Combination of Electron Diffraction and Raman spectroscopy for the index assignment of carbon nanotubes.	170
5.1 Introduction	171
5.2 Presentation of our identification procedure and of an adapted software	172
5.3 Combination of RRS and ED for the index assignment of a SWNT	174
5.4 Combination of RRS and ED for the index assignment of a TWNT	178
5.5 Conclusion	183
References of chapter 5	185
General conclusions	186

General introduction

Carbon nanotubes (CNTs) are tiny hollow cylinders made up of carbon atoms. They may be considered as single molecules or quasi-one dimensional crystals at the same time. Due to their unique physical properties, nanotubes are very promising candidates for the modern electronics, photonics and for the field of constructional materials. However, for the successful use of the nanotubes we need to clearly understand their fundamental properties and the role of environmental interactions in their behaviour.

Hence, the main objective of this work was the study of individual isolated carbon nanostructures in order to address their intrinsic vibrational and optical properties and also to evidence, estimate and quantify the environmental effects. For these purposes, we planned to synthesize by CCVD method a high number of individual single- and multi-walled carbon nanotubes and to achieve their isolation from the environment by means of special substrates and sample preparation techniques. The main aspect of the work involved combined experimental studies — in a perfectly controlled environment — on the same individual nanostructure. In other words, we performed a complete structure analysis of the grown nanotubes by electron diffraction and high-resolution electron microscopy techniques and thus measured vibrational and optical properties on index-identified nano structures which greatly facilitates subsequent data analysis.

Another aspect of the thesis concerned the characterization of the nanotubes by combination of Raman spectroscopy and Electron diffraction. Currently, the lack of the synthesis protocols for the controlled growth of the nanotubes by diameter, chiral angle and electronic type complicates the nanotube research. Thus the key role in both fundamental and applied science play metrology and characterization methods. As a result of this work we were going to propose several experimental criteria for structure diagnostics of multi-walled carbon nanotubes. In particular, a widely used assignment method based on Kataura plot, profile of G-modes and dependence of radial breathing modes (RBM) and G-mode frequencies on diameters was to be elaborated for the case of multi-walled carbon nanotubes by taking into the account the effect of van-der-Waals coupling between the layers. These criteria allow the determination of chiral indices of multi-walled nanotubes by means of Raman spectroscopy.

This thesis is organized into 5 chapters which includes the above mentioned topics. In Chapter 1 we introduce carbon nanotubes and their electronic, optical and vibrational properties. We also review the main advances in the field of Raman spectroscopy of single- and multi-walled carbon nanotubes. Then in Chapter 2 we present our experimental procedure for the

synthesis, localisation and structure characterization of individual ultra-long single- and multi-walled carbon nanotubes. We give several examples of the ED patterns treatment and discuss the existed ambiguities of the index-assignment based on the electron diffraction alone. In Chapter 3 we discuss the Raman spectroscopy of individual single-walled nanotubes (SWNTs) and individual SWNT bundles. In particular, we argue on the possible origin of the environmental terms in the experimental $\omega_{\text{RBM}}(d)$ relations and their deviations from the theoretical relations. In addition, we analyse the structure dependence of the features of G-modes in individual SWNTs and present the measurements of the resonant excitation profiles of RBM and G-modes for several nanotubes. Finally, we discuss the features of phonon modes of an identified inhomogeneous dimer (bundle of two different SWNTs). Chapter 4 is devoted to the Raman spectroscopy of individual double-walled nanotubes. The effect of van-der-Waals coupling is discussed and its consequence on the vibrational and optical properties of double-walled nanotubes is analysed. Besides, we present the analysis of the G-modes of DWNTs. Two types of behavior are evidenced. We explain these behaviors in terms of an effective pressure (which can be negative) between the walls of as-grown DWNT owing to variations in the inter-walls distance. Finally, in Chapter 5 we discuss the complementarity between the Electron diffraction and Raman spectroscopy to characterize CNTs and its application for the index-assignment of single- and multi-walled carbon nanotubes. We introduce a code developed for this particular purpose and give several examples of its use.

Chapter 1

Introduction to carbon nanotubes

1.1 Single-walled carbon nanotubes

In this Chapter we consider the geometrical, electronic, optical and vibrational properties of the carbon nanotubes and present a review of the Raman spectroscopy of individual single-, double- and triple-walled CNTs.

1.1.1 Atomic structure

We begin by introducing the basic concepts that determine properties of carbon nanotubes. Conceptually, a nanotube can be looked at as a rolled-up sheet of graphene, and it is thus common to describe its atomic structure via the graphene lattice vectors [1]. Geometrically we obtain SWNT by cutting the graphene sheet in the direction of the so-called chiral vector C_h and the translational vector T (see Fig. 1.1a). The former goes around the circumference of the final tube and is normally given by

$$C_h = n\mathbf{a}_1 + m\mathbf{a}_2 \quad (1.1)$$

Where \mathbf{a}_1 and \mathbf{a}_2 are the graphene lattice vectors and (n, m) are called the chiral indexes of a tube.

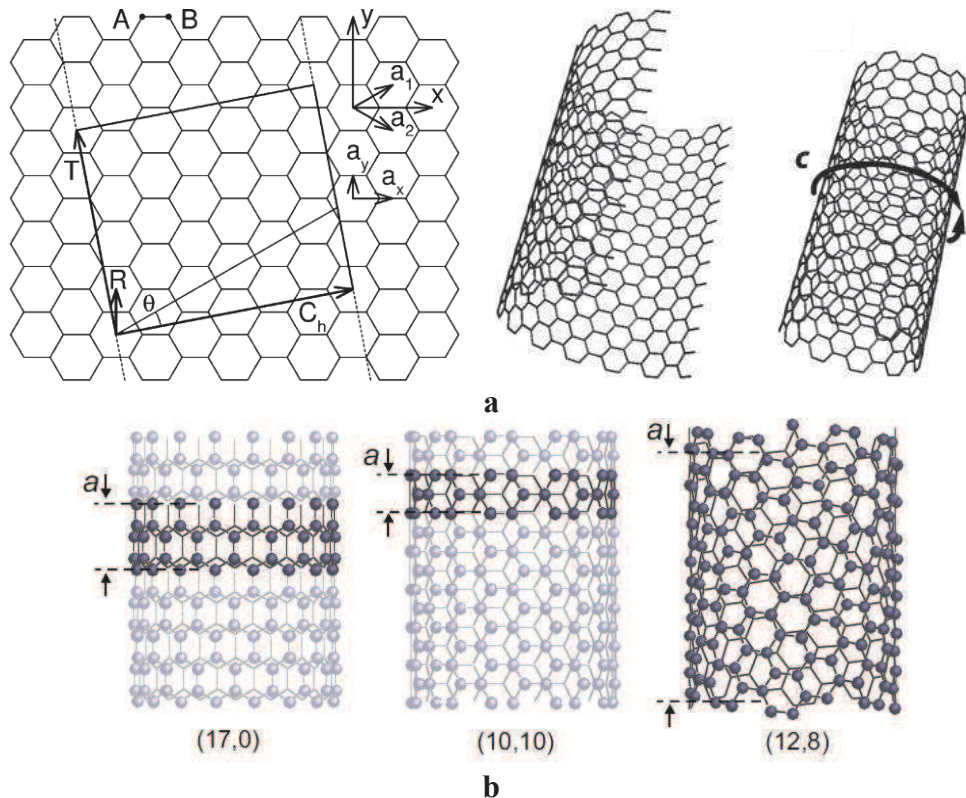


Fig. 1.1: (a) A graphene sheet and its roll-up into a nanotube. From [2,3], (b) Three geometrical type of carbon nanotubes: (17,0) zig-zag, (10,10) armchair and (12,8) chiral with corresponding unit cells shown in dark grey. From [1].

Table 1.1. Parameters of carbon nanotube [2].

Parameter	Definition
Graphene lattice constant a	$a = \sqrt{3}a_{c-c}$
Graphene unit vectors (x,y coordinates) $\mathbf{a}_1; \mathbf{a}_2$	$\left(\frac{\sqrt{3}}{2}, \frac{1}{2}\right)a; \left(\frac{\sqrt{3}}{2}, -\frac{1}{2}\right)a$
Graphene reciprocal lattice unit vectors (in k_x, k_y coordinates)	$\left(\frac{1}{\sqrt{3}}, 1\right)\frac{2\pi}{a}, \left(\frac{1}{\sqrt{3}}, -1\right)\frac{2\pi}{a}$
Chiral vector C_h Length of C_h	$C_h = n\mathbf{a}_1 + m\mathbf{a}_2 \equiv (n, m)$ $C_h = C_h = a\sqrt{n^2 + nm + m^2}$
Diameter d_t	$d_t = \frac{C_h}{\pi} = \frac{a\sqrt{n^2 + nm + m^2}}{\pi}$
Chiral angle θ	$\cos\theta = \frac{2n + m}{2\sqrt{n^2 + nm + m^2}}$
Greatest common divisor d	$\text{gcd}(n, m)$
Greatest common divisor d_R	$\text{gcd}(2n + m, 2m + n) \begin{cases} d \text{ if } (n - m) \text{ is not a multiple of } 3d \\ 3d \text{ if } (n - m) \text{ is a multiple of } 3d \end{cases}$
Number of hexagons in the nanotube unit cell q	$q = \frac{2(n^2 + nm + m^2)}{d_R}$
Number of atoms in the unit cell n_c	$n_c = 2q = \frac{4(n^2 + nm + m^2)}{d_R}$
Translational vector T along nanotube axis Length of T	$T = t_1\mathbf{a}_1 + t_2\mathbf{a}_2 = \frac{2m + n}{d_R}\mathbf{a}_1 - \frac{2n + m}{d_R}\mathbf{a}_2 \equiv (t_1, t_2)$ $T = T = \frac{\sqrt{3}C_h}{d_R} = \frac{a\sqrt{3(n^2 + nm + m^2)}}{d_R}$
Wavevector K_1	$K_1 = -\frac{t_2\mathbf{b}_1 - t_1\mathbf{b}_2}{q}$ $K_1 = K_1 = \frac{2}{d_t}$
Wavevector K_2	$K_2 = \frac{m\mathbf{b}_1 - n\mathbf{b}_2}{q}$ $K_2 = K_2 = \frac{2\pi}{T}$
Line group / Isogonal point group	chiral tubes $T_q^r D_n / D_q$ achiral tubes $T_{2n} D_{nh} / D_{2nh}$

There exist infinitely many geometrical ways to form a nanotube resulting in different diameters and microscopic structure of the tubes [1]. However, all parameters, for example tube's diameter, chiral angle θ , unit vectors, number of atoms in the unit cell, etc. can be deduced from (n,m) numbers in a straightforward way. In the Table 1.1 we present the compilation of these data.

1.1.2 Electronic Properties

The electronic properties of carbon nanotubes depend strongly on their microscopic structure. A small change in the tube's chirality [take as an example two geometrically similar single-wall nanotubes $(10,7)$ and $(10,6)$] may lead to two different types of conductivity (metallic and semiconducting respectively). The simplest way to explain this behavior is to consider a zone-folding approach for calculating electronic properties of a nanotube.

Zone folding maps the reciprocal space of the graphene layer onto the reciprocal space of a carbon nanotube by constructing so-called cutting lines based on the geometrical structure of the carbon nanotube. The concept of cutting lines can easily be understood from the fundamental principles of quantum mechanics. Along the nanotube circumference electrons, phonons and other quasi-particles can only have certain, discrete wavelengths, because of the periodic boundary conditions [1, 2, 4, 5-9]. At the same time along the nanotube axis quasiparticles are not quantified. An infinitely long tube has continuous electronic and vibrational states in this direction [1]. These features of electron wavevectors are represented by the q cutting lines in the reciprocal space of a nanotube (q is a number of hexagons in the unit cell of the nanotube, see Table 1.1 for details) (see Fig 1.2. a,b,c) [2].

The cutting lines can be shifted by the unit vectors \mathbf{b}_1 and \mathbf{b}_2 in the reciprocal space of the graphene to completely cover its first Brillouin zone (as shown in Fig. 1.2d by solid lines; dashed lines denote the ends of the cutting lines). The two alternative representations of the cutting lines plotted in Figure 1.2c and d are called the *fully \mathbf{K}_1 -extended* representation and the *fully reduced* representation. For simplicity, the latter is used in the following to deduce electronic properties of CNT [2].

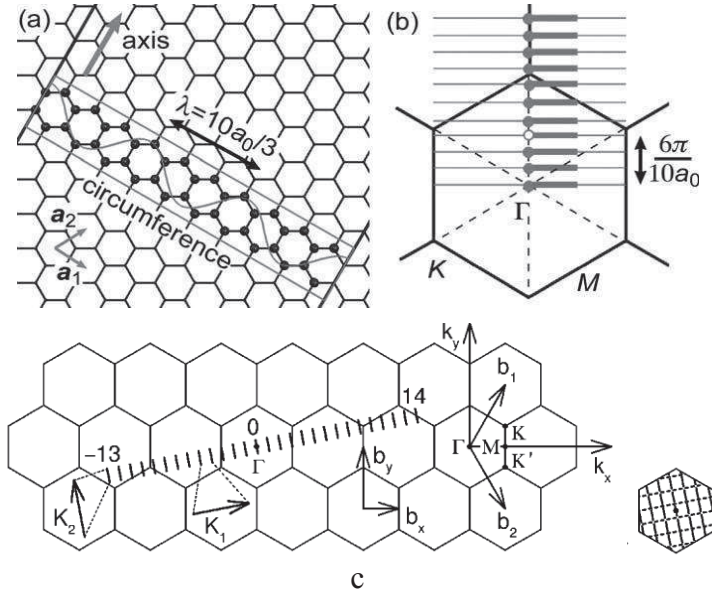


Fig. 1.2: (a) (10,0) nanotube unwrapped to a graphene sheet. The atoms shown are those inside the unit cell of the tube. The gray line is a wave which corresponds to an allowed state of the nanotube. (b) Allowed, discrete wavevectors of a (10,0) tube shown in the Brillouin zone of graphene. The wave in (a) corresponds to the open circle in (b). The thick lines form the one-dimensional Brillouin zone of the (10,0) tube [1]. (c) Fully K_1 -extended and the fully reduced representations for a general chiral nanotube [2]

To proceed further we need to introduce the electronic properties of graphene. Graphene is a semimetal, in other words its valence and conduction bands cross, but the electronic density of states is zero at the Fermi level (the crossing point). The most widely used description of the electronic band structure of graphene is an empirical tight-binding model [4, 5, 10], which consider only the π states perpendicular to the graphene sheet. In this model under the nearest-neighbor approximation the valence (E^-) and conduction (E^+) bands of graphene will be given by the simple analytic expression [1,5,10]

$$E^\pm(k) = \gamma_0 \sqrt{3 + 2\cos(\mathbf{k} \cdot \mathbf{a}_1) + 2\cos(\mathbf{k} \cdot \mathbf{a}_2) + 2\cos(\mathbf{k} \cdot (\mathbf{a}_1 - \mathbf{a}_2))} \quad (1.2)$$

where γ_0 describes the interactions energy between two π electrons, \mathbf{k} is the electronic wavevector for the graphene Brillouin zone.

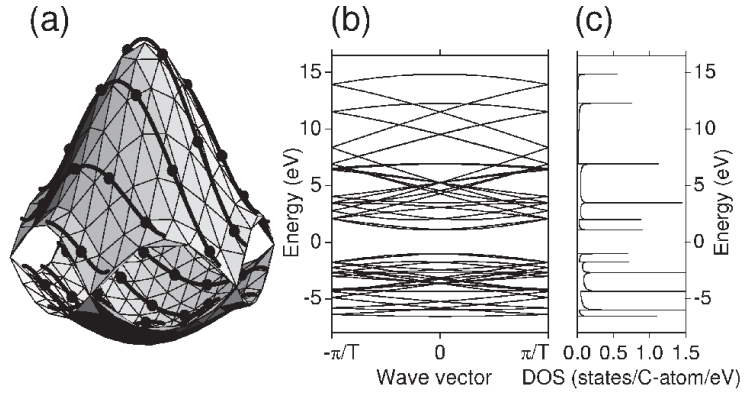


Fig. 1.3: (a) The conduction and valence bands of the graphene layer in the first Brillouin zone calculated according to the π -band nearest-neighbor tight-binding model. Solid curves show the cutting lines for the (4, 2) nanotube in the fully reduced representation. Solid dots show the ends of the cutting lines in the fully \mathbf{K}_1 -extended representation; Note that formula 2 predicts symmetric conduction and valence bands, while in the Fig. 3a they are asymmetric; the difference is due to different approximations used in [1] and [2] (b) Band diagram for the (4, 2) nanotube obtained by zone-folding from (a). (c) Density of electronic states for the band diagram shown in (b). From [2].

If we now superimpose q cutting lines on the energy-momentum contours of these valence and conduction bands in the first Brillouin zone, (Figure 1.3a), we will obtain $2q$ electronic energy subbands in the 1D reciprocal space of the nanotube (Fig. 1.3b) [2]. The band structure for a general (n, m) nanotube will be then given by:

$$E_c^\pm(K_1, K_2) = \gamma_0 \sqrt{3 + 2 \cos\left(p \frac{2n+m}{qd_R} - \frac{m}{q} K_2\right) + 2 \cos\left(p \frac{2m+n}{qd_R} + \frac{nm}{q} K_2\right) + 2 \cos\left(p \frac{n-m}{qd_R} - \frac{n+m}{q} K_2\right)} \quad (1.3)$$

where p is an integer running from $-(q/2-1)$ to $q/2$ [11]

Figures 1.4 shows the electronic band structure of a (10,10) nanotube. Part (a) in the figure is from first-principles calculations, while part (b) was obtained with equation (1.3) (i.e. nearest neighbors Tight Binding, nT.B.), and part (c) is the result of the extended tight-binding model using up to third neighbors [4]. As can be seen, for all practical purposes, the extended tight-binding model is indistinguishable from the ab-initio calculations. The simple nearest-neighbors tight-binding scheme also works reasonably well.

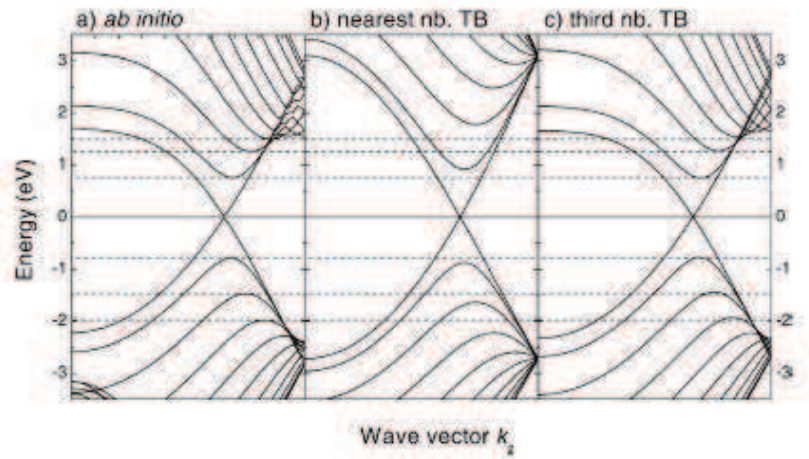


Fig. 1.4: Band structure of a (10,10) armchair nanotube with diameter $d = 1.4$ nm. (a) Ab-initio calculation; (b) nearest-neighbor tight-binding calculation with $\gamma_0 = -2.7$ eV; (c) third-nearest neighbors tight-binding calculation. The dashed lines denote ab-initio calculated energies of the band extrema. The agreement of the energies in (a) and (c) is excellent [4]

1.1.3 Types of single-walled carbon nanotubes

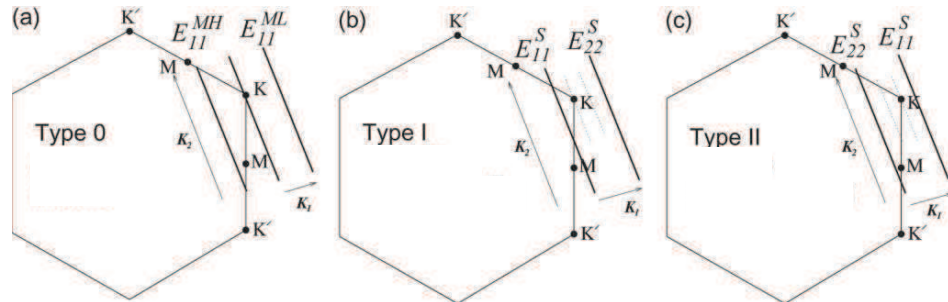


Figure 1.5: Cutting lines near the K point in the 2D Brillouin zone of graphene for (a) Type metallic SWNTs, (b) Type I and (c) Type II semiconducting SWNTs. From [12].

To determine whether a given nanotube is metallic or semiconducting, we consider its cutting lines in the fully reduced representation and check whether the projection of the vector \mathbf{K} (pointing toward the nearest K point in the Brillouin zone) on the \mathbf{K}_1 direction contains an integer (metallic) or a fractional (semiconducting) number of vectors \mathbf{K}_1 . Using the expression for the vector \mathbf{K}_1 derived, one can easily find that $(\mathbf{K} \cdot \mathbf{K}_1) / (\mathbf{K}_1 \cdot \mathbf{K}_1) = (2n+m)/3$ [2]. Thus for semiconducting nanotubes of type I (II) the K point lies at the one-third (two-thirds) position between two cutting lines, while for metallic tubes it is exactly on the cutting line (Type 0, as illustrated in the Fig. 1.5) [12]. This classification is frequently used in the literature (see however Table 1.2 for details).

Table 1.2: Frequently used classifications for a general nanotube in the literature [1]. It should be pointed out that there exist two equivalent classifications of the nanotubes by their electronic behavior, namely ‘Type’ classification by Saito et al and ‘family’ classification by Reich et al.

Classification	Definition	Remark
Nanotube’s family ν (by Reich et al [1])	$\nu = (n - m) \bmod 3 = \begin{cases} 0 & \text{– metallic 0 family} \\ +1 & \text{– semiconducting + 1 family} \\ -1 & \text{– semiconducting - 1 family} \end{cases}$	These two classifications are basically equivalent as 0 family \equiv Type 0 +1 family \equiv Type 2 -1 family \equiv Type 1
Nanotube’s type ν' (by Saito et al [12])	$\nu' = (2n + m) \bmod 3 = \begin{cases} 0 & \text{– metallic type 0} \\ 1 & \text{– semiconducting type I} \\ 2 & \text{– semiconducting type II} \end{cases}$	
Branch index β	$\beta = 2n+m = \text{const}$ Nanotubes in the same branch, so-called, neighbors are connected by the following relation: $(n',m') = (n-1, m+2)$ for $n' < n, m' > m$	In a branch (n',m') is a ‘neighbor to the right’ for a (n,m) nanotube

1.1.4 The “Kataura plot” and excitons in single-walled carbon nanotubes

The electronic density of states of a carbon nanotube (Fig. 1.3c) is dominated by van Hove singularities (VHS), which are kinks in the density of states (DOS). Each VHS in the DOS profile arises from different conduction or valence band extrema (compare Fig. 1.3b and c for example) [2]. Metallic nanotubes have a constant density of states in-between the pair of van Hove singularities closest to the Fermi level, while semiconducting nanotubes have a chirality-dependent energy gap that is on the order of 1 eV and spans the region between the van Hove singularities for filled and empty states [13].

When discussing the electronic band structure of carbon nanotubes we found two dependences on the nanotube chirality through zone folding: The separation between two lines of allowed wavevectors is given by $2/d$. On the other hand, the direction of the allowed lines with respect to the graphene Brillouin zone is connected with the chiral angle θ . The optical transition energies depend, consequently, on these two parameters. Calculating the maxima in the band-to-band absorption probability (the energy separation of the van-Hove singularities) for an ensemble of nanotubes and plotting them as a function of the tube diameter d , we obtain the so-called Kataura plot, Fig. 1.6a. The plot is named after Hiromichi Kataura, who first used it in connection with optical spectroscopy [14]. The energies follow roughly $1/d$. The deviations from

this trend reflect the chiral-angle dependence of the optical (absorption and photoluminescence) spectra [3].

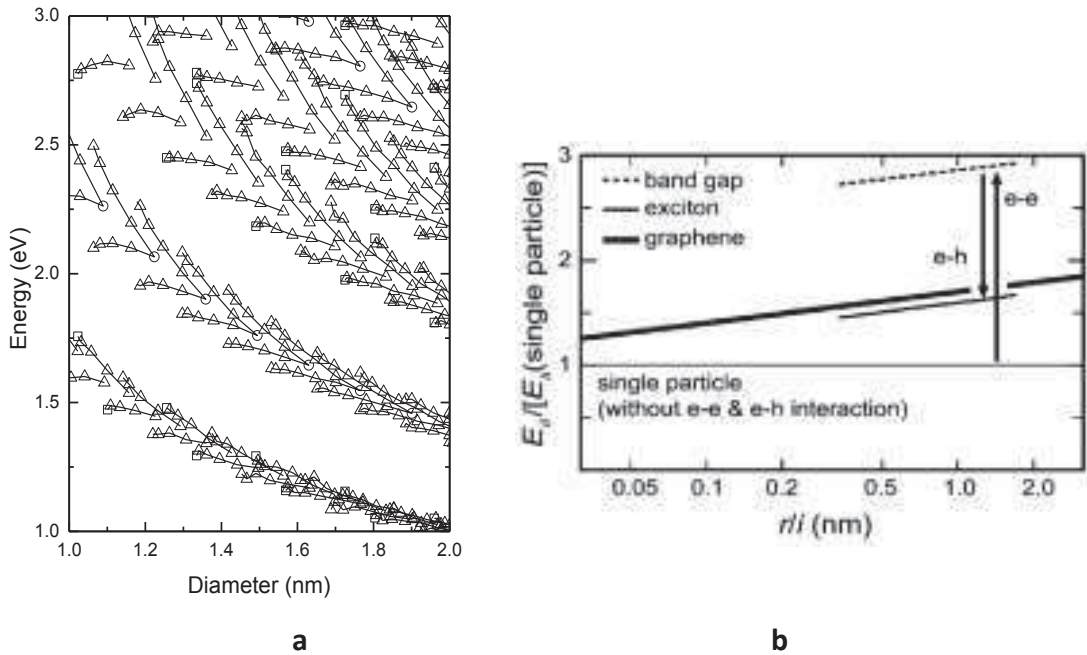


Fig. 1.6. (a) A Kataura plot. **(b)** The many-body effects on the band-to-band transitions. Electron–electron interaction increases the separation between the i th valence and conduction band (dashed lines) by approximately 1.8 eV compared to the single-particle picture (horizontal full line at 1). The binding energy due to electron–hole interaction is around 1.3 eV. The excitonic transitions (full thin lines) are blue shifted compared to the band-to-band transitions. The full thick line was obtained by zone folding [3, 15]

It is worth noting that Kataura plot is widely used to assign the chirality of the nanotubes by Raman scattering and optical spectroscopy [17-21]. However, up to now we discussed the electronic properties of carbon nanotubes within the simple noninteracting electron model (considering only band-to-band transitions). In reality it was proven that electron-electron and electron-hole (e.g. exciton) interactions also play an important role in determining the optical transition energies in carbon nanotubes. Both theoretical calculations and experimental measurements show that the exciton binding energies are anomalously large in carbon nanotubes, corresponding to a substantial fraction of the band gap [22]. Interestingly, electron-hole and electron-electron interactions almost cancels each other and we observe only a slight increase in the energy of the nanotube’s optical transitions in comparison with the single-particle state (see Fig. 1.6b for details) [15,16].

1.1.5 Raman spectroscopy of single-walled carbon nanotubes

Raman spectroscopy appears to be one of the most powerful method for the study of vibrational and optical properties of carbon nanotubes. Its power particularly lies in the exploitation of the resonance effect, which arises from the presence of van Hove singularities in the electronic density of states. Since the discovery of carbon nanotubes the Raman experiments were largely performed on the bulk samples, namely in bundles and solutions (see Ref [1] for a review). Hence, the intrinsic Raman responses of carbon nanotubes were not directly accessible due to the presence of a huge number of different chiralities (aggregated in bundles) in a bulk sample. One way to solve this problem was to develop methods of isolation and sorting of nanotubes. Indeed, with time a substantial success with the separation of nanotubes by their (n,m) structural indices, metallicity (semiconducting or metallic) were achieved by different methods, especially density gradient centrifugation in combination with selective surfactant wrapping [23] or by gel chromatography [24]. However, the production of suspensions still required chemical modification of the CNT surface or addition of surfactants around the individual nanotubes inducing environmental effects [25]. For this reason, these types of samples are not suitable to determine the intrinsic Raman spectra of nanotubes.

Another way to deal with the environmental effects was the direct growth of individual isolated nanotubes on the substrate. A pioneering work of Jorio et al [26] combining AFM and Raman spectroscopy to study vibrational properties of isolated nanotube showed that Raman scattering from one carbon nanotube can easily provide its complete (n, m) structural information (see Fig. 1.7). Making (n, m) SWNT assignments with the Raman technique was to become a major advance for future SWNTs studies.

Nevertheless this approach wasn't ideal since: (i) AFM didn't provide full structural information about the nanotubes in question, (ii) it wasn't possible to independently confirm Raman spectroscopy-based assignments and (iii) the substrate itself can induce very important environmental effect that can modify the Raman spectra (frequencies and line shapes).

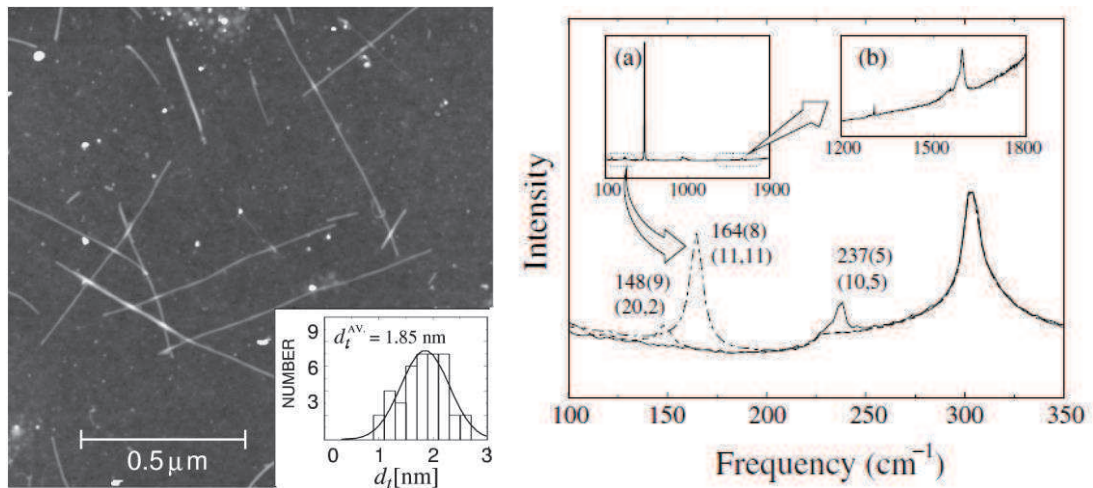


Fig. 1.7: (a) AFM images of the sample. The inset shows the diameter distribution of the sample taken from 40 observed SWNTs. (b) Raman spectra from three different spots on the Si substrate, showing only one resonant nanotube and one RBM frequency for each of 3 spots. From [26].

Finally it is worth noting that in this pioneer study a modelization of the nanotubes' electronic properties was required [26] and some index assignment made from Raman only have appeared to be false as claimed by the authors [42].

In 2005, our group in Montpellier developed a completely new approach based on the combination of several complementary techniques: Resonant Raman spectroscopy (RRS), high-resolution electron microscopy (HRTEM) and electron diffraction (ED) [27]. Initially individual SWNTs were grown by chemical vapor deposition on highly doped silicon substrates with a 200 nm silicon dioxide layer. Then lithographic Au/Cr markers were deposited onto the nanotubes using standard e-beam lithography procedure. Finally, the substrate under the nanotubes was etched by chemicals in such a way that there were air-suspended parts of nanotubes isolated from any environmental effects e.g. tube-tube and tube-substrate interactions. Complementary to Resonant Raman spectroscopy, electron diffraction was used on the very same nanotubes to have an independent determination of the nanotube structure.

From these combined measurements on precisely identified nanotube structures, a direct confrontation between the structure and the Raman active vibrations (that does not depend on any modelization of nanotube electronic properties) has been obtained. [27-30]. This work opened a new perspective for a successful study of intrinsic vibrational and optical properties of carbon nanotubes.

Below we present a brief overview of vibrational properties of carbon nanotubes known so far:

a) Phonon modes of single-walled carbon nanotubes

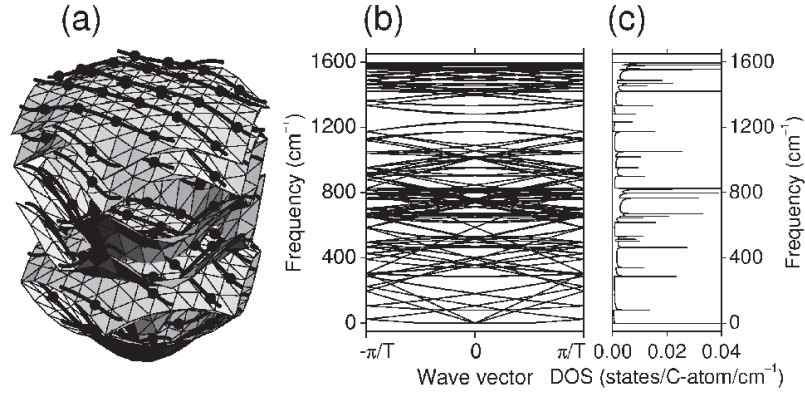


Fig. 1.7: (a) The phonon dispersion relations of the graphene layer in the first Brillouin zone calculated with the force constants fitted to the Raman scattering data for various graphitic materials [33]. Solid curves show the cutting lines for the (4, 2) nanotube in the fully reduced representation. Solid dots show the ends of the cutting lines in the \mathbf{K}_1 -extended representation. (b) Phonon dispersion curves for the (4, 2) nanotube obtained by zone-folding from (a). (c) Corresponding phonon density of states. From [2]

The phonon modes of carbon nanotubes can be treated in a way similar to electronic properties by applying the zone-folding scheme to the 2D phonon dispersion relations of the graphene layer (however, we note that this method is intuitive but not ideal, as it predicts badly the behaviour of the low-frequency vibrational modes). The phonon dispersion relations of the graphene layer can be calculated within a force constant model [5], by tight-binding [31] or ab initio [32] methods.

Two atoms A and B in the unit cell of the graphene layer give rise to six phonon modes, because of the three degrees of freedom per atom. Superimposing the q cutting lines in the \mathbf{K}_1 -extended representation on the six phonon frequency surfaces in the reciprocal space of the graphene layer yields $6q$ phonon modes for each carbon nanotube (see Fig. 1.7a,b). The $6(q/2-1)$ pairs of the phonon modes arising from the cutting lines of the indices μ and $-\mu$ (where $\mu = 1, \dots, (q/2 - 1)$) are expected to be doubly degenerate, whereas the 12 phonon modes arising from the cutting lines of the indices $\mu = 0$ and $\mu = q/2$ are non-degenerate. So the total number of distinct phonon branches is $3(q + 2)$ (q is the number of hexagons in the nanotube's unit cell) [2].

From all these $3(q+2)$ phonon modes only a small number is Raman-active. According to group theory, there are 8 Raman-active phonons in achiral and 14 in chiral nanotubes, namely [34-35]:

$$\text{armchair} \quad 2A_{1g} \oplus 2E_{1g} \oplus 4E_{2g}$$

$$\text{zigzag} \quad 2A_{1g} \oplus 3E_{1g} \oplus 3E_{2g}$$

$$\text{chiral} \quad 3A_1 \oplus 5E_1 \oplus 6E_2$$

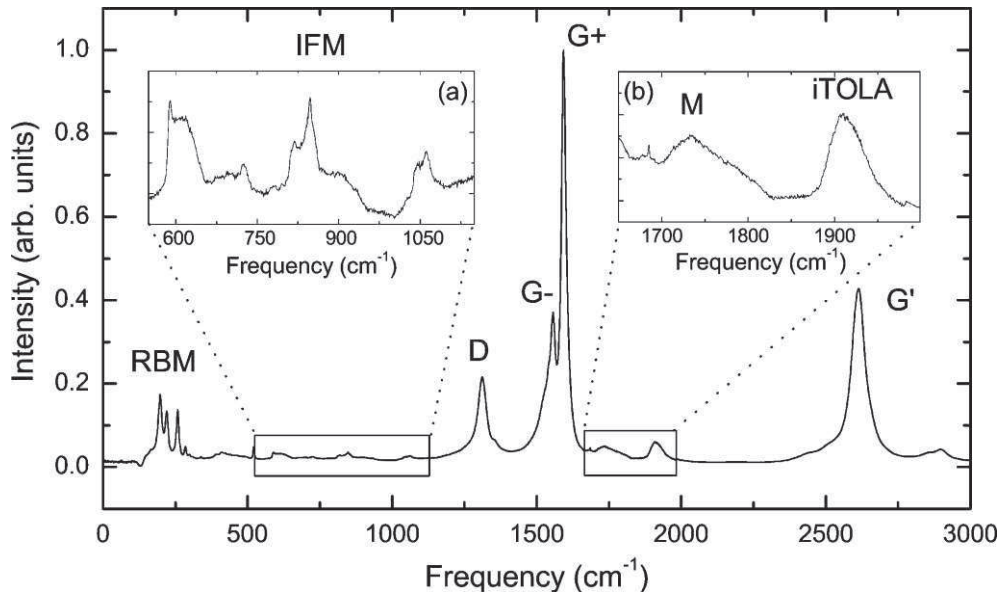


Fig. 1.8: Raman spectrum of SWNT bundles (HiPco) obtained with excitation laser energy $E_L = 1.96$ eV. From [36].

The corresponding Raman spectrum of SWNTs is shown in the Figure 1.8. It is dominated by totally symmetric phonons, namely the radial-breathing mode (RBM) and high-energy phonons (so-called G-band). The other Raman-active phonons are either very low in intensity or not observed at all [12]. Additionally, in the presence of disorder (e.g. defects) the K-point phonon of graphene gives rise to the D mode in the Raman spectra of nanotubes [12, 37-41]. The harmonic of the D mode, so-called 2D-band (or G' in some Ref [36]), is also observed in the spectrum even when there are no defects.

b) The radial breathing mode

The RBM is Raman active normal mode vibration where all the C atoms vibrate in phase in the radial direction, as if the tube is breathing. Since the atomic vibrational motion does not

break the tube symmetry, the RBM is a totally symmetric mode according to group theory, belonging to the A_1 symmetry irreducible representation [1].

The radial breathing mode has an important meaning for nanotube research and metrology. The fact is that its frequency depends inversely on the nanotube diameter and it is even possible to obtain an analytical expression for $\omega_{\text{RBM}}(d)$. This was first done by G.D. Mahan in his pioneering work [43], where he calculated the classical vibrational modes of a thin hollow cylinder composed of isotropic material. This approach remained valid for several years, until recently Rochal et al [44] proposed a new method within a continuous theory of SWNTs. He claims that predictions of Ref [43] for low-frequency vibrational modes seem to be not completely justified. The problem is related to the fact that graphene sheet in the Mahan's work is considered as a finite-thickness plate, though thickness in the continuous theory of membrane dynamics is an essentially macroscopic parameter. This means that continuous mechanics considers bending elasticity of a finite-thickness membrane as a result of the strain difference in the membrane's parts situated above and below its mid-surface. This relation is no more applicable to continuous mechanics of a membrane constituted by a single-atom layer (the case of graphene and carbon nanotube). In a self-consistent continuous model, single-carbon-atom graphene sheet should be considered as a 2D membrane. Corresponding bending elasticity of the 2D membrane is a purely topological quantity related to its curvature variation. Along the same line, all characteristics of the continuous mechanics theory for a 2D material membrane in a three-dimensional (3D) space are easily obtained using methods of differential geometry, in a way similar to classical 3D theory of elasticity.

To obtain an analytical solution for ω_{RBM} according to the theory of elasticity [45], we need to write down the free energy density of the zero-thickness 2D membrane:

$$g = \frac{\lambda}{2}(\varepsilon_{ii})^2 + \mu(\varepsilon_{ij})^2 + K(\Delta H)^2 \quad (1.4)$$

where λ and μ are 2D analogues of Lamé coefficients, K is topological bending rigidity, $\Delta H = H - H_0$, with H and H_0 standing for total and spontaneous mean curvatures of the surface, ε_{ij} is a 2D strain tensor.

Next, the equations of motion for the 2D membrane are obtained by variation of the functional:

$$A = \int L dSdt = \int \left(g(\mathbf{u}) - \frac{\rho \dot{\mathbf{u}}^2}{2} \right) dSdt \quad (1.5)$$

Where L is a Lagrangian, t is time, dS is the membrane area element, and ρ is the surface mass density.

In other words, by solving Euler-Lagrange equation:

$$\frac{\partial L}{\partial u} - \frac{d}{dt} \frac{\partial L}{\partial \dot{u}} = 0 \quad (1.6)$$

with Lagrangian in the approximation of the radial vibration defined as:

$$L(t, u, \dot{u}) = g(\mathbf{u}) - \frac{\rho \dot{u}^2}{2} = \left(\frac{\lambda}{2} + \mu\right) (\varepsilon_{ii})^2 - \frac{\rho \dot{u}^2}{2} = \left(\frac{\lambda}{2} + \mu\right) \left(\frac{u_r}{R}\right)^2 - \frac{\rho \dot{u}^2}{2} \quad (1.7)$$

The resulting equation of radial motion has the following form:

$$\ddot{u}_r \rho = -(\lambda + 2\mu) \frac{u_r}{R^2} \quad (1.8)$$

$$u_r = u_r^0 \cos(\omega t)$$

$$\omega = \frac{2}{d} \sqrt{\frac{\lambda + 2\mu}{\rho}} \quad (1.9)$$

where $d = 2R$ is a nanotube diameter.

Finally, we need to estimate the required material constants λ , μ , ρ from known graphene properties. In Rochal's work [44] the material constants of graphene sheet and carbon nanotube are assumed to be the same. This assumption is justified by the fact that the relation between the RBM frequency and SWNT diameter is practically independent on the nanotube chirality. In reality, due to the local isotropy breaking in the course of nanotube rolling from the graphene sheet the slight splitting and inessential change of material constants in a nanotube are possible.

For a 2D membrane (graphene), Rochal finds that

$$V_{iLA} = \sqrt{\frac{\lambda + 2\mu}{\rho}}, \quad V_{iTA} = \sqrt{\frac{\mu}{\rho}} \quad (1.10)$$

Where $V_{iLA} \approx 21.3 \text{ km/s}$ and $V_{iTA} \approx 13.6 \text{ km/s}$ are the sound velocities in graphene. Taking $\rho \approx 0.762 \text{ mg/m}^2$, he obtains the following reduced material constants: $\lambda/\rho \approx 2400 \text{ cm}^{-2} \text{nm}^2$, $\mu/\rho \approx 5200 \text{ cm}^{-2} \text{nm}^2$, $K/\rho \approx 12.5 \text{ cm}^{-2} \text{nm}^4$. This leads to:

$$\omega (\text{cm}^{-1}) = \frac{A}{d} = \frac{226 \text{ nm} \cdot \text{cm}^{-1}}{d (\text{nm})} \quad (1.11)$$

We note that the coefficient $A = 226 \text{ nm} \cdot \text{cm}^{-1}$ in eq. (1.11) may vary in some other theoretical and experimental works (227 in Ref [43] and 228 in Ref [55]). However, later in this thesis all the relations $226/d$, $227/d$ and $228/d$ are considered equivalent.

Nevertheless, most of the RBM experimental results in the literature have been fitted not to the eq. (1.11) but to the relation $\omega_{\text{RBM}}=A/d+B$, with values for the parameters A and B varying widely from paper to paper (see Ref [1] for a review). In the limit of the tube diameter going to infinity, we ideally expect $\omega_{\text{RBM}} \rightarrow 0$, suggesting that B is associated with an environmental effect, and the environmental conditions differ from one experimental system to another. This environmental effect is present in SWNTs surrounded by different surfactants [46,49,50,51,52], in bundles [48,54], in SWNTs sitting on a SiO₂ substrate [26], and even in tubes suspended in air by posts [53]. Araujo et al proposed a relation to unify all the ω_{RBM} results in the literature, [42]:

$$\omega_{\text{RBM}}^{\text{Lit.}} = \frac{227}{d} \sqrt{1 + C \cdot d^2}, \quad (1.12)$$

$$\text{where } C = \left[6 \frac{1-\nu^2}{Eh} \right] \left[\frac{K}{s_0^2} \right] \text{ nm}^{-2}$$

Parameter C represents the effect of the environment on ω_{RBM} frequency. K (in eV/Å²) gives the van der Waals interaction strength, s_0 is the equilibrium separation between the SWNT wall and the environment shell, E is the Young's modulus, ρ is the mass density per unit volume, ν is the Poisson's ratio, and h represents the thickness of the shell.

The several C values obtained by fitting the RBM results for different commonly found samples in the literature are given in Table 1.3.

Though it was recently experimentally shown that the isolated free-standing nanotubes free from external interactions have ω_{RBM} vs d relation with coefficient $C = 0$ (or equivalently $B = 0$) [55], it is still not clear why experiments performed in our group [53,55] on the isolated free-standing tubes give different results (see Fig. 1.10). We will come back to this problem in the Chapter 3.

Table 1.3: Environmental effects on the RBM frequency of different samples, as measured by the C factor in Equation 1.12.

C, nm⁻²	Sample	Reference
0	Water-assisted CVD	Araujo[42]
	Free-standing	Wang [55]
0.05	Hipco@SDS	Bachilo [49]
0.059	Alcohol-assisted CVD	Araujo [54]
0.065	SWNT@SiO ₂	Jorio [26]
0.065	Free-standing	Meyer [53]

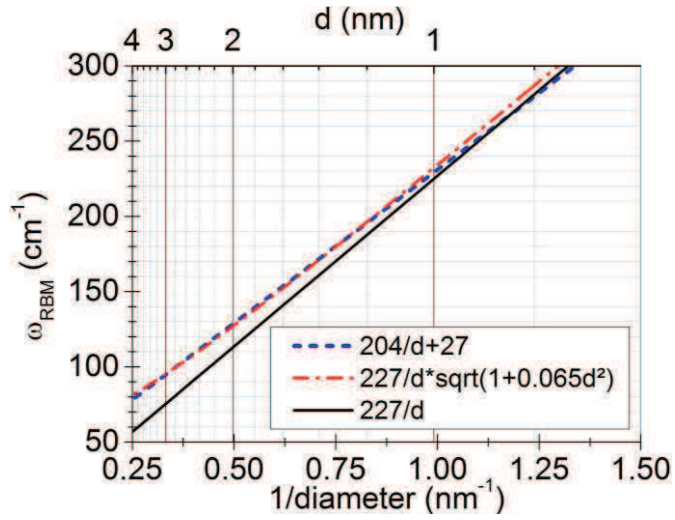


Fig. 1.10: RBM frequency vs. diameter for our individual suspended SWNTs. The two relationships $227/d * \sqrt{1 + cd^2}$ and $204/d+27$ are almost equivalent (note a deviation for diameters < 1 nm) in the diameter range of the CCVD-grown SWNTs. On the other hand, there is a difference of about 20 cm^{-1} between the $227/D$ and $227/d * \sqrt{1 + cd^2}$ for tubes having a diameter close to 2 nm as observed in our samples.

c) The G-modes or Tangential modes

In a 2D graphene the first-order Raman-active G-band mode is a single peak feature ($\omega_G \approx 1584 \text{ cm}^{-1}$) due to the degeneracy of the longitudinal optical (LO) and in-plane transverse optical (iTO) phonons [56]. However, in carbon nanotubes the curvature of the graphene sheet lifts this degeneracy and give rise to a bimodal G-band composed of a G^+ and G^- sub features (totally symmetric A_1 modes).

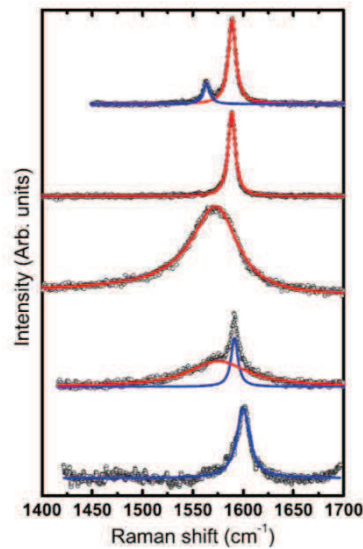


Fig. 1.10: The intrinsic Raman responses in the G-mode range of all the types of chiral and achiral SWNTs. From top to bottom: semiconducting chiral (11,10), semiconducting zigzag

(25,0), metallic zigzag (24,0), metallic chiral (19,16) and metallic armchair (10,10) SWNT. From [29].

Fig. 1.10 shows that the G-band profile depends strongly on the metal vs. semiconducting nature of the tube. Qualitatively, in a chiral semiconducting tube, the profile of each G-mode is narrow and symmetric. The high frequency mode, typically around 1590 cm^{-1} , is assigned to longitudinal mode (LO) and the low frequency mode to the transverse mode (TO). By contrast to the LO vibration, the frequency of the TO mode depends on the tube diameter (see paragraph below) [29].

In the case of chiral metallic SWNTs, the G-band spectra become soft and broad and are represented by the Breit–Wigner–Fano (BWF) lineshape [57]. The phonon softening phenomena for metallic SWNTs is understood by the electron–phonon interaction between phonons and free electrons at the Fermi energy, and are known as the Kohn Anomaly effect [12, 58]. The narrow high-frequency mode is observed typically around 1590 cm^{-1} , while the position of the broad low-frequency line again depends on the diameter. Moreover, in agreement with theoretical works [59, 60], the high-frequency and low-frequency components are assigned to the TO and LO modes respectively (as opposed to the semiconducting nanotubes).

In the case of armchair and zigzag nanotubes only one G-band sub feature is Raman-active: transverse optical (TO) and longitudinal optical (LO) modes respectively. The longitudinal vibration in this case denotes atomic motion along the tube axis and the transverse vibration corresponds to atomic motion perpendicular to the tube axis. For chiral nanotubes the atomic vibrations of the G-modes have a mixed character and depend on the chiral angle (see Fig. 1.11) [61,62].

In other words, the number of G-modes in the (*// //*) polarized Raman spectrum permits to identify the chiral or achiral character of the tube under investigation. A number of components greater than two identifies the measurement of a bundle or that of a multi-walled nanotube (for example, double- or triple-walled). The lineshape of the low frequency component clearly identifies the semiconducting or metallic character of the chiral tubes under investigation [29].

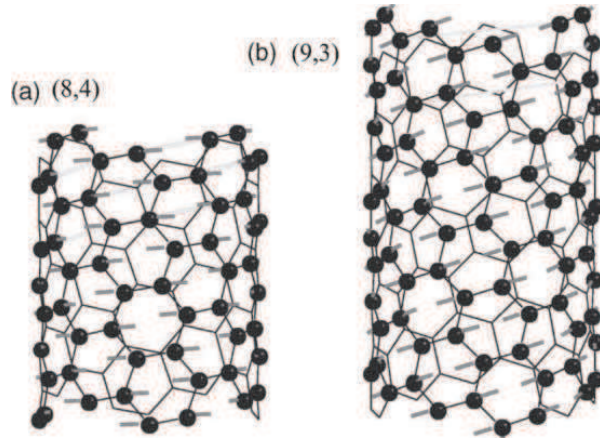


Fig. 1.11: (a) The totally symmetric G-band eigenvectors for the (8,4) semiconducting SWNT. The atomic displacements are almost parallel to the circumference. (b) The totally symmetric G-band eigenvector for the (9,3) metallic SWNT. The atomic displacements are almost parallel to the carbon–carbon bonds. From [62].

The diameter dependence of the G band phonon frequencies is displayed in the Fig. 1.12 below for semiconducting and metallic SWNTs.

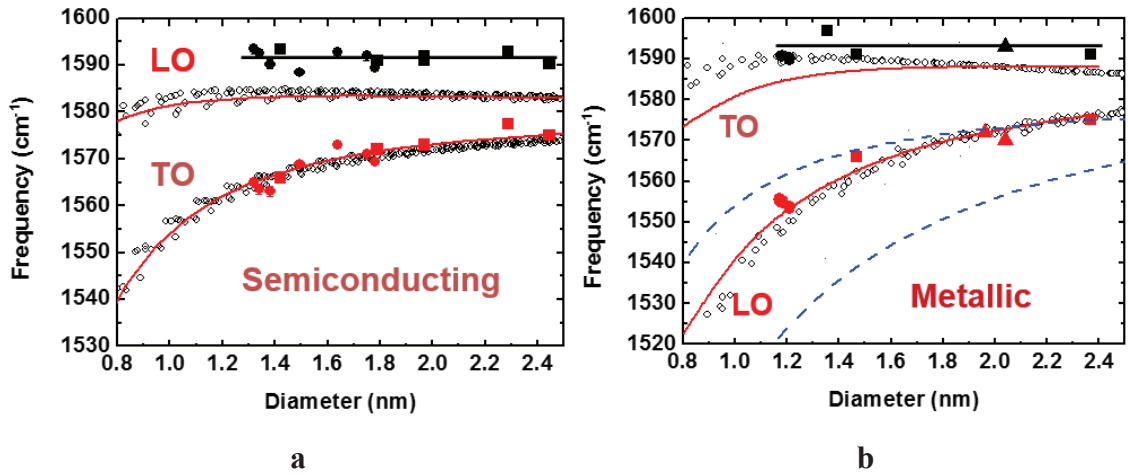


Fig. 1.12: Comparison between LO and TO phonons. (a) For semiconducting tubes: calculations; in adiabatic approximation (red dotted lines and open symbols, from [59] and [63] respectively). Solid symbols are experimental data measured on identified individual SWNTs. (b) For metallic tubes the phonon frequencies are calculated in adiabatic (blue dashed lines) and non-adiabatic approximation (red dotted lines and open symbols).

A diameter dependent downshift in frequency of the G-modes, coming from strain and from curvature-induced effect (out-of-plane components), is expected. In the time-independent perturbation picture (adiabatic approximation), the ω_{LO} G mode frequency is expected to be independent of diameter (especially for diameter larger than 1.2 nm), since the atomic vibrations are along the tube axis. In contrast, the ω_{TO} G mode has atomic vibrations along the tube circumference, and increasing the curvature increases the out-of-plane component, thus decreasing the spring constant with a $1/d^2$ dependence.

This picture holds for semiconducting SWNTs, where G^+ now stands for the LO mode, and G^- stands for the TO mode [64]. For instance, it was found recently that the experimental frequency of the G^- mode of semiconducting SWNTs can be fit with [65]:

$$\omega_{G^-} = 1582 - 27.5/d^2 \quad (1.12)$$

In the Fig. 1.12a, a comparison between the experimental data measured on identified individual semiconducting SWNT and calculations performed in an adiabatic approximation are displayed. A good agreement between these two sets of data and the recent results of Telg et al [65] is found.

For metallic SWNTs, on the other hand, it is necessary to take into account the non-adiabatic correction to describe the experimental dependence of the LO mode. This is directly associated with the strength of the electron-phonon coupling in metallic SWNT and the presence of Kohn anomaly at the Γ point.

Obviously, G-band frequency is also extremely sensitive to different external effects, for example doping [66] or strain [67].

1.2 Double-walled carbon nanotubes

1.2.1 Structure and configurations

A double-walled carbon nanotube (DWNT) has two concentric carbon layers. This structure makes DWNTs the simplest system for studying the effects of inter-wall coupling on the physical properties of CNTs. Compared to single-walled carbon nanotubes, DWNTs have higher mechanical strength and thermal stability and also possess interesting electronic and optical properties [68].

A DWNT can have one of four possible electronic configurations with each wall being either semiconductor (S) or metallic (M): S@S, M@S, M@M, and S@M (inner-tube@outer-tube). Every configuration may have different electronic properties (see Fig. 1.13)



Fig. 1.13: (a) Schematic of a S@M DWNT and its electronic structure. From [68].

1.2.2 Electronic properties of DWNTs

Electronic and optical properties of double-walled carbon nanotubes are strongly related to those of the participating SWNTs and in addition are modulated by the inter-layer interaction. This interaction directly depends on the inter-wall (wall-to-wall, interlayer etc.) distance. Calculations [69] demonstrated that the interlayer distance in a DWNT can vary from 0.33 to 0.41 nm, which is quite different from that of the normal MWNTs (0.34 nm). Indeed, experimental values for the interlayer distance were observed by HRTEM to be between 0.32 [70] and 0.42nm [71].

Theoretical models as described below were developed to find the lowest interaction energy between concentric tubes with respect to their inter-wall distance and tube-tube orientation. From the lattice symmetry point of view, the inner- and outer-tubes can be either incommensurate or commensurate. A DWNT is commensurate if the ratio between the unit cell

lengths of the inner and outer-tubes is a rational number and incommensurate if the ratio is irrational [72]. A commensurate DWNT has a periodical lattice structure while for incommensurate DWNTs the symmetry is broken. [73]. As a consequence of the general incommensurability between the inner- and outer-shell tubes, the unit cells of the DWNTs can be very large. Thus, the first principles calculations, i.e. DFT, can only be applied to selected tube pairs such as armchair–armchair or zigzag–zigzag tubes where commensurability is provided. In other cases, empirical potentials are used such as Lennard-Jones potentials for the intertube interaction and Brenner potentials or Tersoff potentials [74] for the covalent carbon–carbon interaction [75].

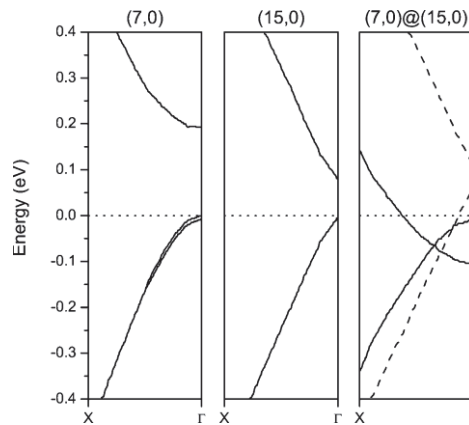


Fig. 1.14: Band structure of two SWNTs and the combined DWNT. The dashed bands in DWNT (the right part of the figure) are derived from the outertube bands, while the solid bands are derived from the inner-tube bands [75, 79].

For instance, Bellarosa et al [76] investigated the dependence of the ground-state energy for DWNT pairs with respect to wall-to-wall distance and chirality and found its weak chiral angle dependence. Moreover, Okada and Oshiyama [77] calculated ground-state energies for zigzag tubes [(7, 0), (8, 0), (10, 0)] in various outer zigzag tubes. It was found that the minimum ground-state energies for WtWD were slightly larger than the interlayer distance in graphite. For example, for a (7, 0) inner tube, the lowest energy was found for 0.35nm WtWD for a (16, 0) outer tube. While the (7, 0) and the (16, 0) tubes were semiconducting, the combination (7, 0)@(16, 0) turned out to be metallic. This metallization was due to a difference in the downshifts of energy bands between the inner-shell and outer-shell tubes. Due to a stronger σ - π rehybridization, the inner tubes, in particular the π^* -band, exhibits a stronger downshift, leading eventually to a finite DOS at the Fermi level.

Other calculations [78, 79, 80] confirmed these results. Figure 1.14 depicts electronic bands for (7, 0), (15, 0) and for (7, 0)@(15, 0) close to the Fermi level. Both isolated tubes exhibit a gap. For (15,0) tube it is induced by the curvature. Due to different energy-level

downshifts in the combination of the two tubes, the Fermi level is crossed by two bands. In this particular case the valence band and the conduction band from the inner tube become overlapping. For larger wall-to-wall distances, the different shifts of the inner tube π and π^* bands become weaker so that they no longer overlap. For larger-diameter inner tubes such as (8, 0), the downshift of the bands was smaller and did not lead to a metallic state.

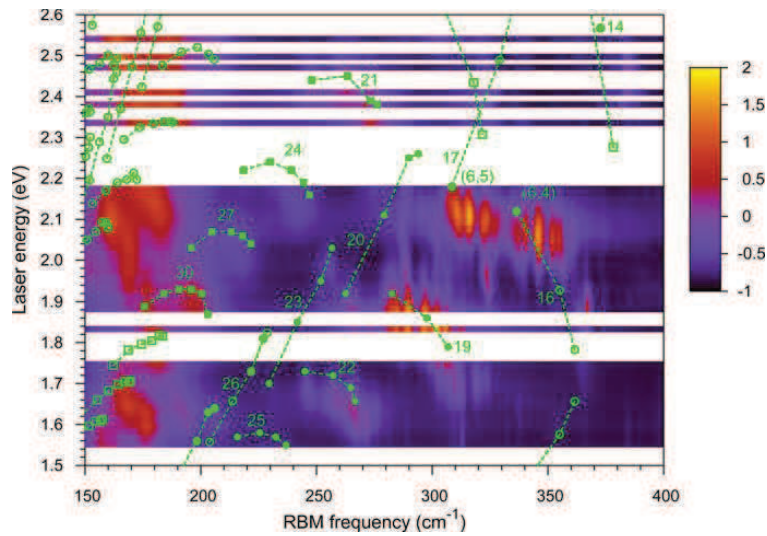


Fig. 1.15: Raman map for DWNTs. The color-coded Raman intensities represent the response from the outer-shell tubes (low-frequency side) and from the inner-shell tubes (main part of the figure). The open symbols depict values for individual tubes as calculated from a symmetry-adapted nonorthogonal tight-binding model corrected for many-body effects after. The full symbols represent experiments recorded for HiPco tubes. The dashed lines connect tube families $2m + n = \text{const}$. From [75].

The fact, that the inter-tube interactions drive the systems to a metallic state or at least noticeably reduce the gap energy, is consistent with the downshift of the electronic transitions for double-walled nanotubes, that was observed in [82] (see Fig.1.15). In the absence of large systematic experimental data on the optical properties of DWNTs, the Kataura plot established for individual single-walled carbon nanotubes may be used as a first approximation. However, in case of contradiction, the possible deviations due to complex character of DWNTs should be taken into account.

1.2.3 Raman spectroscopy of DWNTs

The Raman scattering is the main analytical tool to study structural bulk effects in DWNTs. However, as in the case of SWNTs spectroscopic experiments on DWNTs have been

largely performed on solution-based samples or in bundles [81-85]. For this reason, it has been difficult to identify and learn about the Raman spectroscopic signatures that are specific to individual DWNTs. Lately, more evolved experiments using combinations of different complementary techniques (e.g., atomic force microscopy (AFM), electron diffraction and Raman spectroscopy) were performed to measure the Raman spectra from the inner and the outer tubes of individual DWNTs [86, 87, 12].

One of the focuses of this work is the study of vibrational properties of DWNTs. The main discussion, especially related to the environmental effects, will be presented in the Chapter 4. Below, however, we review some important works that appeared mainly before 2010 (prior the thesis).

a) Radial-breathing like modes in DWNTs.

We present below two approaches for calculating radial breathing-like modes of DWNTs: the discrete model of Popov and Henrard [88] and the 2D continuous model of Rochal et al [44].

Discrete model

Popov and Henrard in the work [88] showed that the radial-breathing modes of double-walled nanotubes have a more complicated behavior than the ones in the individual SWNTs. The eigenmodes of the inner and outer tubes combine into in-phase and out-of-phase modes in the double-walled tube, and their coupling is described best by the graphite interlayer coupling strength. Using a valence-force field model, it was shown that the both coupled radial modes increase in frequency compared to the same tube in single-walled form (see Fig.1.16) [3, 88]. The first experimental observation of these radial breathing-like modes in individual and isolated DWNTs was made in the framework of this thesis and will be discussed in the Chapter 4.

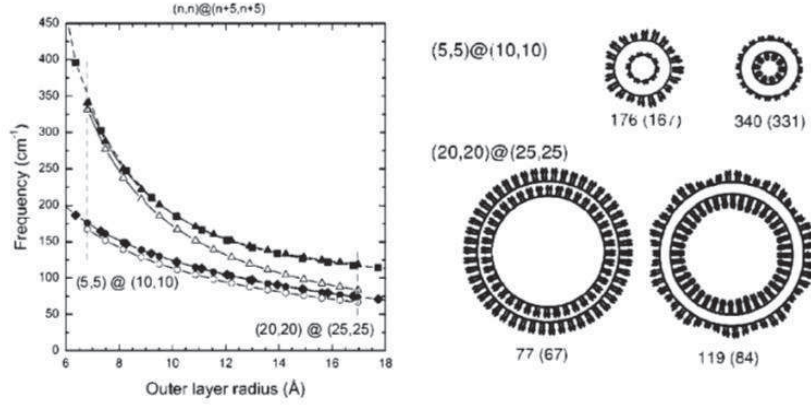


Fig. 1.16: (left) Frequencies of coupled radial-breathing modes in double-walled nanotubes as a function of the outer layer radius. Open symbols belong to uncoupled tubes of the same diameter, solid symbols to double-walled nanotubes. The coupled frequencies are always higher than the uncoupled ones. (right) Eigenvectors and eigenfrequencies (in cm^{-1}) of the radial-breathing mode of two different diameters DWNTs. In-phase and corresponding out-of-phase modes are seen. After [88].

The 2D continuous model [44]

The calculation of the RBLM frequencies of DWNTs is similar to the single-walled case. However, here we need to include the contribution of van der Waals interaction between co-axial SWNTs to the full free energy of the DWNT, namely:

$$U_{int} = \frac{G}{2} \int (u_r^{(1)} - u_r^{(2)})^2 d\phi dl \quad (1.13)$$

where $u_r^{(1)}$ and $u_r^{(2)}$ are the radial displacement fields of the first and the second nanotubes, respectively; G is a measure of van der Waals interaction .

Then, the full action of the system is expressed as a sum of actions (1.5) for two nanotubes plus a coupling contribution (1.13):

$$A = A_1 + A_2 + \int U_{int} dt \quad (1.14)$$

By solving Euler-Lagrange equation, we get the following system

$$\begin{vmatrix} \frac{\lambda+2\mu}{R_1} - R_1\rho\omega^2 + G & -G \\ -G & \frac{\lambda+2\mu}{R_2} - R_2\rho\omega^2 + G \end{vmatrix} = 0 \quad (1.15)$$

where R_1 and R_2 are the radii of the inner and outer tubes, respectively. Replacing $(\lambda + 2\mu)/R_1$ in Eq. (1.15) with ω_i^2 and introducing $G' = G/\rho$ we obtain bi-quadratic equation:

$$(R_1(\omega_1^2 - \omega^2) + G')(R_2(\omega_2^2 - \omega^2) + G') - (G')^2 = 0 \quad (1.16)$$

where ω_1 and ω_2 are the RBM frequencies of the inner and outer tubes in the absence of the interaction, respectively.

Equation (1.16) represents a user-friendly tool for the BLM behavior analysis.

Experimental observations

The interactions between the inner and outer-tubes were also observed by Pfeiffer et al [84]. They investigated the Raman response of the inner-tube RBMs in DWNTs and found that the number of observed RBMs is two or three times larger than the number of possible nanotubes in the studied frequency range. The discrepancy was reconciled by inter-wall interaction-induced splitting of the inner-tube Raman response (see Fig. 1.17) and also by the fact that several inner tubes can be accommodated in the same outer tube.

F. Villalpando-Paez et al. reported a detailed study of 11 individual C₆₀@SWNT peapod-derived DWNTs with a semiconducting (6,5) inner-tube and various outer metallic tubes [87]. They observed that the ω_{RBM} of the inner (6,5) semiconducting tube hardens as the diameter of the outer metallic tube decreases. In other words, the stronger the interaction, the further the inner-tube RBM shifts to higher frequencies.

Moreover, the intrinsic linewidth of the inner tubes can be as small as 0.4 cm⁻¹ [89]. This indicates rather long phonon lifetimes and thus remarkably defect-free inner tubes. Hence, the outer tube can be regarded as providing a nano clean room in which the inner tubes grow.

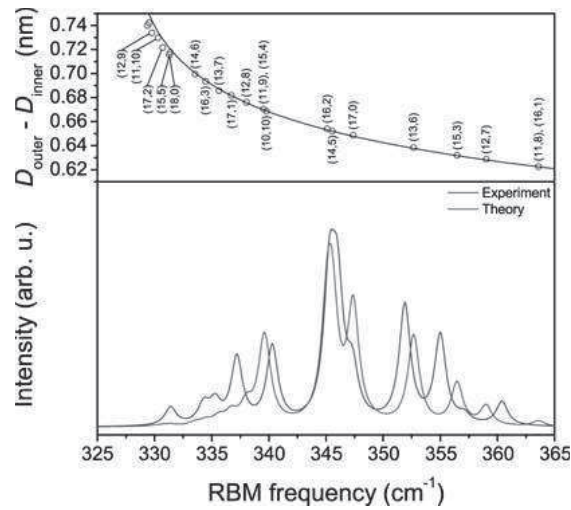


Fig. 1.17: Calculated RBM frequencies of inner-shell tubes as a function of wall-to-wall distance (top) and the constructed Raman response for the (6, 4) cluster and the spectrum obtained from the calculation with the frequencies dressed with Lorentzian lines (bottom). Constructed means the height of each peak was normalized to the maximum scattering intensity from the Raman map [81].

b) G-modes in DWNT

Several attempts were made to reveal the G-line components from the inner and outer tubes. F. Villalpando-Paez et al. observed a frequency upshift of $\omega(G^-)$ which was correlated with an upshifted ω_{RBM} for the inner nanotube [87]. Hence, they attributed the upshift of $\omega(G^-)$ to the increasing inter-tube interactions in the DWNTs (see Fig. 1.18 (a)). Yet there were no splitting of the G^+ and G^- components of the inner and outer tubes observed.

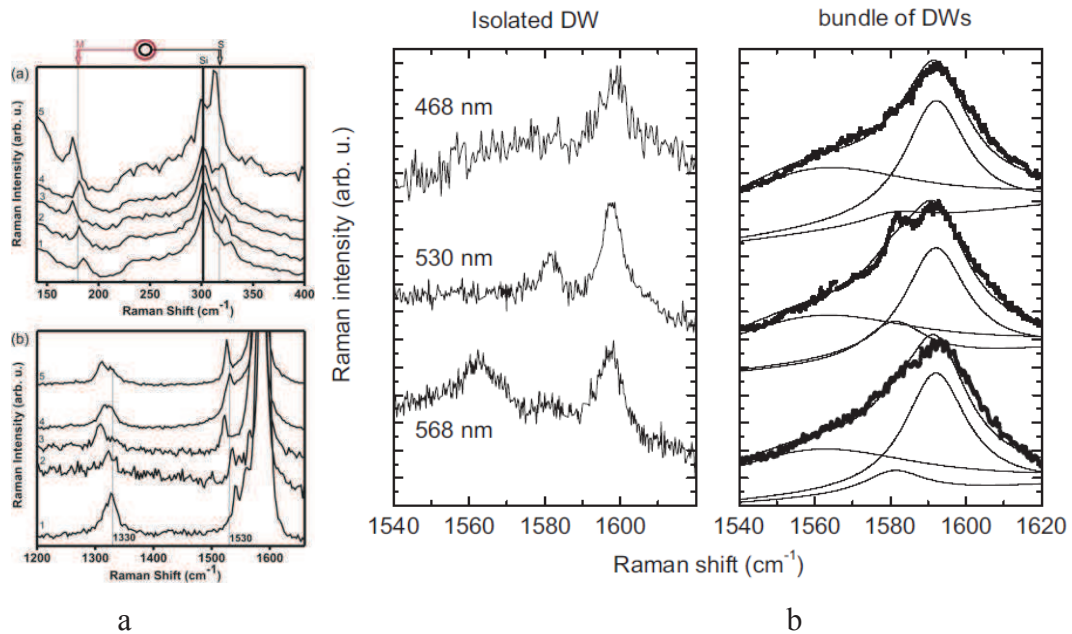


Fig. 1.18: (a) RBM-band, D and G-band regions of the Raman spectra corresponding to five different DWNTs whose inner and outer walls are simultaneously in resonance with the same (b) Raman spectra of a bundle of DWs at different excitation wavelengths.

laser line $E_{\text{Laser}} = 2.10 \text{ eV}$, from [86]. (b) G band of individual DWNT (left side) and bundles of DWNTs (right side) using three different excitation energies, from [90].

In contrast to the previous work, Puech et al [90] measured Raman spectra of individual double wall carbon nanotubes on silica. They explained the splitting of the G band due to contributions of the inner and outer tube when using an excitation energy in resonance with the inner metallic tube and outer semiconducting tube. It was believed that the spectral splitting indicated the strong coupling between the layers (see Fig. 1.18 (b)).

The in-depth study of tangential modes of double-walled carbon nanotube will be presented in the Chapter 4.

1.3 Triple-walled carbon nanotubes

Triple-walled carbon nanotube (TWNT) is another example of a complex nanosystem whose properties are determined not only by the constituent layers but also by their intrinsic interactions. Recently Hirschmann et al [91] studied 5 individual TWNTs by Resonant Raman spectroscopy. They managed to locate, distinguish, and characterize individual TWNTs with three different flavors (S@M, S@S, and M@S) for the individual, inner DWNTs (Fig. 1.19).

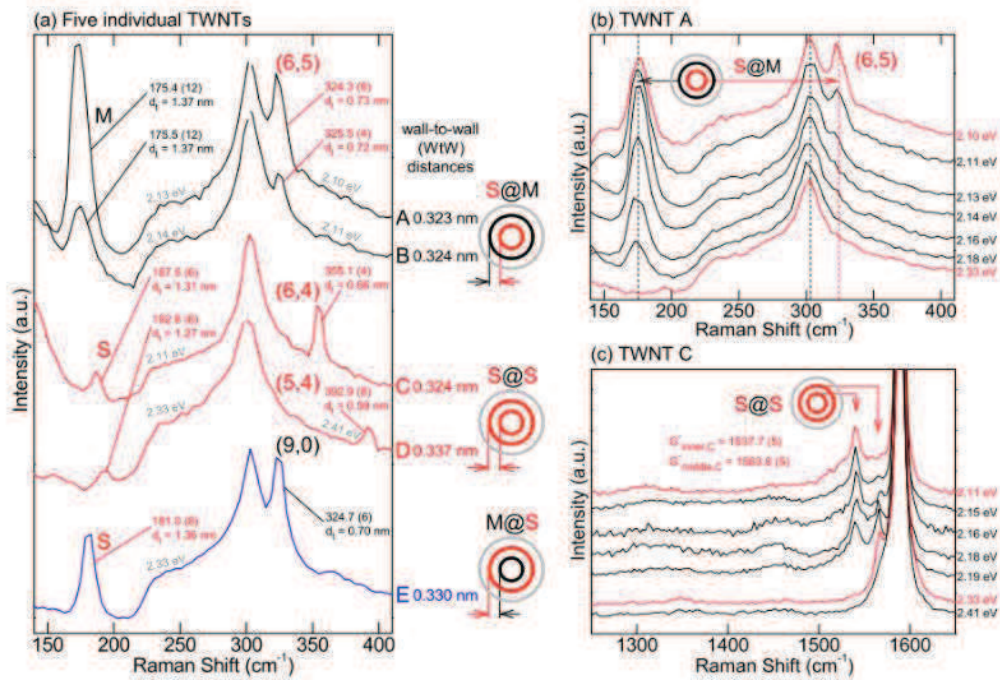


Fig. 1.19: (a) The spectra show the RBMs of the inner and middle tubes of five individual TWNTs, marked with capital letters (A-E). (b) The spectra represent the RBM resonance evolution of the TWNT A with a S@M DWNT flavor. The RBM of the metallic middle tube has its maximum intensity at 2.13 eV, in contrast to what occurs to the RBM of the semiconducting

inner tube (6,5) between 2.10 and 2.13 eV. (c) G-band of the TWNT C taken by different E_{Laser} . The absence of a significant D-band and the (decreasing) increasing of the G occurrence for the semiconducting middle and inner tube are seen. From [91].

By using ω_{RBM} vs d relations, they found the WtW distances of the two inner tubes of individual TWNTs to be 0.330 ± 0.007 nm. Characteristic high-frequency G-band and low-frequency RBLMs spectra of the TWNTs are presented in the Fig. 1.19.

We also emphasize that the RBLM frequency of the outer layer was never measured.

Summary

In this chapter we have briefly reviewed the structural, electronic and vibrational properties of individual carbon nanotubes. Furthermore, we considered the Raman spectroscopy study of individual single- and multi-walled CNTs and presented theoretical and experimental data that were present in the literature prior to this work.

We also analyzed a 2D continuous membrane theory for the frequency calculations of the radial breathing and breathing-like modes of single- and double-walled nanotubes respectively.

Finally, a short review of the Raman spectroscopy study of triple-walled carbon nanotubes was done.

References of Chapter 1:

1. S. Reich, C. Thomsen, J. Maultzsch: Carbon Nanotubes: Basic Concepts and Physical Properties (Wiley-VCH, Berlin 2004).
2. Ge. G. Samsonidze, R. Saito, A. Jorio, M. A. Pimenta, A. G. Souza Filho, A. Grüneis, G. Dresselhaus, and M. S. Dresselhaus, The Concept of Cutting Lines in Carbon Nanotube Science, *J. Nanosci. Nanotech.* 2003, Vol. 3, No. 6.
3. Christian Thomsen and Stephanie Reich, Raman Scattering in Carbon Nanotubes, *Light Scattering in Solid IX, Topics Appl. Physics* 108, 115–232 (2007) by M. Cardona, R. Merlin.
4. S. Reich, J. Maultzsch, C. Thomsen, P. Ordejon: Tight-binding description of graphene, *Phys. Rev. B* 66, 035412 (2002).
5. R. Saito, G. Dresselhaus, M. S. Dresselhaus: Physical Properties of Carbon Nanotubes (Imperial College Press, London 1998).
6. J. W. Mintmire, B. I. Dunlap, C. T. White: Are fullerene tubules metallic?, *Phys. Rev. Lett.* 68, 631 (1992).
7. N. Hamada, S.-I. Sawada, A. Oshiyama: New one-dimensional conductors: Graphitic microtubules, *Phys. Rev. Lett.* 68, 1579 (1992).
8. R. Saito, M. Fujita, G. Dresselhaus, M. S. Dresselhaus: Electronic structure of graphene tubules based on C₆₀, *Phys. Rev. B* 46, 1804 (1992).
9. S. Reich, C. Thomsen: Chirality dependence of the density-of-states singularities in carbon nanotubes, *Phys. Rev. B* 62, 4273 (2000).
10. P. R. Wallace: The band theory of graphite, *Phys. Rev.* 71, 622 (1947).
11. M. Damnjanovic, I. Milosevic, T. Vukovic, R. Sredanovic: Full symmetry, optical activity, and potentials of single-wall and multiwall nanotubes, *Phys. Rev. B* 60, 2728 (1999).
12. R. Saito, M. Hofmann, G. Dresselhaus, A. Jorio & M. S. Dresselhaus (2011): Raman spectroscopy of graphene and carbon nanotubes, *Advances in Physics*, 60:3, 413-550.
13. M. C. Hersam, Progress towards monodisperse single-walled carbon nanotubes, *Nat. Nanotechnol.*, 2008, 3, 387.
14. H. Kataura, Y. Kumazawa, Y. Maniwa, I. Umezumi, S. Suzuki, Y. Ohtsuka, Y. Achiba: Optical properties of single-wall carbon nanotubes, *Synth. Met.* 103, 2555 (1999).
15. C. L. Kane, E. J. Mele, Electron Interactions and Scaling Relations for Optical Excitations in Carbon Nanotubes, *Phys. Rev. Lett.* 93, 197402 (2004).
16. C. D. Spataru, S. Ismail-Beigi, L. X. Benedict, S. G. Louie, Excitonic Effects and Optical Spectra of Single-Walled Carbon Nanotubes, *Phys. Rev. Lett.* 92, 077402 (2004).

17. S. M. Bachilo, M. S. Strano, C. Kittrell, R. H. Hauge, R. E. Smalley, R. B. Weisman: Structure-assigned optical spectra of single-walled carbon nanotubes, *Science* 298, 2361 (2002).
18. S. Lebedkin, F. Hennrich, T. Skipa, M. M. Kappes: Near-infrared photoluminescence of single-walled carbon nanotubes prepared by the laser vaporization method, *J. Phys. Chem. B* 107, 1949 (2003).
19. H. Telg, J. Maultzsch, S. Reich, F. Hennrich, C. Thomsen, Chirality Distribution and Transition Energies of Carbon Nanotubes, *Phys. Rev. Lett.* 93, 177401 (2004).
20. C. Fantini, A. Jorio, M. Souza, M. S. Strano, M. S. Dresselhaus, M. A. Pimenta, Optical Transition Energies for Carbon Nanotubes from Resonant Raman Spectroscopy: Environment and Temperature Effects, *Phys. Rev. Lett.* 93, 147406 (2004).
21. J. Lefebvre, Y. Homma, P. Finnie: Bright band gap photoluminescence from unprocessed single-walled carbon nanotubes, *Phys. Rev. Lett.* 90, 217401 (2003).
22. M. S. Dresselhaus, Exciton Photophysics of Carbon Nanotubes, *Annu. Rev. Phys. Chem.* 2007. 58:719–47.
23. M. S. Arnold, A. A. Green, J. F. Hulvat, S. I. Stupp, M. C. Hersam, Sorting carbon nanotubes by electronic structure using density differentiation, *Nat. Nanotechnol.* 1, 60 (2006).
24. H. Liu, D. Nishide, T. Tanaka, H. Kataura, Large-scale single-chirality separation of single-wall carbon nanotubes by simple gel chromatography, *Nat. Commun.* 2, 309 (2011).
25. Sun, Tinghui; Zeng, Tao; Xia, Chuanqin; Li, Shoujian; Wu, Haichen, Purification and Separation of Single-Walled Carbon Nanotubes (SWCNTs), *Journal of Nanoscience and Nanotechnology*, Volume 12, Number 4, April 2012 , pp. 2955-2963(9).
26. A. Jorio, R. Saito, J. Hafner, C. Lieber, M. Hunter, T. McClure, G. Dresselhaus, and M.S. Dresselhaus, Structural (n,m) Determination of Isolated Single-Wall Carbon Nanotubes by Resonant Raman Scattering, *Phys. Rev. Lett.* 86(6) (2001), pp. 1118–1121.
27. J. C. Meyer, M. Paillet, T. Michel, A. Moreac, A. Neumann, G. S. Duesberg, S. Roth and J.-L. Sauvajol, Raman Modes of Index-Identified Freestanding Single-Walled Carbon Nanotubes, *Phys. Rev. Lett.* 95, 2005, 217401.
28. T. Michel, M. Paillet, A. Zahab, D. Nakabayashi, V. Jourdain, R. Parret and J.-L. Sauvajol, About the indexing of the structure of single-walled carbon nanotubes from resonant Raman scattering, *Adv. Nat. Sci.: Nanosci. Nanotechnol.* 1 (2010) 045007 (5pp).
29. M. Paillet, T. Michel, A. Zahab, D. Nakabayashi, V. Jourdain, R. Parret, J. Meyer, and J.-L. Sauvajol, Probing the structure of single-walled carbon nanotubes by resonant Raman spectroscopy, *Phys. Status Solidi B* 247, Nos. 11–12, 2762–2767 (2010).

30. R. Parret, D. Levshov, T. X. Than, D. Nakabayashi, T. Michel, M. Paillet, R. Arenal, V. N. Popov, V. Jourdain, Yu. I. Yuzyuk, A. A. Zahab, and J.-L. Sauvajol, Raman Spectroscopy on Individual Identified Carbon Nanotubes, *Mater. Res. Soc. Symp. Proc. Vol. 1407*, 2012 Materials Research Society.
31. M. Menon, E. Richter, and K. R. Subbaswamy, Structural and vibrational properties of fullerenes and nanotubes in a nonorthogonal tight-binding scheme, *J. Chem. Phys.* 104, 5875 (1996).
32. O. Dubay and G. Kresse, Accurate density functional calculations for the phonon dispersion relations of graphite layer and carbon nanotubes, *Phys. Rev. B* 67, 035401 (2003).
33. A. Grüneis, R. Saito, T. Kimura, L. G. Cançado, M. A. Pimenta, Jorio, A. G. Souza Filho, G. Dresselhaus, and M. S. Dresselhaus, Determination of two-dimensional phonon dispersion relation of graphite by Raman spectroscopy, *Phys. Rev. B* 65, 155405 (2002).
34. O. E. Alon, Number of Raman- and infrared-active vibrations in single-walled carbon nanotubes, *Phys. Rev. B* 63, 201403 (2001).
35. M. V. Avramenko, S. B. Rochal, and Yu. I. Yuzyuk, Symmetry of the carbon nanotube modes and their origin from the phonon branches of graphene, *Phys. Rev. B* 87, 035407 (2013).
36. A. Jorio, G. Dresselhaus, M. S. Dresselhaus (Eds.): Carbon Nanotubes, *Topics Appl. Physics* 111, 495–530 (2008) Springer-Verlag Berlin Heidelberg 2008.
37. M.S. Dresselhaus, A. Jorio, M. Hofmann, G. Dresselhaus, and R. Saito, Perspectives on Carbon Nanotubes and Graphene Raman Spectroscopy, *Nano Lett.* 10 (2010), pp. 953–973.
38. F. Tuinstra and J.L. Koenig, Raman Spectrum of Graphite, *J. Chem. Phys.* 53(3) (1970), p. 1126.
39. E.H. Martins Ferreira, M.V.O. Moutinho, F. Stavale, M.M. Lucchese, R.B. Capaz, C.A. Achete, and A. Jorio, Evolution of the Raman spectra from single-, few-, and many-layer graphene with increasing disorder, *Phys. Rev. B* 82(12) (2010), p. 125429.
40. M.A. Pimenta, G. Dresselhaus, M.S. Dresselhaus, L.G. Cancado, A. Jorio, and R. Saito, Studying disorder in graphite-based systems by Raman spectroscopy, *Phys. Chem. Chem. Phys.* 9(11) (2007), pp. 1276–1290.
41. E.B. Barros, A. Jorio, G.G. Samsonidze, R.B. Capaz, A.G. Souza Filho, J. Mendes Filho, G. Dresselhaus, and M.S. Dresselhaus, Review on the symmetry-related properties of carbon nanotubes, *Phys. Rep.* 431(6) (2006), pp. 261–302.
42. P.T. Araujo, I.O. Maciel, P.B.C. Pesce, M.A. Pimenta, S.K. Doorn, H. Qian, A. Hartschuh, M. Steiner, L. Grigorian, and K. Hata, Nature of the constant factor in the relation between

- radial breathing mode frequency and tube diameter for single-wall carbon nanotubes, *Phys. Rev. B* 77(24) (2008), p. 241403.
43. G.D. Mahan, Oscillations of a thin hollow cylinder: Carbon nanotubes, *Phys. Rev. B* 65(23) (2002), p. 235402
 44. S.B. Rochal, V.L. Lorman, Yu.I. Yuzyuk, Two-dimensional elasticity determines the low-frequency dynamics of single- and double-walled carbon nanotubes *Phys. Rev. B* 88, 235435 (2013).
 45. L.D. Landau, and E.M. Lifshitz, *Theory of Elasticity*, (Addison-Wesley, Reading, MA, 1959)
 46. H. Telg, J. Maultzsch, S. Reich, F. Hennrich, and C. Thomsen, Chirality Distribution and Transition Energies of Carbon Nanotubes, *Phys. Rev. Lett.* 93 (2004), p. 177401.
 47. M. Milnera, J. Kürti, M. Hulman, and H. Kuzmany, Periodic Resonance Excitation and Intertube Interaction from Quasicontinuous Distributed Helicities in Single-Wall Carbon Nanotubes, *Phys. Rev. Lett.* 84(6) (2000), pp. 1324–1327.
 48. S.M. Bachilo, L. Balzano, J.E. Herrera, F. Pompeo, D.E. Resasco, and R. Bruce Weisman, Narrow (n,m)-Distribution of Single-Walled Carbon Nanotubes Grown Using a Solid Supported Catalyst, *J. Am. Chem. Soc.* 125(37) (2003), pp. 11186–11187.
 49. C. Fantini, A. Jorio, M. Souza, M.S. Strano, M.S. Dresselhaus, and M.A. Pimenta, Optical Transition Energies for Carbon Nanotubes from Resonant Raman Spectroscopy: Environment and Temperature Effects, *Phys. Rev. Lett.* 93(14) (2004), p. 147406.
 50. A. Hartschuh, H.N. Pedrosa, L. Novotny, and T.D. Krauss, Simultaneous Fluorescence and Raman Scattering from Single Carbon Nanotubes, *Science* 301(5638) (2003), p. 1354.
 51. S.M. Bachilo, M.S. Strano, C. Kittrell, R.H. Hauge, R.E. Smalley, and R.B. Weisman, Structure-Assigned Optical Spectra of Single-Walled Carbon Nanotubes, *Science* 298(5602) (2002), p. 2361.
 52. S.K. Doorn, D.A. Heller, P.W. Barone, M.L. Usrey, and M.S. Strano, *Appl. Phys. A* 78(8) (2004), Resonant Raman excitation profiles of individually dispersed single walled carbon nanotubes in solution, 1147–1155.
 53. T. Michel, M. Paillet, P. Poncharal, A. Zahab, J.-L. Sauvajol, J.C. Meyer, and S. Roth, Raman spectroscopy of isolated single-walled carbon nanotubes, *Carbon Nanotubes* 222(II) (2006), pp. 121–122.
 54. P.T. Araujo, S.K. Doorn, S. Kilina, S. Tretiak, E. Einarsson, S. Maruyama, H. Chacham, M.A. Pimenta, and A. Jorio, Third and Fourth Optical Transitions in Semiconducting Carbon Nanotubes, *Phys. Rev. Lett.* 98(6) (2007), p. 67401.

55. K. Liu, W. Wang, M. Wu, F. Xiao, X. Hong, S. Aloni, X. Bai, E. Wang, and F. Wang, Intrinsic radial breathing vibrations in suspended single-walled carbon nanotubes, *Phys. Rev. B* **83**, 113404 (2011).
56. A.C. Ferrari, J. Meyer, V. Scardaci, C. Casiraghi, M. Lazzeri, F. Mauri, S. Piscanec, D. Jiang, K. Novoselov, S. Roth, and A. Geim, Raman Spectrum of Graphene and Graphene Layers, *Phys. Rev. Lett.* **97**(18) (2006), p. 187401.
57. S.D.M. Brown, A. Jorio, P. Corio, M.S. Dresselhaus, G. Dresselhaus, R. Saito, and K. Kneipp, Origin of the Breit-Wigner-Fano lineshape of the tangential G-band feature of metallic carbon nanotubes, *Phys. Rev. B* **63**(15) (2001), p. 155414.
58. W. Kohn, Image of the Fermi Surface in the Vibration Spectrum of a Metal, *Phys. Rev. Lett.* **2** (1959), p. 393.
59. S. Piscanec, M. Lazzeri, J. Robertson, A.C. Ferrari, and F. Mauri, Optical phonons in carbon nanotubes: Kohn anomalies, Peierls distortions, and dynamic effects, *Phys. Rev. B* **75**(3) (2007), p. 35427.
60. O. Dubay and G. Kresse, Accurate density functional calculations for the phonon dispersion relations of graphite layer and carbon nanotubes, *Phys. Rev. B* **67**(3) (2003), p. 35401.
61. R. Saito, T. Takeya, T. Kimura, G. Dresselhaus, and M.S. Dresselhaus, Raman intensity of single-wall carbon nanotubes, *Phys. Rev. B* **57** (7) (1998), pp. 4145–4153.
62. S. Reich, C. Thomsen, P. Ordejon, Phonon eigenvectors of chiral nanotubes, *Phys. Rev. B* **64**, (2001), 195416.
63. V. Popov, P. Lambin, Radius and chirality dependence of the radial breathing mode and the G-band phonon modes of single-walled carbon nanotubes, *Phys. Rev. B* **73**, (2006) 085407.
64. A. Jorio, A.G. Souza Filho, G. Dresselhaus, M.S. Dresselhaus, A. Swan, M. Ünlü, B. Goldberg, M.A. Pimenta, J. Hafner, C.M. Lieber, and R. Saito, G-band resonant Raman study of 62 isolated single-wall carbon nanotubes, *Phys. Rev. B* **65**(15) (2002), p. 155412.
65. H. Telg, J. G. Duque, M. Staiger, X. Tu, F. Hennrich, M. M. Kappes, M. Zheng, J. Maultzsch, C. Thomsen, and S. K. Doorn, Chiral Index Dependence of the G⁺ and G⁻ Raman Modes in Semiconducting Carbon Nanotubes, *ACS Nano* **6**, 904 (2012).
66. M. Kalbac, H. Farhat, L. Kavan, J. Kong, M. S. Dresselhaus, Competition between the Spring Force Constant and the Phonon Energy Renormalization in Electrochemically Doped Semiconducting Single-Walled Carbon Nanotubes, *Nano Lett.*, 2008, **8** (10), pp 3532–3537.
67. D. I. Levshov, Yu. I. Yuzyuk, T. Michel, C. Voisin, L. Alvarez, S. Berger, P. Roussignol, and J.-L. Sauvajol, Raman Probing of Uniaxial Strain in Individual Single-Wall Carbon Nanotubes in a Composite Material *J. Phys. Chem. C* **2010**, **114**, 16210–16214.

68. Cai Shen, Alexandra H. Brozena and Yu Huang Wang, Double-walled carbon nanotubes: Challenges and opportunities, *Nanoscale*, 2011, 3, 503–518.
69. J.-C. Charlier, J.-P. Michenaud: Energetics of multilayered carbon tubules, *Phys. Rev. Lett.* 70, 1858–1861 (1993).
70. M. Xia, S. Zhang, X. Zuo, E. Zhang, S. Zhao, J. Li, L. Zhang, Y. Liu, R. Liang: Assignment of the chiralities of double-walled carbon nanotubes using two radial breathing modes, *Phys. Rev. B* 70, 205428 (2004).
71. J. Wei, B. Jiang, X. Zhang, H. Zhu, D. Wu: Raman study on double-walled carbon nanotubes, *Chem. Phys. Lett.* 376, 753–757 (2003).
72. M. Damnjanovic, I. Milosevic, T. Vukovic and R. Sredanovic, Full symmetry, optical activity, and potentials of single-wall and multiwall nanotubes, *Phys. Rev. B* 60, 1999, 2728.
73. H. Muramatsu, T. Hayashi, Y. A. Kim, D. Shimamoto, M. Endo, V. Meunier, B. G. Sumpter, M. Terrones and M. S. Dresselhaus, Bright Photoluminescence from the Inner Tubes of “Peapod”-Derived Double-Walled Carbon Nanotubes, *Small*, 2009, 5, 2678.
74. J. Tersoff: Empirical interatomic potential for carbon, with applications to amorphous carbon, *Phys. Rev. Lett.* 61, 2879–2882 (1988)
75. Rudolf Pfeiffer, Thomas Pichler, Yoong Ahm Kim, and Hans Kuzmany, Double-Wall Carbon Nanotubes from A. Jorio, G. Dresselhaus, M. S. Dresselhaus (Eds.): *Carbon Nanotubes, Topics Appl. Physics* 111, 495–530 (2008) Springer-Verlag Berlin Heidelberg 2008
76. L. Bellarosa, E. Bakalis, M. Melle-Franco, F. Zerbetto: Interactions in concentric carbon nanotubes: The radius vs. the chirality angle contributions, *Nano Lett.* 6, 1950–1954 (2006)
77. S. Okada, A. Oshiyama: Curvature-induced metallization of double-walled semiconducting zigzag carbon nanotubes, *Phys. Rev. Lett.* 91, 216801 (2003)
78. V. Zolyomi, J. Koltai, A. Ruzsnyák, J. Körti, A. Gali, F. Simon, H. Kuzmany, A. Szabados, P. R. Surjan: Inter-shell interaction in double walled carbon nanotubes: Charge transfer and orbital mixing, *Phys. Rev. B* 77, 245403 (2008).
79. W. Song, M. Ni, J. Lu, Z. Gao, S. Nagase, D. Yu, H. Ye, X. Zhang: Electronic structures of semiconducting double-walled carbon nanotubes: Important effect of interlayer interaction, *Chem. Phys. Lett.* 414, 429–433 (2005)
80. S. D. Liang, Intrinsic properties of electronic structure in commensurate double-wall carbon nanotubes, *Phys. B*, 2004, 352, 305.
81. R. Pfeiffer, C. Kramberger, F. Simon, H. Kuzmany, V.N. Popov, and H. Kataura, Interaction between concentric tubes in DWCNTs, *Eur. Phys. J. B* 42(3) (2004), pp. 345–350.

82. R. Pfeiffer, F. Simon, H. Kuzmany, and V.N. Popov, Fine structure of the radial breathing mode of double-wall carbon nanotubes, *Phys. Rev. B* 72(16) (2005), p. 161404.
83. R. Pfeiffer, F. Simon, H. Kuzmany, V.N. Popov, V. Zolyomi, and J. Kurti, Tube–tube interaction in double-wall carbon nanotubes, *Phys. Stat. Solidi B* 243(13) (2006), pp. 3268–3272.
84. R. Pfeiffer, H. Peterlik, H. Kuzmany, F. Simon, K. Pressl, P. Knoll, M.H. Rummeli, H. Shiozawa, H. Muramatsu, Y.A. Kim, T. Hayashi, and M. Endo, A detailed comparison of CVD grown and precursor based DWCNTs, *Phys. Stat. Solidi B* 245(10) (2008), pp. 1943–1946.
85. H. Kuzmany, W. Plank, R. Pfeiffer, and F. Simon, Raman scattering from double-walled carbon nanotubes, *J. Raman Spectrosc.* 39(2) (2008), pp. 134–140.
86. F. Villalpando-Paez, H. Muramatsu, Y.A. Kim, H. Farhat, M. Endo, M. Terrones, and M.S. Dresselhaus, Wall-to-wall stress induced in (6,5) semiconducting nanotubes by encapsulation in metallic outer tubes of different diameters: A resonance Raman study of individual C60-derived double-wall carbon nanotubes, *Nanoscale* 2(3) (2010), pp. 406–411.
87. F. Villalpando-Paez, H. Son, D. Nezich, Y.P. Hsieh, J. Kong, Y.A. Kim, D. Shimamoto, H. Muramatsu, T. Hayashi, M. Endo, M. Terrones, and M.S. Dresselhaus, Raman Spectroscopy Study of Isolated Double-Walled Carbon Nanotubes with Different Metallic and Semiconducting Configurations, *Nano Lett.* 8 (2008), pp. 3879–3886.
88. V. N. Popov, L. Henrard, Breathing-like phonon modes of multiwalled carbon nanotubes, *Phys. Rev. B* 65, 235415 (2002)
89. R. Pfeiffer, H. Kuzmany, C. Kramberger, C. Schaman, T. Pichler, H. Kataura, Y. Achiba, J. Kurti, V. Zolyomi: Unusual high degree of unperturbed environment in the interior of single-wall carbon nanotubes, *Phys. Rev. Lett.* 90, 225501 (2003).
90. P. Puech, S. Nanot, B. Raquet, J.-M. Broto, M. Millot, A. Waheed Anwar, E. Flahaut, W. Bacsá, Comparative Raman spectroscopy of individual and bundled double wall carbon nanotubes, *Phys. Status Solidi B* 248, No. 4, 974–979 (2011).
91. T. Ch. Hirschmann, P. T. Araujo, H. Muramatsu, X. Zhang, K. Nielsch, Y. A. Kim, and M. S. Dresselhaus, Characterization of Bundled and Individual Triple-Walled Carbon Nanotubes by Resonant Raman Spectroscopy, *ACS Nano*, 2013, 7 (3), pp 2381–2387.

Chapter 2
Synthesis and structural identification
of individual carbon nanotubes

In our group we had developed an experimental procedure for studying vibrational and optical properties of individual well-identified single-walled carbon nanotubes by combination of Raman spectroscopy, high-resolution electron microscopy (HRTEM) imaging and electron diffraction (ED). For the use of all these techniques on the same nanotubes, CNTs must be spatially isolated and suspended in order to be accessible for the electron beam.

The very first way to prepare such samples, used since 2005, consisted in the synthesis of individual CNTs on substrates, followed by lithography and etching steps to isolate nanotubes [1]. The main disadvantage of this protocol was in the use of different chemicals: resists, KOH, TMAH etc., which led to the potential contamination of the CNTs.

Hence, this chapter is organized in the following way: we first present an improved protocol of the synthesis of suspended isolated CNTs performed in only one step on specially designed substrates (with no chemicals). Then we discuss the spatial localization and structure identification steps and give a short review on the structure identification of nanotubes by electron diffraction. Finally, we present several examples of ED pattern analysis of single- and multi-walled nanotubes.

2.1 The synthesis of ultra-long individual nanotubes

Catalytic chemical vapor deposition (CCVD) is a comparably low-temperature method (600°C – 900°C) in which a carbon molecular precursor is thermally decomposed to produce reactive carbon species and ultimately CNTs. This process can be driven using a template or a substrate and with use of a catalyst. A variety of carbon precursors and metal nano-particles as catalysts can be used in this process [2].

Substantial work on CCVD protocol was done within the framework of Tinh Than's PhD thesis, developed in our group [3]. Here we will remind only its main points and not discuss growth mechanisms as they are beyond the scope of this manuscript. Tinh Than studied the influence of growth parameters on the synthesis of CNTs, namely the type and the size of the catalysts, the type of precursors (ethanol, methane), temperature, pressure, atmosphere composition, slow and fast cooling methods etc. It was found that the growth can be achieved with different CCVD temperatures and different total flow rates, but there existed several CCVD conditions, which gave higher reproducibility:

2.1.1 Slow-heating protocol with methane (or ethanol) as precursors.

Before heating and gas purge stages, the sample was put in the center of the furnace. To hold the sample a tubule of 6 mm in diameter and 11 cm in length was usually used in order to promote a laminar flow close to the substrate. The protocol is shown in figure 2.1a (for methane). Before heating, all gas lines and the reactor tube were purged by Ar at a flow rate of 1400 sccm for 30 minutes. Then the furnace was heated to 900°C at a ramping rate of 20°C/min under an Ar flow of 1400 sccm. The ramp lasted about 44 minutes. When the temperature reached 900°C, argon was replaced by hydrogen at a flow rate of 100 sccm for 17 minutes. Then, the temperature was increased from 900°C to 950°C in about 3 minutes. When the temperature reached 950°C, the hydrogen flow rate was increased to 200 sccm. After 5 minutes, methane was injected into the reactor tube by increasing steps of 25 sccm in order to reach 100 sccm after 1 minute. The temperature and gas flows were left constant for 60 minutes to perform the growth of nanotubes. The furnace was then switched off and left cooling by itself. During cooling, hydrogen and methane were replaced by Ar at a flow rate of 60 sccm.

For ethanol the protocol was slightly different though the general procedure remained the same (see Fig. 2.1b below).

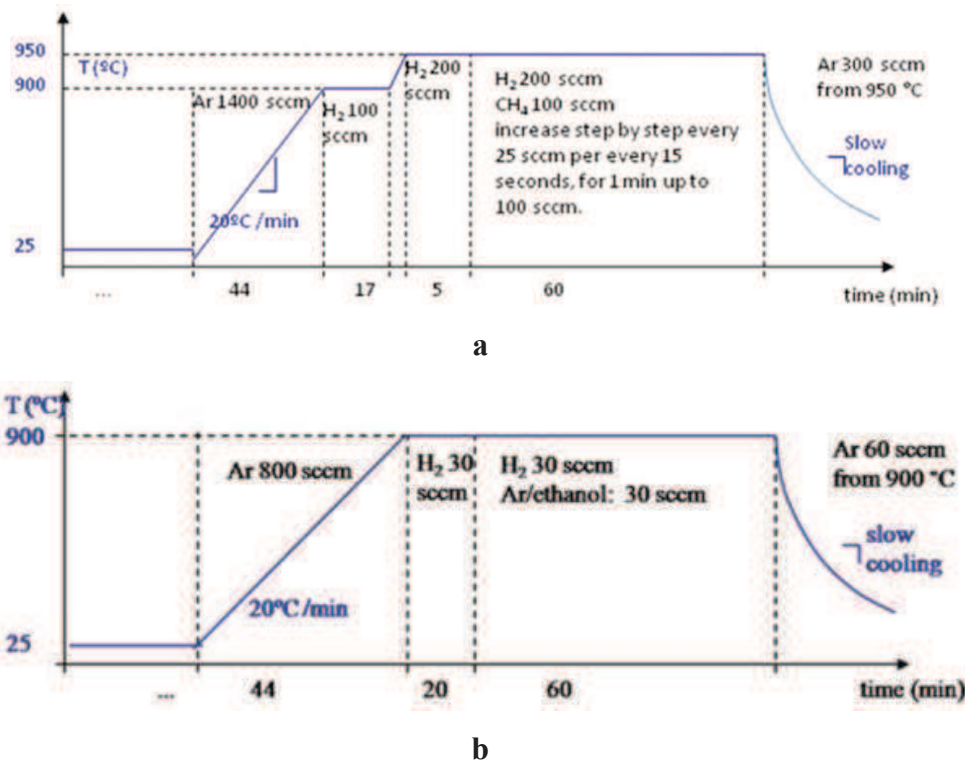


Figure 2.1: Slow-heating CCVD protocols with methane (a) and ethanol (b) as precursors. Adapted from [3].

2.1.2 Fast-heating protocol with methane (or ethanol) as precursors.

In this protocol a sample was inserted in the reactor tube but kept outside of the heating zone. As in the former method, the sample was usually held inside a quartz tubule with 6 mm in diameter and 11 cm in length. Before heating all gas lines and the reactor tube were purged by Ar at a flow rate of 1400 sccm for 30 minutes to remove air. Then the furnace was heated to 950°C at a ramping rate of 20°C/min in Ar at a flow rate of 1400 sccm for 47 minutes. When the temperature reached 950°C, argon was replaced by hydrogen and methane at flow rates of 200 sccm and 100 sccm, respectively. After 5 minutes, the sample was rapidly transferred in the heated zone with the help of the magnetic insertion bar or by sliding the furnace. The temperature and gas flows were left constant for 60 minutes to perform the growth of nanotubes. After that, the furnace was switched off and left for cooling. Hydrogen and methane were replaced by argon at a flow rate of 300 sccm.

The experimental protocol for ethanol is presented in the Fig. 2.2b.

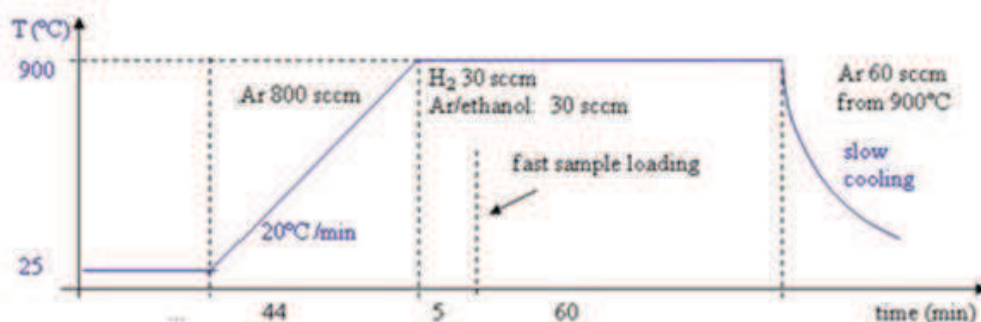
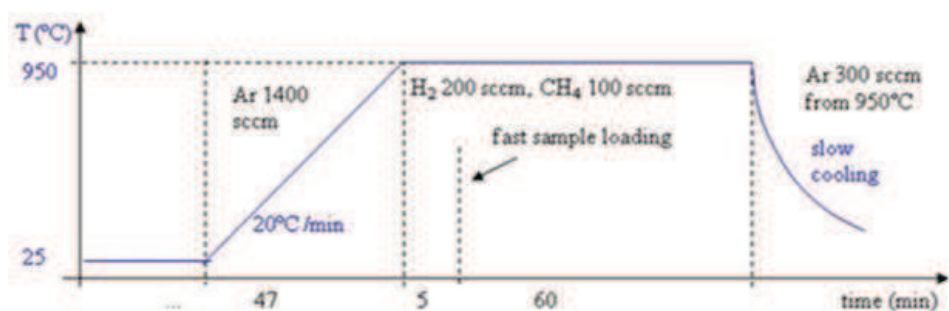


Figure 2.2: Fast-heating CCVD protocols with methane (a) and ethanol (b) as precursors. Adapted from [3].

Tinh Than showed that these experimental protocols may produce ultra-long nanotubes (as long as 5 cm) [3] being able to overcome millimeter-large trenches or a 500 μ m-high barrier during growth. In other words, using described CCVD methods we can produce suspended nanotubes by growing them directly on commercial perforated silicon nitride TEM grids [4] for

subsequent Raman studies [5]. Moreover, to avoid CNT contamination it was possible to use a separated substrate for the catalyst, placed near the grid (which acts as a receiving substrate) in the CCVD furnace. Figure 2.3a shows a low-resolution TEM overview of the commercial grid after the synthesis. In the thinned middle part, long as-grown individual CNTs are deposited across several holes on the perforated Si_3N_4 membrane, as shown on the SEM picture of Fig. 2.3b. The typical diameter of the holes is $3\ \mu\text{m}$ and we can see that most of the time only one nanotube is found in a given hole. Figure 2.3c displays a TEM image of one of these suspended CNT at the edge of a hole (the latter can be used to improve the focus during TEM experiments).

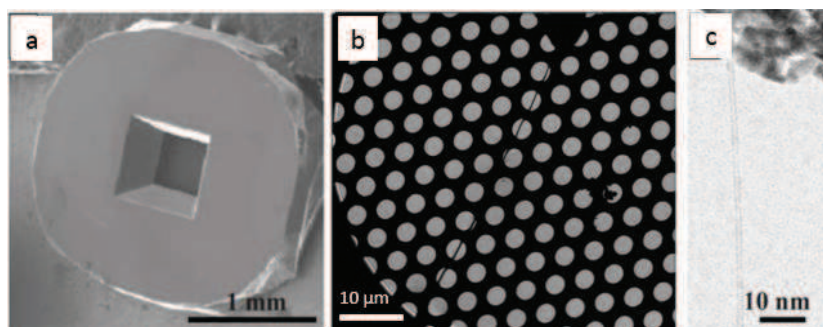


Figure 2.3: a) SEM image of a commercial silicon nitride TEM grid, b) TEM image of the central part of the TEM grid showing suspended CNTs, c) TEM micrograph of an individual suspended CNT.

Finally we note that other types of receiving samples were used in this study consisting of typical Si/SiO_x wafers with an open-ended slits (several tens of microns in width) produced by standards micro-fabrication techniques before the synthesis. These substrates were especially suitable for Raman mapping (described later in this chapter) but, unfortunately, we encountered some difficulties with TEM and ED characterization of the CNTs suspended on this kind of samples.

In Table 2.1 we present a summary of all the samples studied in this work. The type of substrates, growth conditions, characterization techniques as well as the kind of nanotubes synthesized are shown below.

Table 2.1. List of different samples studied in this work (in order of interest).

#	Code name	Substrate	Growth conditions	Characterization techniques	Nanotubes
1	V65	TEM grid	Ethanol, Catalyst: FeCl ₃ (0,01M), Total flow in CCVD process: 60 sccm, 900 °C, Slow heating+ Slow cooling. CVD in 60min	HRTEM+ED	iSWNTs+iDWNTs
2	V66	TEM grid	Ethanol, Catalyst: FeCl ₃ (0,01M), Total flow: 60 sccm, 900 °C, Fast heating+ Slow cooling. CCVD in 60min	HRTEM+ED	iSWNTs+iDWNTs
3	V127b	TEM grid	Ethanol, Catalyst: Fe 10 Å, Total flow: 20 sccm, 1000 °C, Fast heating+ Fast cooling, CCVD in 30min	HRTEM+ED	Mostly iDWNTs +iTWNT
4	F385-2 (B15)	TEM grid	Protocole F121; synthesis with CH ₄ 30sccm (10%) 60min, 1000°C, FeCl ₃ (0,01M) on separate SiO ₂ , H ₂ 60sccm (8,5%)	HRTEM+ED	One long iDWNT
5	F385-8 (B16)	TEM grid	Protocole F121; synthesis with CH ₄ 30sccm (10%) 60min, 1000°C, FeCl ₃ (0,01M) on separate SiO ₂ , H ₂ 60sccm (8,5%)	HRTEM+ED	Mostly iDWNTs, iTWNTs and bundles
6	V14A2	TEM grid	Protocole F121; synthesis with CH ₄ 30sccm (10%) 60min, 1000°C, FeCl ₃ (0,01M) on the same SiO ₂ as the nanotubes, H ₂ 60sccm (8,5%)	HRTEM+ED	Mostly iDWNTs
7	V126a	TEM grid	Ethanol, Catalyst: Fe 5 Å, Total flow: 30 sccm, 950 °C, Fast heating+ Fast cooling. CCVD in 30min	HRTEM	Mostly bundles
8	V75a	Slit	Ethanol, Catalyst: Fe 5 Å, Total flow: 60 sccm, 900 °C, Fast heating+ Slow cooling, CCVD in 60min	Raman imaging	iSWNTs, iDWNTs + bundles
9	V75b	Slit	Ethanol, Catalyst: Fe 5 Å, Total: 60 sccm, 900 °C, Fast heating+ Slow cooling, CCVD in 60min	Raman imaging	iSWNTs, iDWNTs + bundles
10	V79b	Slit	Ethanol, Catalyst: Fe 5 Å, Total flow: 60 sccm, 900 °C, Fast heating+ Fast cooling, CCVD in 60min	Raman imaging	iSWNTs, iDWNTs + bundles
11	V80a	Slit	Ethanol, Catalyst: Fe 5 Å, Total: 40 sccm, 900 °C, Fast heating+ Slow cooling, CCVD in 60min	HRTEM + Raman imaging	iSWNTs, iDWNTs + bundles
12	V110d	Slit	Ethanol, Catalyst: Fe 5 Å, Total flow: 30 sccm, 1000 °C, Fast heating+ Fast cooling. CCVD in 30min	Raman imaging	iSWNTs, iDWNTs + bundles
13	V112c	Slit	Ethanol, Catalyst: Fe 5 Å, Total flow: 30 sccm, 1000 °C, Fast heating+ Fast cooling. CCVD in 30min	Raman imaging	iSWNTs, iDWNTs + bundles
14	V126c	Slit	Ethanol, Catalyst: Fe 10 Å, Total flow: 30 sccm, 950 °C, Fast heating+ Fast cooling. CCVD in 30min	Raman imaging	iSWNTs, iDWNTs + bundles

In the framework of this thesis we performed consistent studies of several samples from Table 2.1 by high-resolution electron microscopy. It was found that the above presented synthesis protocols might give single- and multi-walled (mainly double- and triple-) nanotubes, sometimes organized in small bundles (see Table 2.1). However, a systematic and statistical study of the samples was not the aim of our work and we cannot give a complete and accurate trend between the synthesis parameters and the structural characteristics of the CNTs.

As an example, we show in the Fig. 2.4 HRTEM images of different structural types of carbon nanotubes that we analyzed and studied during this work, e.g. medium size and extra-large SWNTs, medium and extra-large DWNTs, bundles of single-walled nanotubes and triple-walled nanotubes. Regardless of the number of walls, the smaller nanotubes found in our samples have diameters of about 1.4-1.5 nm (probably because of the size of the catalyst nanoparticles). Moreover, these HRTEM images show that the as-grown carbon nanotubes are straight and have high crystalline quality. Finally, a few amount of amorphous carbon is observable at the CNTs surface, sometimes deposited during the TEM analysis.

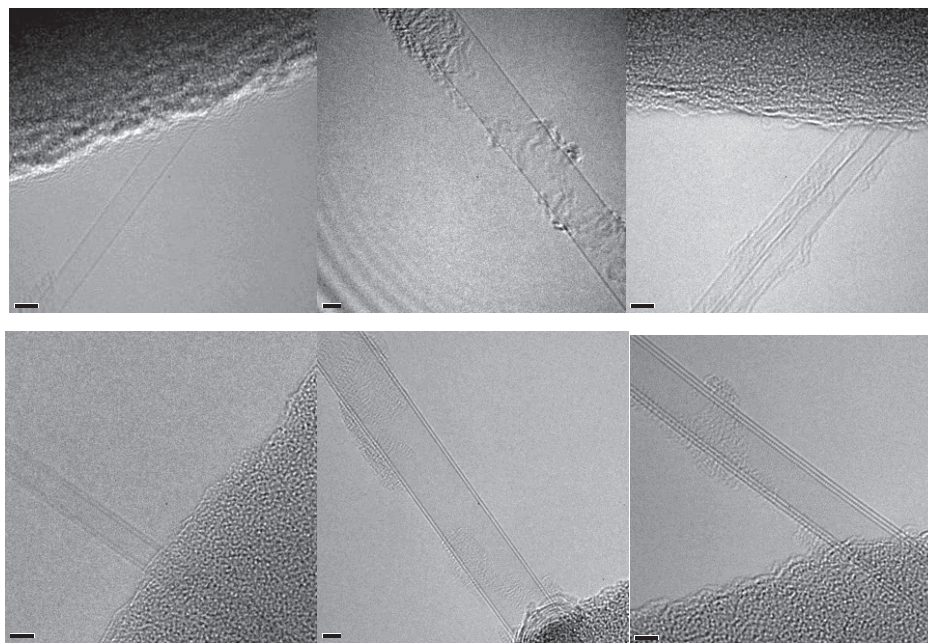


Figure 2.4: HRTEM images of (a) SWNT with $d = 2.4 \text{ nm}$, (b) SWNT with $d = 5.9 \text{ nm}$, (c) Bundle of two SWNTs, $d_1 = 1.8 \text{ nm}$, $d_2 = 1.9 \text{ nm}$, (d) DWNT with $d_{in} = 2.0 \text{ nm}$, $d_{out} = 2.8 \text{ nm}$, (e) DWNT with $d_{in} = 6.4 \text{ nm}$, $d_{out} = 7.1 \text{ nm}$, (f) TWNT with $d_1 = 3.3 \text{ nm}$, $d_2 = 4.0 \text{ nm}$, $d_3 = 4.7 \text{ nm}$;

2.2 Localization of as-grown individual carbon nanotubes

The growth mechanism associated with CCVD synthesis is beyond the scope of this work. However, it was shown previously [3] that the tubes are first grown in the gas phase before to be deposited on the substrate (kite growth) during the CCVD process. Consequently, we cannot control the position of the nanotubes on the sample. Moreover, our CCVD protocols produce CNTs deposited on the grid with a favored orientation (probably aligned by the gas flow, see for instance sketch of Fig. 2.5c). The first point make thus essential to localize the nanotubes in order to perform micro-Raman measurements. On the other hand the rather good alignment of the tubes on the substrate greatly facilitate Raman measurements, in particular the sample orientation with respect to incident polarization is kept the same to measure different nanotubes on a given sample. In this work we used three types of localization techniques: scanning electron microscopy (SEM), low-resolution TEM and Raman mapping as detailed hereafter.

2.2.1 Scanning electron microscopy (SEM) or Low-resolution TEM

Electron microscopy (SEM and TEM) offers an efficient way to visualize positions of carbon nanotubes on the samples. We usually start in a low-magnification mode and search for reference points on the substrates. They may be simple bunches of amorphous carbon, small cracks in the HRTEM grid or any other imperfections (dust etc...). With respect to these micro-metric markers, we then scan again the sample with a higher magnification and mark the nanotubes' locations. It should be pointed out that at this stage it is impossible to say anything about the structure of the nanotubes. Only subsequent HRTEM studies may reveal this information.

Fig. 2.5a shows a low-resolution electronic image of a TEM grid with as-grown carbon nanotubes. Fig. 2.5b shows some parts of this grid in more details (individual carbon nanotube is highlighted by red line). A final map of the sample is given in the Fig. 2.5c.

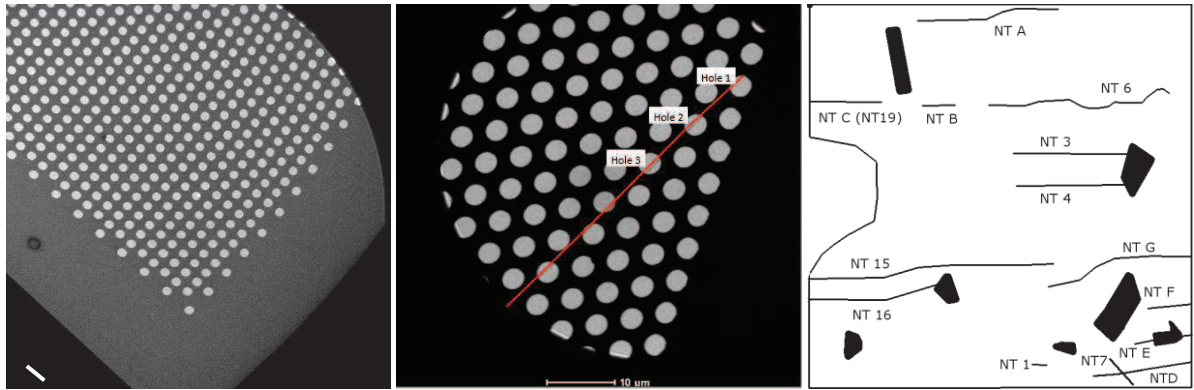


Fig. 2.5: (a) TEM overview of the grid showing a default used as a marker in the left hand side (the scale bar is 10 μm) (b) the different holes near this marker are labeled (individual carbon nanotube highlighted by thick line) (c) Final map of the sample showing the different localized markers and nanotubes.

2.2.2 Raman mapping

Raman mapping is another approach for the localization of carbon nanotubes that combines the non-destructive character of Raman effect (assuming a low laser power density) with the visualization advantages of the microscopy. As mentioned in the Chapter 1, carbon nanotubes due to their 1D structure have a resonant response to the incident radiation. Thus, high-intensity vibrational lines in the Raman spectra can be used to map CNTs on the samples.

We used two different techniques of micro-Raman mapping, namely point-by-point mapping and global imaging.

The point-by-point method involves acquiring spectra sequentially from a series of (X, Y) positions on the sample. Then a given Raman mode is selected (for instance G mode) to produce images indicating the intensity of this spectral line (encoded with false colors) as a function of the (X, Y) coordinates on the sample.

The second method consists in visualizing the sample using the excitation laser rather than the white light. To do this, the laser beam is expanded to illuminate a disc-shaped area on the sample. The resulting scattered light is spectrally filtered choosing a band pass filter with wavelength equal to a Raman mode (e.g. G mode) and focused to produce a 2D image directly on the CCD detector. Note that in this configuration the grating does not disperse light but acts as a mirror. The size of the illuminated disc is inversely proportional to the magnification of the objective lens; it is typically 50 μm diameter for a 50 \times objective. This mode is well suitable to locate rapidly the resonant nanotubes (see Fig. 2.6). However, no spectral information is available since there is no dispersion of the scattered light.

The point-by-point method has been successfully used to acquire a 1D map (line mapping) of the samples. Though this method is very appealing we cannot use it to map TEM grids-based samples due to the small size of the holes (which are only about 3 microns) and due to the strong reflectivity of the membrane.

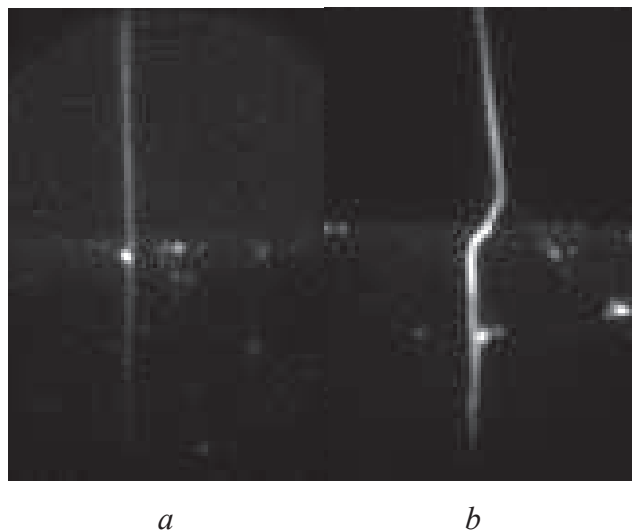


Fig. 2.6: Raman images of a slit with individual carbon nanotubes.

Summary

In the two previous sections, we have shown our experimental procedure for the synthesis and the spatial localization of the individual carbon nanotubes.

A typical synthesis protocol had the following characteristics:

Carbon feed: Methane (CH₄) or Ethanol (C₂H₅OH)

Atmosphere: Argon and (or) Hydrogen (H₂)

Catalysts: FeCl₃ or Fe

Growth temperature: 900 - 1000 °C

Growth time: 30 - 60 min

As nanotube localization techniques, we used SEM, low-resolution TEM and Raman mapping. Electron microscopy however has a disadvantage as it exists a certain chance of the contamination of the nanotubes (e.g. by amorphous carbon) during electron beam irradiation. Nevertheless, it is still attractive because it locates all the nanotubes on a given sample in a single run. Raman mapping, on the other hand, shows only the resonant nanotubes at a given excitation wavelength but in principle is free of contamination.

2.3 Structure identification of individual carbon nanotubes.

2.3.1 Introduction and experimental section

Identifying atomic structure of carbon nanotubes is essential for the consequent studies of their vibrational and optical properties. Electron diffraction is one of the best choices for that matter. In addition, it can be combined with direct imaging of the sample, including high-resolution imaging of the crystal lattice (HRTEM).

We note however that the distances (or CNTs diameters...) measured by HRTEM are very sensitive to the orientation of the tubes with respect to the electron beam and to the defocus conditions. Therefore, the atomic structure of a nanotube can be obtained by HRTEM only under particular observation conditions, which limits the use of this technique for such studies. Electron diffraction does not have these limiting factors and is therefore the most reliable technique to obtain the nanotube's atomic structure.

Early electron diffraction studies using standard selected area electron diffraction (SAED) techniques were performed on multi-wall [8-10], bundled [11,12] and individual single wall tubes [13,14]. The diffraction pattern quality was typically poor and therefore analysis limited. In 1997 the use of nano-beam electron diffraction (NBED), in which a coherent and parallel electron beam of width a few tens of nanometres is incident on the carbon nanotube, was first used to study ropes containing multiple SWNTs [11,15]. This technique significantly improves the quality of electron diffraction patterns and allows for a more analytical approach to chirality assignment [7,17]. It has been also employed to investigate borone nitride nanotubes [18].

Figure 2.7 illustrates three modes of electron diffraction: SAED (fig. 2.7a), nano-area or NBED (fig. 2.7), and convergent-beam electron diffraction (CBED, fig. 2.7c). A schematic diagram of the principle of parallel-beam (or nano-beam) electron diffraction from a nanometer-sized area in a TEM is shown in the Fig.2.7b. The electron beam is focused onto the focal plane of the objective lens, which forms a parallel beam illumination on the sample. For a condenser aperture of 10 μm in diameter, the probe diameter is around 50 nm, which is much smaller than conventional SAED, and does not suffer from aberration induced image shift. The third condenser lens (available for example, at JEOL and FEI Titan microscopes), or mini-lens, in this mode provides the flexibility and demagnification for the formation of a nanometer-sized parallel beam. In electron microscopes with two condenser lenses in the illumination system, the first lens is used to demagnify the electron source and the second lens to transfer the demagnified

source image to the sample at focus (for probe formation) or under-focused to illuminate a large area [16].

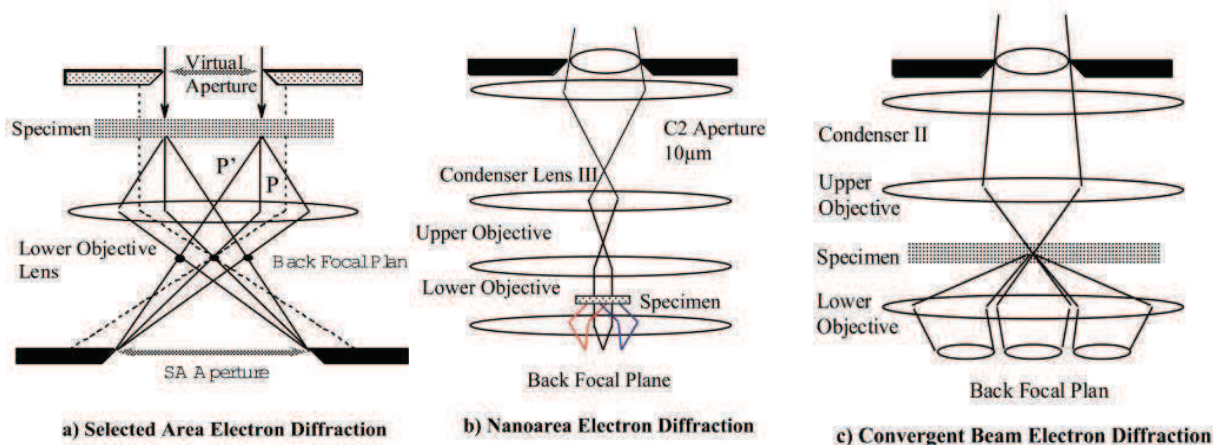


Fig. 2.7: Three modes of electron diffraction. Both selected area electron diffraction (SAED) (a) and nanoarea electron diffraction (NED) (b) use parallel illumination. SAED limits the sample volume contributing to electron diffraction by using an aperture in the image plane of the image forming lens (objective). NED achieves a very small probe by imaging the condenser aperture on the sample using a third condenser lens. Convergent beam electron diffraction (CBED) (c) uses a focused probe. Nano-beam electron diffraction is important for the investigation of CNTs because of the small scattering cross section of carbon and the requirement of a straight tube for electron diffraction. Adapted from [16].

In this work HRTEM and NBED experiments were performed in a FEI Titan Cubed C_s corrected 60-300 kV TEM of the Laboratorio de Microscopias Avanzadas (Instituto de Nanociencia de Aragon, U. de Zaragoza, Zaragoza (Spain)), operating at 80 kV. For the NBED, the smallest condenser aperture was employed, providing a highly coherent and parallel nanoprobe (40–50 nm). The CNTs electron diffraction patterns (EDPs) were recorded using a charge-coupled device (CCD) camera (Gatan Ultrascan 2Kx2K) with two different camera lengths: 285 mm and 460 mm. We note that no "blooming" effect was observable. The acquisition time of each EDP was <10 s. We have checked that with this procedure several EDPs can be acquired without any radiation damage of the tube. Indeed, for avoiding any damage, we limited the electron beam dose. [17]

2.3.2 Electron diffraction of carbon nanotubes

a) Single-walled nanotubes

In Chapter 1 we have seen that the structure of carbon nanotube may be determined in a unique way either by a set of (d, θ) parameters or by a pair of (n, m) indices. Knowledge of structural information is an essential step in the correct analysis of optical and vibrational

properties of the nanotubes. Below we consider the electron diffraction by single-walled nanotubes and show that it provides a direct way to determine all the structural data of the nanotubes in question.

An electron diffraction pattern of a SWNT can be seen as an image of its reciprocal space superimposed with some extra features. We can distinguish here two effects:

Diffraction from two parallel sheets of graphene

Figure 2.8b shows reciprocal space (and hence the diffraction pattern) for three graphene sheets having armchair (left), zig-zag (center) and chiral (right) geometries. An incident electron beam normal to the tube axis passes sequentially through two graphene sheets (corresponding to the ‘top’ and ‘bottom’ wall of the carbon nanotube). The resultant diffraction pattern is the sum of that from each graphene sheet. If the graphene sheets are rotated with respect to one another about the axis normal to the plane of the sheets (as in the case of chiral nanotubes), then the two diffraction patterns will also be rotated with respect to one another by the same angle.

As it is clear from Fig. 2.8a,b the reciprocal lattice orientation corresponds to those of the real space honeycomb structure. Consequently, we are able to retrieve the nanotube chiral angle by analyzing hexagonal structure of the ED patterns.

In real ED patterns however the sharp diffraction spots from Fig. 2.8b appear smeared in the radial direction due to the finite diameter and radial curvature of the nanotube. The smeared spots form a series of so-called layer lines (see Fig. 2.9a).

Diffraction from the nanotube as a whole

Carbon nanotube may act as a slit for an incoming electron beam, which results in a diffraction pattern similar to those of a single slit diffraction in optics (Fig. 2.8c). Keeping in mind that positions of maxima and minima in such diffraction pattern depend on the size of the slit, we may be able to access the nanotube diameter from EDP.

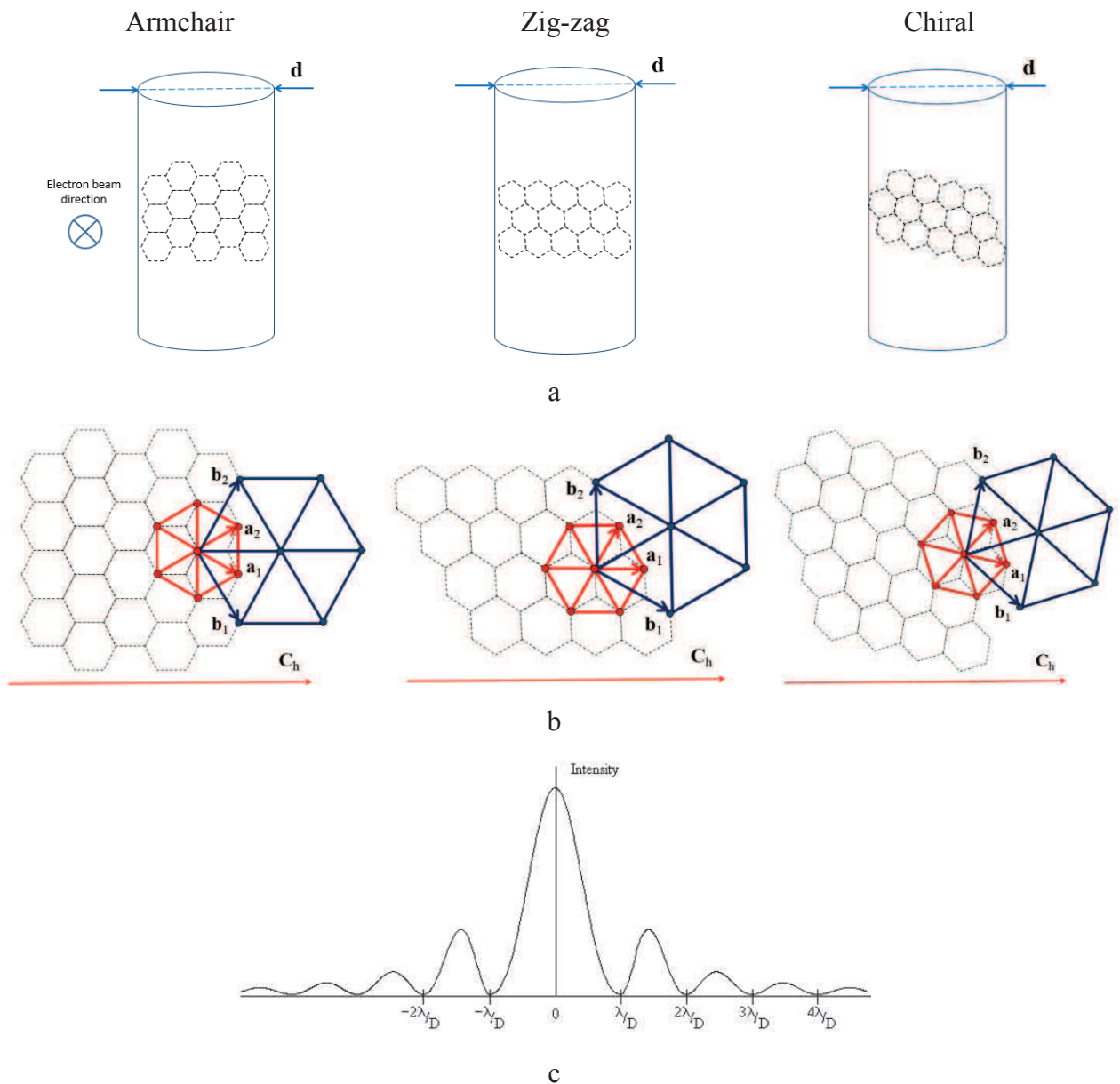


Fig. 2.8: (a) Electron diffraction of the single-walled carbon nanotubes as a superposition of the two effects: (b) Diffraction from the nanotube walls. Figure shows the honeycomb structure (dashed black lines in the background) of the graphene sheet, its hexagonal direct space lattice (in red) and hexagonal reciprocal lattice (in blue) for armchair (left), zig-zag (center) and chiral (right) nanotubes. (c) Diffraction from a nanotube as a whole resembling single-slit diffraction from optics.

b) A review on the structure identification of carbon nanotubes by electron diffraction

The structural information from electron diffraction patterns may be retrieved either by measuring axial positions of the layer lines or by determining the intensity distribution in the radial direction (see Ref [7] for a review). We now examine each approach in detail.

Axial measurements

Gao et al [19] was the first to explicitly use the axial positions of the layer lines to determine SWNT structure. By applying simple geometrical arguments, he determined the chiral angle of the nanotube in the following way:

$$\theta = \arctan\left(\frac{1}{\sqrt{3}} \frac{d_2 - d_1}{d_3}\right) = \arctan\left(\frac{1}{\sqrt{3}} \frac{2d_2 - d_3}{d_3}\right) \quad (2.1)$$

where d_i is the distance of the i^{th} layer line from the equatorial line (see Fig 2.9a). Note that eq. (2.1) is based on a ratio between distances in the EDP. The calculation of the chiral angle is then free from calibration of the EDPs. In the following, we will actively use the relation (2.1) to calculate θ .

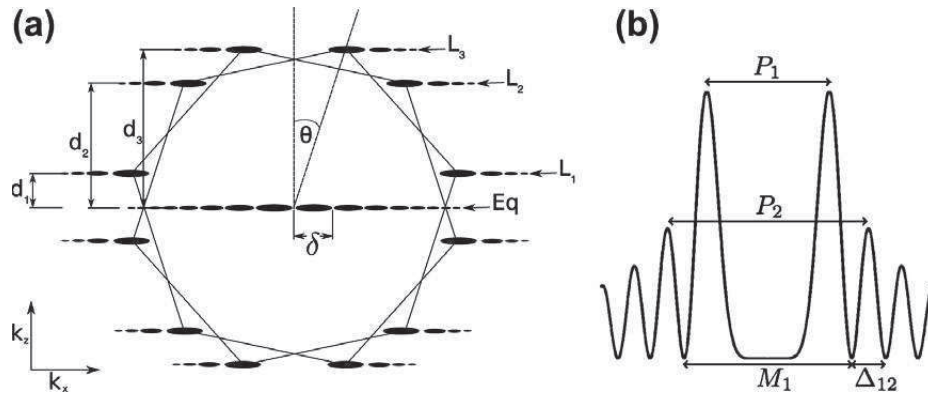


Fig. 2.9: (a) A schematic depiction of the diffraction pattern obtained from a SWNT. The hexagons mark the first order reflections from the graphene lattice. The first three layer lines are indicated (L_1 – L_3) as is the equatorial oscillation and its oscillatory period, δ . The chiral angle θ is shown and the axial distances of each of the layer lines (d_1 to d_3) are marked. (b) The theoretical form of the radial intensity distribution of one of the layer lines. The separation of the first and second order peaks (P_1 and P_2) are shown as is the separation of the first order minima (M_1) and the oscillatory period (Δ_{12}). From [7].

The further development of this analysis was performed by Liu et al in 2005 [19]. In particular, he related the ratio of the chiral indices m/n to the d_i values measured from EDP [19, 20]:

$$\frac{m}{n} = \frac{d_2 - d_1}{d_2 + 2d_1} \quad (2.2)$$

$$\frac{m}{n} = \frac{d_3 - 2d_1}{d_3 + d_1} \quad (2.3)$$

$$\frac{m}{n} = \frac{2d_2 - d_3}{2d_3 - d_2} \quad (2.4)$$

The use of d_i ratios allows a calibration-free analysis and in addition makes it robust against any tilt of the axial plane of the SWNT away from normal to the incident electron beam.

Approximating the Ewald sphere to a plane (due to the high energy of the electrons used in diffraction experiments), simple geometric considerations show that tilting the tube away from normal to the incident electron beam increases the measured d_i distances by a factor of $1/\cos\tau$, with τ being the axial (out-of-plane) tilt angle of the tube [21] axis. For very large tilt angles ($\tau > 45^\circ$) the planar approximation of the Ewald sphere will introduce a systematic error approaching the order of magnitude of experimental uncertainties. However, for realistic values of τ this approximation is sufficient [7].

Jiang et al [21] in 2007 proposed an alternative way to determine chiral indices of carbon nanotubes. He proposed to divide the d_i distances by the period of the equatorial oscillations δ . In that way, Jiang obtained the dimensionless (and hence calibration independent) parameters ξ_i , which are related to (n,m) indices by the following formulas:

$$\begin{aligned} n_{12} &= \frac{\pi}{3\sqrt{3}} \cdot (\xi_2 + 2\xi_1) & m_{12} &= \frac{\pi}{3\sqrt{3}} \cdot (\xi_2 - \xi_1) \\ n_{13} &= \frac{\pi}{3\sqrt{3}} \cdot (\xi_3 + \xi_1) & m_{13} &= \frac{\pi}{3\sqrt{3}} \cdot (\xi_3 - 2\xi_1) \\ n_{23} &= \frac{\pi}{3\sqrt{3}} \cdot (\xi_2 + 2\xi_1) & m_{23} &= \frac{\pi}{3\sqrt{3}} \cdot (2\xi_2 - \xi_3) \end{aligned} \quad (2.5)$$

Here the subscripts correspond to the pairs of d_i distances used in the calculation with $n_{12} = n_{13} = n_{23} = n$ and $m_{12} = m_{13} = m_{23} = m$. The chiral indices calculated in this way, while being independent of the calibration of the diffraction pattern, are not independent of any tilt of the axial plane of the SWNT with respect to the incident electron beam. The measured values of ξ_i are therefore a factor of $1/\cos\tau$ greater than the real values. Thus axial tilt will result in the calculation of non-integer values for $n_{i,j}$ and $m_{i,j}$ [7].

Radial measurements

A more complete description of electron diffraction through an individual SWNT, first introduced by Qin in 1994 [10], is obtained by considering the tube as a series of molecular helices [20]. Within this description the radial intensity distribution of each layer line is described by the square of a Bessel function, the order of which is directly related to the chiral indices of the tube:

$$\begin{aligned}
I_1(X) &\propto |J_{n+m}(\pi D_0 X)|^2 \\
I_2(X) &\propto |J_n(\pi D_0 X)|^2 \\
I_3(X) &\propto |J_m(\pi D_0 X)|^2 \\
I_4(X) &\propto |J_{n-m}(\pi D_0 X)|^2 \quad (2.6)
\end{aligned}$$

where $I_i(X)$ is the radial intensity distribution of the i^{th} layer line, D_0 the diameter of the SWNT and X the reciprocal space distance in the radial direction [7]. Within this molecular helix model the radial intensity of the equatorial oscillation, I_{Eq} can be described by the square of a zero order Bessel function:

$$I_{Eq} \propto |J_0(\pi D_0 X)|^2 \quad (2.7)$$

A zero order Bessel function $J_0(x)$ can, for $x \gg 0$, be approximated to [29]:

$$J_0(x) = \sqrt{\frac{2}{\pi x}} \cos\left(x - \frac{x}{4}\right) \quad (2.8)$$

Eq. (2.8) is equal to zero at values of $x = \left(j - \frac{1}{4}\right)\pi$ where j is an integer. As in this case $x = \pi D_0 X$, the diameter of the SWNT can therefore be approximated from the period of the equatorial oscillations, δ [\AA^{-1}]:

$$D_0 = \frac{1}{\delta} \quad (2.9)$$

Note that the calculation of D_0 with formula (2.9) requires the calibration of the EDP.

The oscillatory period of a Bessel function of a particular order is unique. The ratio of peak separations is defined as:

$$R_p = \frac{P_1}{P_2} \quad (2.10)$$

where P_1 and P_2 are the separation of the first and second order peaks, respectively (see Fig. 2.9). First proposed by Liu and Qin in 2005, the order of the dominant Bessel function of a particular layer line can be determined from measurement of P_1 and P_2 , calculation of R_p and subsequent comparison with theoretical values [23]. As the Bessel function order increases, the difference between theoretical R_p values decreases, resulting in the need for very accurate measurement of P_1 and P_2 to assign high order Bessel functions.

This limitation was addressed in the subsequent work of Jiang and co-workers in 2006 [24]. They suggest that high order Bessel functions can be more accurately determined by the

use of the ratio of the first peak (P_1) or minimum separation (M_1) to the distance between the first two minima (Δ_{12} , see Fig. 2.9) [24]:

$$R_{PD} = \frac{P_1}{\Delta_{12}} \quad (2.11)$$

$$R_{MD} = \frac{M_1}{\Delta_{12}} \quad (2.12)$$

Any tilt of the axial plane of a SWNT away from normal to the incident electron beam results in a change in the positions of the peaks in the radial intensity distribution [24,25]. For high order Bessel functions this can be accounted for by scaling the radial distance along each layer line using the expression

$$X' = \frac{\sqrt{d_i^2 \sin^2 \tau + X^2}}{L\lambda} \quad (2.13)$$

where d_i is the distance of the layer line in the axial direction, τ the axial tilt of the tube, λ the wavelength of the incident electrons and L the distance between the sample and the imaging plane (the product $L\lambda$ is generally referred to as the camera constant of the microscope). However, as noted by Jiang et al., for low order Bessel functions a tube tilt of as little as 6° can cause the strongest peaks in the radial intensity distribution to merge, thus causing the Bessel function assignment to fail [24].

Finally, it is possible to determine chiral indices of individual SWNTs by comparing experimental EDPs to the simulations [30-32]. The kinematical simulations of the EDP has been developed using a C++ code adapted by M. Kociak (LPS, Orsay (France)) from the code *Diffra* developed by L. Henrard and P. Lambin (U. Namur, Belgium).

c) ED pattern calibration

In the previous section we mentioned the need of an EDP calibration for the measurements of carbon nanotube diameter. In fact, the accurate calibration of the diffraction pattern is one of the most important factor in the correct determination of the chiral indices of a SWNT. The basic idea behind this procedure is to connect the length of the reciprocal wave vector in pixels (from EDP) to those in \AA^{-1} in reciprocal space.

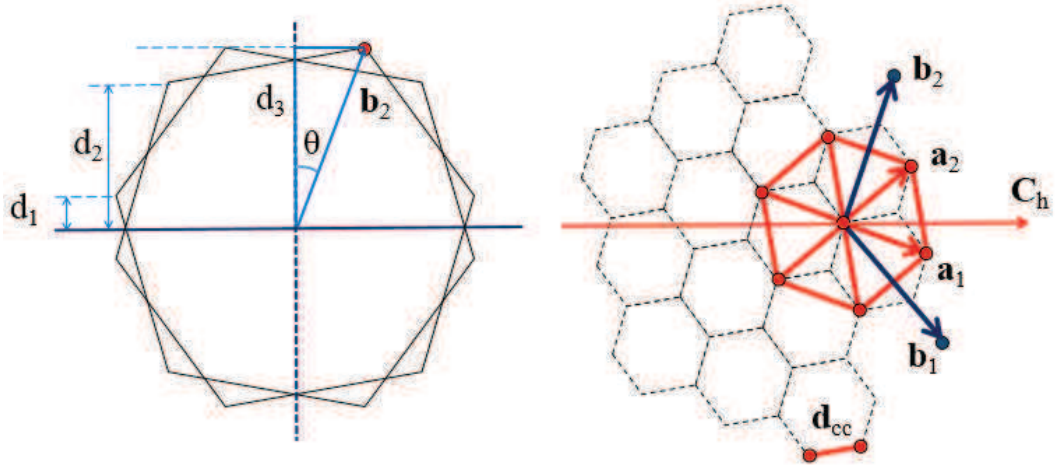


Fig. 2.10: EDP of a single-walled carbon nanotube (left) and the corresponding honeycomb structure of the nanotube wall (right). Direct and reciprocal lattice unit vectors are shown in red and blue respectively.

Simple geometric considerations (see Fig. 2.10) give

$$\cos\theta = \frac{d_3(\text{pixels})}{b_2} \quad (2.14)$$

And from solid state physics we know that

$$a_2 = \sqrt{3}d_{cc} \quad (2.15)$$

$$b_2 = \frac{1}{a_2} = \frac{1}{\sqrt{3}d_{cc}} \quad (2.16)$$

Hence

$$d_3 = \frac{\cos\theta}{\sqrt{3}d_{cc}} \quad (2.17)$$

We now introduce calibration coefficient C such as

$$C = \frac{\cos\theta}{\sqrt{3}d_{cc}d_3} (\text{pixels} \cdot \text{\AA})^{-1} \quad (2.18)$$

Where $d_{cc} = 0.142$ nm, and θ is derived from the same ED pattern using equation (2.1). Consequently, by multiplying any quantity in pixels derived from EDP by the right side of the eq. (2.18), we obtain its value in nm^{-1} (or sometimes expressed in \AA^{-1}).

On the presence of 2π coefficient

In the literature [33] we may sometimes find a different form of the equation (2.16), namely

$$b_2 = \frac{2\pi}{a_2} \quad (2.19)$$

A 2π coefficient then will be found in all subsequent formula, including calibration equation (2.18). The question, whether to include or not a 2π , may be confusing at the first glance. We try now to elucidate this aspect.

The tradition to use a 2π coefficient to relate direct and reciprocal space vectors comes from the Solid State Physics when regarding, for example, electron waves having periodicity of the Bravais lattice. It is common to write in this case the periodic conditions for the wave in the following form:

$$e^{i\mathbf{k}(\mathbf{r}+\mathbf{R})} = e^{i\mathbf{k}\mathbf{r}} \rightarrow e^{i\mathbf{k}\mathbf{R}} = 1 \quad (2.20)$$

And then

$$\mathbf{k}\mathbf{R} = 2\pi n \rightarrow \mathbf{k} = \frac{2\pi}{\mathbf{R}} \quad (2.21)$$

or equivalently by taking unit vectors

$$\mathbf{b} = \frac{2\pi}{\mathbf{a}} \quad (2.22)$$

In the applied science however it is common to omit this 2π factor and keep it in the \mathbf{b} vector implicitly. Thereby for EDP calibration we will only use formulas (2.16) and (2.18) without an additional coefficient.

d) Double-walled nanotubes

The diffraction patterns from individual double-walled carbon nanotubes may be considered as a superposition of EDP of constituent SWNTs. Hence, the majority of methods developed for single-walled nanotubes is still applicable for the case of DWNTs.

Diameters

Diffraction pattern and index assignment of DWNTs have been extensively discussed in the paper of Kociak et al [33]. They interpreted the DWNT diffraction pattern by making use of the theory developed by Lambin and coworkers [26,29] for the general case of a SWNT, a MWNT or a rope of tubes. They claim that a kinematic theory is also fully justified for such thin objects like the DWNT.

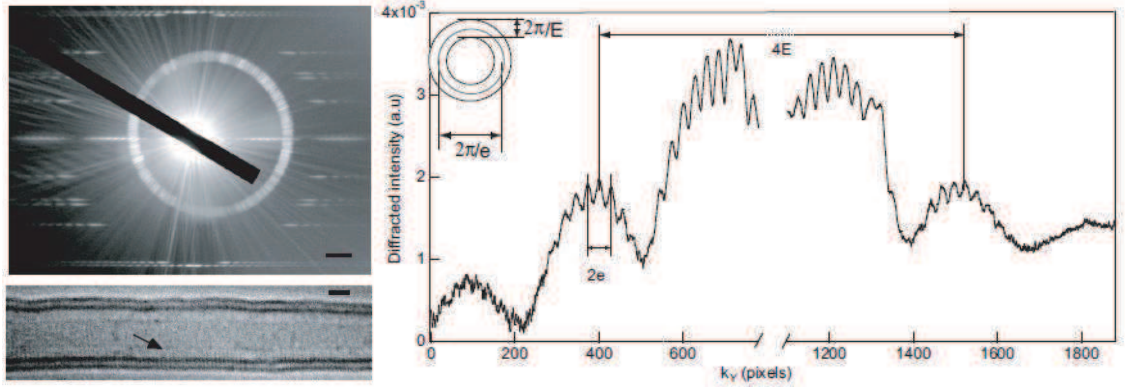


Fig. 2.11: (a) Diffraction pattern and image of the same DWNT and (b) Intensity profile of the equatorial line. The central spot has been skipped for clarity. From [33]

To analyze equatorial line oscillations of the DWNT ED pattern (Fig. 2.11b) Kociak proposed the following formula:

$$I_{d\omega,0}(\mathbf{k}) \sim f_c^2(\mathbf{k}) \times \left\{ \left(\cos^2 \left(k_{\perp} \bar{R} - \frac{\pi}{4} \right) \cos^2(k_{\perp} \delta R) + \frac{1}{4} \frac{\delta R}{\bar{R}} \sin \left(2k_{\perp} \bar{R} - \frac{\pi}{2} \right) \sin(2k_{\perp} \bar{R}) + o \left(\frac{\delta R^2}{\bar{R}^2} \right) \right) \right\} \quad (2.23)$$

Here, $\delta R = |R_A - R_B|/2$ and $\bar{R} = (R_A + R_B)/2$.

This expression is similar to that extracted from a simple model where the main contribution to the equatorial line comes from the Young-slit-like diffraction by the generator lines of the two tubes. The intensity along the equatorial line oscillates with a period of $e = 2\pi/2\bar{R}$, within an oscillatory envelope of period $E = 2\pi/2\delta R$. This appears on the experimental diffraction pattern (Fig. 2.11a) as well as in the intensity profile of Figure 2.11b.

Chiral angles

The chiral angle determination from the EDP of the DWNT is similar to that of the SWNT, except that the analysis become more complicated due to the higher number of reflexes. Below we draw EDPs for different DWNT combinations: chiral/chiral, armchair/chiral, zigzag/chiral and armchair/zigzag and show how to assign different reflexes.

For instance, for a general case of two chiral layers we have 6 different reflexes in every quadrant of the EDP (see Fig. 2.12, top part). However, by analyzing carefully the EDP we may conclude that the 1st, 4th and 5th reflexes correspond to the nanotube with the biggest θ , while the 2nd, 3rd and the 6th to those with the smallest θ .

When chiral angle increases, the 4th and 5th reflexes approach each other and completely coincide in the case of the armchair nanotube. The 1st reflex then is situated on the equatorial line and practically is not observed (see Fig.2.12, bottom left). Similarly decreasing the chiral angle, we make the 2nd and 3rd reflexes coincide till the extreme case of the zig-zag nanotube (see Fig. 2.12 bottom center part).

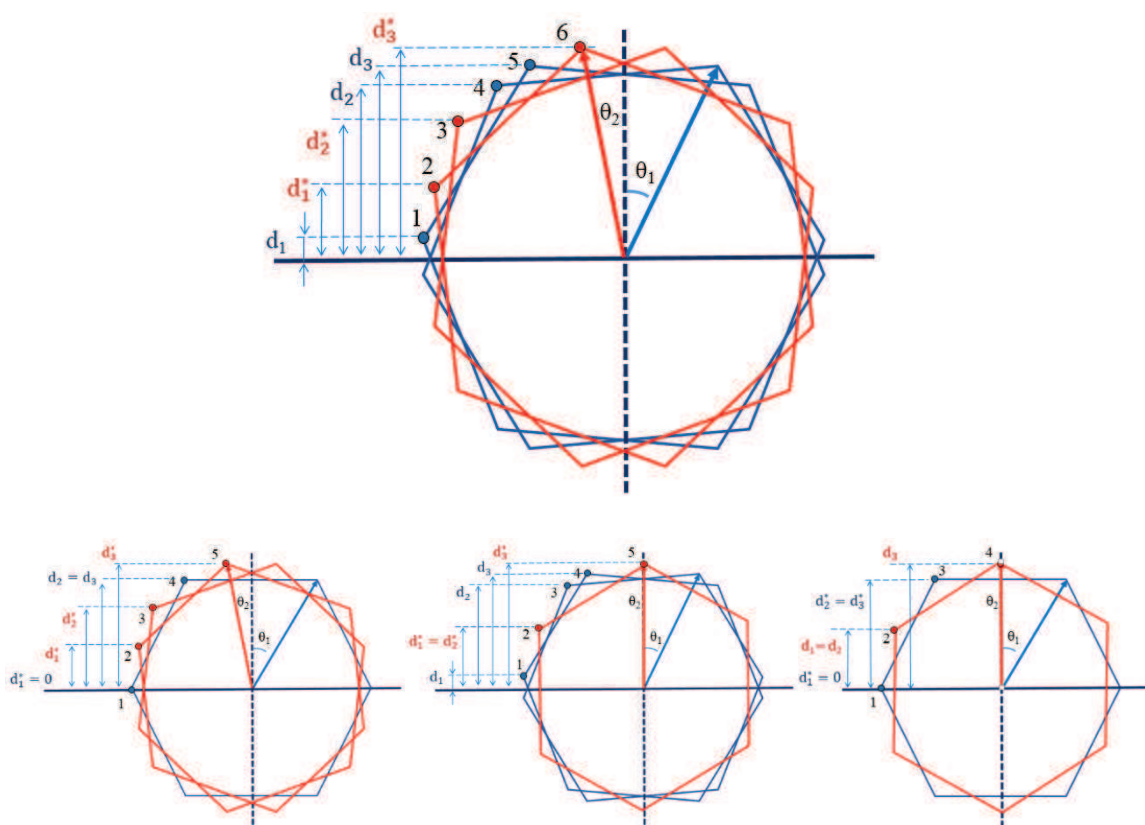


Fig. 2.12: The electron diffraction patterns of the double-walled nanotubes: general case of two chiral layers (top), armchair and chiral layers (bottom left), zig-zag and chiral layers (bottom center) and armchair and zig-zag layer (bottom right). Notice different number of reflexes (see numbers 1,2,3 etc in the figures) for different configurations. For the general case of two chiral tubes 1st, 4th and 5th reflexes always correspond to the tube with the biggest θ , while 2nd, 3rd and 6th to the one with the smallest θ (see text for details).

Measured two sets of d_i values for two different layers of the DWNT, we calculate the corresponding θ_i by eq. (2.1). We emphasize that a-priori we don't know which θ_i corresponds to what layer. Hence to assign definite (n,m) indices we need to consider two different combinations, namely:

$$(D_{\min}, \theta_1) @ (D_{\max}, \theta_2)$$

$$(D_{\min}, \theta_2) @ (D_{\max}, \theta_1)$$

e) Triple-walled nanotubes

Finally, there is no special way to treat the EDP of TWNTs. In general, we follow the same procedures as for the DWNTs except for the equatorial line analysis. The fact is that the equatorial line oscillations in the ED patterns of TWNT do not have such an intuitive form as in the case of single- and double-walled nanotubes. We thus need to provide a HRTEM image of the nanotube for an unambiguous assignment of chiral indices. From the HRTEM image we extract the mean diameters of the internal, intermediate and external layers. Combining this information with the three chiral angles calculated as usual we can obtain possible chiral indices of all the layers.

We just note that in the general case of a TWNT with three chiral layers the reflexes are organized in the following way:

1st, 6th and 7th correspond to the layer with biggest θ (θ_1 in the Fig.2.13);

2nd, 5th and 8th –to the medium θ (θ_2 in the Fig.2.13) and

3rd, 4th and 9th to the smallest θ (θ_3 in the Fig.2.13).

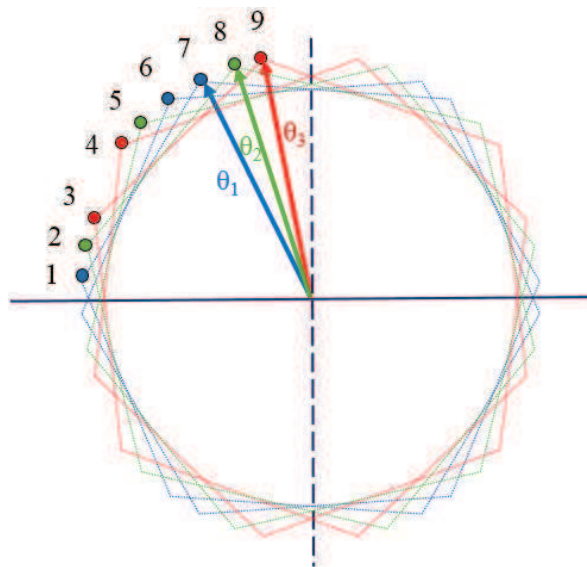


Fig. 2.13: Position of the reflexes for the general case of TWNT with three chiral layers.

Summary

In the previous section different ways to analyze EDP from the literature were presented. We may remind that the atomic structure of SWNTs (d , θ) can be obtain through the measurements of (i) the eq. line oscillation period and (ii) the layer line distances (d_i) ratio. The latter is independent of calibration, while the diameter determination is sensitive to the calibration constant. There exist also others methods, which are calibration free and provide directly the (n,m) indices but are very sensitive to tilt angles. For DWNTs, the EDP is equivalent to the sum of the two constituting SWNT's EDPs and their chiral angles determination is straightforward. By contrast, the diameter of each constituting SWNT is not directly measured from diffraction pattern, but can be derived from the mean diameter \bar{D} and the interlayer distance δD . They are defined by:

$$\bar{D} = \frac{D_{out} + D_{in}}{2}$$
$$\delta D = \frac{D_{out} - D_{in}}{2}$$

Where D_{in} (D_{out}) stands for the diameter of the inner (outer) tube.

When (d , θ) parameters are known with a good accuracy, it is possible to find the corresponding (n,m) indices which are more suitable to interpret the Raman spectra of the same CNTs. However when the CNT diameter is large enough (roughly $\sim > 2$ nm), the problem to find the pair of (n,m) equivalent to (d , θ) is not straightforward since several CNTs can fall within the experimental uncertainties. To resolve this problem we have written a code that allows to identify the different candidates. It takes into account Raman data for the given nanotube and will be presented in the Chapter 5.

2.4 Results. Index-assignment. Data treatment and existing problems.

Following the procedures described in Section 2.3 we analyzed 12 individual single-walled, 13 individual double-walled and 3 individual triple-walled carbon nanotubes from different synthesis protocols (see Table 2.1 for synthesis details). A summary is presented in the tables 2.6 and 2.11 for SWNTs and DWNTs respectively.

2.4.1 Single-walled carbon nanotubes

Below we give two examples of EDPs and HRTEM images treatment of the individual single-walled nanotubes: SWNT-2 and SWNT-1 from Table 2.6.

Example 1 (SWNT-2)

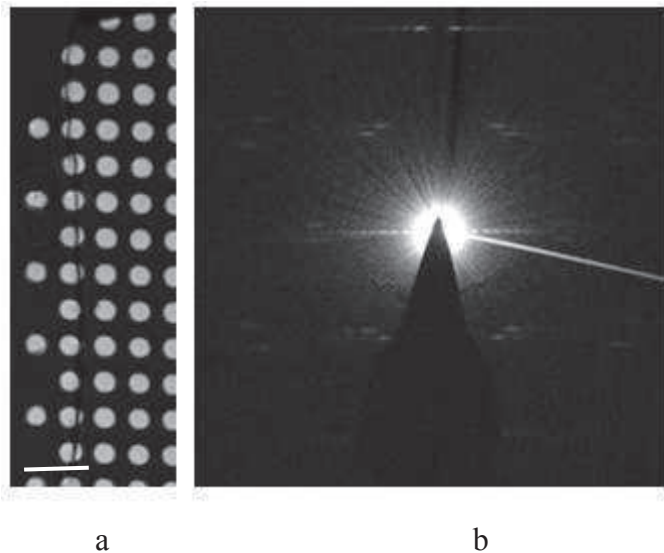


Fig. 2.14: (a) a low-resolution TEM image of an individual SWNT-2 (the scale bar is 10 μm). (b) Corresponding EDP.

Fig. 2.14 shows a low-resolution TEM image and an ED pattern for the SWNT-2. Unfortunately, for this example we could not obtain any HRTEM images due to high vibrations of nanotube under the electron beam. Hence, all the assignments will be based only on the ED pattern analysis. First of all, we conclude that this tube is long and homogenous, because ED patterns were not changing at different areas along the nanotube.

The period of the equatorial oscillation from EDPs (fig. 2.14b) was found to be $\langle\delta\rangle = 19.5 \pm 1$ pixels. Using equation (2.9) and proper calibrations for the EDPs, the diameter of the SWNT was calculated to be $\langle D_0 \rangle = 2.45 \pm 0.3$ nm.

The d_i values measured from the Fig. 2.14b have the following values:

$$\langle d_1 \rangle = (14.7 \pm 1) \text{ pixels},$$

$$\langle d_2 \rangle = (180.6 \pm 1) \text{ pixels}$$

$$\langle d_3 \rangle = (196 \pm 1) \text{ pixels}.$$

Inserting them in the relation (2.1), we find the chiral angle to be $\langle \theta \rangle = 26.07^\circ \pm 0.2^\circ$.

We additionally crosscheck our further assignments by considering m/n ratios from EDPs. They are calculated by equations (2.2-2.4) and presented in the last columns of Table 2.2.

Table 2.2. Experimental values measured from ED patterns of the SWNT-2.

EDP	d_1 (pix)	d_2 (pix)	d_3 (pix)	Δ (pix)	Calibr. (pix.Å ⁻¹)	D (nm)	Θ (°) (d_1, d_2)	Θ (°) (d_2, d_3)	m/n (d_1, d_2)	m/n (d_2, d_3)
1 (285 mm)	14.8	180.7	195.6	19	0.0021	2.51	26.09	26.08	0.7890	0.7876
2 (285 mm)	14.6	180.6	196	20	0.0021	2.38	26.06	25.95	0.7920	0.7815

Combining diameter and chiral angle values from table 2.2, we calculate the following possible combinations (within experimental uncertainties):

Table. 2.3: Possible candidates for the SWNT-2.

(n,m)	D, nm	θ	Type ($2n+m$) mod 3	m/n
(18,14)	2.18	25.87	2	0.778
(19,15)	2.31	26.11	2	0.789

According to tables 2.2 and 2.3 m/n ratio for the (19,15) tube is closer to the experimental ratio than those of (18,14). We thus conclude that the example 1 is a (19,15) single-walled carbon nanotube.

Example 2 (SWNT-1)

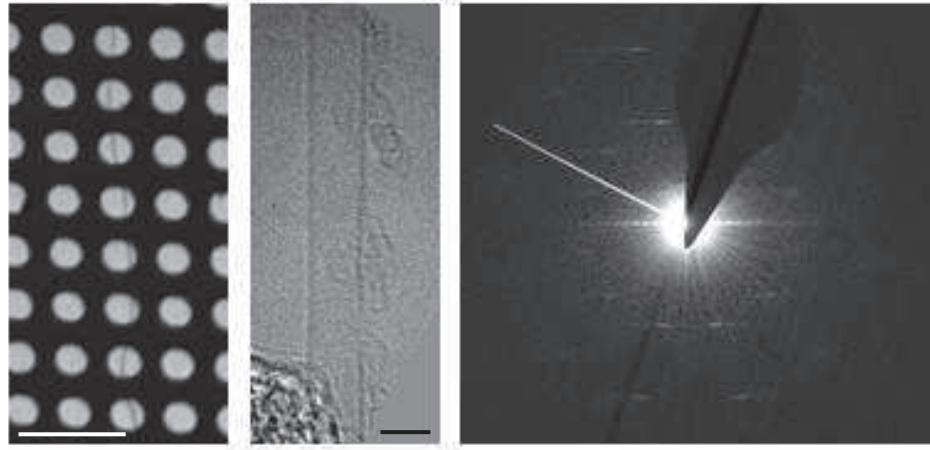


Fig. 2.15: (a) A low-resolution (the scale bar is 10 μm) and (b) a high-resolution (the scale bar is 2 nm) TEM images of an individual SWNT (SWNT-1). (c) Corresponding EDP.

Fig. 2.15 shows the second individual single-walled carbon nanotube. We note that the tube is long and homogenous, which was proved by several measurements of the EDP and HRTEM images in different areas along the nanotube (see Fig. 2.15a).

Estimations of the nanotube diameter from real space HRTEM images (fig. 2.15b) give diameter of 2.2 ± 0.5 nm. The period of the equatorial oscillation from EDP (fig. 2.15c) was found to be $\delta = 20 \pm 1$ pixels. Using equation (2.9) and proper calibrations for the EDPs, the diameter of the SWNT was calculated to be $D_0 = 2.4 \pm 0.3$ nm.

The d_i values measured from the 3 different ED patterns have the following average values:

$$d_1 = (62 \pm 1) \text{ pixels},$$

$$d_2 = (154 \pm 1) \text{ pixels}$$

$$d_3 = (216.5 \pm 1) \text{ pixels}.$$

Inserting them in the relation (2.1), we find the chiral angle to be $\theta = 13.9^\circ \pm 0.2^\circ$.

We additionally crosscheck our further assignments by considering m/n ratios from EDPs. They are calculated by equations (2.2-2.4) and presented in the last columns of Table 2.4.

Table 2.4. Experimental values measured from ED patterns of the SWNT-1.

EDP	d ₁ (pix)	d ₂ (pix)	d ₃ (pix)	Δ (pix)	Calibr. (pix.Å ⁻¹)	D (nm)	Θ (°) (d ₁ ,d ₂)	Θ (°) (d ₂ ,d ₃)	m/n (d ₁ ,d ₂)	m/n (d ₂ ,d ₃)
1 (285 mm)	61.6	154.7	217.25	21	0.0021	2.38	13.90	13.76	0.3373	0.3293
2 (285 mm)	61.75	153.8	216.2	19.85	0.0021	2.4	13.81	13.72	0.3335	0.3281
3 (285 mm)	60.6	153.8	216.35	-	0.0021	-	13.97	13.69	0.3436	0.3272

Combining diameter and chiral angle values from Table 2.4, we calculate the following possible combinations (within experimental uncertainties):

Table 2.5. Possible candidates for the SWNT-1.

(n,m)	D, nm	θ	Type (2n+m) mod 3	m/n
(24,8)	2.26	13.9	2	0.3333
(27,9)	2.54	13.9	0	0.3333

We are now able to make several conclusions. It is clear from table 2.5 that m/n ratios for this example do not allow to discern between two existing candidates. Secondly, if we consider HRTEM derived diameter we may opt for the (24,8) nanotube, but due to the high experimental error of these measurements, this can not be a very solid assignment. So we state that for the SWNT-1, the further experimental data is necessary to unambiguously assign its (n,m) indices.

Table 2.6. Structural information on individual single-walled carbon nanotubes studied in this work. Real diameter or real angle stand for parameters derived from the (n,m) values and not from experiments. For experimental errors of diameter and chiral angles measurements see text.

#	Experimental parameters			Possible indices	Real D, nm	Real θ , Degrees	Type
	D _{HRTEM} , nm	D _{diff} , nm	θ _{diff} , degrees				
1	2.2	2.4	13.8	(24,8) (27,9)	2.26 2.54	13.9 13.9	2 0
2	-	2.54	26.05	(19,15)	2.32	26.11	2
3	2.25	2.4	3.34	(29,2)	2.35	3.3	0
4	2.1	2.38	13.8	(24,8)	2.26	13.9	2
5	-	2.35	13.87	(24,8)	2.26	13.9	2
6	2.14	2.97	13.91	-	-	-	-
7	-	2.7	5.35	(35,4) (36,4)	2.91 2.99	5.35 5.21	2 1
8	2.7	3.15	7.25	(38,6)	3.24	7.22	1
9	2.5	2.76	6.7	(29,4)	2.44	6.38	2
10	-	5.88	13.12	(60,19)	-	-	-
11	2.3	-	-	-	-	-	-
12	1.95	-	-	-	-	-	-

2.4.2 Double-walled carbon nanotubes

In this section, we show the structural analysis of double-walled carbon nanotubes and illustrate it by several examples (for the results of the EDP treatment of all other DWNTs in this study refer to the Table 2.11).

Example 1 (DWNT-6)

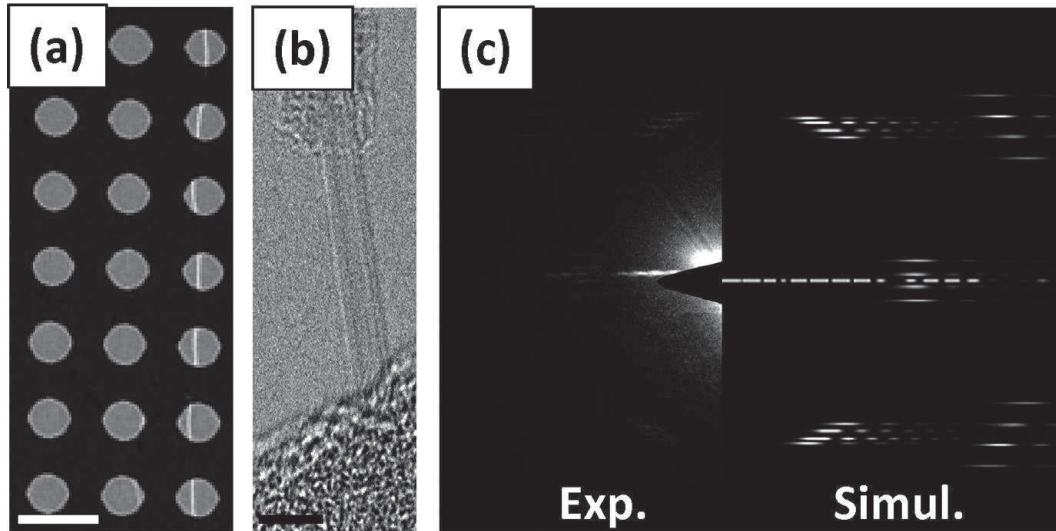


Figure 2.16: (a) Low magnification TEM image of the suspended nanotube on the Si_3N_4 grid, the scale bar is $4 \mu\text{m}$. (b) HRTEM of the same DWNT, the scale bar is 3 nm . (c) Experimental (left) and simulated (right) diffraction pattern of the DWNT-6.

Figure 2.16 shows TEM images and ED pattern of the first example of the DWNT. We should note that the analysis of EDPs for this nanotube have a certain difficulty. The information on the equatorial line oscillations is not available with a good accuracy due to the presence of the beam stop which masks the equatorial line on one side of the diffraction pattern. Consequently, the value obtained for the average diameter is found to be 1.9 nm with an error bar estimated at 10% .

The analysis of the layer-lines provided the following values of the chiral angle of each layer: 23.4° and 27.7° , with an error bar of (0.2°) . Considering these values as a starting point for the indexation of the DWNT, we compute all the possible (n,m) tubes that have chiral angles of 23.4° and 27.7° within the error bars. For $d \leq 2.5 \text{ nm}$, this leads to six possibilities for chiral angles $(23.4 \pm 0.2)^\circ$ and four possible indices for chiral angles $(27.7 \pm 0.2)^\circ$, giving 24 different indices for the DWNT.

Keeping in mind that the difference of the two diameters in a DWNT should be close to 0.68 nm, only two pairs of indices are possible: (8,7)@(15,10) and (12,8)@(16,14). The former DWNT can be ruled out because it disagrees with the average diameter derived from the equatorial line analysis.

Furthermore, this identification of the atomic structure is confirmed by the comparison of the experimental and the simulated ED pattern, as displayed in Figure 2.16c. The diameters of these chiral nanotubes are respectively $d_{in} = 1.36$ nm and $d_{out} = 2.03$ nm in agreement with the estimation provided by the HRTEM images. We note that each layer of this DWNT is semiconducting, the inner being of type I ($\text{mod}(n-m;3) = 1$) and the outer being of type II ($\text{mod}(n-m;3)=2$).

Example 2 (DWNT-1)

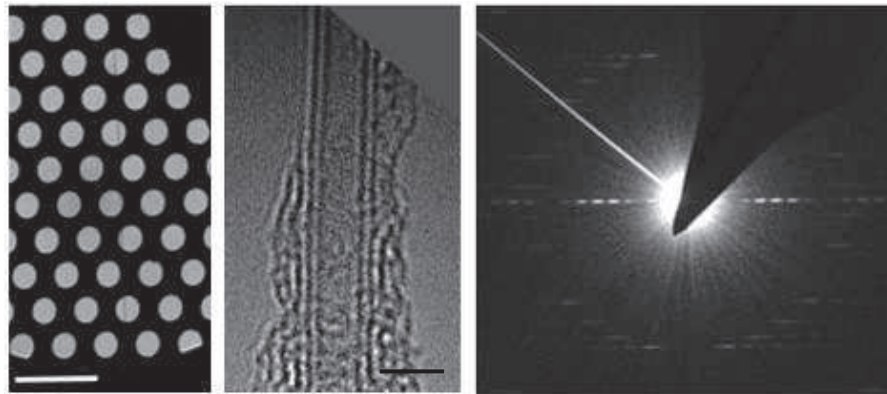


Figure 2.17: (a) Low magnification TEM image of the suspended nanotube on the Si₃N₄ grid, the scale bar is 10 μm . (b) HRTEM of the same DWNT, the scale bar is 2 nm. The amorphous carbon on the nanotube's surface was deposited during HRTEM imaging (c) Experimental diffraction pattern of the DWNT-1.

Fig. 2.17 shows the second individual DWNT. Again, the tube appeared to be homogenous and long enough so that we performed measurements at different areas. We note that the amorphous carbon on the surface of the tube (as seen in the Fig. 2.17) was deposited during HRTEM imaging and is located near the edge of the hole.

Estimations of the nanotube diameter from real space HRTEM images (fig. 2.17b) give $\langle D \rangle = 2 \pm 0.4$ nm. From the equatorial line oscillations of the EDP (fig. 2.17c) we found $E = 206 \pm 1$ pixels and $e = 39 \pm 1$. These correspond according to equation (2.23) to $\langle D \rangle = 1.99 \pm 0.3$ nm and $\delta r = 0.37$ or equivalently to $D_{out} = 2.36$ nm and $D_{in} = 1.62$ nm.

The d_i values measured from the 3 different ED patterns have the following average values:

$$d_1 = (23 \pm 1) \text{ pixels},$$

$$d_2 = (181 \pm 1) \text{ pixels}$$

$$d_3 = (203 \pm 1) \text{ pixels}.$$

$$d_{1^*} = (67 \pm 1) \text{ pixels},$$

$$d_{2^*} = (151 \pm 1) \text{ pixels}$$

$$d_{3^*} = (219 \pm 1) \text{ pixels}.$$

Inserting them in the relation (2.1), we find the 2 chiral angles

$$\theta_1 = 24.14^\circ \pm 0.2^\circ.$$

$$\theta_2 = 12.49 \pm 0.2^\circ$$

We additionally crosscheck our further assignments by considering m/n ratios from EDPs. They are calculated by equations (2.2-2.4) and presented in the last columns of Table 2.7.

Table 2.7. Experimental values measured from one of the ED patterns of the DWNT-1.

NT	d_1 (pix)	d_2 (pix)	d_3 (pix)	e (pix)	E (pix)	Calib. (pix.Å) ⁻¹	$\langle D \rangle$ (nm)	δr (nm)	Θ (°) (d_1, d_2)	Θ (°) (d_2, d_3)	m/n (d_1, d_2)	m/n (d_2, d_3)
a	23	181	203	38.7	205.8	0.0013	1.99	0.37	24.14	24.21	0.6947	0.7013
b	67	151	219						12.49	12.34	0.2972	0.2892

Combining diameter and chiral angle values from Table 2.7 for two constituent layers and taking the value of the intertube distance as $\delta D = 0.68 \pm 0.1$ nm, we get the following combinations (within experimental uncertainties):

Table 2.8. Possible candidates for the DWNT-1 (taking $\delta D = 0.68 \pm 0.1$ nm)

#	(n,m)	D, nm	δD (nm)	Θ (°)	Type ($2n+m$) mod 3	m/n
1	(13,9)	1.5	0.71	24.01	2	0.692
	(24,7)	2.21		12.43	1	0.292
2	(17,5)	1.56	0.75	12.52	0	0.294
	(20,14)	2.32		24.18	0	0.700

Unfortunately, on the basis of the EDP and HRTEM images analysis we cannot discern between the two possible candidates. The m/n ratios for both candidates 1 and 2 are very close to the experimental ones. However, given very different electronic type of the constituent layers of the two combinations, the final assignments may be made after spectral measurements. Therefore, we conclude that for the DWNT-1, the further experimental data is necessary to unambiguously assign its chiral indices.

Example 3 (DWNT-4)

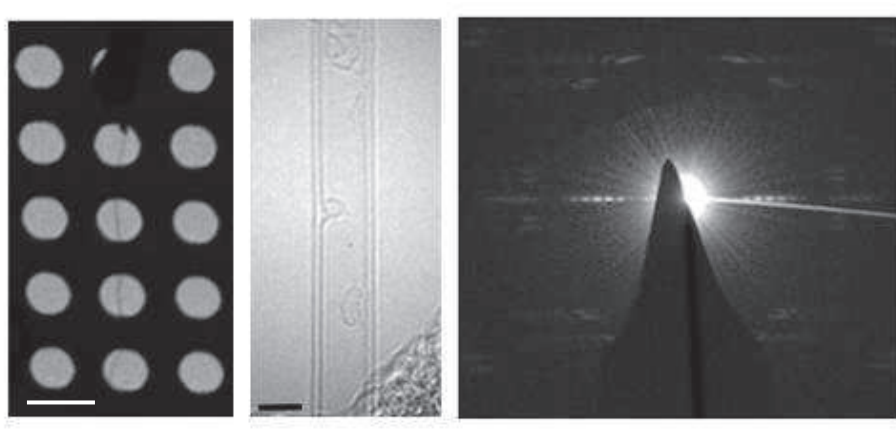


Fig. 2.18: (a) Low magnification TEM image of the suspended nanotube on the Si₃N₄ grid, the scale bar is 5 μ m. (b) HRTEM of the same DWNT, the scale bar is 2 nm. (c) Experimental diffraction pattern of the DWNT-4.

Fig. 2.18 shows the third example of a long individual DWNT. Estimations of the nanotube diameter from real space HRTEM images (fig. 2.18b) give $D_{out} = 3.2 \pm 0.5$ nm and $D_{in} = 2.5 \pm 0.5$ nm. From the equatorial line oscillations of the EDP (fig. 2.18c) we found $E = 124 \pm 1$ pixels and $e = 17 \pm 1$. These correspond according to equation (2.23) to $\langle D \rangle = 2.97 \pm 0.3$ nm and $\delta r = 0.4$ or equivalently to $D_{out} = 3.37$ nm and $D_{in} = 2.57$ nm.

The d_i values measured from the 3 different ED patterns have the following average values:

$$d_1 = (44 \pm 1) \text{ pixels,}$$

$$d_2 = (168 \pm 1) \text{ pixels}$$

$$d_3 = (210 \pm 1) \text{ pixels.}$$

$$d_{1^*} = (29 \pm 1) \text{ pixels,}$$

$$d_{2^*} = (176 \pm 1) \text{ pixels}$$

$$d_{3^*} = (205 \pm 1) \text{ pixels.}$$

Inserting them in the relation (2.1), we find the 2 chiral angles

$$\theta_1 = 19.06^\circ \pm 0.2^\circ.$$

$$\theta_2 = 22.49 \pm 0.2^\circ$$

We additionally crosscheck our further assignments by considering m/n ratios from EDPs. They are calculated by equations (2.2-2.4) and presented in the last columns of Table 2.9.

Table 2.9. Experimental values measured from one of the ED patterns of the DWNT-4.

NT	d_1 (pix)	d_2 (pix)	d_3 (pix)	e (pix)	E (pix)	Calib. (pix.Å) ⁻¹ ₁	$\langle D \rangle$ (nm)	δr (nm)	Θ (°) (d_1, d_2)	Θ (°) (d_2, d_3)	m/n (d_1, d_2)	m/n (d_2, d_3)
a	43.5	168	210	16.85	124.4	0.002	2.97	0.4	19.06	19.16	0.4947	0.5019
b	29	176	205						22.48	22.51	0.6261	0.6292

Combining diameter and chiral angle values from table 2.9 for two constituent layers and taking the value of the intertube distance as $\delta D = 0.68 \pm 0.1$ nm, we get the following combinations (within experimental uncertainties):

Table. 2.10. Possible candidates for the DWNT-4 (taking $\delta D = 0.68 \pm 0.1$ nm)

#	(n,m)	D, nm	δD (nm)	Θ (°)	Type ($2n+m$) mod 3	m/n
1	(22,14)	2.46	0.65	22.69	1	0.6364
	(30,15)	3.11		19.11	0	0.5000
2	(24,15)	2.67	0.65	22.41	0	0.6250
	(20,14)	3.32		19.11	2	0.7000
3	(22,11)	2.28	0.73	19.11	1	0.5000
	(27,17)	3.01		22.52	2	0.6296
4	(24,12)	2.49	0.73	19.11	0	0.5000
	(29,18)	3.22		22.30	1	0.6207
5	(26,13)	2.69	0.66	19.11	2	0.5000
	(30,19)	3.35		22.62	1	0.6333
6	(28,14)	2.90	0.66	19.11	1	0.5000
	(32,20)	3.56		22.41	0	0.6250

This example also shows a high number of possible candidates for the given DWNT. We state again that further experimental data is needed for unambiguous index-assignment. It is worth to note that two from six candidates are purely semiconducting. Thus information on the electronic structure of the DWNT-4 may help in the (n,m) indices determination.

Table 2.11. Structural information on individual double-walled carbon nanotubes studied in this work. . Real diameter or real angle stand for parameters derived from the (n,m) values and not from experiments. For the value of the experimental error, see text.

#	Experimental parameters			Indices	Real D, nm	Real θ , Degrees	Type	Δd , nm
	D_{HRTEM} , nm	D_{diff} , nm	θ_{diff} , degrees					
1	-	1.44@2.1	12.4, 23.9	(13,9)@(24,7)	1.5@2.206	24.01@12.43	2@1	0.71
2	-	<d>=1.8	19.1, 19.1	(16,8)@(22,11)	1.66@2.28	19.11@19.11	1@1	0.62
3	-	-	-	(18,2)@(20,12)	1.49@2.19	5.21@21.79	2@1	0.7
4	2.45@3.2	2.4@3.20	19.1, 22.73	(22,11)@(27,17) (26,13)@(30,19)	2.28@3.01 2.69@3.35	19.11@22.52 19.11@22.62	1@2 2@1	0.73 0.66
5	1.94@2.7	2.05@2.79	9.8, 25.9	(23,5)@(22,17) (23,5)@(23,18) (14,11)@(27,6)	2.03@2.65 2.03@2.79 1.7@2.39	9.64@25.77 9.64@25.97 26.04@9.83	0@1 0@1 0@0	0.63 0.76 0.68
6	-	1.36@2.03	23.4, 27.7	(12,8)@(16,14)	1.37@2.04	23.41@27.8	2@1	0.67
7	<D> = 2.7	1.87@2.54	8.6, 26.2	(21,4)@(20,16) (20,4)@(20,16)	1.82@2.45 1.74@2.45	8.57@26.33 8.95@26.33	1@2 2@2	0.63 0.7
8	-	2.19@2.99	13.54, 9.93	(22,5)@(28,9)	1.95@2.62	10.02@13.49	1@2	0.67
9	<D> = 3.2	3.25@4.06	12.41, 2.91	(34,10)@(47,3) (38,11)@(52,3)	3.13@3.8 3.49@4.2	12.52@3.07 12.35@2.78	0@1 0@2	0.68 0.71
10	5.1@5.8	5.61@6.51	22.04, 9.62	(61,13)@(55,33) (62,13)@(55,34)	5.36@6.03 5.44@6.09	9.47@21.79 9.33@22.24	0@2 2@0	0.67 0.66
11	3@3.7	3.69@4.46	10.63, 10.63	(37,9)@(45,11) (41,10)@(49,12)	3.31@4.03 3.67@4.38	10.64@10.68 10.66@10.70	2@2 2@2	0.72 0.72
12	5.45@6.2	6.35@7.12	24.15@20.51	(56,31)@(58,41) (57,31)@(58,41)	5.98@6.75 6.06@6.75	20.58@24.34 20.32@24.34	2@1 1@1	0.77 0.69
13	-	4.5@5.2	28.7, 21.5	(39,23)@(38,35) (44,26)@(42,39)	4.25@4.95 4.8@5.5	21.53@28.64 21.56@28.78	2@0 0@0	0.7 0.7

2.4.3. Triple- and multi-walled nanotubes

Finally, we apply the same procedure to the individual triple-walled carbon nanotube.

Example 1 (TWNT-1)

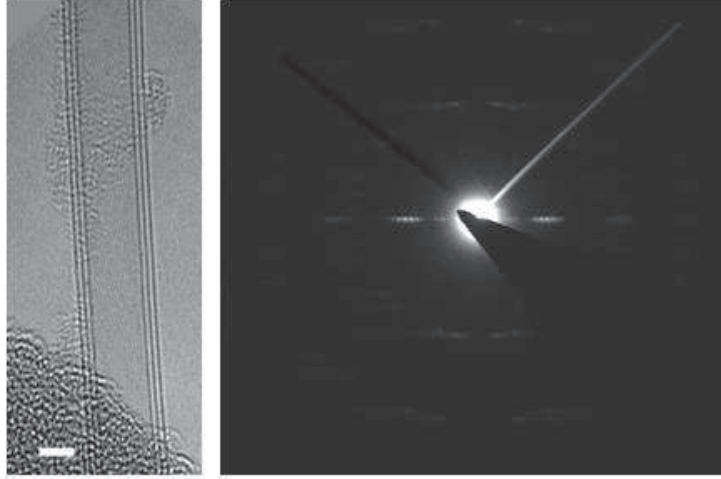


Fig. 2.19: (a) High-resolution TEM image (the scale bar is 2nm) and (b) ED pattern of the individual triple-walled carbon nanotube.

HRTEM image and ED pattern of the triple-walled carbon nanotube are presented in the Fig. 2.19 a,b. From the EDP we get three values of chiral angles:

$$\theta_1 = (17.72 \pm 0.2)^\circ$$

$$\theta_2 = (10.85 \pm 0.2)^\circ$$

$$\theta_3 = (8.88 \pm 0.2)^\circ$$

We remind that we cannot extract any structural information from equatorial line due to the complex character of its oscillations. Instead, we measure diameters from HRTEM images:

$$D_{\text{in}} = 3.31 \pm 0.5 \text{ nm}$$

$$D_{\text{mid}} = 4.0 \pm 0.5 \text{ nm}$$

$$D_{\text{out}} = 4.7 \pm 0.5 \text{ nm}$$

However, due to the big average diameter of the TWNT and higher experimental uncertainties of the HRTEM derived data, we get 19 possible combinations for this set of (D_i, θ_i) . We thus conclude that for big MWNTs it's almost impossible to assign unambiguously the chiral indices solely from the structural data. Later in Chapter 5 we will show, how the combination of ED and Raman data may help to greatly decrease the number of possible candidates for big multi-walled nanotubes.

2.5 Conclusion

In this chapter we have presented the synthesis of samples of individual single-, double- and multi-walled carbon nanotubes with different growing conditions. The summary of all the samples studied in this work précising the type of substrates, growth conditions, characterization techniques as well as the kind of nanotubes synthesized were given (see Table 2.1).

Then we described our experimental procedure for the localization and structural analysis of carbon nanotubes based on the SEM, Raman imaging, HRTEM and Electron diffraction. We discussed the main advantages and disadvantages of each method. Next, a review on the structure identification of carbon nanotubes by electron diffraction was presented, and we gave several examples of its application for single-, double- and triple-walled nanotubes. Overall, we analyzed 12 individual single-walled, 13 individual double-walled and 3 individual triple-walled nanotubes (see Tables 2.6 and 2.11). The indices derived for all the CNTs presented in this chapter will be used in the following to discuss their Raman spectra.

Finally, it was shown that for some nanotubes (especially for multi-walled) an unambiguous index assignment based exclusively on the ED and HRTEM data cannot be proposed. We will see in the last chapter of this manuscript how the complementarity between Raman spectroscopy and Electron diffraction can be used to solve this problem.

References of Chapter 2:

1. J. C. Meyer, M. Paillet, T. Michel, A. Moreac, A. Neumann, G.S. Duesberg, S. Roth and J.-L. Sauvajol, Raman Modes of Index-Identified Freestanding Single-Walled Carbon Nanotubes, *Phys. Rev. Lett.* 95 (2005) 217401.
2. V. Jourdain, C. Bichara, Current understanding of the growth of carbon nanotubes in catalytic chemical vapour deposition, *Carbon*, Volume 58, July 2013, Pages 2–39
3. PhD thesis of Tinh Than: Croissance catalytique et etude de nanotubes de carbon multi-feuillets produits en masse et de nanotubes de carbon ultra-long individuels a quelques feuillets, 21 November 2011.
4. <http://www.2spi.com/catalog/grids/>
5. D.I. Levshov, Yu. I.Yuzyuk, T.X. Than, R. Arenal, V.N. Popov, R. Parret, M. Paillet, V. Jourdain, A.A. Zahab, T. Michel, J.-L. Sauvajol, Experimental Evidence of a Mechanical Coupling between Layers in an Individual Double-Walled Carbon Nanotube, *Nanoletters*, 11, 4800 – 4804, 2011
6. A. Loiseau et al., *Understanding Carbon Nanotubes*, *Lect. Notes Phys.* 677 (Springer, Berlin Heidelberg 2006), Chapter 3, Structural Analysis by Elastic Scattering Techniques.
7. C.S. Allen, C. Zhang, G. Burnell, A.P. Brown, J. Robertson, B.J. Hickey, A review of methods for the accurate determination of the chiral indices of carbon nanotubes from electron diffraction patterns, *CARBON* 49 (2011) 4961 –4971.
8. S. Iijima, Helical microtubules of graphitic carbon. *Nature* 1991;354:56–8.
9. M. Li, J. M. Cowley, Structures of the helical carbon nanotubes, *Carbon* 1994; 32(3):393–403.
10. L. Qin, Electron diffraction from cylindrical nanotubes, *J Mater Res* 1994;9(9):2450–6.
11. L.-C. Qin, S. Iijima, H. Kataura, Y. Maniwa, S. Suzuki, Y. Achiba, Helicity and packing of single-walled carbon nanotubes studied by electron nanodiffraction, *Chem Phys Lett* 1997;268(1–2):101–6.
12. D. Bernaerts, A. Zettl, N. G. Chopra, A. Thess, R. E. Smalley, Electron diffraction study of single-wall carbon nanotubes, *Solid State Commun.* 1998;105(3):145–9.

13. S. Iijima, T. Ichihashi, Single-shell carbon nanotubes of 1-nm diameter, *Nature* 1993; 363:603–6.
14. X. B. Zhang, X. F. Zhang, S. Amelinckx, G. Van Tendeloo, J. Van Landuyt, The reciprocal space of carbon tubes: a detailed interpretation of the electron diffraction effects, *Ultramicroscopy* 1994; 54:237–49.
15. J. M. Cowley, P. Nikolaev, A. Thess, R. E. Smalley, Electron nanodiffraction study of carbon single-walled nanotube ropes, *Chem. Phys. Lett.* 1997; 265(3–5):379–84.
16. J. M. Zuo, M. Gao, J. Tao, B.Q. Li, R. Twosten, and I. Petrov, Coherent Nano-area Electron diffraction, *Microscopy Research and Technique* 64:347–355 (2004).
17. R. Arenal, P. Löthman, M. Picher, T. Than, M. Paillet, and V. Jourdain, Direct Evidence of Atomic Structure Conservation Along Ultra-Long Carbon Nanotubes, *J. Phys. Chem. C* 2012, 116, 14103–14107.
18. R. Arenal, A. C. Ferrari, S. Reich, L. Wirtz, J.-Y. Mevellec, S. Lefrant, A. Rubio, and A. Loiseau, Raman Spectroscopy of Single-Wall Boron Nitride Nanotubes, *Appl. Phys. Lett.* (2006).
19. M. Gao, J. M. Zuo, R. D. Twosten, I. Petrov, L.A. Nagahara, R. Zhang, Structure determination of individual single-wall carbon nanotubes by nanoarea electron diffraction, *Appl. Phys. Lett.* 2003; 82(16):2703–5.
20. Z. Liu, Q. Zhang, L. Qin, Accurate determination of atomic structure of multiwalled carbon nanotubes by nondestructive nanobeam electron diffraction, *Appl. Phys. Lett.* 2005; 86(29):191903.
21. L. Qin, Determination of the chiral indices (n,m) of carbon nanotubes by electron diffraction, *Phys Chem Chem Phys* 2007; 9:31–48.
22. H. Jiang, A. G. Nasibulin, D. P. Brown, E. I. Kauppinen, Unambiguous atomic structural determination of single-walled carbon nanotubes by electron diffraction, *Carbon* 2007;45(3):662–7.
23. Z. Liu, L. Qin, A direct method to determine the chiral indices of carbon nanotubes, *Chem. Phys. Lett.* 2005;408:75–9.
24. H. Jiang, D. P. Brown, A. G. Nasibulin, E. I. Kauppinen, Robust Bessel-function based method for determination of the (m,n) indices of single-walled carbon nanotubes by electron diffraction, *Phys. Rev. B* 2006;74:035427.

25. J.-M. Zuo, T. Kim, A. Celik-Aktas, J. Tao, Quantitative structural analysis of individual nanotubes by electron diffraction, *Z Kristallogr* 2007;222(11):625–33.
26. P. Lambin, A. A. Lucas, Quantitative theory of diffraction by carbon nanotubes, *Phys. Rev. B* 1997;56(7):3571–4.
27. L. Qin, T. Ichihashi, S. Iijima, On the measurement of helicity of carbon nanotubes, *Ultramicroscopy* 1997;67(1–4):181–9.
28. L. Qin, Measuring the true helicity of carbon nanotubes, *Chem. Phys. Lett.* 1998;297:23–8.
29. S. Amelinckx, A. Lucas, P. Lambin, Electron diffraction and microscopy of nanotubes, *Rep. Prog. Phys.* 1999; 62:1471–524.
30. K. Hirahara, M. Kociak, S. Bandow, T. Nakahira, K. Itoh, Y. Saito, Chirality correlation in double-wall carbon nanotubes as studied by electron diffraction, *Phys. Rev. B* 2006; 73(19):195420.
31. M. Gao, J. M. Zuo, R. Zhang, L. A. Nagahara, Structure determinations of double-wall carbon nanotubes grown by catalytic chemical vapor deposition, *J. Mater. Sci.* 2006; 41:4382–8.
32. J. C. Meyer, M. Paillet, G. S. Duesberg, S. Roth, Electron diffraction analysis of individual single-walled carbon nanotubes, *Ultramicroscopy* 2006; 106(3):176–90.
33. M. Kociak, K. Hirahara, K. Suenaga, S. Iijima, How accurate can be the determination of the chiral indices of carbon nanotube be? , *Eur. Phys. Journal B* (2002).

Chapter 3

The study of vibrational and optical properties of individual free-standing single-walled carbon nanotubes.

In this chapter, we discuss vibrational and optical properties of individual single-walled carbon nanotubes (SWNTs) and bundles made up of SWNTs. We start by considering the low-frequency part of Raman spectra, namely radial breathing modes (RBM), and focus on the evolution of the RBM frequencies as a function of tube diameters. We define the problems existed in the literature prior to this work and then present new experimental data on individual index-identified SWNTs. On the basis of these results, we propose several hypotheses to explain the origin of the deviation of our experimental ω_{RBM} vs. d relation with respect to the expected theoretical one.

In the second part, we present new experimental results regarding the dependence of the main features of the G-modes on diameter and excitation energy. We compare our result with those previously published in the literature and discuss the observed controversy. Moreover, we give a short presentation of the Raman resonance profiles performed on index-identified single nanotubes.

Finally, we propose an analysis of the Raman spectrum of an inhomogeneous dimer (bundles of two single-walled carbon nanotubes). Differences and similarities in the features of RBM and G-modes are discussed with respect to those in individual single- and double-walled carbon nanotubes.

3.1. Raman spectroscopy of individual single-walled carbon nanotubes.

3.1.1 The Radial Breathing Modes. The nature of ω_{RBM} vs d relations.

We remind briefly some of the conclusions of the Chapter 1 in what regards radial breathing modes of single-walled nanotubes. We said that the frequency of radial vibrations inversely depends on the tube diameter and that there exist several ways to derive this dependence:

- A continuous approach where carbon nanotubes is considered as thin cylinders (see for example Ref.1-2).
- Based force-constant approach (see for example Ref. 3)
- Direct first-principle calculations of phonons of carbon nanotubes (see for example Ref.4).

Theory predicts that for an isolated individual SWNT, environmental-free, the frequency of RBM has the following relation:

$$\omega_{RBM} = \frac{A}{d} \quad (3.1)$$

where A is established in the recent studies to be in the range: 226-227 $\text{cm}^{-1} \cdot \text{nm}$ [1,2]

3.1.2 Experimental diameter dependence of RBM frequencies measured in individual SWNTs.

A huge number of experimental studies were devoted to the measurement of the $\omega_{RBM}(d)$ relationship (for a review see Ref [5]) using different approaches. In this manuscript, we will only remind experimental studies performed at the single nanotube level.

The first attempt to determine experimentally the relationship between RBM frequency and tubes diameters on individual isolated SWNT were made by Jorio et al. for tubes lying on a substrate [6]. In this pioneer study the main problems were: (i) the indirect identification of the nanotube structures (some bad (n,m)-assignment are found in [6] as written by the same authors in [7]), and (ii) the environment effect arising from the substrate.

To minimize this environmental effect and to have a direct determination of the SWNT structure we performed in our group in 2005 [8] the Raman measurement of free-standing (suspended in air) SWNTs index-identified by electron diffraction. The SWNTs were grown by chemical vapor deposition on highly doped silicon substrates with a 200 nm silicon dioxide layer, which were then etched to obtain suspended nanotubes. The illustration of the etching process is done in Fig. 3.1. After the chemical etching, the sample was transferred into deionized water, isopropanol, and acetone before a critical point drying step.

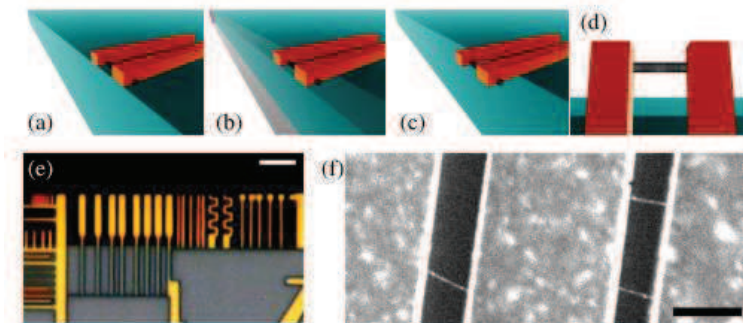


Fig. 3.1: Sample preparation procedure from Meyer et al [8].

Meyer et al. identified five semiconducting: (11, 10), (17, 9), (15, 14), (27, 4) and (23, 21), and four metallic: (10, 10), (15, 6), (16, 7) and (12, 12), individual free-standing SWNTs

and measured their radial-breathing mode frequencies. By fitting experimental data, they obtained the following relationship (Figure 3.2f):

$$\omega_{\text{RBM}} (\text{cm}^{-1}) = 204/d (\text{nm}) + 27 (\text{cm}^{-1}) \quad (3.2)$$

This experimental relation was established independently from any modelization for SWNTs in the diameter range 1.35–3 nm. However, contrary to the theoretical prediction established for the environment-free SWNTs, a relatively large constant factor $B = 27 \text{ cm}^{-1}$ was found in the experiment, though environmental effects in these types of samples were supposed to be weak or absent.

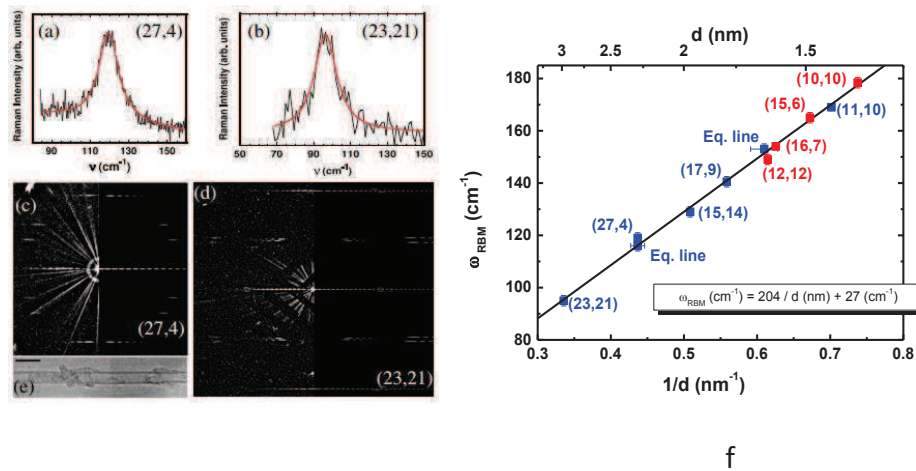


Fig. 3.2: (a) RBM of the (27,4) SWNT ($E_{\text{Laser}} = 1.92 \text{ eV}$) and (b) RBM of the (23,21) nanotube ($E_{\text{Laser}} = 1.6 \text{ eV}$). The electron diffraction patterns are shown in (c) and (d). In each pattern, the left half is the experimental image, while the right half is the simulated one for comparison. (e) High resolution image of the (27,4) SWNT. Scale bar is 5 nm. (f) Experimental diameter dependence of the RBM frequency measured on index-identified free-standing SWNTs (From [8]).

In 2011 Liu et al [9] performed similar series of experiments on individual SWNTs, combining Raman spectroscopy and Electron diffraction. As opposed to the work of Meyer et al, Liu's samples consisted of ultra-long SWNTs suspended over open slits. The slits (20–50 μm wide and 0.4 mm long) were fabricated on the $\text{Si}_3\text{N}_4/\text{Si}$ substrate using standard photolithography and wet etching processes. Millimeter-long isolated SWNTs were grown across the slit by chemical vapor deposition (CVD) method at 900 °C for 1 h. They used methane in hydrogen ($\text{CH}_4 : \text{H}_2 = 1:2$) as feedstock and an ultrathin film ($\sim 0.25 \text{ nm}$) of Fe as the catalyst. Liu et al claim that this growth condition yields extremely clean suspended nanotubes free of amorphous carbon and other adsorbates (Fig. 3.3b,c).

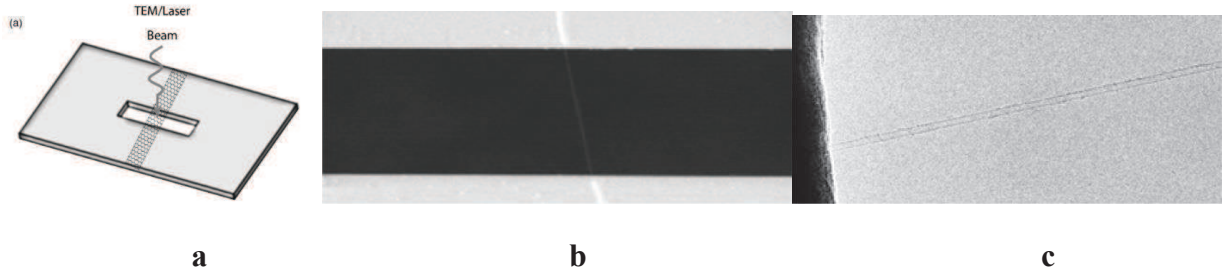


Fig. 3.3: (a) Schematic illustration for combined TEM electron diffraction and Raman-scattering techniques on the same suspended nanotubes. (b) Scanning electron micrograph of a SWNT suspended across an open slit on the $\text{Si}_3\text{N}_4/\text{Si}$ substrate. (c) High-resolution transmission electron micrograph of a SWNT. It is seen to be a single-walled character with clean surface. Scale bars in (b) and (c) are $20\ \mu\text{m}$ and $20\ \text{nm}$, respectively (Adapted from Liu et al [9]).

Next, they measured the low-frequency part of Raman spectrum of 26 individual suspended SWNTs (See Fig. 3.4; all their data are summarized in Table 3.1) with diameters from 1.8 to 4.8 nm and established the following experimental relations (Fig. 3.4g) in very good agreement with theoretical predictions:

$$\omega_{\text{RBM}} = 228/d\ (\text{nm}), \quad (3.3)$$

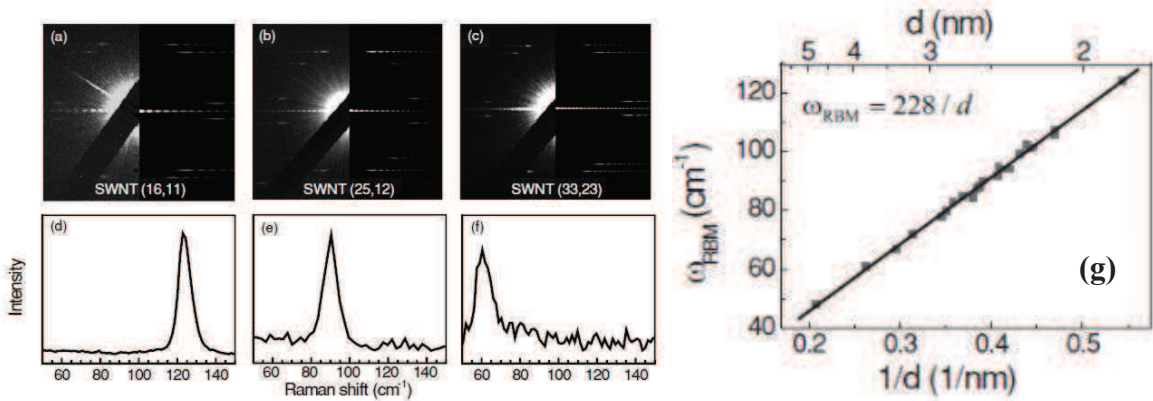


Fig. 3.4: Electron-diffraction patterns and RBM Raman spectra of three representative SWNTs. (a)–(c) Electron-diffraction patterns of the nanotube allow us to determine their chiral indices as (16,11), (25,12), and (33,23). The corresponding nanotube diameters are 1.84, 2.56, and 3.82 nm, respectively. (d)–(f) RBM Raman spectra of (16,11), (25,12), and (33,23) SWNTs. The RBM frequencies are located at 124 , 90 , and $61\ \text{cm}^{-1}$, respectively; (g) RBM frequencies ω_{RBM} versus inverse nanotube diameters $1/d$ (squares).

Table 3.1: Chiral indices and RBM frequencies for 26 individual SWNTs from Ref [9].

Sample	(n, m)	d (nm)	ω_{RBM} (cm⁻¹)
1	(16,11)	1.84	124.0
2	(23,7)	2.13	107.0
3	(23,7)	2.13	106.0
4	(25,4)	2.13	105.5
5	(19,15)	2.25	101.5
6	(26,5)	2.26	101.0
7	(25,7)	2.28	102.0
8	(20,14)	2.32	99.0
9	(27,6)	2.38	94.0
10	(27,6)	2.38	94.0
11	(18,18)	2.44	94.0
12	(21,15)	2.45	95.0
13	(28,6)	2.46	92.0
14	(25,12)	2.56	90.0
15	(21,17)	2.58	88.5
16	(32,2)	2.59	88.0
17	(24,14)	2.61	87.5
18	(26,12)	2.63	84.5
19	(22,18)	2.72	85.0
20	(24,17)	2.79	83.0
21	(21,21)	2.85	80.0
22	(27,15)	2.89	78.0
23	(24,23)	3.19	72.0
24	(32,17)	3.37	67.0
25	(33,23)	3.82	61.0
26	(46,24)	4.82	48.0

Summary

In the first part of Chapter 3, we have examined the radial vibrations of the individual single-walled carbon nanotubes and presented several theoretical and experimental data existed in the literature prior to this work. First, we recalled the form of the theoretical diameter dependence of the radial breathing mode frequency, namely $\omega_{\text{RBM}} = A/d$, where $A = 226\text{-}227 \text{ cm}^{-1}\cdot\text{nm}$ depending on the authors [1,2]. Secondly, we have analyzed experimental studies devoted to the measurement of the $\omega_{\text{RBM}}(d)$ relationship in the individual SWNTs and have evidenced two distinct results:

- A. Meyer et al (Montpellier group) [8] found: $\omega_{\text{RBM}} (\text{cm}^{-1}) = 204/d (\text{nm}) + 27 (\text{cm}^{-1})$
- B. Liu et al [9] found: $\omega_{\text{RBM}} (\text{cm}^{-1}) = 228/d (\text{nm})$,

In addition, we note that the other groups [10,11] have also performed this kind of studies and showed that their experimental dependence of the RBM frequency is closer to the $204/d+27$ relation than the $228/d$ relation.

We now proceed as follows:

1. We present the new experimental data obtained in the framework of this thesis to clarify the existing controversy. The main difference with the previous work of Meyer et al [9] lies in the improved synthesis protocol of SWNTs that is free of chemical treatment.
2. We propose possible explanations to the discrepancies between the results of the above-mentioned studies A and B. Especially we will argue the nature of environmental effects that can arise in the samples.

3.2 Additional experimental results on index-identified individual SWNTs.

In order to clarify the existing controversy between the two experimental relations: $\omega_{RBM} = 204/d + 27$ and $\omega_{RBM} = 228/d$, we performed the analysis of the new series of suspended individual SWNTs. A detailed description of the synthesis was already done in Chapter 2. We just remind here that the nanotubes used in this work are ultra-long and there is no processing of the sample after the synthesis. It is also worth noting that our new growth conditions seem to be quite similar to those described in the work of Liu et al [9].

In total, we analyzed 12 individual SWNTs by Resonant Raman spectroscopy. For two of them we performed also the measurements of Raman excitation profile. The overall summary is shown in the Table 3.2.

Table 3.2: Structural and vibrational information on individual single-walled carbon nanotubes studied in this work. Bold characters indicate SWNT for which the resonance profile was measured. The error bar is $\pm 1\text{cm}^{-1}$ (if not stated otherwise).

SWNT	Indices	d, nm	θ°	Type	Results		
					$\omega_{RBM}^{204/d+27}$	$\omega_{RBM}^{228/d}$	ω_{RBM}^{exp}
1	(24,8)	2.26	13.9	2	117	101	123 [$\pm 2\text{cm}^{-1}$]
2	(19,15)	2.32	26.11	2	115	99	120
3	(29,2)	2.35	3.3	0	114	97	119
4	(24,8)	2.26	13.9	2	117	101	118 [$\pm 2\text{cm}^{-1}$]
5	(24,8)	2.26	13.9	2	117	101	-
6	(24,8)	2.26	13.9	2	117	101	120 [$\pm 2\text{cm}^{-1}$]
7	(35,4)	2.91	5.35	2	-	-	-
8	(38,6)	3.152	7.25	1	-	-	-
9	(29,4)	2.44	6.38	2	110	93	111 [$\pm 2\text{cm}^{-1}$]
10	(60,19)	5.88	13.12	-	-	-	-
11	-	2.30	-	SC	116	99	106
12	-	1.95	-	Met	132	117	121

It is clear from the table that all nanotubes measured in this work are in a limited diameter range. Moreover, four SWNTs were found to have the same (n,m) indices even if they are different (#1,4,5,6). In these conditions it is not possible to derive an accurate relationship $\omega_{RBM}(d)$ from this limited series of data. Nevertheless, our results should point out the validity of one or another previously reported relationship for suspended SWNTs. Indeed in the diameter

range: 2.0-2.5 nm, the difference in frequency between the two relations are in the range: 15-20 cm^{-1} (see Fig. 3.8, for instance).

We also note that the full combination of Raman, TEM and ED measurements was only applied for a few of the 12 SWNTs. Below we choose some of these nanotubes (namely #1, #2 and #3 from Table 3.2) to detail the analysis of our results. Moreover, in order to fully characterize the nanotubes (metallic vs semiconducting, chiral vs achiral) we present also the G-mode range of Raman spectra.

Example 1 (SWNT-1)

The first example (SWNT-1) is the (24,8) semiconducting SWNT. Its HRTEM image is presented in the Fig. 3.5a. The Raman spectra measured in a broad excitation range are displayed in the Figure 5.3c (only one spectrum was selected from the infrared range). On the HRTEM image, we clearly see the presence of some amorphous carbon on the surface of the tube. However, Fig. 3.5c shows that there is no D-band in the Raman spectra at 458, 488, 514, 568 and 710 nm. 710 nm.

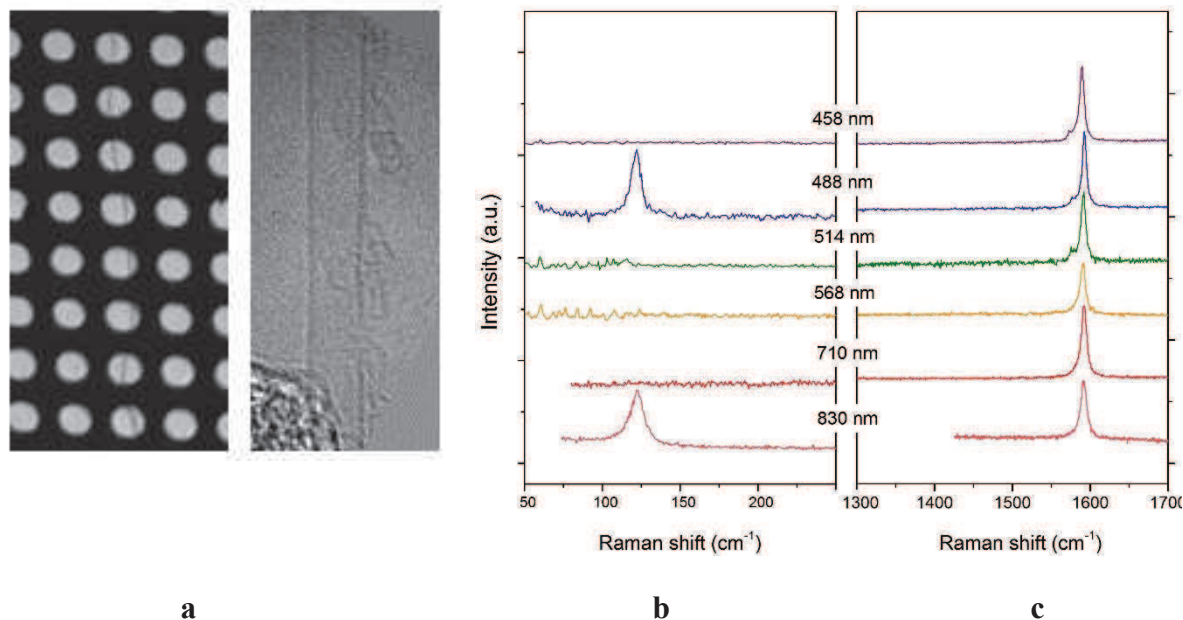


Fig. 3.5: (a) HRTEM image and (b) RBM- and (c) G-mode parts of Raman spectra of semiconducting (24,8) individual single-walled carbon nanotubes. Note that at 514 and 568 nm the low-frequency oscillations are the artifacts of the spectrometer.

For all the incident excitations, the RBM is located close to 123 cm^{-1} . Its frequency is upshifted by 5 cm^{-1} (22 cm^{-1}) from $204/d+27$ ($228/d$) relation. In the same figure, the G-mode range of the Raman spectra is displayed. The profile is the one expected for a chiral semiconducting SWNT. The TO and LO mode frequencies are located at 1577 and 1591 cm^{-1} respectively.

Example 2 (SWNT-2)

The second carbon nanotube (SWNT-2) was identified as (19,15) from ED and Raman spectroscopy. Unfortunately we didn't have a HRTEM image because of the active vibration of the tube during the TEM experiments. The Raman spectra are shown in Fig. 3.6a,b. We observe the frequency of the RBM at 120 cm^{-1} (115 and 99 cm^{-1} are predicted from $204/d+27$ and $228/d$ relations respectively). The profile of the G-band is the one expected for a chiral semiconducting SWNT with 2 components at 1573 and 1588 cm^{-1} (Fig. 3.6 b)

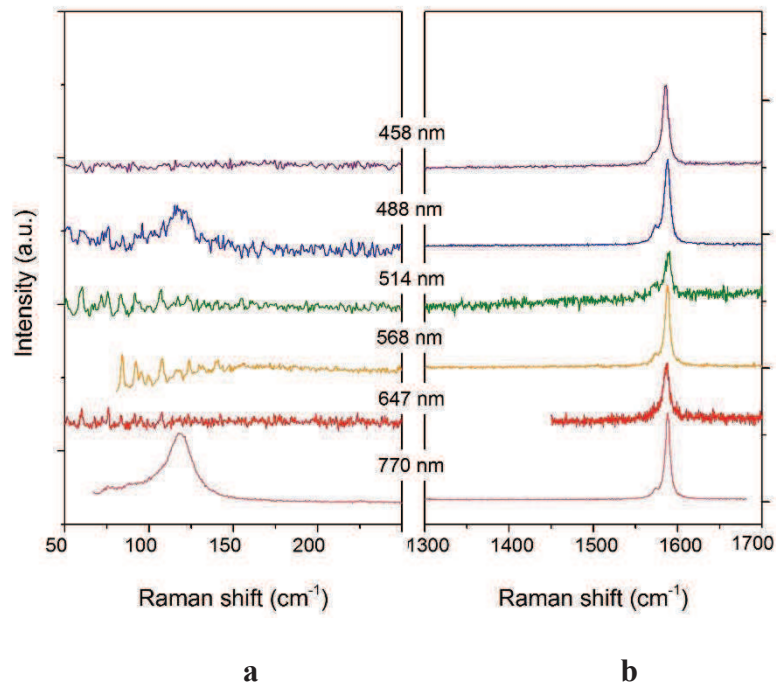


Fig. 3.6: Low-frequency (a) and high-frequency (b) parts of Raman spectra of (19,15) individual semiconducting SWNT.

Example 3 (SWNT-3)

The third example (SWNT-3) is a metallic single-walled carbon nanotube which was identified as (29,2) from ED. The corresponding Raman spectra measured at 514 and 530 nm are shown in the Figure 3.7b. The RBM is located at 119 cm^{-1} . We note that RBM frequency is

upshifted by 5 cm^{-1} and 22 cm^{-1} from $204/d+27$ and $228/d$ relations respectively. The LO G-mode is close to 1572 cm^{-1} with a shoulder assigned to the TO mode, at around 1591 cm^{-1} . The HRTEM image of this nanotube (Fig. 3.7a) indicates that there is a smaller percentage of the amorphous carbon on its surface than in the other examples. We do not observe any D-band in Raman spectra.

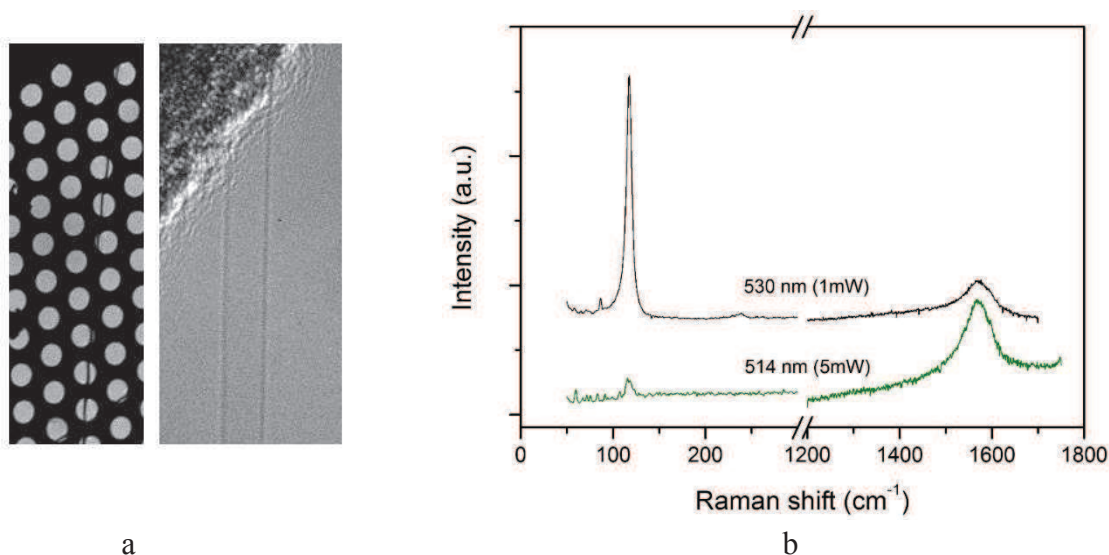


Fig. 3.7: (a) HRTEM image and (b) Raman spectra of metallic individual single-walled carbon nanotubes which from ED was identified as (29,2).

To summarize, in Figure 3.8 we plot RBM frequencies of 6 new individual SWNTs (blue open symbols) as a function of their diameter and compare them with our old data (black filled symbols).

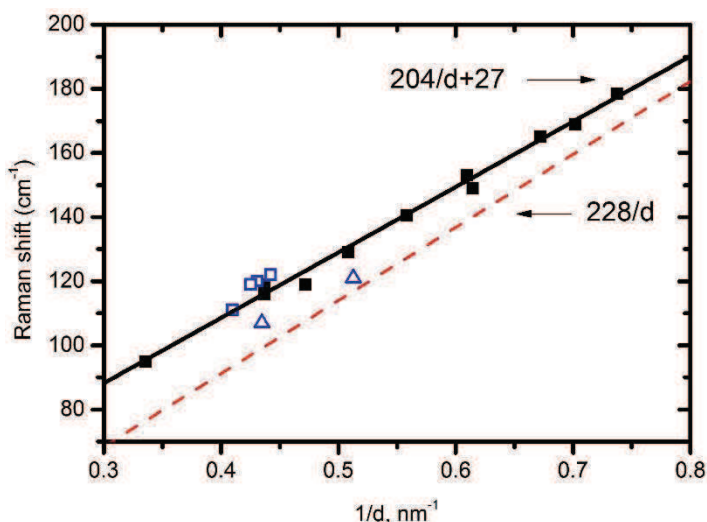


Fig. 3.8. Frequencies of the radial breathing modes as a function of tube's diameter. The new data analyzed in this work are shown by blue open symbols, while the old data from Montpellier group [8] are represented by black filled squares. Squares correspond to the nanotubes whose diameters were identified from ED; triangles are SWNTs identified from HRTEM.

It is clear from the figure that the new data match better the relation $\omega_{\text{RBM}} = 204/d + 27$ (black line) than the theoretical one $228/d$ (red dashed line). Surprisingly, some of the new tubes are even more shifted from the $228/d$ line than the old data of Meyer et al. In contrast, the two tubes, whose diameters were identified only by HRTEM (represented by triangles), are closer to $228/d$ relation. However, the higher experimental errors in the diameter estimations for both tubes do not permit to conclude definitively in favor of the better agreement with the $228/d$ relation.

These new data show:

- Some new individual SWNTs have a small upshift of the RBM frequency in respect to $204/d+27$ relation (about 5cm^{-1}).
- No significant shift of the G-band modes were found in respect to the diameter dependence of the LO and TO G-modes, previously established (will be analyzed in more detail in the future paragraph).
- In all our SWNTs, the D-mode Raman peak is almost never observed, independently of laser excitation energy.

Hence, despite the improvements of the growing conditions, we still observe a systematic shift of the RBM frequencies from the theoretical $228/d$ relation. Its possible origins are considered and presented below.

3.3 The presence of strains or external pressure.

We argue that the existence of certain strains in our as-grown individual free-standing carbon nanotubes are responsible for the RBM frequency shift. Several cases are possible:

Uniaxial and torsional strains

Gao et al [13] reported the appearance of tensile strains in as-grown individual SWNTs. Two regimes are possible. First, substrate-induced tensile strain appears when thermal contraction is different for SWNTs and the substrate (in other words, if the coefficient of the thermal expansion of SWNTs is different from that of the substrate). In this situation, upon cooling after the growth process, the SWNTs may appear under strain stress. Moreover, if the substrate is not smooth due to the existence of defects and steps and if the cooling rate is not uniform, the strain should be localized spatially.

Secondly, a self-built tensile strain may arise due to the presence of nanodots on the carbon nanotubes. These nanodots can form from accumulation of carbon species from ethanol CVD during the synthesis process. Compared to a pristine SWNT, the decorated carbon nanodots could cause structural disturbance and physical strain in the tube. Similar to the strain induced by AFM tip, the strains caused by the carbon nanodots are not confined to a small region where the tube is distorted, but rather extend for long distances along the SWNT [13].

Independent of nature, the uniaxial strain should have certain features in Raman spectra of SWNTs. For instance, we analyzed these features in individual SWNTs emerged in gelatin [14]. The results obtained in this study are well understood by considering, that the change of temperature induces a uniaxial compression on the tube. This uniaxial compression results from the thermal expansion mismatch between the nanotube and the surrounding gelatin at low temperature. Using theoretical predictions of the values of Gruneisen parameters [15], the temperature dependence of the frequencies of G-modes allows an evaluation of the average strain induced on the nanotubes by the temperature change. By changing temperature from 300 K to 20 K (i.e. increasing the uniaxial compression), a significant upshift of the G-mode frequency and almost no change in RBM frequency were measured (see Fig.3.9). Similar results were found by Cronin et al and Gao et al, under mechanical uniaxial expansion of isolated individual tubes [13,16].

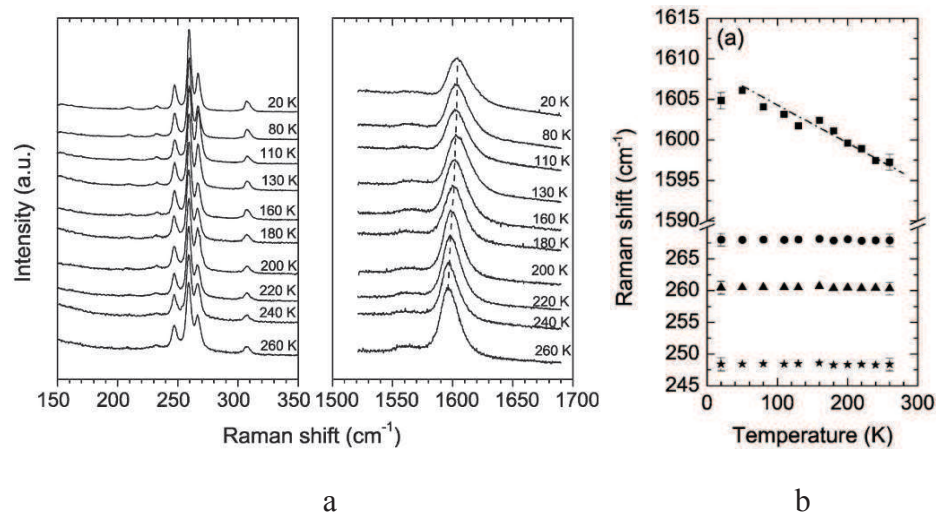


Figure 3.9: (a) RBMs and G modes ranges of the Raman spectra measured at 1.70 eV. For clarity, the spectra are normalized in intensity. The dashed line is a guide for the eyes [14]. (b) The dependence of the RBM and G mode frequencies on the uniaxial strain (induced by temperature increase).

Torsional strains, if exist, should also lead to the upshift of both G-band and RBM frequencies [17].

We now present the following reasoning. In our samples the frequency of RBM is initially shifted (in comparison with the theoretical relation $228/d$). So to tell whether the observed $\omega_{\text{RBM}}(d)$ deviations are due to the strain effect, we need to analyze the shift of the G-band. In all our samples we did not observe any significant changes of the G modes. For instance, for the tangential G^+ mode the resonance frequencies were found mainly in the range $1591\text{-}1592\text{ cm}^{-1}$ that is in agreement with theoretical predictions (see next section on G-band). We thus conclude that our suspended nanotubes have minimal built-in uniaxial or torsional strains, and this option may be discarded.

A hydrostatic pressure: the effect of air.

As our experiments are performed on individual suspended SWNTs in air, one of the assumption would be to relate the RBM frequency shift to the interaction between the nanotubes and the surrounding air. To test this assumption, we performed Raman experiments on the same suspended individual SWNT in air and in vacuum (10^{-6} mbar) (note that this experiment has been planned and realized before the publication of Liu et al [9]).

During the experiments in the air, a diameter close to 2.11 nm was derived from the measurement of the RBM on a free-standing SWNT by using $204/d+27$ relation. This later relation fits the experimental data measured on the same series of SWNTs. For such a diameter, a RBM downshift of about 17 cm^{-1} is expected when the tube is measured free of environment, or in other words under vacuum (corresponding to $228/d$ relation, see figure 3.10a). The spectra in air and under vacuum for the same SWNT are displayed in Figure 3.10b. In complete disagreement with this prediction, no measurable shift is experimentally observed under vacuum, though the RBM has a slightly decreased FWHM. We assume that the narrowing of the mode is a consequence of a small change in the transition energy under vacuum.

Despite the difficulty of these experiments explained by the very low signal (the spectra were collected with a 50x objective inside a vacuum cell), similar results have been obtained on three other individual SWNTs. These experimental findings rule out the interaction between the tube and the surrounding air as the reason for the observed RBM upshift with respect to theoretical predictions.

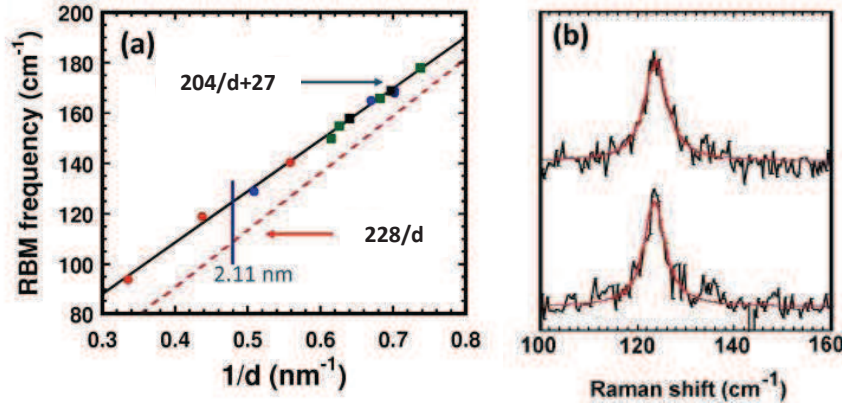


Figure 3.10: (a) RBM frequency vs. inverse diameter: Relations $204/d+27$ (full line) and $228/d$ (dashed line). (b) Raman spectra of the same individual suspended SWCNT ($d=2.11$ nm) in air (top) and under vacuum (bottom).

In that way, we consider other intuitive assumptions regarding the origin of the frequency shift in non-theoretical ω_{RBM} vs d relations as due to the interaction between the nanotube and an environment.

3.4 The nature of environmental effects in ω_{RBM} vs d relations

We are interested here to define what experimental parameters may affect the change of the RBM frequency. For this reason, we adopt the approach of Araujo et al [7].

Araujo et al performed the analysis of different experimental relations present in the literature and proposed the following model (based on the work of Longhurst and Quirke [12]). The RBM of a coupled system ‘SWNT-environment’ was considered composed of two spring constants: one coming from the C-C bond strength and the other coming from the interaction between the SWNT and its surroundings. The problem of addressing the environmental effect on RBM may be reduced to solving a simple harmonic oscillator for a cylindrical shell subjected to an inwards pressure $p(x)$:

$$\frac{2x(t)}{d} + \frac{\rho h}{Eh} (1 - \nu^2) \frac{\partial^2 x(t)}{\partial t^2} = -\frac{(1-\nu^2)}{Eh} p(x) \quad (3.5)$$

where $x(t)$ is the displacement in the radial direction; $p(x) = (24K/s_0^2)x(t)$; K in $(\text{eV}/\text{\AA}^2)$ gives the van der Waals interaction strength, s_0 is the equilibrium separation between the SWNT wall and the environment shell, E is the Young’s modulus, ρ is the mass density per unit volume, ν is the Poisson’s ratio, and h represents the thickness of the shell. If $p(x)$ is null, Eq. (3.5) gives the fundamental ω_{RBM}^0 for a pristine SWNT,

$$\omega_{RBM}^0 = \left\{ \frac{1}{\pi c} \sqrt{\frac{Eh}{\rho h(1-\nu^2)}} \right\} \frac{1}{d} = \frac{A^0}{d} \quad (3.6)$$

where the term inside the curly bracket, A^0 , is equals to $227 \text{ cm}^{-1}\text{nm}$.

For $p(x)$ non-null we have:

$$\omega'_{RBM} = 227.0 \sqrt{\frac{1}{d^2} + \frac{6(1-\nu^2)K}{Eh} \frac{1}{s_0^2}} = \frac{227}{d} \sqrt{1 + C \cdot d^2} \quad (3.7)$$

where $[6(1 - \nu^2)/Eh] = 26.3 \text{ \AA}^2/\text{eV}$, $K/s_0^2 = (2.2 \pm 0.1)\text{meV}/\text{\AA}^4$ was obtained after the fit of the data from different experimental relations (see Fig. 3.11).

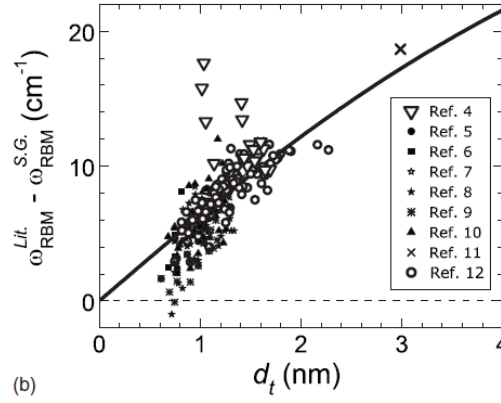


Fig. 3.11: Difference between ω_{RBM} data from the literature and $\omega_{RBM} = 227/d$ as a function of d . Each symbol represents data from different references. From [7].

The relation (3.7) fits very well our experimental data with $C=0.065 \text{ nm}^{-2}$ (see Fig. 3.8).

We now summarize the forms of theoretical and non-theoretical ω_{RBM} vs d relations and define explicitly some of their parameters, namely A^0 and C :

$$\omega_{RBM}^{theoretical} = \frac{A^0}{d} \quad [3.1]$$

$$\omega_{RBM}^{experimental 1} = \frac{A}{d} + B \quad [3.2]$$

$$\omega_{RBM}^{experimental 2} = \frac{A^0}{d} \sqrt{1 + C \cdot d^2} \quad [3.7]$$

$$A^0 = \frac{1}{\pi c} \sqrt{\frac{Eh}{\rho h(1-\nu^2)}} \quad (3.9)$$

$$C = \frac{6(1-\nu^2)K}{Eh} \frac{1}{s_0^2} \quad (3.10)$$

We distinguish between A^0 and A in equations (3.1) and (3.2) on purpose. In fact, A and B coefficients are inter-dependent, in other words the change of A also affects B . So strictly speaking, we cannot apply eq. (3.9) to A in the formula (3.2). However, we suppose that the parameters that change A^0 will affect A and B simultaneously.

Since for our tubes we find that $A = 207 \text{ cm}^{-1}\cdot\text{nm}$ and $B = 27 \text{ cm}^{-1}$ or equivalently $A^0=227 \text{ cm}^{-1}\cdot\text{nm}$ and $C=0.065 \text{ nm}^{-2}$, we propose the following reasons of deviation from the theoretical $228/d$ relation:

- a) The change of the elastic constants E , ν (from eq. (3.9) and (3.10))
- b) The change of mass density ρ due to chemical doping or adsorption (from eq. (3.9))
- c) The presence of environmental interaction (K , s_0 from eq. (3.10))

Below we analyze each point in detail:

3.4.1 The change of elastic constants

Young's modulus E and Poisson's ration ν are the elastic characteristics of the material. Their slight change should indicate the serious deviations in structure and composition of the nanotube, for example the substitution of carbon atoms by some other element. It is thus very unlikely that the deviation from theoretical $228/d$ relation is due to this factor, as we do not see any abnormal features in the Raman spectra of our nanotubes or in the HRTEM images.

3.4.2 The change of mass density ρ due to contamination (chemical doping or adsorption).

By analyzing the synthesis conditions of our individual SWNTs, we propose following possible contaminants:

CH₄, H₂, Ar, EtOH

Recent experiments showed that hydrogen chemisorption onto SWNTs can result in the carbon-carbon (C-C) bond expansion in both axial and radial directions [18]. Such a hydrogenation process can only occur at the condition of high energy treatments in order to break sp^2 C-C and form sp^3 C-H. This always leads to a relatively strong D band. Similar effects can be expected for other gases.

However, in our nanotube the D band is very weak in intensity and is often not observable (see experimental results in Section 3.2).

Metallic catalysts

We note that the metallic catalysts were never observed during TEM experiments performed in the framework of this thesis.

Amorphous carbon

We can suspect the presence of amorphous carbon to be responsible for the shift of RBM frequencies. We may estimate its percentage with respect to the nanotube's mass.

Below are reported HRTEM images of seven individual suspended SWNTs from the series of our free-standing SWNTs (Fig. 3.12). We see that AC indeed constitutes a reasonable fraction of the nanotube surface.

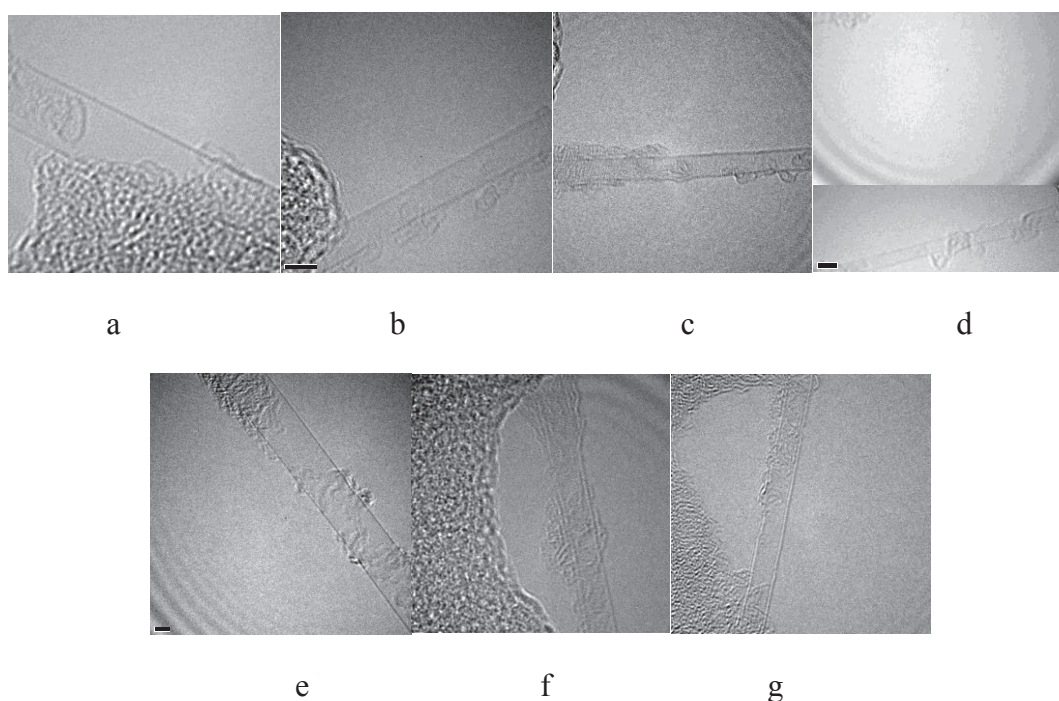


Fig. 3.12: (a) V65 NT3 ; (b) V65 NT6 ;(c) V65 NT19; (d) V65 NT1; (e) V65 NT7; (f)V66 NT15; (g) V66 NTA.

Let us roughly estimate the mass of amorphous carbon from a TEM image (Fig. 3.13). We will consider the amorphous layer as a cylinder having a thickness of one carbon atom (shown as blue rectangle on the Figure 3.13; nanotube is represented by red rectangle). By measuring the length and diameters of the cylinders from TEM images and taking ρ_{AC} as $2.15 \cdot 10^{-21} \text{g/nm}^3$ [19], $\rho_{NT}=6.6 \cdot 10^{-21} \text{g/nm}^3$ (calculated from purely geometric principles), carbon atom

diameter $d_c=0.182$ nm, carbon atom mass $m_c=12*1.66*10^{-21}$ g, we get the ratio $m_{AC}/m_0 = 23\%$. However, the determination of the percentage of amorphous carbon is not straightforward and we cannot ensure that this percentage of amorphous carbon (about 20%) is the same in all the SWNTs of this series.

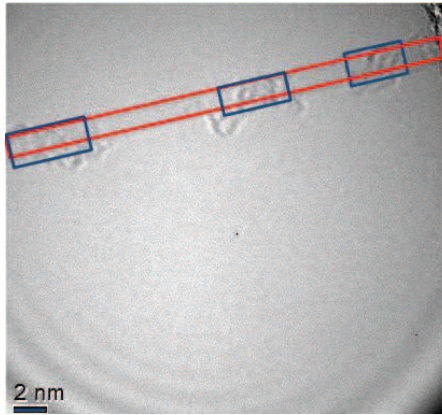


Fig. 3.13: The analysis of the tube shown in Fig. 3.12d

In addition, it is noteworthy to say that in several cases of Fig. 3.12 the amorphous carbon was deposited during the TEM study under the irradiation of the electron beam. The areas on the nanotube that were not irradiated for a long enough time remained clean.

3.4.3 The presence of the environmental interaction.

We try to describe the environmental effect in the framework of the 2D continuous membrane theory of SWNTs [2] (see Chapter 1 for explanation). In that way, we introduce a ‘trapping’ potential, $\frac{p}{2}u_r^2$, to the equation for the surface energy density g of SWNT (chapter 1, equation 1.4). The effect of the trapping potential is to hinder the radial vibrations of the nanotube:

$$g = \frac{\lambda}{2}(\epsilon_{rr})^2 + \mu(\epsilon_{rr})^2 + \frac{p}{2}u_r^2 \quad (3.18)$$

Eq. (3.18) is written in the approximation of the symmetric vibrations, λ and μ are 2D analogues of Lamé coefficients, p is a coefficient representing the environmental interaction, ϵ_{rr} is the strain in the radial direction, u_r represents a radial displacement.

The strain is defined as:

$$\varepsilon_{rr} = \frac{u_r}{R} \quad (3.19)$$

Then:

$$g = \left(\frac{\lambda}{2} + \mu + \frac{p}{2} R^2 \right) \frac{u_r^2}{R^2} \quad (3.20)$$

The total potential energy of the nanotube is obtained by multiplying g and the total surface of the nanotube $S=2\pi Rl$, where l is the length of the nanotube.

$$E = 2\pi Rl \left(\frac{\lambda}{2} + \mu + \frac{p}{2} R^2 \right) \frac{u_r^2}{R^2} = \pi l (\lambda + 2\mu + pR^2) \frac{u_r^2}{R} \quad (3.21)$$

The restoring force acting on the nanotube is defined as the derivative of the energy by u_r :

$$F = -\frac{dE}{du_r} = -2\pi l (\lambda + 2\mu + pR^2) \frac{u_r}{R} \quad (3.22)$$

On the other hand $F = ma = m\ddot{u}_r = \rho 2\pi Rl \ddot{u}_r$, (3.23)

where ρ is the mass density of the nanotube and the mass was set as $m = \rho 2\pi Rl$

It follows from eq. (3.22) and (3.23) that

$$-(\lambda + 2\mu + pR^2) \frac{u_r}{R} = \rho R \ddot{u}_r, \quad (3.24)$$

The vibrations in the radial direction may be described as

$$u_r = u_0 \cos(\omega t) \quad (3.25)$$

$$\ddot{u}_r = -\omega^2 u_r \quad (3.26)$$

By substituting eq. (3.25), (3.26) in (3.24) we get:

$$\omega = \sqrt{\frac{\lambda+2\mu}{\rho R^2} + \frac{p}{\rho}} = \sqrt{\left(\frac{226}{d}\right)^2 + p'} \quad (3.27a)$$

where term $\frac{\lambda+2\mu}{\rho R^2} = \left(\frac{226}{d}\right)^2$, $p' = \frac{p}{\rho}$ as was shown by Rochal in Ref [2] (see also Chapter 1).

$$\omega = \sqrt{\frac{\lambda+2\mu}{\rho R^2} + \frac{p}{\rho}} = \left(\frac{226}{d}\right) \sqrt{1 + \left(\frac{d}{226}\right)^2 p'} \quad (3.27b)$$

Equation (3.27a,b) represents the frequency of the radial breathing vibrations of the nanotube in the presence of some external constraints derived in the framework of the 2D continuous membrane theory of SWNTs. This expression has the same form as the one of Araujo (see equation 3.7). Obviously, this formula fit well our experimental data. RBM frequencies of

our 15 individual single-walled nanotubes (previous data from Ref. [8] and the data of this work) were fitted by relation (3.27) and relation (3.7). Table 3.3 shows the deviations average $\Delta\omega$ between the frequencies calculated from these formulas and the experimental frequencies. C or equivalently $p'/(226)^2$ is close to $0.065 \text{ cm}^2\text{nm}^{-2}$ (or p' is close to 3335 cm^{-2})

Table 3.3: The comparison between the experimental data and the formula $\omega=227/d (1+Cd^2)^{1/2}$ (3.7 and 3.27) with $C= 0.065 \text{ nm}^{-2}$.

#	d, nm	ω_{exp}	$\Delta\omega$ (eq. 3.7 and 2.37)
1	1.43	169	-1.16
2	1.40	165	0.86
3	1.63	149	-3.37
4	1.64	153	1.61
5	1.79	140.5	-0.44
6	1.97	129	-1.73
7	2.29	119	2.92
8	2.29	116	-0.08
9	2.98	95	-0.46
10	1.36	178.5	0.96
11	2.12	119	-4.23
12	2.32	120	5.07
13	2.26	122	4.73
14	2.44	111	0.39
15	2.35	119	5.19

In the 2D continuous membrane theory of SWNTs, the parameter p' is independent of nanotube diameter and represents the additional energy density of the nanotube surface due to the environmental interaction. Below some of the origins of this interaction are examined:

The interaction between the nanotube and the layer of amorphous carbon.

Previously we have shown that the amorphous carbon may constitute up to 20% of the nanotube mass in our samples. So can the interaction between the CNT and amorphous carbon be responsible for the observed deviations?

In Ref [9] Liu et al presented the HRTEM image of their single-walled nanotube. In Fig. 3.14 we show a magnification of this image. It is clear that their nanotubes also contain a certain amount of amorphous carbon on the surface. Still they managed to confirm the theoretical $228/d$ relation.

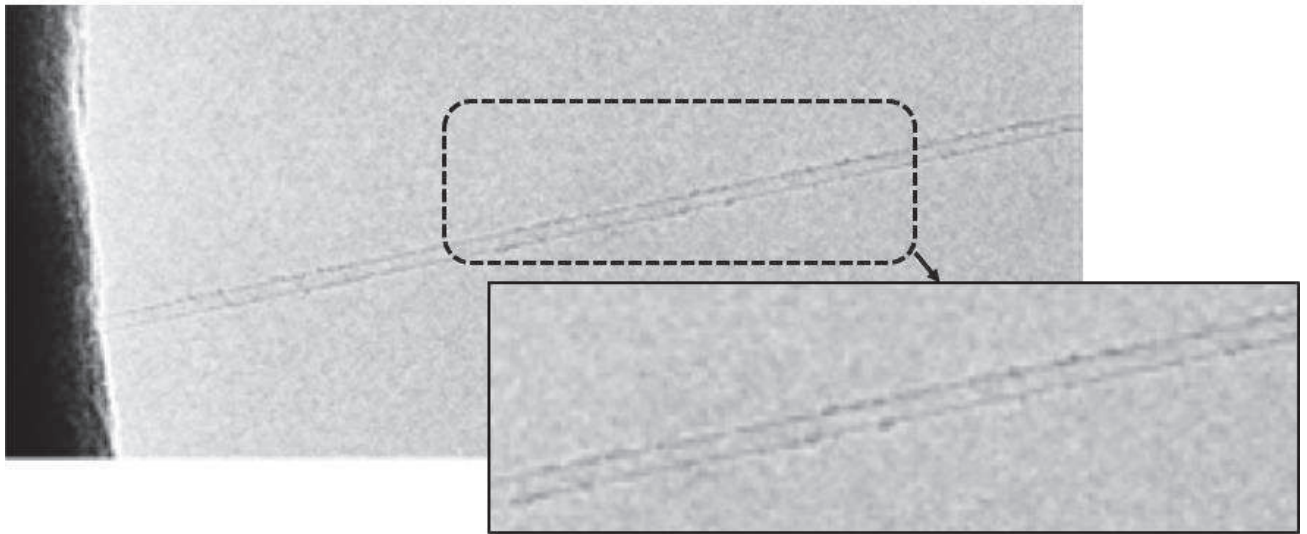


Fig. 3.14: The HRTEM image of individual suspended single-walled nanotube from Ref [9].

We thus think that the effect of amorphous carbon seems to be non-dominant to explain alone the deviation between the ω_{RBM} vs d relations.

The interaction between the nanotube and the substrate.

Another difference in the experimental conditions in our work and that of Liu et al [9] concerns the post-synthesis measurement conditions, namely the type of the support. In the work of Liu et al carbon nanotubes were suspended over the slits 20-50 μm wide. While in our case they were lying on the perforated HRTEM grids with holes 3 μm in diameter. This fact is illustrated in the Fig. 3.15. It is clear that in our measurements tubes were in a more close contact with the substrate.

How this may influence the radial vibrations of the SWNTs? In theory, a real crystal may be treated as ideal only when its dimensions are big enough (hence edge effects are not seen). In analogy, a carbon nanotube may be considered ideal (and hence following theoretical relations) only

when it is far enough from the substrate. However, when the nanotube is mainly lying on the support (see Fig. 3.15b), the interaction between the supported part and the substrate can influence the vibration of the suspended part of the SWNT.

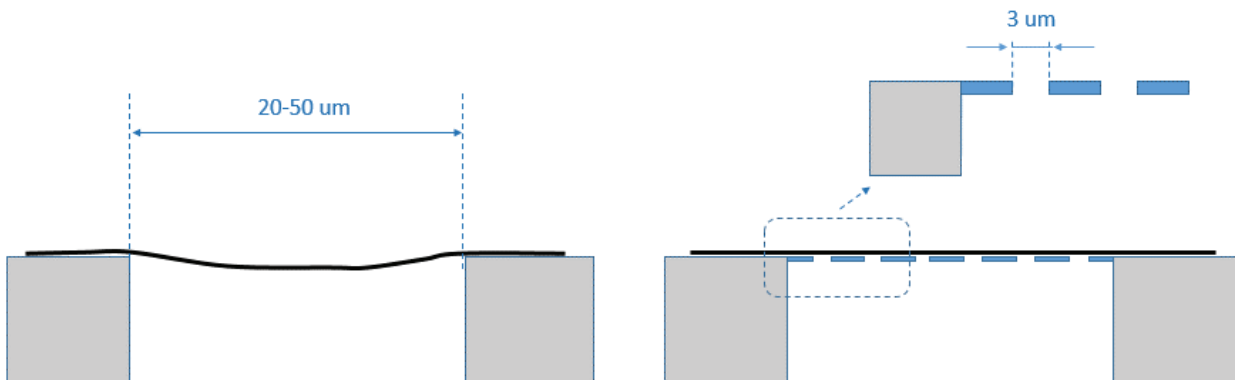


Fig. 3.15: (a) The position of individual carbon nanotubes in the work of Liu et al [9] (left) and in our experiments (right). In the first case carbon nanotubes are suspended over the slits 20-50 μm wide. In our case, SWNTs were lying on the perforated HRTEM grids with holes 3 μm in diameter.

Another argument in favor of the interaction with the substrate is the following. Araujo et al [7] also experimentally measured $227/d$ relation on samples of vertically aligned SWNTs (the so-called ‘super growth’ nanotubes). One of the features of these samples was the low-density of carbon nanotubes. This means that on average there exists one 3 nm diameter SWNT in a substrate area of 190 nm^2 and the average distance between tubes is of about 14 nm. Consequently, the SWNTs occupy 3.6% of the total volume, thus meaning that more that 96% is empty space. A schematic of the forest assuming complete uniformity is given in Figure 3.17 [20, 21, 22]. In consequence, in super growth samples the effect of the substrate is very low due to the small contact area between the SWNT and the support.

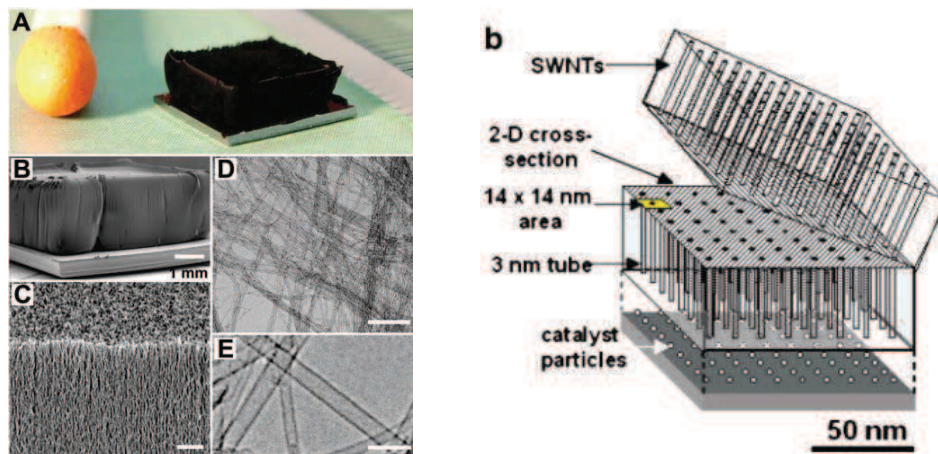


Fig. 3.16: Adapted from Ref. 7.

However, to definitely confirm the deviations as due to the substrate, we need to perform a series of additional measurements. For example, to grow individual SWNTs (following our synthesis protocol) on the substrate with a series of slits (1, 3, 10, 20, 50 μm etc) and to measure Raman spectra at the center of the suspended parts of every slit. The comparison between RBMs at different suspended areas of the nanotube may clearly show the role of the substrate.

Summary

We have presented the analysis of the new series of ultra-long suspended individual SWNTs (12 in total). It is appeared that in spite of the improvements of the growing conditions (which were similar to those described in the work of Liu et al [9]), we still get some systematic effect that tends to shift the RBM frequencies from the theoretical $228/d$ relation (See Fig. 3.8). To explain these observations we proposed the following hypothesis:

1. The presence of external strains in the SWNTs.
2. The effect of air pressure.
3. The contamination of the CNT surface.
4. The presence of the environmental interaction.

We carefully examined every point in a series of experiments and we ruled out the effects of strains and air pressure. However, combined effects of adsorbed species, including amorphous carbon, and of the substrate may be the major ingredients to explain the frequency deviations from the theoretical $228/d$ relation.

Regarding this latter point, experiments with different slits are scheduled for the future on the index-identified free-standing single-walled carbon nanotubes.

3.5 The G-modes (or Tangential Modes)

We remind that the intrinsic profile, depending on the nature of SWNT, as well as the diameter dependence of the LO and TO G-modes, have been established for chiral and achiral SWNTs few years ago (see Chapter 1).

Considering the “environmental conditions” (their different natures are discussed above) on SWNT as being the origin of the gap between our experimental ω_{RBM} vs. d relation and the $228/d$ theoretical relation, we would like to precise how these “environmental conditions” influence (or not) G-modes of individual suspended single-walled carbon nanotubes.

Recently Telg et al [23] reported the study of the LO and TO Raman modes of 14 different small-diameter ($d < 1.1$ nm) semiconducting nanotubes suspensions sorted by chirality. They found that the Raman shift of both peaks can be described using the formula:

$$\omega_{ph}(d) = a_0 + \frac{a_1}{d^2} + \frac{a_2}{d} \quad (3.28)$$

with the parameters given in table 3.4.

Table 3.4: Parameters of the equation (3.28). See Ref [23] for details.

	Reference	a_0 (cm ⁻¹)	a_1 (cm ⁻¹ nm ²)	a_2 (cm ⁻¹ nm)
G+/A _{LO}	Telg + Paillet et al	1582	-14.9	24.9
	Jorio et al (experim.)	1591	0	0
	Dubay et al (theory)	1593	-13.2	17.6
	Popov et al (theory)	1582	-20.8	31.5
G-/A _{TO}	Telg et al + Paillet et al	1582	-27.5	0
	Jorio et al (experim.)	1591	-47.7	0
	Dubay et al (theory)	1591	-22.9	0
	Popov et al (theory)	1582	-22.0	0

Telg et al give the following explanation of this dependence. Assuming that with increasing diameter, the frequencies of both the TO(G-) and LO(G+) peaks approach the value of the E_{2g} mode in graphite and graphene respectively, the value a_0 is fixed to 1582 cm⁻¹. The second term, a_1/d^2 , describes the strong decrease of both peaks for small diameter nanotubes. The third term in eq. 3.28, a_2/d , accounts for the fact that the frequency of the LO G-mode initially increases with decreasing diameter before it decreases again for very small diameter tubes. It has been shown that simulating confinement by applying zone-folding to a graphene sheet results in

an upshift of the LO G-mode frequencies with decreasing diameter that is proportional to $1/d$. Therefore, the third term in eq. 3.28 can be associated with confinement, while the second term results from the curvature of the tube wall. In the case of the TO(G-) peak, the monotonic decrease of the frequency with diameter is well described by the first two terms, making the third term unnecessary. Hence, a_2 is equal to zero for TO G-mode.

A good agreement is found between the data of Telg et al. measured on SWNT wrapped in a surfactant and the data of Paillet et al [24], measured on suspended individual SWNT (Fig. 3.17a). That means that the environment effects, excluding doping, are weak for the G-modes. We remind, that under doping, the profile and frequency of the LO mode, especially in metallic tube, strongly depends on the doping level [25].

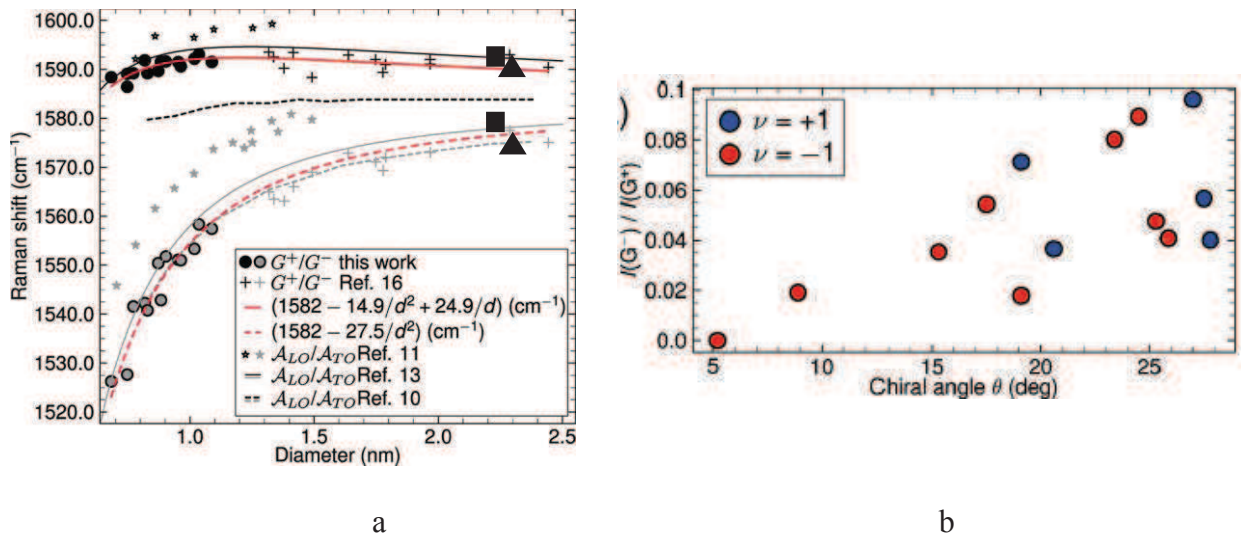


Fig. 3.17: (a) G^+ (LO) and G^- (TO) frequencies as a function of tube diameter in semiconducting SWNT. Solid and dashed red lines represent fits of eq. (3.28) to the combined data from Telg et al (circles) and ref [21] (plus symbols). Black and gray stars and solid and dashed lines are theoretical predictions based on *ab-initio*, non-orthogonal tight-binding, and *ab-initio* on graphene plus zone-folding approximations, respectively; Black squares and triangles correspond to the (24,8) and (19,15) nanotubes from this work (b) Ratio of G^- (TO) and G^+ (LO) intensities ($I(G^-)/I(G^+)$) as a function of chiral angle θ . From Ref [23].

The observed diameter dependence of the G- peak is sufficient to allow its use in determining the diameter of small nanotubes. We note that the LO and TO mode frequencies extracted from the fit of the Raman spectra of our (19, 15) and (24, 8) SWNTs (see for example Fig. 3.18b (Fig. 3.19b) respectively) are in good agreement with the data of Telg et al.

In addition, Telg et al found both peak positions to depend on chiral angle (Fig. 3.17b), that was also attributed to the rehybridization. As predicted, the observed intensities of the G-peaks are almost absent for chiral angles close or equal to zero degrees and steadily increase with

increasing angle. This chiral angle dependence of the $I(G^-)/I(G^+)$ ratio is reported in figure 3.17b. The plot shows a general decreasing trend of the intensity ratio for smaller chiral angle. However, significant scatter is observed at specific values due to the overlapping diameter dependence. More precisely, it was established that a concomitant decrease of the intensity ratio with chiral angle and a decrease of this ratio with increasing diameter is in a good agreement with theoretical predictions based on tight-binding approximations [26]. In this paper, the authors claim that the values of their intensity ratio are different from the one measured on free-standing index-identified SWNT in the Montpellier's group [27]. They assigned this disagreement to the damage of the free-standing SWNT introduced by the etching process used for sample preparation.

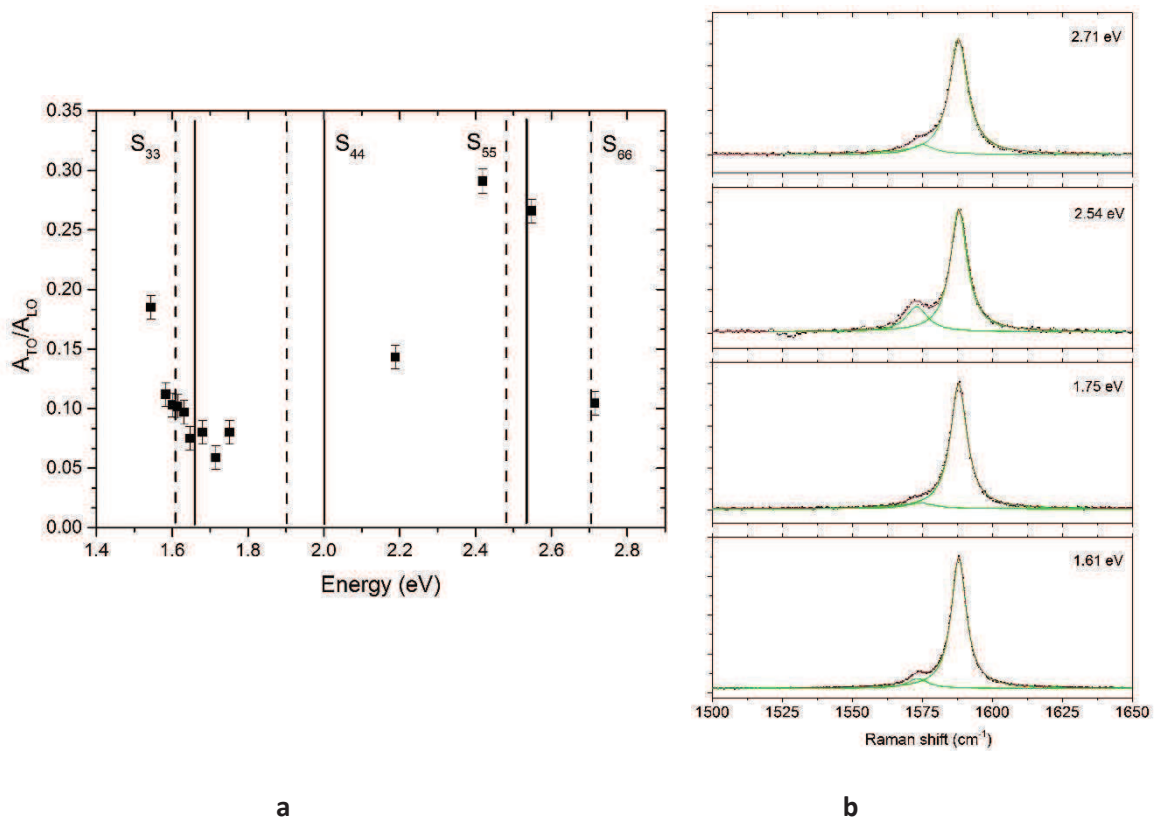


Fig. 3.18: (a) Excitation frequency dependence of the $A(G^-)/A(G^+)$ (A is a peak area) ratios; Solid and dashed lines correspond to the calculations of Popov et al [28] and Liu et al [29] respectively; (b) High-frequency part of Raman spectra of (19,15) SWNT showing different intensity ratios for different excitation energies.

In order to shed light on this question, we analyze in detail the intensity ratio of our new series of free-standing SWNTs (without the etching process during the sample preparation). For example, the incident excitation dependences of the intensity ratio of the (19,15) and (24,8) SWNTs have been measured in a wide variety of excitation wavelengths. The corresponding data are presented in Table 3.4 and 3.5, and the excitation dependence of the integrated area ratio

A_{TO}/A_{LO} is displayed in the Fig. 3.18a and 3.19a (note, that I_{TO}/I_{LO} give similar results; see for example Table 3.4 and 3.5).

Table 3.5: The excitation frequency dependence of the $I(G^-)/I(G^+)$ and $A(G^-)/A(G^+)$ (A is a peak area) ratios for the (19,15) SWNT.

Excitation wavelength	Excitation frequency	$A(G^-)/A(G^+)$	$I(G^-)/I(G^+)$
458	2.71	0.10	0.08
488	2.55	0.27	0.21
514	2.42	0.29	0.25
568	2.19	0.14	0.098
710	1.75	0.08	0.05
725	1.71	0.06	0.04
740	1.68	0.08	0.05
755	1.65	0.07	0.06
762	1.63	0.10	0.07
770	1.61	0.10	0.075
777	1.60	0.10	0.08
785	1.58	0.11	0.086
805	1.54	0.19	0.09

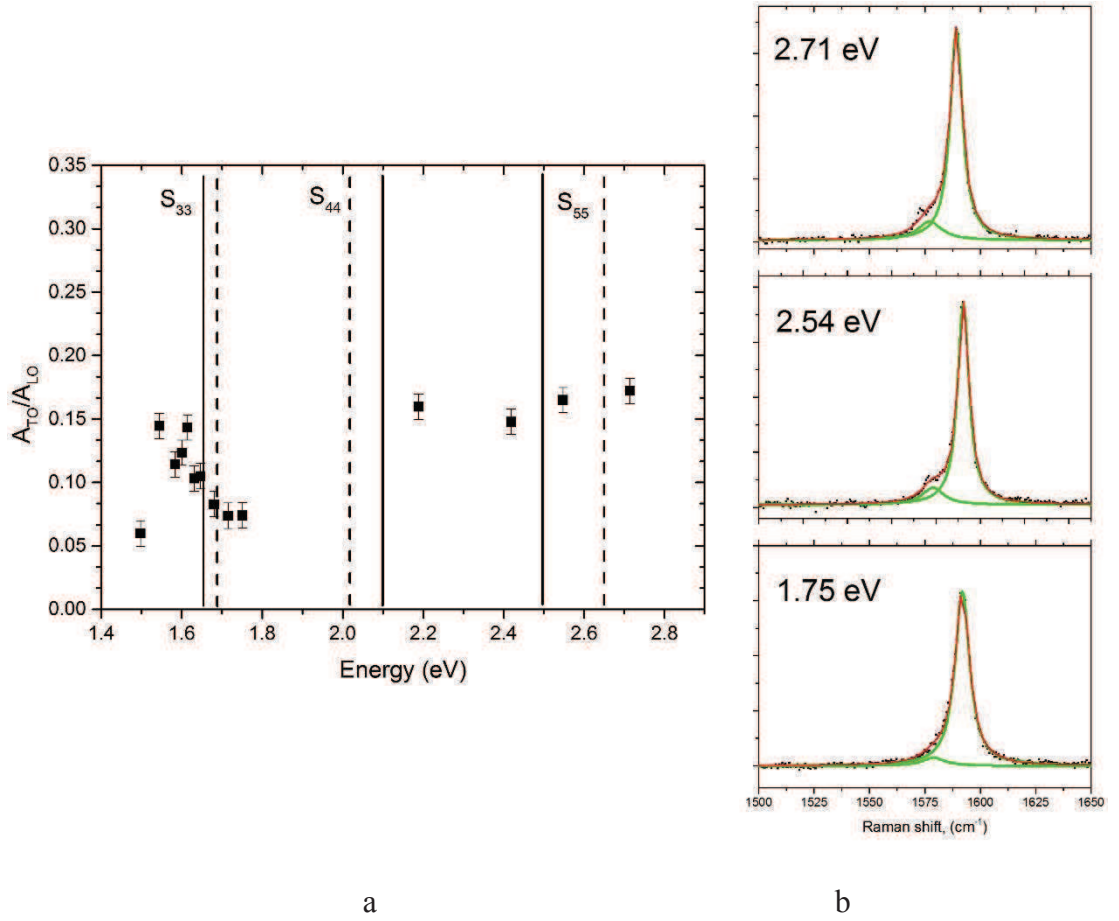


Fig. 3.19: (a) Excitation frequency dependence of the $A(G^-)/A(G^+)$ (A is a peak area) ratios. Solid and dashed lines correspond to the optical transitions calculated by Popov et al [28] and Liu et al [29] respectively; (b) High-frequency part of Raman spectra of (24,8) SWNT showing different intensity ratios for different excitation energies.

Table 3.6: The excitation frequency dependence of the $A(G^-)/A(G^+)$ (A is a peak area) and $I(G^-)/I(G^+)$ ratios for the (24,8) SWNT.

Excitation wavelength	Excitation frequency	$A(G^-)/A(G^+)$	$I(G^-)/I(G^+)$
458	2.71	0.172	0.0897
488	2.55	0.165	0.0861
514	2.42	0.148	0.0855
568	2.19	0.160	0.0936
710	1.75	0.074	0.0474
725	1.71	0.074	0.0473
740	1.68	0.083	0.0504
755	1.65	0.105	0.0643
762	1.63	0.103	0.0625
770	1.61	0.143	0.0816
777	1.60	0.123	0.0740
785	1.58	0.114	0.0671
805	1.54	0.145	0.0859
830	1.50	0.060	0.0430

For measurements performed around the S_{33} transition, the average value of the intensity ratio is of about 0.075-0.08 for both (19,15) and (24,8) SWNTs which is in agreement with Telg et al (See last columns of Tables 3.3 and 3.4). At the higher excitation wavelengths the maximum value of the ratio $I(G^-)/I(G^+)$ is different for (19,15) and (24,8) nanotubes: 0.25 and 0.09 respectively. We thus suppose that the intensity ratio may depend on the excitation energy, and probably on the order of the transition. However, more experimental data are necessary to make some definite conclusions.

3.6 Optical transitions of individual free-standing SWNTs from the measurements of the excitation profile of the RBM and G-modes.

The excitation profiles of RBM and G-modes of two free-standing index-identified SWNT have been measured. Two examples of such profiles are reported in figures 3.20 and 3.21 (for (19,15) and (24,8) SWNTs respectively). We emphasize that this kind of measurements are complicated and time-consuming due to the need of continuous lasers and the exact control of experimental conditions. In consequence, the resonance profiles of SWNTs were obtained previously only by a group of Debarre [11] and for only one individual SWNT.

We fitted the resonance profiles of (19,15) and (24,8) SWNTs using the following expression:

$$I(E_{Laser}) \propto \frac{1}{\left[(E_{laser} - E_{ii})^2 + \frac{\Gamma^2}{4} \right] \left[(E_{laser} - E_{ii} + \hbar\omega_{phonon})^2 + \frac{\Gamma^2}{4} \right]}$$

where E_{ii} is a transition energy, Γ is a width of the resonance window (related to the lifetime of the excited state) and $\hbar\omega_{phonon}$ is the phonon energy involved the scattering process.

We found $S_{33} = 1.608$ eV (FWHM = 50 ± 1 meV) for the (19,15) SWNT and $S_{33} = 1.607$ eV (FWHM = 80 ± 10 meV) for the (24,8) SWNT. The comparison between the experimental values of S_{ii} and the theoretical calculations of Popov et al [28] and Liu et al [29] for (24,8) SWNT shows that there exist an energy shift of 50-80 meV between the data (we remind that the calculations of S_{33} from Popov et al were up-shifted by ~ 0.4 eV). However, for the (19,15) SWNT the experimental value of S_{33} coincides almost perfectly with the S_{33} from Ref [29].

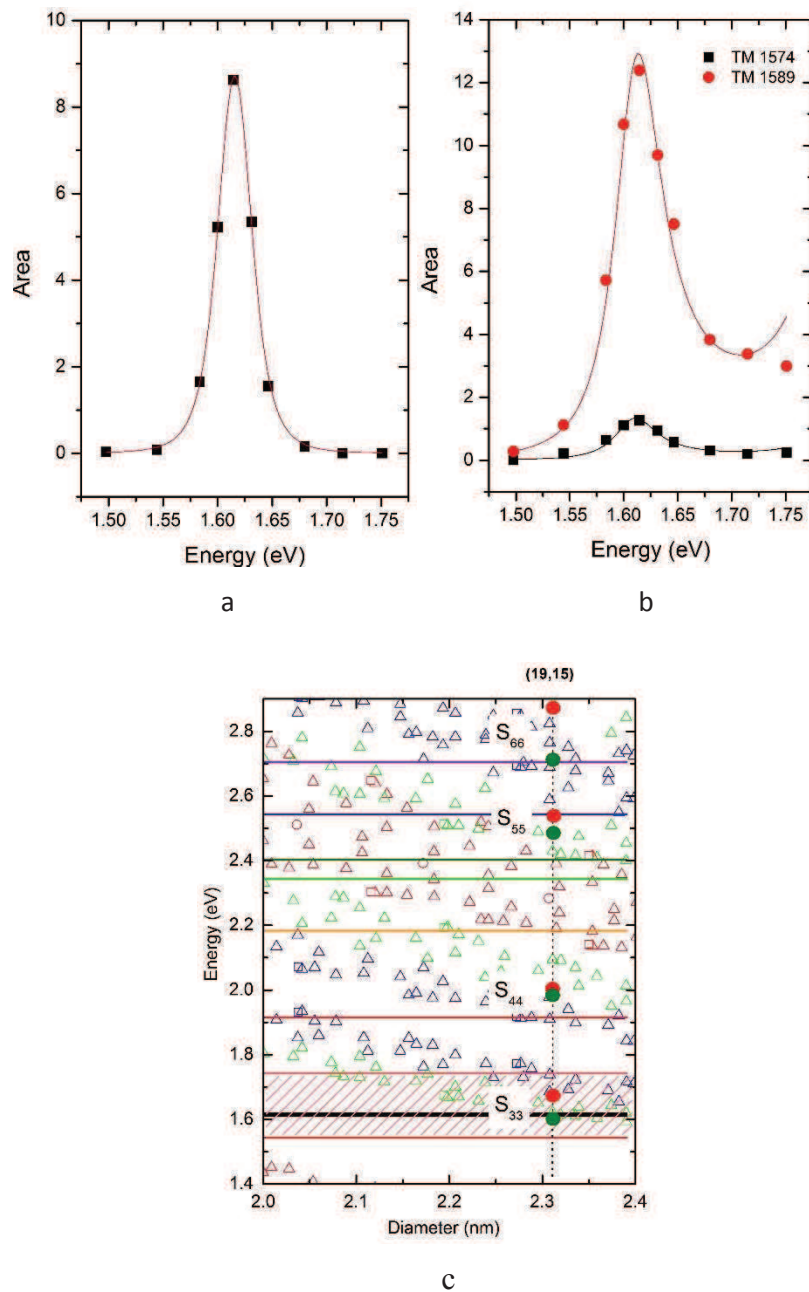


Fig. 3.20: Resonance profiles for the (a) RBM and (b) G-band of the (19,15) SWNT; (c) Kataura plot for the (19,15) SWNT. Red and green dots correspond to the calculations of Popov et al. [28] and Liu et al. [29] respectively. Black line correspond to the $S_{33} = 1.608$ eV.

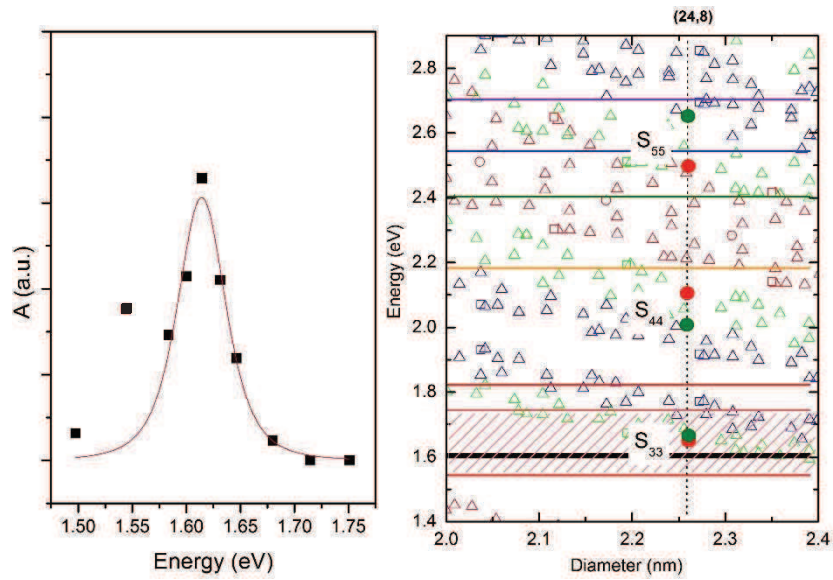


Fig. 3.21: (a) A resonance profile for the RBM of the (24,8) SWNT and (b) Kataura plot for the (24,8) SWNT. Red and green dots correspond to the calculations of Popov et al [28] and Liu et al [29] respectively. Black line correspond to the $S_{33} = 1.607$ eV.

Table 3.7: Comparison between experimental and theoretical data

#	(19,15) SWNT			(24,8) SWNT		
	Exp.	Popov et al [28]	Liu et al [29]	Exp.	Popov et al [28]	Liu et al [29]
S ₁₁	-	0.585	0.507	-	0.586	0.523
S ₂₂	-	0.919	0.869	-	0.944	0.905
S ₃₃	1.608	1.667	1.604	1.607	1.659	1.685
S ₄₄	-	2.003	1.903	-	2.104	2.010
S ₅₅	-	2.537	2.485	-	2.498	2.655
S ₆₆	-	2.884	2.708	-	3.107	2.915

3.7 Raman spectroscopy of an individual free-standing bundle of single-walled nanotubes.

In this paragraph we analyze the optical and vibrational properties of individual bundles of single-walled carbon nanotubes. This bundle is composed of 2 SWNTs in interaction. This system gives a unique opportunity to compare experimental results with theoretical approaches by focusing on the low-frequency range of inhomogeneous dimer [30, 31], the so-called breathing-like modes (BLM).

Figure 3.22 shows a TEM image of the bundle under consideration. It is clear that the bundle is relatively long (more than 40 μm). According to high-resolution image, there is a certain level of amorphous carbon on the surface of the tubes. However, we do not observed any significant D-band in the Raman spectra (see D-band in Fig. 3.25a, for example). Electron diffraction experiments were performed at different holes (e.g. at different areas of the bundle) and the results of the data treatment are presented below.

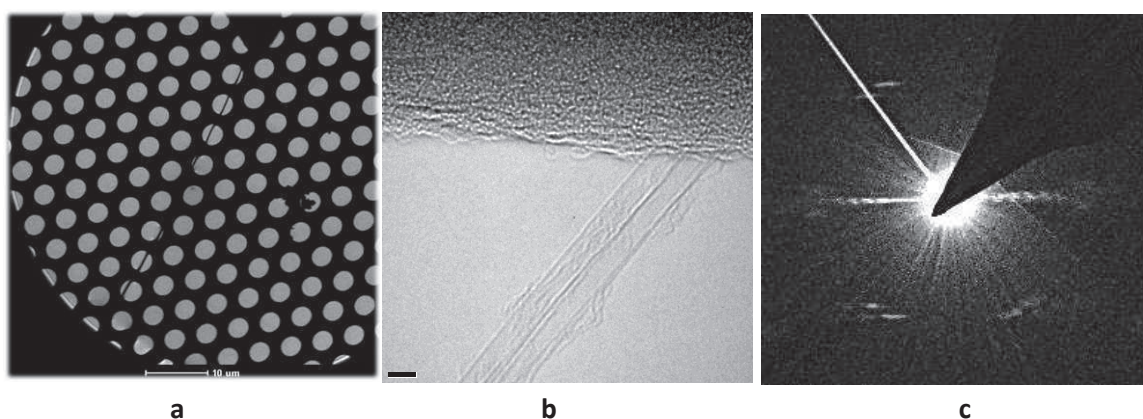


Fig. 3.22: (a) Low- and (b) high-resolution TEM images of the bundle of two iSWNTs; (c) the corresponding ED pattern.

3.7.1 Structural data

It should be pointed out that diameters of constituent single-walled nanotubes were extracted only from HRTEM images leading to the values: $d_1 = 1.7 \pm 0.3$ nm and $d_2 = 1.95 \pm 0.3$ nm. In addition, the treatment of the ED patterns showed that the two tubes have similar chiral angles around 25.1° . The corresponding indices are (15,11) and (16,12) (see information below). The method we used to index these SWNTs will be described in details in the Chapter 5.

As usual we performed several Raman measurements at different holes of the TEM grid and all the results are consistent. BLM and G-modes were recorded using 7 laser excitation wavelengths: 676, 647, 568, 514, 530, 488 and 458 nm. We note however that there was no signal observed on 458 and 530 nm. The data are presented and analyzed in the following paragraphs.

3.7.2 Radial-breathing like modes range.

The single-walled carbon nanotubes were in resonance with the incident radiation in the red region, namely at 647 and 676 nm (see Fig. 3.23a). At 647 nm, two peaks are observed in the BLM range: an intense mode located at 131 cm^{-1} and a shoulder around 139 cm^{-1} . At 676 nm, only, one mode is observed at 138 cm^{-1} .

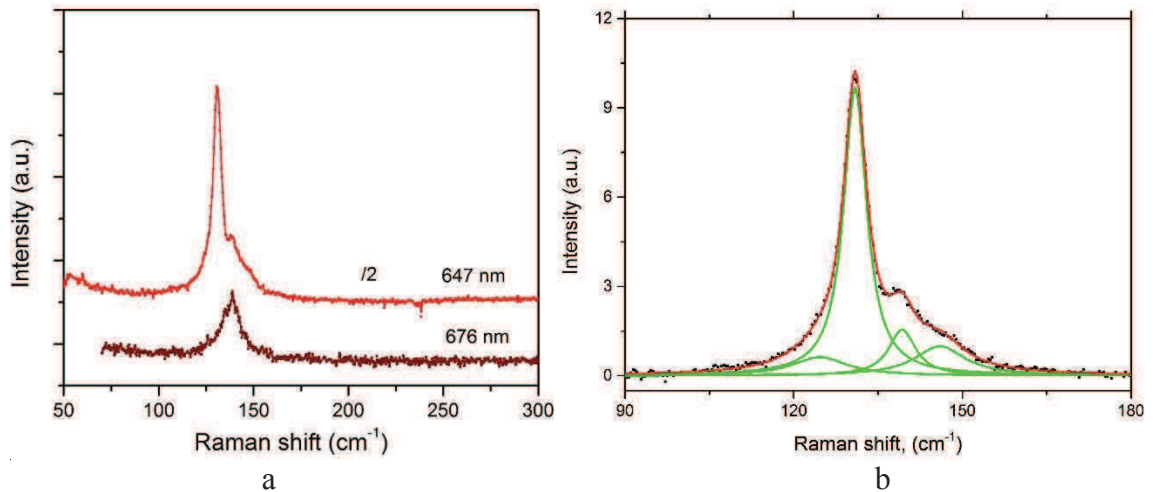


Fig. 3.23: (a) Breathing like modes region of Raman spectra measured on a bundle of two single-walled carbon nanotubes. Excitation wavelengths: 647 and 676 nm; (b) The fit of the RBLM region of the Raman spectra at 647 nm (4 Lorentzians are used);

We compare the positions of these modes with the RBM frequencies calculated using formulas $228/d$ (relation-1) and $204/d+27$ (relation-2), established for individual free-standing SWNTs:

$$(15,11): d= 1.7708\text{ nm}; \theta = 24.92^\circ$$

$$\omega_{\text{BLM1}} = 138\text{ cm}^{-1} \quad \omega_{\text{Relation-1}} = 129\text{ cm}^{-1} \quad \omega_{\text{Relation-2}} = 142\text{ cm}^{-1}$$

$$(16,12): d=1.906\text{ nm}; \theta = 25.28^\circ$$

$$\omega_{\text{BLM2}} = 131\text{ cm}^{-1} \quad \omega_{\text{Relation-1}} = 120\text{ cm}^{-1} \quad \omega_{\text{Relation-2}} = 134\text{ cm}^{-1}$$

The first relation predicts a significant upshift (by 10 cm^{-1}) of the experimental frequencies (131 and 138 cm^{-1} respectively) with regard to calculations [120 cm^{-1} for the (16,12)

nanotube and 129 cm^{-1} for (15,11)]. The second relation gives frequencies (134 and 142 cm^{-1}) slightly upshifted with regard to the corresponding experimental frequencies.

L. Henrard et al. [30] and K. Sbai et al. [31] have studied BLMs of inhomogeneous dimer of SWNTs. In particular, L. Henrard et al. calculated the Raman spectrum of the dimer made of a (9,9) and a (10,10) tubes and found that two pair of modes appear close to the RBM positions of isolated SWNTs (see Fig. 9 in Ref [30]). The split in two components is due to the lower symmetry of the environment. The lower-frequency pair of peaks is mainly related to the vibration of the (10, 10) tube and the higher-frequency pair of peaks is associated with the vibrations of (9,9) tube. Similar conclusions were established by K. Sbai et al. (see Figure 4 in Ref [31]). In addition, these calculations demonstrate that when RBM frequencies of isolated SWNTs are rather different, we can evidence 4 individual components of the bundle in the experimental spectra. In our case, despite the fact that RBMs of isolated SWNTs are only separated by 8 cm^{-1} , the experimental data are in agreement with the theoretical predictions. The lower-frequency peak is mainly related to the vibration of the (16,12) tube and the higher-frequency peak is associated with the vibrations of (15,11) tube. The relatively large width of the higher-frequency measured at 676 nm could be related to the splitting due to the environment. Moreover, in qualitative agreement with the above-mentioned theoretical studies, the spectra at 647 nm may be fitted by 4 components (see Fig. 3.23b) centered around 125 (FWHM = 12 cm^{-1}), 131 (5), 139 (6) and $146 (11) \text{ cm}^{-1}$. This observed splitting is then the characteristic of the bundle.

In a bundle, due to the interaction between the tubes, we can expect an upshift of the BLM frequencies. However, calculations for an infinite dimer with diameter larger than 2 nm predict that the hybrid breathing-like modes can be at a lower frequency than the RBM in the isolated tube. The comparison of these predictions with our experimental results does not allow to conclude about the direction of the RBM shift in the dimer under consideration. Indeed, comparison with the $228/d$ relation shows an upshift of around 8 cm^{-1} of the two modes in dimer. By contrast, from the comparison with the $204/d+27$ relation, a slight downshift of both the modes in dimer was found. The impossibility to conclude about the direction of the shift underlines the necessity to know precisely for each series of SWNTs the adapted ω_{RBM} vs d relation.

Regarding the resonance conditions, we encounter certain difficulties while using the Kataura plot (Fig. 3.24). In fact, theory [28] predicts the S_{33} transition for the (15,11) and (16,12) SWNTs at 2.019 and 1.916 eV, respectively. However, the (15,11) nanotube is observed at 1.92 and 1.83 eV, while the (16,12) is at resonance at 1.92 eV. In this case, a simple rigid shift of the

theoretical transitions cannot explain the observed experimental energies of S_{33} . We thus assume that use of Kataura plot for this bundle of two SWNTs is not straightforward. The solution to this problem would be to measure the Resonance profiles of the bundle.

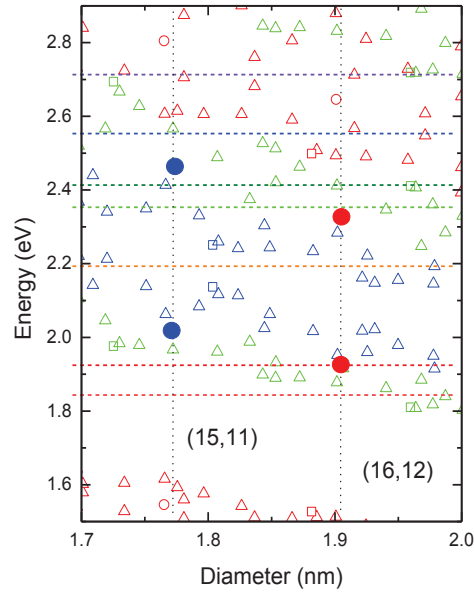


Fig. 3.24: Kataura plot with optical transitions highlighted for (15,11) (blue dot) and (16,12) (red dot) carbon nanotubes. Horizontal lines represent the excitation energies used in this study.

3.7.3 G-modes

We examine now the G-modes range of the Raman spectrum of the bundle. The corresponding spectra are shown in the Fig 3.25 for different laser excitations energies and laser power. As clear from the Figure 3.25, we observe here a certain difference with the spectra of individual single-walled carbon nanotubes. However, the shape of the G-band indicates the semiconducting nature of the constituent nanotubes that is in agreement with our chiral index assignments.

We fit the G-band of the bundle with 4 Lorentzians following standard procedures of data analysis. The TM frequencies are 1568, 1571, 1586 and 1596 cm^{-1} . The first two frequencies correspond to the TO modes, the second two to LO modes of the constituent semiconducting carbon nanotubes. As was shown in the Chapter 1 the TO mode's frequency show a strong dependence on the nanotube's diameter, while LO modes almost do not change. Based on that dependence we assign the 1568, 1586 cm^{-1} to a (15,11) nanotube and 1571, 1596 cm^{-1} to a (16,12).

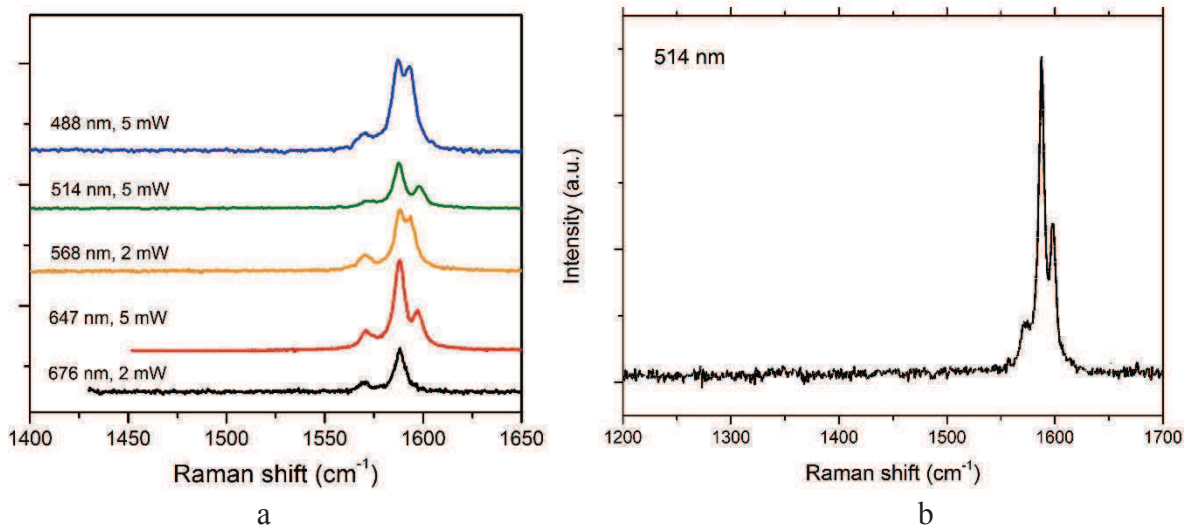


Fig. 3.25: (a) High-frequency region of Raman spectrum of the bundle of two SWNTs measured at 676, 647, 568, 514 and 488 nm; (b) A closer look on the D-band and G-band of the the bundle in question at 514 nm.

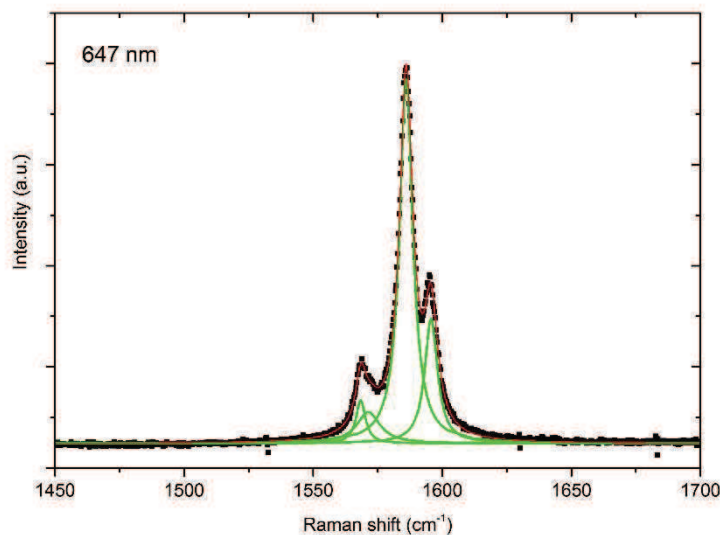


Fig. 3.26: The fit of the G-band of the bundle of two semiconducting SWNTs measured at 647 nm.

In the TO vs. d plot established from individual SWNTs (Figure 3.27) we report the frequencies of the TO modes expected for isolated individual SWNTs (15,11) and (16,12) (blue and red circles respectively). The plot predicts their frequency to be close to 1571.5 cm^{-1} and 1573 cm^{-1} respectively. These frequencies are slightly upshifted ($\sim 3 \text{ cm}^{-1}$) with respect to the corresponding TO modes in the bundle.

Assuming a weak interaction between the tubes, and using the plot established for individual SWNTs, we can determine the diameters of the both SWNTs in the bundle from the

positions of TO modes (figure 3.27, square symbols). We find 1.5 and 1.75 nm respectively. These values are in the lower limit of the diameter range found by HRTEM.

Considering a correct (n,m) index-assignment for both SWNTs, we observe that the difference between the frequency of the TO mode in (16,12) and (15,11) individual SWNTs is around 1.5 cm^{-1} , that is slightly smaller than the difference measured experimentally in the bundle (around 3 cm^{-1}). In this assumption, for TO modes, the interaction between the tubes leads to a small downshift of the frequency of the both TO modes and to an increase in their frequency separation. In this framework these two features could be considered as the signature of the coupling between the TO modes of SWNTs in this bundle.

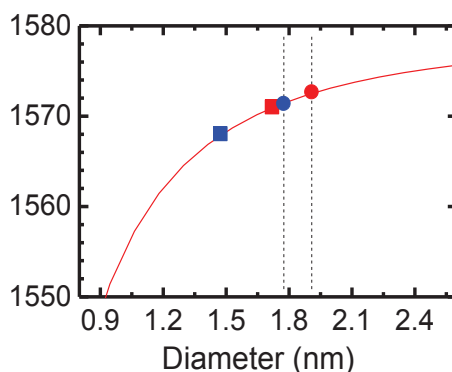


Fig. 3.27: The frequencies of the TO modes of two individual SWNTs (15,11) (blue circle) and (16,12) (red circle) in comparison with their frequencies in the bundle (blue and red squares correspondingly).

Finally, a careful examination of the LO modes lead to a more clear evidence of the coupling between SWNTs in this bundle. Indeed, there is a strong deviation of the LO frequencies of the bundled SWNTs from those found in isolated individual tubes. Assuming the average frequency of the LO mode in individual semiconducting SWNTs as 1590 cm^{-1} (see Chapter 1), the observation of a lower- (1586 cm^{-1}) and higher-LO frequency (1596 cm^{-1}) in the bundle is considered to be a consequence of the coupling between the LO G-modes of the two SWNTs. The same feature will be addressed in the Chapter 4 on DWNTs in more detail.

In conclusion, we would like to emphasize, that from this experiment performed on an index-identified individual bundle (dimer of two SWNTs), the coupling between the modes is evidenced, especially regarding the G-modes. Coupling between SWNT in complex nanostructures like bundles and DWNTs play a significant role in the understanding of their vibrational and optical properties. We leave the deep analysis of this effect on DWNTs to the next chapter.

3.8 Summary and Conclusion

In Chapter 3, we have examined the radial vibrations of the individual single-walled carbon nanotubes and presented several theoretical and experimental data established in the literature prior to this work. Then we presented the new experimental data obtained in the framework of this thesis to clarify the existing controversy. The main difference with the previous work of Meyer et al [9] lies in the improved synthesis protocol that is free of CNT chemical treatment.

Two possible explanations of the observed deviation of the experimental $\omega_{\text{RBM}}(d)$ relation from the theoretical one ($228/d$) were given:

- The contamination of the nanotube by amorphous carbon leading to the increase of the mass density of the SWNT.

- The interaction between the substrate and the carbon nanotube.

In the second part, we have presented new experimental results regarding the G-mode. We compared our result with those previously published in the literature and discussed the observed controversy. Moreover, we gave a presentation of the Raman resonance profiles performed on free-standing single-walled carbon nanotubes.

Finally, we proposed an analysis of Raman spectra of an identified dimer (bundle of two single-walled carbon nanotubes). Differences and similarities were discussed with respect to the experimental and theoretical studies of individual single-walled nanotubes.

References of Chapter 3:

- 1) G.D. Mahan, Oscillations of a thin hollow cylinder: Carbon nanotubes, *Phys. Rev. B* 65(23) (2002), p. 235402
- 2) S.B. Rochal, V.L. Lorman, Yu.I. Yuzyuk, Two-dimensional elasticity determines the low-frequency dynamics of single- and double-walled carbon nanotubes *Phys. Rev. B* 88, 235435 (2013).
- 3) R.A. Jishi, L. Venkataraman, M.S. Dresselhaus, G. Dresselhaus, Phonon modes in carbon nanotubes, *Chem. Phys. Lett.* **209**, 77 (1993)
- 4) J. Kürty, G. Kresse, H. Kuzmany, First-principles calculations of the radial breathing mode of single-wall carbon nanotubes, *Phys. Rev. B* **58**, R8869 (1998)
- 5) S. Reich, C. Thomsen, J. Maultzsch, *Carbon Nanotubes: Basic concepts and physical properties* Wiley-VCH, Weinheim, Germany, 2004
- 6) A. Jorio, R. Saito, J. Hafner, C. Lieber, M. Hunter, T. McClure, G. Dresselhaus, and M.S. Dresselhaus, Structural (n,m) Determination of Isolated Single-Wall Carbon Nanotubes by Resonant Raman Scattering, *Phys. Rev. Lett.* 86(6) (2001), pp. 1118–1121.
- 7) P.T. Araujo, I.O. Maciel, P.B.C. Pesce, M.A. Pimenta, S.K. Doorn, H. Qian, A. Hartschuh, M. Steiner, L. Grigorian, and K. Hata, Nature of the constant factor in the relation between radial breathing mode frequency and tube diameter for single-wall carbon nanotubes, *Phys. Rev. B* 77(24) (2008), p. 241403.
- 8) J. C. Meyer, M. Paillet, T. Michel, A. Moreac, A. Neumann, G. S. Duesberg, S. Roth and J.-L. Sauvajol, Raman Modes of Index-Identified Freestanding Single-Walled Carbon Nanotubes, *Phys. Rev. Lett.* 95, 2005, 217401.
- 9) K. Liu, W. Wang, M. Wu, F. Xiao, X. Hong, S. Aloni, X. Bai, E. Wang, and F. Wang, Intrinsic radial breathing vibrations in suspended single-walled carbon nanotubes, *Phys. Rev. B* 83, 113404 (2011).
- 10) Berciaud et al (to be published)
- 11) A. Débarre, M. Kobylko, A. M. Bonnot, A. Richard, V. N. Popov, L. Henrard, and M. Kociak, Electronic and Mechanical Coupling of Carbon Nanotubes: A Tunable Resonant Raman Study of Systems with Known Structures, *Phys. Rev. Lett.* 101, 197403 (2008)
- 12) M. J. Longhurst, N. Quirke, The environmental effect on the radial breathing mode of carbon nanotubes in water, *J. Chem. Phys.* 124, 234708 (2006).
- 13) P. Gao, L. Zheng, Q. Zhang, S. Yuan, Y. You, Z. Shen, and D. He, Self-Built Tensile Strain in Large Single-Walled Carbon Nanotubes, *ACS Nano* Vol. 4, No. 2, 992-998, 2010.

- 14) D. I. Levshov, Yu. I. Yuzyuk, T. Michel, C. Voisin, L. Alvarez, S. Berger, P. Roussignol, and J.-L. Sauvajol, Raman Probing of Uniaxial Strain in Individual Single-Wall Carbon Nanotubes in a Composite Material *J. Phys. Chem. C* **2010**, 114, 16210–16214.
- 15) G. Wu, J. Zhou, J. Dong, Raman modes of the deformed single-walled carbon nanotubes, *Phys. Rev. B* **2005**, 72, 115411
- 16) S.B. Cronin, A.K. Swan, M.S. Unlu, B.B. Goldberg, M.S. Dresselhaus, M. Tinkham, Measuring the uniaxial strain of individual single-walled carbon nanotubes : Resonance Raman spectra of Atomic-Force-Microscope Modified Single-Wall Nanotubes, *Phys. Rev. Letters*, Vol. 93, 16, 167401, 2004
- 17) X. Duan, H. Son, B. Gao, J. Zhang, T. Wu, G. G. Samsonidze, M. S. Dresselhaus, Z. Liu, J. Kong, Resonant Raman Spectroscopy of individual strained single-wall carbon nanotubes, *Nano Letters*, 2007, Vol. 7, No.7 2116-2121.
- 18) Q. Wang and J. K. Johnson, Molecular simulation of hydrogen adsorption in single-walled carbon nanotubes and idealized carbon slit pores, *J. Chem. Phys.* 110, 577 (1999);
- 19) M. Iwaki, Estimation of the atomic density of amorphous carbon using ion implantation, SIMS and RBS, *Surface and Coatings Technology* 158 –159 (2002) 377–381
- 20) K. Hata, D. N. Futaba, K. Mizuno, T. Namai, M. Yumura, and S. Iijima, Water-assisted highly efficient synthesis of impurity-free single-walled carbon nanotubes, *Science* **306**, 1362 (2004).
- 21) D. N. Futaba, K. Hata, T. Yamada, K. Mizuno, M. Yumura, and S. Iijima, Kinetics of Water-Assisted Single-Walled Carbon Nanotube Synthesis Revealed by a Time-Evolution Analysis, *Phys. Rev. Lett.* **95**, 056104 (2005).
- 22) D. N. Futaba, K. Hata, T. Yamada, T. Hiraoka, Y. Hayamizu, Y. Kakudate, O. Tanaike, H. Hatori, M. Yumura, and S. Iijima, Shape-engineerable and highly densely packed single-walled carbon nanotubes and their application as super-capacitor electrodes, *Nat. Mater.* **5**, 987 (2006).
- 23) Hagen Telg, Juan G. Duque, Matthias Staiger, Xiaomin Tu, Frank Hennrich, Manfred M. Kappes, Ming Zheng, Janina Maultzsch, Christian Thomsen, and Stephen K. Doorn, Chiral Index dependence of the G⁺ and G⁻ Raman modes in semiconducting carbon nanotubes, *ACS Nano* 6, 904 (2012).
- 24) M. Paillet, T. Michel, J. C. Meyer, V. N. Popov, L. Henrard, S. Roth, J.-L. Sauvajol, Raman Active Phonons of Identified Semiconducting Single-Walled Carbon Nanotubes. *Phys. Rev. Lett.* 2006, 96, 257401.

- 25) J. C. Tsang, M. Freitag, V. Perebeinos, J. Liu, Ph. Avouris, Doping and phonon renormalization in carbon nanotubes, *Nature Nanotechnology* 2, 725 - 730 (2007).
- 26) R. Saito, A. Jorio, J. H. Hafner, C. M. Lieber, M. Hunter, T. McClure, G. Dresselhaus, and M. S. Dresselhaus, Chirality-dependent G-band Raman intensity of carbon nanotubes, *Phys. Rev. B* 64, 085312 (2001).
- 27) T. Michel, M. Paillet, D. Nakabayashi, M. Picher, V. Jourdain, J. C. Meyer, A. A. Zahab, and J.-L. Sauvajol, Indexing of individual single-walled carbon nanotubes from Raman spectroscopy, *Phys. Rev. B* 80, 245416 (2009).
- 28) V. N. Popov and L. Henrard, Comparative study of the optical properties of single-walled carbon nanotubes within orthogonal and nonorthogonal tight-binding models, *Phys. Rev. B* 70, 115407 (2004).
- 29) K. Liu, J. Deslippe, F. Xiao, R. B. Capaz, X. Hong, S. Aloni, A. Zettl, W. Wang, X. Bai, S. G. Louie, E. Wang and F. Wang, An atlas of carbon nanotube optical transitions, *Nature Nanotechnology* 7, 312 (2012).
- 30) L. Henrard, V. N. Popov, A. Rubio, Influence of packing on the vibrational properties of infinite and finite bundles of carbon nanotubes *Phys. Rev. B* 64, 205403 (2001).
- 31) K. Sbai, A. Rahmani, H. Chadli, J.-L. Sauvajol, Raman-active modes in homogeneous and inhomogeneous bundles of single-walled carbon nanotubes, *J. Phys. Condens. Matter* 21, 045302 (2009).

Chapter 4
**Raman spectroscopy of individual free-standing double-walled
carbon nanotubes**

In this chapter, we extend our experimental procedure to investigate intrinsic properties of main Raman-active phonons in the double-walled carbon nanotubes (DWNTs). The experimental data on double-walled carbon nanotubes that were available in the literature at the beginning of this thesis dealt mainly with macroscopic samples (ensemble of DWNTs) and didn't tell much about internal properties of double-walled nanotubes (refer to Chapter 1 for the summary). Only a few data concerned studies on these individual nanostructures [1].

In our goal to elucidate the intrinsic properties of DWNTs we followed the experimental procedure that was explained in the Chapter 2. Several effects, specific to DWNTs, were found and we present them here in details.

The Raman spectra of 11 identified individual free-standing DWNT have been recorded and analyzed in detail. In the following, we show that the Van-der-Waals coupling between walls lead to collective radial breathing-like modes (RBLM). The dependence of these RBLMs as a function of diameter and inter-wall distance as well as the resonance conditions of these modes is discussed. On the other hand, the profile of the G-modes of individual DWNT is reported and discussed. Distinct behaviors of the G-modes are evidenced and explained in terms of "negative" pressure effect.

Firstly, we focus on Raman spectroscopy of the (12,8)@(16,14) DWNT. At the best of our knowledge, it is on this DWNT that, for the first time, the unambiguous evidence of mechanical coupling between the walls was identified [2].

4.1 Raman spectroscopy of (12,8)@(16,14) DWNT. First direct evidence of mechanical coupling in a DWNT

This first investigated long individual suspended DWNT was synthesized by chemical vapor deposition (CVD) directly onto a Si₃N₄ TEM grid with holes (3 μm in diameter). The details of the method used to prepare individual suspended DWNTs are reported in [3].

We remind that the Resonant Raman scattering measurements were carried out using a Jobin Yvon T64000 spectrometer equipped with a liquid-nitrogen-cooled silicon CCD detector. The scattered light was collected through a 100 objective (N.A. = 0.95) using a back-scattering configuration. In all the measurements, both incident and scattered light polarizations are along the nanotube axis (*// //* polarized Raman spectrum). In this investigation, incident excitations from Ar⁺ and Kr⁺ lasers were used: 488 nm (2.54 eV), 514.5 nm (2.41 eV), 568.1 nm (2.18 eV), and 647.1 nm (1.92 eV). In order to avoid heating effects, the laser power impinging the sample

was kept below 50 μW .

4.1.1 Structural information

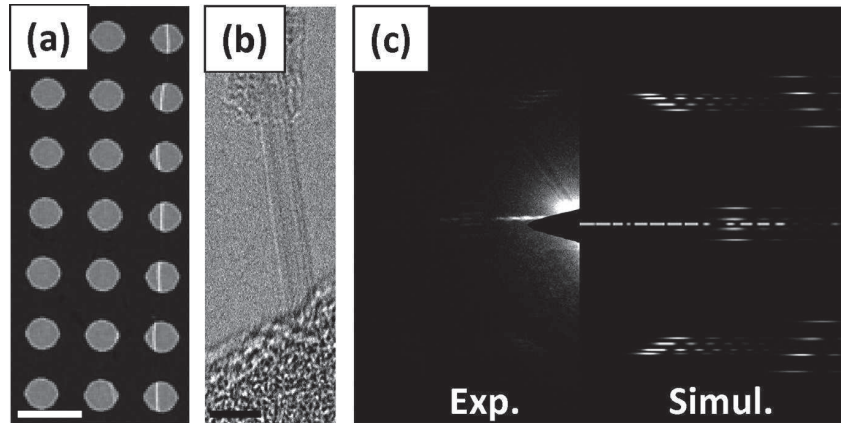


Figure 4.1: (a) Low magnification TEM image of the suspended nanotube on the Si_3N_4 grid, the scale bar is 4 μm . (b) HRTEM of the same DWNT, the scale bar is 3 nm. (c) Experimental (left) and simulated (right) diffraction pattern of the $(12,8)@(16,14)$ DWNT.

Figure 4.1 shows the investigated DWNT placed across holes of the grid. This configuration minimizes the effects (upshift of the Raman modes and downshift of the optical transitions) caused by tube-tube interactions within a rope, tube-substrate interactions for tubes deposited on a substrate, and tube-surfactant interactions in measurements on ensembles of DWNTs wrapped in surfactant.

The structural data derived from TEM and ED for this DWNT (Figure 4.1) can be summarized as follows: the nanotube is longer than 30 μm (Figure 4.1a). The HRTEM image (Figure 4.1b) clearly allows one to identify this tube as a DWNT and shows the presence of a certain quantity of amorphous carbon on its surface. TEM measurements at different holes of the grid also confirm that the structure of the tube is conserved along its length. However, due to the vibration of the nanotube under the electron beam, it was impossible to derive the diameter of each layer with a good accuracy from the HRTEM image.

In Chapter 2 we presented the structural analysis of this double-walled nanotube (refer to section 2.4.2, Example 1 for details). We remind here that the tube was identified as $(12,8)@(16,14)$ having

$$d_{\text{in}} = 1.37 \text{ nm}; \theta_{\text{in}} = 23.4^\circ$$

$$d_{\text{out}} = 2.04 \text{ nm}; \theta_{\text{out}} = 27.8^\circ$$

$$\Delta d = 0.68 \text{ nm}$$

4.1.2 The Radial breathing-like modes

As reminded in Chapter 1, the radial breathing-like modes (RBLM) appears in the low-frequency range of the Raman spectrum. The lowest-frequency RBLM and the highest-frequency RBLM are assigned to collective oscillations with concerted in-phase and out-of-phase motion of the two walls. The frequencies of these modes give additional information about the diameters of the inner and outer tubes. However, the evaluation of the diameters is not straightforward and adapted theoretical models have to be developed and discussed in relation with experimental data.

Figure 4.2 displays the low frequency region of the Raman spectrum of the (12,8)@(16,14) DWNT for different laser excitation energies E_L . At $E_L = 2.41$ eV (Figure 4.2, top), two strong components are observed at 133 cm^{-1} (full width at half-maximum, FWHM = 6.5 cm^{-1}) and 186 cm^{-1} (FWHM = 3 cm^{-1}), respectively (instrumental width close to 2 cm^{-1}). At $E_L = 2.18$ eV, only the component at 133 cm^{-1} is observed with a very low intensity. Finally, the two peaks are retrieved at almost the same frequency and width when the excitation is tuned at 1.92 eV. At this energy, the widths of the two RBLMs are comparable to those observed at 2.41 eV, i.e., 6 cm^{-1} for the low frequency peak and 3 cm^{-1} for the high frequency peak. The small intrinsic width for the out-of-phase RBLM (close of 1 cm^{-1}) can be emphasized and understood by considering that the inner tube is protected to environmental effects by the outer tube. In addition, the density of structural defects is necessary weak on this tube (large life time of phonons).

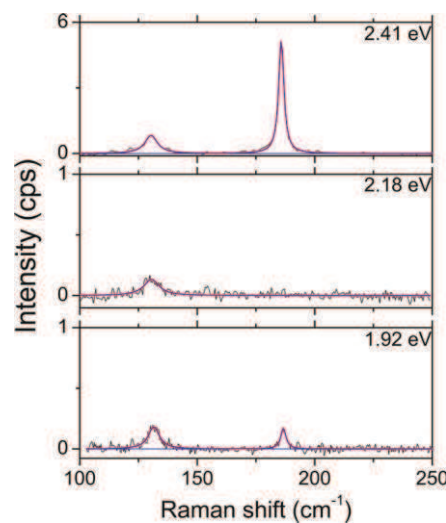


Figure 4.2: Low frequency range of the Raman spectra of the (12,8)@ (16,14) DWCNT measured at three excitation energies (for top to bottom: 2.41, 2.18, 1.92 eV).

Usually, the diameters of the inner and outer tubes are derived from their RBLM frequencies using ω_{RBM} vs. d established for SWNTs. We definitively state in the following that this procedure is wrong in a larger number of situations.

Indeed, we have been able to measure the Raman spectrum of the individual (12,8) SWNT (the inner tube) and the one of the (15,14) SWNT which is close in diameter to the (16,14) (outer tube). On the Figure 4.3 the Raman spectrum of the (12,8) SWNT ($d = 1.36$ nm, $\theta = 23.4^\circ$) and the one of the (15,14) SWNT ($d = 1.97$ nm, $\theta = 28.9^\circ$) are directly compared with the spectrum of the (12,8)@(16,14) DWNT.

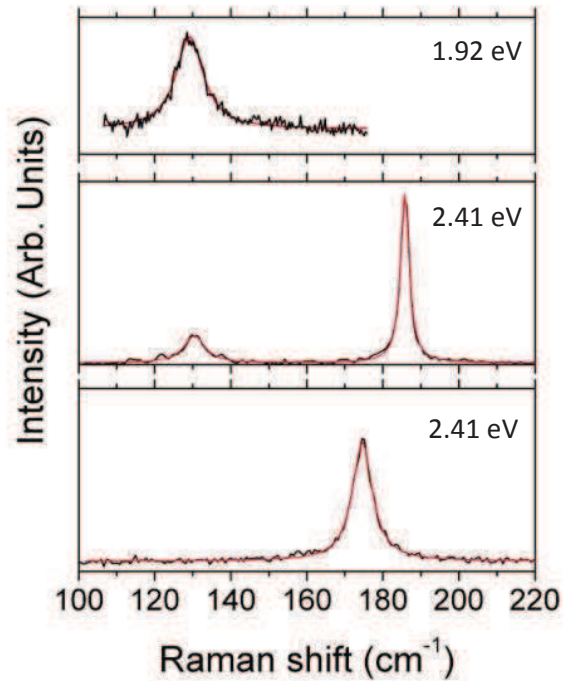


Figure 4.3: Low frequency range of the Raman spectrum of (15,14) SWNT (Top), (12,8)@(16,14) DWNT (Middle) and (12,8) SWNT (Bottom).

The RBM frequency of the (12,8) SWNT is located at 174.6 cm⁻¹, downshifted by about 11 cm⁻¹ with respect to the out-of-phase RBLM, and the RBM frequency of the (15,14) SWNT is downshifted by about 5 cm⁻¹ with respect to the in-phase RBLM. These shifts are a clear signature of the interlayer interaction.

We remind that for individual suspended index-identified SWNTs in air, two different relations were proposed, namely, $\omega_{\text{RBM},1}(d) = 228/d$ (nm) [4] and $\omega_{\text{RBM},2}(d) = 204/d$ (nm) + 27 [5] (in the following, the relation $\omega = 204/d + 27$ and the relation $\omega = (226/d) \sqrt{1 + Cd^2}$ established in Chapter 3 (equations 3.7 and 3.27) are supposed to be equivalent). The diameter

of the (12,8) and (16,14) derived from the frequency of in-phase and out-of-phase RBLM using both relations are given in Table 4.1 and they are significantly underestimated.

Table 4.1. Calculated diameter of the inner and outer tube from the two relations $\omega_{RBM,1}(d) = 228/d$ (nm) and $\omega_{RBM,2}(d) = 204/d$ (nm) + 27 (see text).

(n,m)	d (nm)	d ₁ (nm)	d ₂ (nm)
(12,8)	1.36	1.22	1.28
(16,14)	2.04	1.71	1.92

In conclusion, *the first important result of our study* is that all $\omega_{RBM}(d)$ relations established for SWNTs do not work, when deriving the diameters of the inner and outer tubes of a DWNT from the higher- and lower-frequency RBLMs respectively.

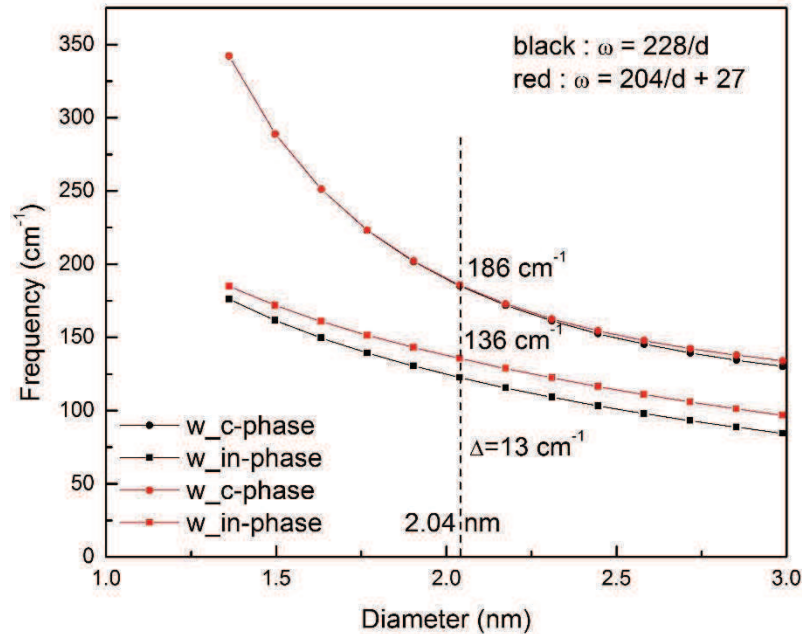


Fig. 4.4: Dependence of the frequencies of the radial breathing mode of two layer tubes on the outer layer radius calculated using two models of ref. [6]. The frequencies of the RBLM's in the two assumptions are designated by red [7] (dark) symbols and red (dark) solid line, respectively (see text).

The Raman data can be compared to the predictions of theoretical models for calculation of phonons in DWNT, in particular concerning the diameter dependence of the RBLMs [6,8]. In this context, we use the theoretical predictions of Ref [6], which take into account the coupling between the walls.

As detailed in Ref. [6], the mechanical coupling depends on the interlayer distance and diameter:

1. For an interlayer distance larger than 0.4 nm, a weak interaction between both layers is expected (independently of tube diameter).
2. However, when the interlayer distance is close to 0.34 nm, two coupling regimes are theoretically found as a function of tube diameter:
 - a. For outer tube diameters smaller than 2 nm, the vibrations of the inner and the outer tubes are independent. In this weak coupling regime, the in-phase RBLM (at low frequency) and the out-of-phase RBLM (at high frequency) tend to the RBM of the outer and inner tubes, respectively. In comparison with the RBM of the corresponding SWNT, only a frequency upshift is expected depending on the interactions between the tubes.
 - b. On the contrary, for outer tube diameter larger than 2 nm, moderate and strong coupling regimes are expected, where the RBLMs become collective breathing vibrations of both layers (Fig. 4.5).

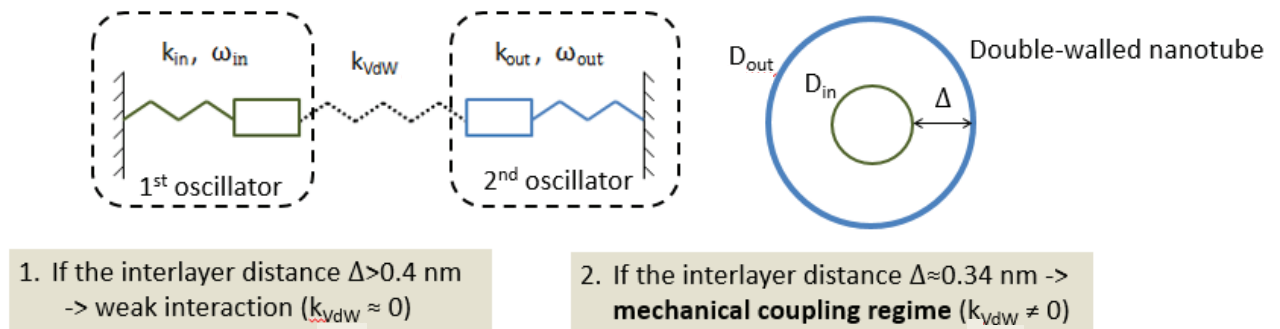


Fig. 4.5: Two different regimes in a double-walled carbon nanotube: mechanical coupling (right) and non-interacting regime (left).

In the work of Popov, the shift of the RBLMs with respect to the RBM frequency of the individual inner and outer layers (given by $\omega_{RBM}(d) = 228/d$ (nm) for each independent layer), is calculated by taking into account the van-der-Waals interactions between the layers (a review of this model was done in the Chapter 1).

According to Figure 4.4 (black symbols and lines), the mode at 186 cm^{-1} corresponds to the out-of-phase RBLM of DWNT with an outer tube diameter close to 2.02 nm (the diameter of the (16,14)). From the same figure, the in-phase mode is predicted at 123 cm^{-1} , significantly lower than the measured one.

A better agreement with experiment is achieved by considering two different relations for

the RBM frequency of each independent layer, namely: $\omega_{\text{RBM}}(d) = 228/d$ (nm) for the inner tube and $\omega_{\text{RBM}}(d) = 204/d$ (nm) + 27 for the outer tube. The presence of amorphous carbon around the outer tube justifies this latter assumption. In this case, taking an outer tube diameter = 2.02 nm, we find the frequency of the out-of-phase RBLM near 186 cm^{-1} and that of the in-phase mode around 136 cm^{-1} , in very well agreement with the experimental values (Fig. 4.4, red symbols and lines).

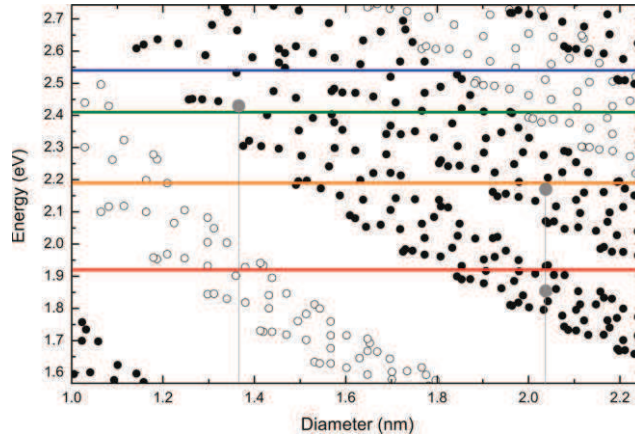


Figure 4.6: Normalized Kataura plot: open (black) symbols, transition energies for metallic (semiconducting) SWNTs; gray symbols, transitions for the (12,8) and (16,14) SWNTs; horizontal lines, laser excitation energies used in this work.

Regarding the resonance conditions, a striking result is the appearance of the two RBLMs at the same excitation energy (Fig. 4.2). To understand it, we use the Kataura plot calculated for SWNTs within a non-orthogonal tight-binding model (NTB) [9] and corrected with a rigid upshift to agree with the transitions measured on the well index-identified free-standing SWNTs. The use of such a Kataura plot is validated by the fact that measurements of the transition energies in DWNTs only display a slight shift with respect to the transition energies in the corresponding SWNTs [10] (tens of meV). The Kataura plot is presented in Figure 4.6 and the transition energies for the third and fourth semiconducting transitions of the corresponding (12,8) and (16,14) SWNTs are denoted by gray dots. It must be pointed out that the diameters of the inner and outer layers (indicated by vertical gray lines in Figure 4.6) are obtained by electron diffraction as discussed previously.

At 2.54 eV, no transition is expected for the two tubes, which explains why no RBLM is detected. At 2.41 eV, the laser energy is very close to the E_{33} transition (2.43 eV) of the (12,8) inner tube. By contrast, no transition is expected at this energy for the (16,14) outer tube. At 2.18 eV, the laser energy is close to the $E_{44} = 2.17$ eV transition energy of the (16,14) outer nanotube.

Finally, at 1.92 eV the difference between the laser and the $E_{33} = 1.85$ eV of the (16,14) is small enough to assume that the outer tube is in incoming resonance at this energy.

The examination of the resonance conditions for the investigated DWNT on the basis of the Kataura plot yields conclusions that disagree with usual behavior observed in SWNT. Indeed, at 2.41 and 1.92 eV excitation energies, only one tube of the DWNT is in resonance though we measure two distinct RBLMs. This result is explained by considering the coupling between the two layers. We state, for the first time at the best of our knowledge, that in presence of the coupling, only the optical resonance of one tube is necessary to observe the response of the coupled system. This effect has already been reported for individual bundles [11] and, it is, for the first time, directly evidenced here in the case of a DWNT.

The second important conclusion of our study is that both coupled RBLMs will be resonantly excited if an electronic transition of either wall matches the excitation energy. However, a relatively small intensity of the mode assigned to the non-resonant layer is systematically found. Taking into account the coupling between the layers is the only way to explain coherently all our results.

It is important to emphasize that the same conclusion was recently confirmed by Liu et al. from Raman experiments performed on individual identified free-standing DWNTs [12].

All these first conclusions regarding the RBLM of the (12,8)@(16,14) DWNT have been confirmed by measuring the Raman spectrum of 11 individual index-identified double-walled carbon nanotubes. The additional information provided from experiments performed on a large number of DWNTs and by using a broad range of excitation energy allows to precise our conclusions.

All structural and vibrational information obtained on these 11 DWNTs are summarized in the Table 4.2. We claim that the effect of mechanical coupling between the walls is general in all these DWNTs. To illustrate this statement, we focus on the Raman spectrum of the (13,9)@(24,7) DWNT (Figure 4.7 and 4.8). The two layers are semiconducting, the diameter of the inner tube is $d_{in} = 1.5$ nm, and its chiral angle $\theta_1 = 12^\circ$ (from ED, $d_{in} = 1.44 \pm 0.15$ nm and $\theta_1 = 12.4^\circ$), the diameter of the outer tube is $d_{out} = 2.2$ nm and its chiral angle $\theta_2 = 24^\circ$ (from ED, $d_{out} = 2.1 \pm 0.15$ nm and $\theta_2 = 23.9^\circ$). The interlayer distance equals 0.355 nm which indicates the possibility of the mechanical coupling in the system.

The RBLM and G-modes regions of the Raman spectra measured at different incident excitations (458, 488, 514, 530, 568, 633, 647, 676 nm and in IR (710-900 nm) range) are shown

in Fig. 4.7a. Fig. 4.8 details the RBLM region of Raman spectrum excited at 647 nm. The in-phase and out-of-phase RBLM are located at 123 and 169 cm^{-1} respectively.

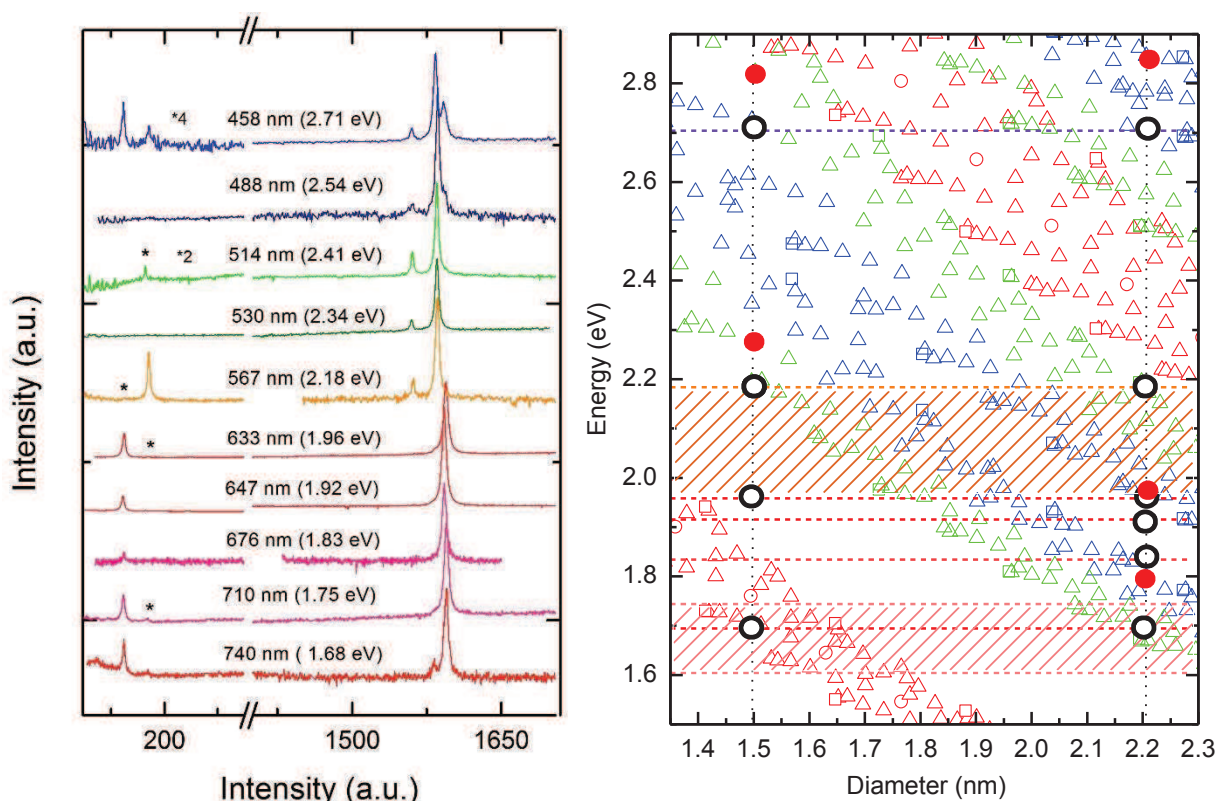


Fig. 4.7: (a) The RBLM and G-modes regions of the Raman spectrum of (13,9)@(24,7) DWNT measured at a wide variety of excitation wavelengths from blue (458 nm) to IR (740 nm). (b) Kataura plot: the optical transitions of (13,9) and (24,7) single-walled nanotubes are indicated by red filled dots. Open circles refer to the excitation energies for which RBLMs were observed in (13,9)@(24,7) DWNT. Red, blue and green open symbols at the background correspond to metallic, semiconducting type 1 and semiconducting type 2 SWNTs respectively.

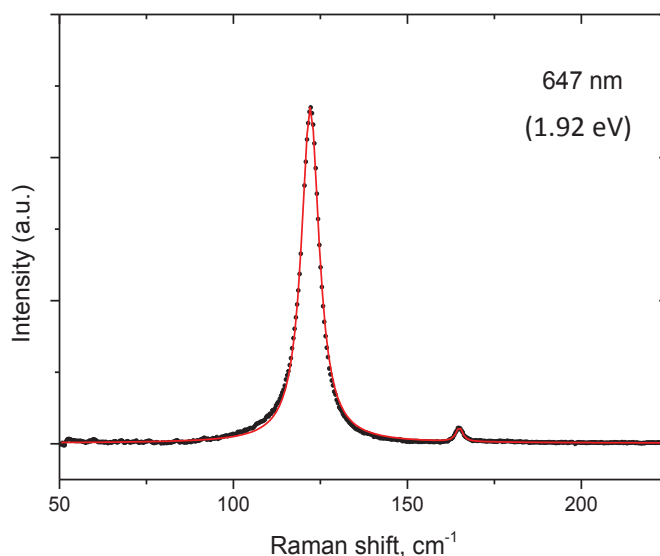


Fig. 4.8: The RBLM region of the Raman spectrum of (13,9)@(24,7) DWNT measured at 647 nm.

We compare the Raman frequencies of the RBLMs to the predictions of the theoretical model described previously (Fig. 4.4). Our model gives 127 and 170 cm^{-1} for the in-phase and out-of-phase RBLM respectively, in relative good agreement with the experimental data, proving the presence of the interaction between the layers in the (13,9)@(24,7) DWNT.

Regarding the resonance conditions of RBLMs: in Fig. 4.7 b, we highlight by red filled dots the optical transitions expected for the (13,9) and (24,7) single-walled carbon nanotubes. The observed transitions in the corresponding double-walled tubes are shown by white open circles. On the contrary to the previous (12,8)@(16,14) DWNT, to explain these results, we have to consider a downshift of the electronic energies by about 100 meV in comparison with those of the related SWNTs. We stress that this is due to the interlayer interaction inside the tube as was observed in Ref. 13.

According to Fig. 4.7b, there are two different situations. First of all, at 458 nm we clearly observe two radial-breathing like modes (Fig. 4.7a). At this excitation energy (the blue line at the top part of the Fig. 4.7b), the “rigidly downshifted Kataura” plot predicts that both inner and outer layers are in resonance with the incident radiation.

Secondly, at 633, 647 and 710 nm laser wavelengths, the outer layer is in resonance, while the optical transitions in the inner tube are forbidden. Nevertheless, as clearly seen in the Fig. 4.8, the two RBLMs are present in the same spectrum. The resonance conditions are interchanged at 568 nm. It is now the inner layer in resonance and the outer not, but we still see the two RBLMs (the RBLM of the outer tube is indicated by the star in the Fig. 4.7a). This observation again confirms our statement that the optical resonance of only one tube is necessary to observe the response of the coupled system.

Summary

In the first part of Chapter 4 we have presented the study of the low-frequency part of Raman spectrum of double-walled carbon nanotubes. As an example, we focused on the (12,8)@(16,14) DWNT. The unambiguous evidence of mechanical coupling between the walls was observed for the first time on this DWNT [2]. We showed that Van-der-Waals coupling between the walls lead to collective radial breathing-like modes (RBLM). The dependencies of these RBLMs as a function of diameter and inter-wall distance as well as the resonance conditions of these modes were discussed.

For instance, we have shown that all $\omega_{\text{RBM}}(d)$ relations established for individual SWNTs do not work when deriving diameters of the inner and outer tubes of a DWNT from the higher- and lower-frequency RBLMs respectively. Furthermore, we have evidenced that both coupled RBLMs are resonantly excited if an electronic transition of either wall matches the excitation energy. However, a relatively small intensity of the mode assigned to the non-resonant layer is systematically found.

In that way, we concluded that taking into account the coupling between the layers of DWNT is the only way to explain coherently the behavior of low-frequency part of its Raman spectrum.

Table 4.2. Structural and vibrational information on the DWNTs studied in this work.

#	Indices	Real diameter, nm	Real angles, Degrees	Type	ΔD , nm	RBLMs Observed, cm^{-1}	Popov calc. (DWNTs) , cm^{-1}		G-band frequencies, cm^{-1}
							204/d+27	228/d	
1	(13,9)@(24,7)	1.5@2.21	24.01@12.43	2@1	0.71	123, 169	127, 170	114, 168	1560, 1584, 1592
2	(16,8)@(22,11)	1.66@2.28	19.11@19.11	1@1	0.62	88.5, 127, 169.5	123, 164	110, 163	1561, 1585, 1593
3	(18,2)@(20,12)	1.49@2.19	5.21@21.79	2@1	0.7	124, 167	128, 171	114, 170	1550,1569, 1578, 1587, 1590
4	(22,11)@(27,17)	2.28@3.01	19.11@22.52	1@2	0.73	98, 121	{96, 134 95, 116}	84, 130	1562, 1583, 1592
5	(14,11)@(27,6)	1.7@2.39	26.04@9.83	0@0	0.68	110, 153	119, 158	105, 156	1573, 1590
6	(12,8)@(16,14)	1.37@2.04	23.41@27.8	2@1	0.67	133, 186	136, 186	123, 185	1564.5, 1570, 1590
7	(21,4)@(20,16)	1.82@2.45	8.57@26.33	1@2	0.63	111, 153, 223,	116, 154	103, 152	1567, 1580, 1591
	(20,4)@(20,16)	1.74@2.45	8.95@26.33	2@2	0.7	390, 437	116, 154	103, 152	
8	(22,5)@(28,9)	1.95@2.62	10.02@13.49	1@2	0.67	96, 110, 142, 152, 229, 304, 335	109, 146	96, 144	1582, 1589
9	(34,10)@(47,3)	3.13@3.8	12.52@3.07	0@1	0.68	119	77, 120	66, 115	1572, 1590
	(38,11)@(52,3)	3.49@4.2	12.35@2.78	0@2	0.71		71, 116	59, 110	
10	(61,13)@(55,33)	5.36@6.03	9.47@21.79	0@2	0.67	-	52, 106	40, 100	1578,1587
	(62,13)@(55,34)	5.44@6.09	9.33@22.24	2@0	0.66		52, 106	39, 100	
11	(37,9)@(45,11)	3.31@4.03	10.64@10.68	2@2	0.72	-	-	-	1578, 1584
	(41,10)@(49,12)	3.67@4.38	10.66@10.70	2@2	0.72				
12	(56,31)@(58,41)	5.98@6.75	20.58@24.34	2@1	0.77	-	-	-	1548, 1603
	(57,31)@(58,41)	6.06@6.75	20.32@24.34	1@1	0.69				
13	(39,23)@(38,35)	4.25@4.95	21.53@28.64	2@0	0.7	90, 108	-	-	1565.5, 1584.5 1586, 1590.5
	(44,26)@(42,39)	4.8@5.5	21.56@28.78	0@0	0.7				

4.1.3 Discussion and comparison with other experimental and theoretical studies.

Quantum-coupled RBLM in DWNT

Recently, Liu et al. [12] performed the study of coupled RBLM vibrations in DWNTs by combination of Raman spectroscopy, Rayleigh scattering and Electron diffraction. Overall, they confirmed our observations of mechanical coupling on the basis of their 13 individual DWNTs (see Table 4.3 for information). Their tubes were also synthesized by CVD method and have diameters similar to ours. It is important to emphasize that the separation between the inner- and outer-tubes varies from 0.34 to 0.37 nm in their as-grown DWNTs, in other words the inter-tube distance is equal or larger than 0.34 nm. Figures 4.9 b,c confirm that the in-phase and out-phase RBLM frequencies of their DWNTs display an upshift in comparison with RBM frequencies of the related individual single-walled carbon nanotubes.

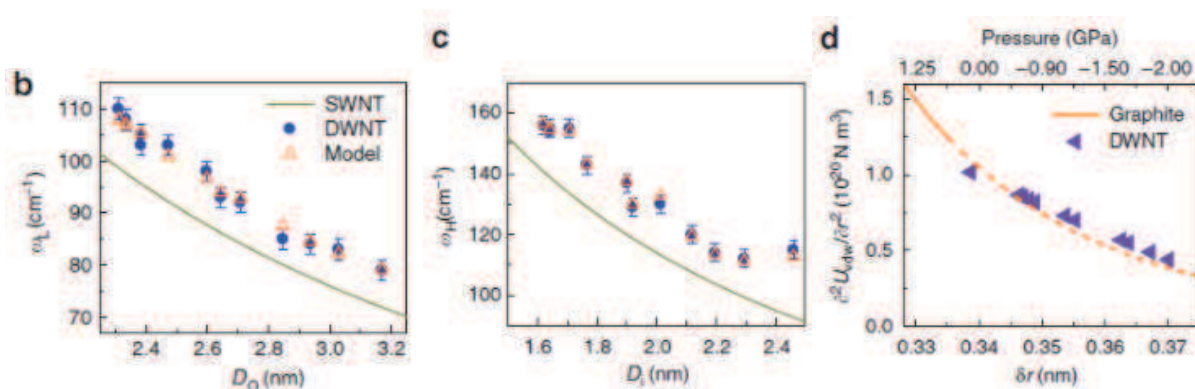


Figure 4.9: Coupled mechanical oscillations in double-walled carbon nanotubes. Adapted from [12].

Using the model of two coupled harmonic oscillators, Liu et al. calculated the tube-dependent k_c (force constant corresponding to van der Waals interaction) and showed how this interaction varies with the separation between the inner- and outer-wall tubes. The unit-length coupling force constant k_c was expressed approximately using the average unit-area inter-tube van der Waals potential U_{vdw} with $k_c = (\partial^2 U_{vdw} / \partial r^2) \cdot \pi \bar{d}$, where the mean diameter $\bar{d} = (d_i + d_o) / 2$. Figure 4.9d displays the data for unit-area force constant $(\partial^2 U_{vdw} / \partial r^2)$, which changes by over two times over the range of inter-tube separation existing in their DWNTs. These results were compared with the van der Waals interaction between unit-area graphene sheets under pressure obtained from compressibility measurements of graphite (solid line) and theoretical extrapolation in the negative pressure range (dashed line), and a good agreement was found. This comparison showed that the “negative” effective pressure between the walls of as-grown DWNTs reaches

gigapascals owing to variations in the tube–tube separation.

On the other hand, using data of Rayleigh scattering, Liu et al. managed to better explain the resonance phenomena in DWNTs. They proved that indeed the collective DWNT oscillations ω_L and ω_H contain both inner- and outer-wall motion, and they couple simultaneously to electronic transitions in both walls (Fig. 4.10b) unlike separated inner- and outer-SWNTs RBM excitations (illustrated in Fig. 4.10a). They thus came to our early assumption namely that both coupled RBM oscillations are resonantly excited if an electronic transition of either wall matches the excitation photon energy.

Liu et al. also studied the Raman quantum interference. It was shown that quantum interference depends sensitively on the chirality of the inner- and outer-SWNTs. Its value is related to the relative motion direction of the inner- and outer-wall nanotubes immediately after the optical excitation. A physical picture of this process in outer- and inner-SWNTs is provided by recalling Frank–Condon effects (Fig. 4.10e): the excited state has a displaced potential energy surface compared with that of the ground state. The displacement is extremely small (\sim fm), but is essential for the exciton–phonon coupling. Upon optical excitation, the SWNT lattice, initially at the ground-state equilibrium configuration, relaxes based on the excited-state potential energy surface and sets of the RBM vibration.

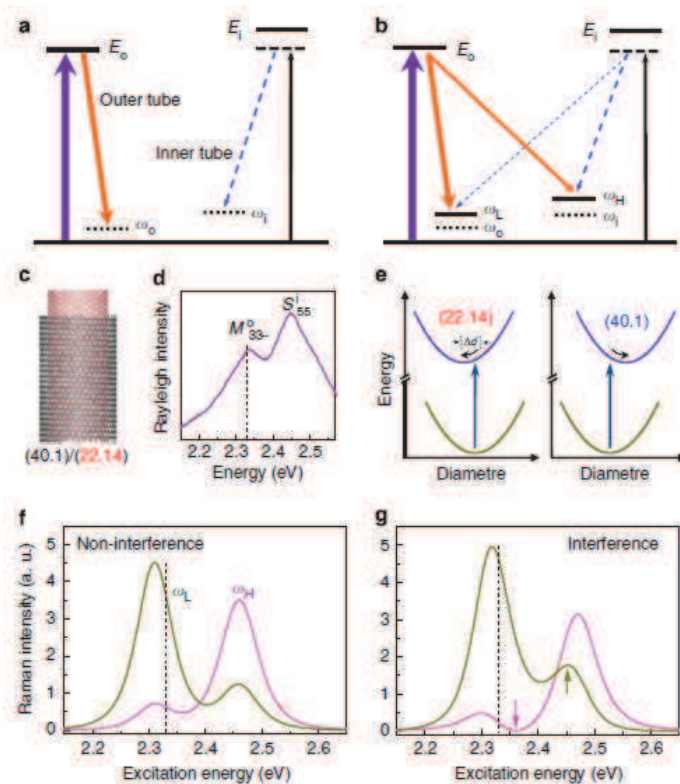


Figure 4.10: Quantum interference in resonance Raman process in double-walled carbon nanotubes (from [12]).

They further plotted the calculated RBLM Raman intensity of the (40,1)@(22,14) DWNT at different excitation energies without (Fig. 4.10f) and with the quantum interference (Fig. 4.10g), which displays the variation of quantum interference effects with the excitation laser energy. They showed that the relative displacement of the excited-state potential energy surface varies with the nanotube chirality, and it can be described by a simple family pattern: the excited-state potential energy surface is displaced inwards for transitions on one side of the zig-zag cut through K point of the graphene Brillouin zone, which includes even transitions of $\text{mod}(n-m,3) \text{ mod } 1$ semiconducting, odd transitions of $\text{mod}(n-m,3) \text{ mod } 2$ semiconducting and higher branch transitions of non-armchair metallic nanotubes. The displacement is outwards for all other transitions.

Finally, we note that there also exist some discrepancies between our work and that of Liu et al.:

About the relation between the RBLM frequency and the diameter of the tubes

As in the case of individual single-walled carbon nanotubes, we find that the relation $\omega_{\text{RBLM}} = 204/d + 27$ is more adapted than the $228/d$ relation to describe the RBLM of the uncoupled outer tube (see Fig. 4.4 and Tables 4.1 and 4.2).

More interesting is that in both studies an upshift of the RBLM with respect to the corresponding RBM is found although, in the majority of our samples, the inter-tubes distance is around 0.34 nm and, while in the work of Liu et al., it is predominantly larger than 0.34 nm.

About the resonance conditions.

In agreement with our conclusions, Liu et al. also claim that RBLM oscillations are resonantly excited if an electronic transition of either wall matches the excitation photon energy. However, they claim that the RBLM are mostly either not observable (in 21 tubes) or appearing in pairs (in 13 tubes) in resonant Raman scattering spectra of DWNTs. The use of a broad excitation range (by contrast to Liu et al. who performed experiments only at two excitation energies) allows to show that either pairs of RBLMs or just single RBLM may appear in an investigated DWNT depending of the excitation energy.

To illustrate this latter statement, we compare the low-frequency part of Raman spectra of two individual DWNTs: the (13,9)@(24,7) (Fig. 4.11a) and the (22,11)@(27,17) (Fig. 4.11b).

The spectra of the (13,9)@(24,7) DWNT were measured with incident excitations in the 567-633 nm range with step of 3-5 nm (not all spectra are reported in the Figure 4.11a, see also Fig. 4.7a and 4.8 for measurements at other excitation energies). The inner layer is in resonance with incident radiation around 569.5 nm. The RBLM range of the spectrum of the (13,9)@(24,7) DWNT, excited at 569.5 nm, is detailed in Fig. 4.12a. It is clear that the intensity of the in-phase RBLM is too weak (ratio of intensity of low-frequency in-phase to high-frequency counter-phase mode $(I_L/I_H)_{\text{exp}} = 0.03$), that it may be barely seen in other incident wavelengths in the 567-600 nm range. In the spectrum excited at 647 nm (Fig. 4.8 and 4.12b), the situation is completely inverted with the outer tube in resonance leading to a strong in-phase RBLM and a weak out-of-phase RBLM.

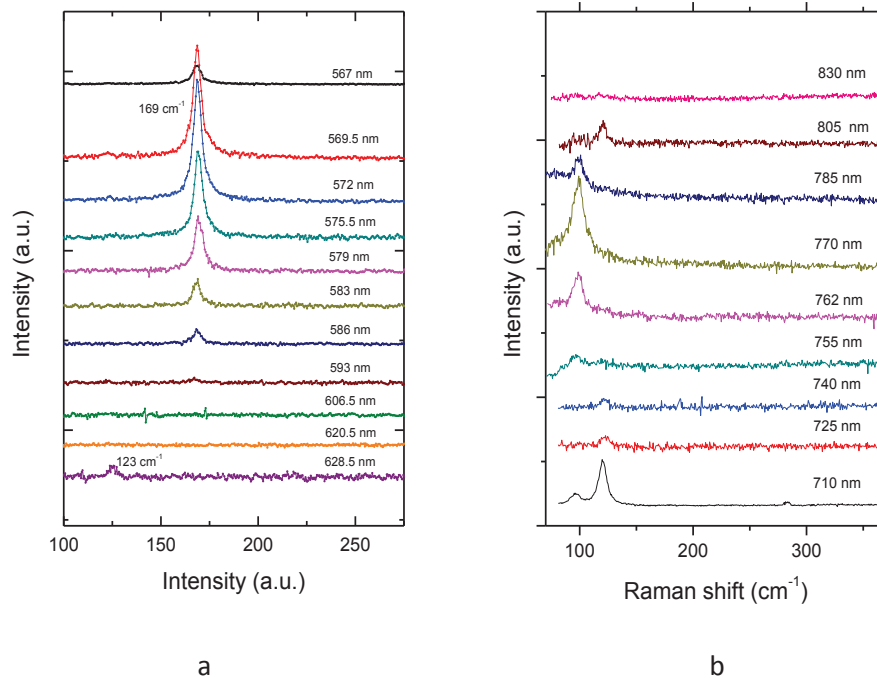


Fig. 4.11: (a) Low-frequency region of Raman spectra of (13,9)@(24,7) DWNT; (b) Low-frequency region of Raman spectra of (22,11)@(27,17) DWNT;

The example of the (13,9)@(24,7) DWNT may still count as the appearance of a pair of RBLMs but with a very low $(I_L/I_H)_{\text{exp}}$ ratio (Raman spectrum excited at 569.5nm) or a very low $(I_H/I_L)_{\text{exp}}$ (Raman spectrum excited at 647 nm). In their work Liu et al. showed a DWNT with $(I_L/I_H)_{\text{exp}} = 0.08$ that is close to the situation reported in this DWNT in the Raman spectrum excited at 569.5nm.

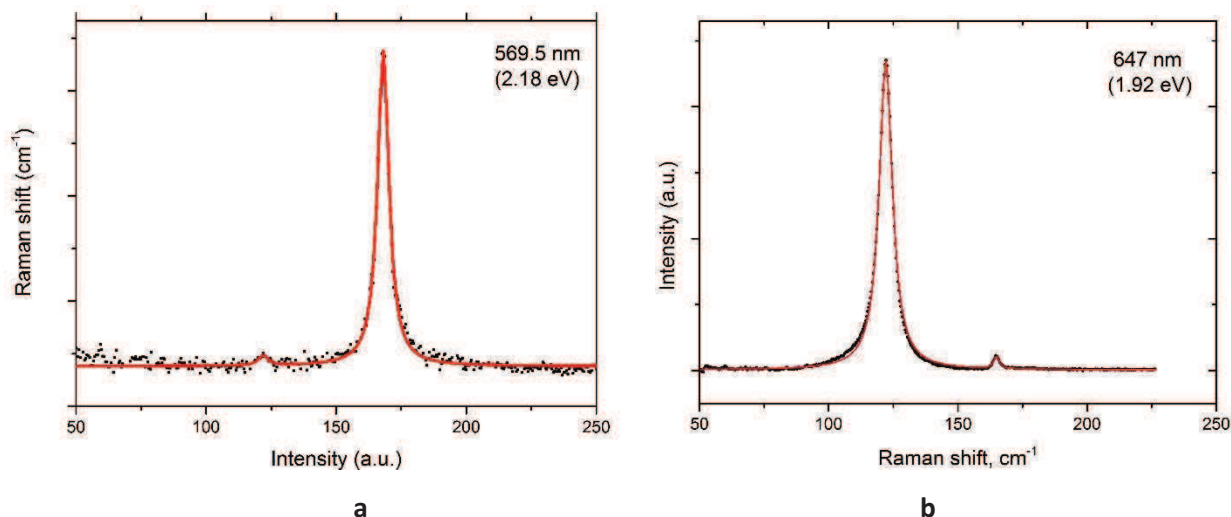


Fig. 4.12: (a) RBLM range of the Raman spectrum of the (13,9)@(24,7) carbon nanotube excited at 569.5 (b) RBLM range of the Raman spectrum of the (13,9)@(24,7) DWNT excited at 647 nm.

Fig. 4.11b presents the low-frequency spectra of the (22,11)@(27,17) DWNT. As it is clearly seen, the inner layer is close to the resonance at 710 nm, while the resonance of the outer is maximum around 770 nm. These two situations are detailed in Fig. 4.13a and b. Contrary to the tube (13,9)@(24,7), we don't see the second layer at all in the spectrum excited at 770 nm. The same result is found in several DWNTs.

Unfortunately, in the absence of other optical data like Rayleigh scattering or optical absorption of these DWNTs, we cannot say definitely whether the quantum destructive interference is at the origin of the non-observation of the out-of-phase RBLMs.

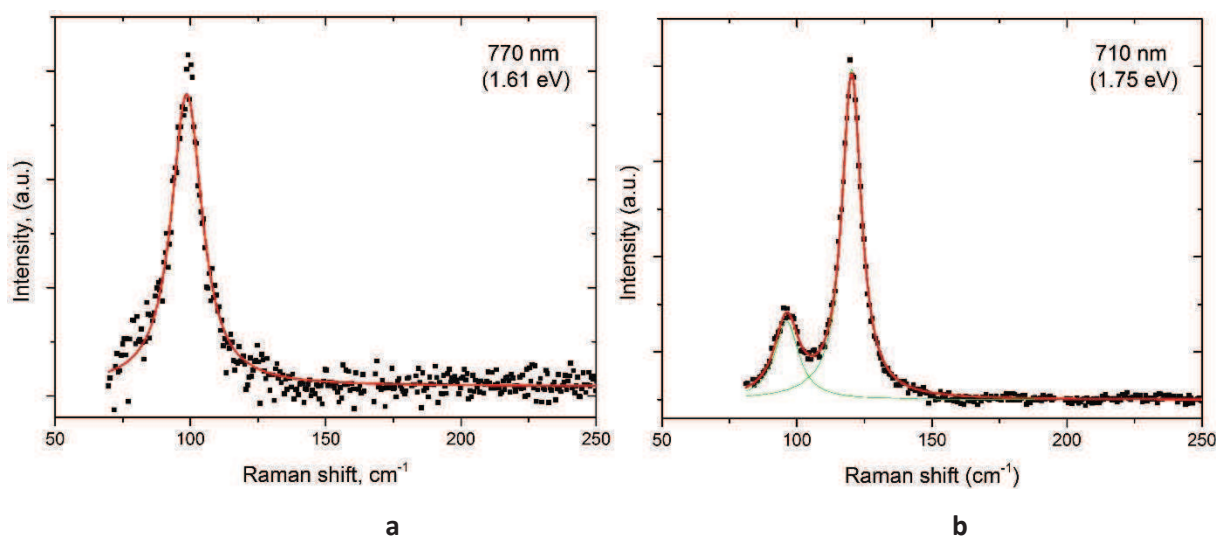


Fig. 4.13: RBLM range of the Raman spectrum of the (22,11)@(27,17) DWNT measured at (a) 770 nm and (b) 710 nm.

The 2D continuous membrane theory.

Recently Rochal et al. [14] analyzed the low-frequency spectrum of double-walled carbon nanotubes in the framework of the 2D continuous membrane theory. A theoretical background of this work was given in the Chapter 1. Here we will present only its main points and then apply the theory to the case of our DWNTs:

Simple analytical expression for radial breathing-like vibrations of DWNTs

The application of the 2D continuous membrane theory to the case of DWNTs leads to the following expression (see Chapter 1):

$$\left(\frac{d_i}{2}(\omega_{i,SWNT}^2 - \omega^2) + G'\right) \cdot \left(\frac{d_o}{2}(\omega_{o,SWNT}^2 - \omega^2) + G'\right) - G'^2 = 0 \quad (4.1)$$

where $d_i(d_o)$ is the diameter of inner(outer) layer respectively, $\omega_{i,SWNT}$ ($\omega_{o,SWNT}$) are the RBM frequencies of the inner(outer) layer in the absence of interaction, $G'(d_i, d_o)$ is a coupling constant, having the sense of coupling force per unit mass.

A-priori the coupling constant G' is not known, but given enough experimental data, we may determine its form. In that way, Rochal at al. fitted the experimental data of Liu et al. [12] and found the (d_i, d_o) dependence of the coupling constant G' :

$$G'(d_o, d_i) = [A + B(d_o - d_i) + C(d_o + d_i)] \cdot (d_o + d_i) \quad (4.2)$$

where $A= 7210$, $B = -9670$ ¹ and $C = 61$.

The result of this analysis is shown in Table 4.3 (for the analysis and the fit of our experimental data, refer to the next subsection and Table 4.4). The standard deviation between Rochal's theoretical model and the experimental data of Liu et al. is 1.31 cm^{-1} , which is better than in the model proposed by Liu et al. [12] (see last four columns of the Table 4.3).

Table 4.3. Comparison between the experimental data and theoretical model of the Ref [12] and the results of 2D continuous membrane theory (the last two columns).

#	(n,m) indices	d_i , nm	d_o , nm	ω_L^{exp} , cm^{-1}	ω_H^{exp} , cm^{-1}	ω_L^{Liu} , cm^{-1}	ω_H^{Liu} , cm^{-1}	ω_L^{Rochal} , cm^{-1}	ω_H^{Rochal} , cm^{-1}
1	(22,14)@(40,1)	2.46	3.17	79	115	78.7	113.0	78.9	114.8
2	(15,13)@(31,4)	1.90	2.60	98	137	95.9	137.2	95.9	137.2
3	(18,5)@(27,5)	1.64	2.33	108	155	106.9	155.4	106.7	154.9
4	(23,10)@(32,11)	2.30	3.03	83	112	81.5	112.6	81.6	113.0
5	(27,2)@(26,17)	2.20	2.94	84	114	83.2	113.9	83.1	113.6
6	(26,2)@(21,21)	2.12	2.85	85	120	86.4	119.8	86.3	119.5
7	(24,1)@(20,19)	1.92	2.64	93	129	93.5	131.8	93.3	131.2
8	(19,3)@(19,15)	1.62	2.31	110	156	107.7	156.9	107.6	156.4
9	(20,9)@(27,12)	2.01	2.71	93	133	92.2	131.8	92.2	132.1
10	(14,12)@(23,13)	1.76	2.47	103	143	100.1	143.3	99.9	142.6
11	(15,10)@(27,6)	1.71	2.38	103	154	105.6	154.5	105.6	154.6
12	(15,10)@(27,6)	1.71	2.38	105	155	105.6	154.5	105.6	154.6
13	(18,5)@(27,5)	1.64	2.33	108	154	106.0	155.4	106.7	154.9

To summarize, the 2D continuous membrane theory appeared to be an effective tool for the analysis of radial vibrations of DWNTs and may offer some insight into the behavior of RBLMs.

On the character of the coupled vibrations

Rochal argues that the in-phase and out-of-phase description of RBLMs of DWNTs may only be correct when the coupled harmonic oscillators have equal masses. In a DWNT however this is not true as the two layers have different diameters and hence masses (see Fig. 4.14 bottom part). He then proposes the terms ‘co-directional’ and ‘counter-directional’ modes. Moreover, by analyzing amplitudes of radial vibrations of DWNTs he comes to the following conclusion:

The co-directional motion has the dominant contribution of the outer wall plus small component of the inner layer. The counter-directional motion has the dominant contribution of the inner wall plus small component of the outer layer. We illustrated this behavior in the Fig. 4.14.

Note that in the approach of Popov and Henrard [6] this situation corresponds to the small coupling regime, which is dominant for outer tube diameter smaller than 2 nm.

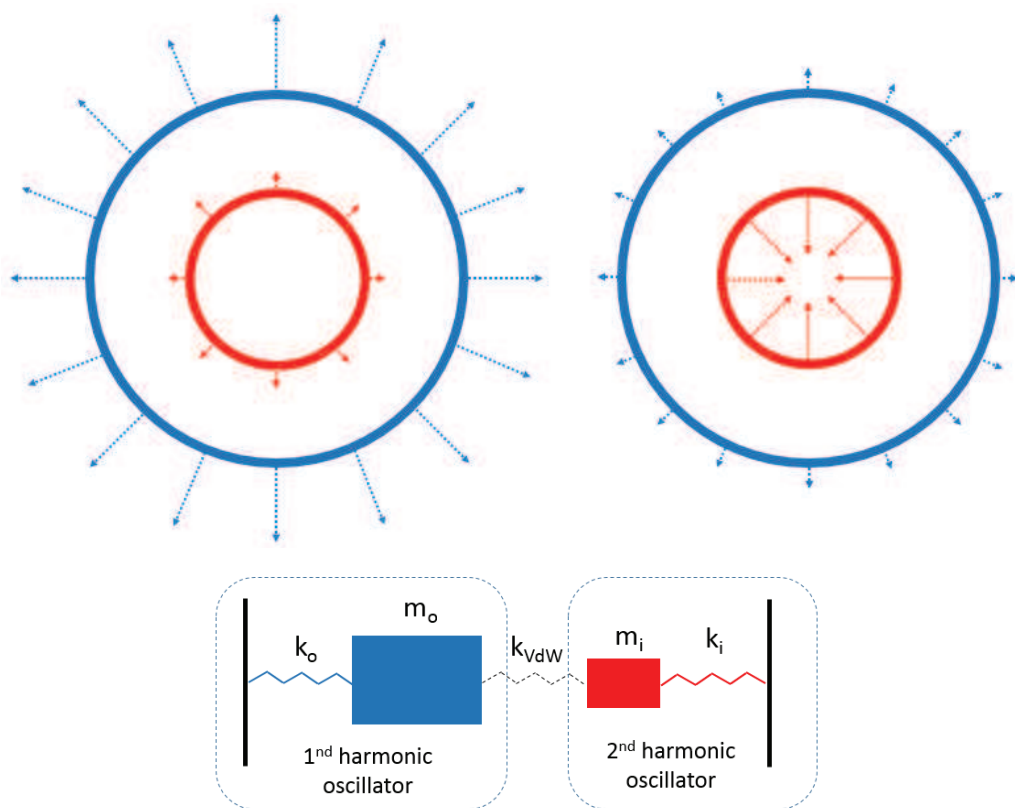


Fig. 4.14: Co-directional (low-frequency) and counter-directional (high-frequency) radial breathing-like modes of DWNTs. The co-directional motion has the dominant contribution of the outer wall plus small component of the inner. The counter-directional motion has the dominant contribution of the inner and small component of the outer wall.

On the radial vibrations of DWNTs.

In Chapter 3 we considered radial breathing vibrations of SWNTs and argued on the possible origin of the deviation of experimental $\omega_{\text{RBM}}(d)$ relations from theoretical ones. We said that the combined environmental effects such as the adsorbed species (amorphous carbon) and the ‘trapping’ potential may be the major ingredients to explain the frequency deviations. We are now able to test some of these assumptions by analyzing RBLMs of DWNTs. Let us assume (maybe erroneously) that the environmental interaction is due to the amorphous carbon (general assumption in the literature). Then the interaction between the environment and the nanotube leads to an experimental relation $\omega = 204/d+27$ (or equivalently $\omega = (227/d) \sqrt{1 + 0.065d^2}$), while ideal nanotube has $\omega_{\text{RBM}} = 228/d$.

In that way, a double-walled nanotube is appeared to be a perfect model system for our studies. It is common to say that the inner layer of a DWNT is clean and protected from the environment by the outer tube (and hence the inner follows the relation $228/d$). While the outer layer is assumed to be always dirty (following $204/d+27$ relation). This fact was reflected in the discrete model of Popov et al. [6], used in Section 4.1.1 to simulate RBLM frequencies of (12,8)@(16,14) DWNT.

To get insight into the origin of experimental $\omega_{\text{RBLM}}(d)$ relation in DWNTs we present the comparison of 3 theoretical models:

Model 1: Discrete model of Popov et al. (the details are given in ref [6]).

This model assumes that the inner tube is clean and thus follows $\omega = 228/d$ relation, while the outer tube is covered by amorphous carbon and in consequence follows a $\omega = 204/d+27$ law.

Model 2: Continuous approach. 2D continuous membrane theory with inner tube following $\omega = 228/d$ and the outer one following $\omega = 204/d+27$ relations (in analogy with model 1):

$$\left\{ \begin{array}{l} \left(\frac{d_i}{2} (\omega_{i,SWNT}^2 - \omega^2) + G' \right) \cdot \left(\frac{d_o}{2} (\omega_{o,SWNT}^2 - 1.25\omega^2) + G' \right) - G'^2 = 0 \\ \omega_{i,SWNT} = \frac{228}{d_i} \\ \omega_{o,SWNT} = \frac{204}{d_o} + 27 \end{array} \right. \quad (4.3)$$

To obtain equation (4.3) for model 2 we modified the 2D continuous membrane theory by supposing different effective mass densities of the layers of DWNTs. In Chapter 3 the difference between the clean ‘ideal’ tube and those with adsorbed AC was estimated to be 10-25%. We take the maximum value and thus assume $\rho_{\text{out}} = 1.25\rho_{\text{in}}$ (the mass density of the ‘dirty’ outer layer in comparison with the ‘clean’ inner). This fact is represented in the first formula of eq. (4.3).

Model 3: Continuous approach. 2D continuous membrane theory with inner and outer tubes both following $\omega = 204/d+27$ relation (both layers are ‘dirty’).

$$\left\{ \begin{array}{l} \left(\frac{d_i}{2} (\omega_{i,SWNT}^2 - \omega^2) + G' \right) \cdot \left(\frac{d_o}{2} (\omega_{o,SWNT}^2 - \omega^2) + G' \right) - G'^2 = 0 \\ \omega_{i,SWNT} = \frac{204}{d_i} + 27 \\ \omega_{o,SWNT} = \frac{204}{d_o} + 27 \end{array} \right. \quad (4.4)$$

In our work seven of eleven individual DWNTs had both RBLMs observed in the Raman spectra. By using the diameters of these nanotubes in the above models, we have calculated the

deviation between the theoretical and experimental frequencies $\Delta\omega_{L/H}^i = \omega_{L/H}^i - \omega_{L/H}^{exp}$. Table 4.4 shows the results of this analysis.

$\Delta\omega_i^{(1)}$, $\Delta\omega_i^{(2)}$, $\Delta\omega_i^{(3)}$ correspond to the deviation according to the 1st, 2nd and 3rd models respectively.

Table 4.4. Comparison between three theoretical models (see text) and experimental data. The diameters d are given in nm and frequencies ω in cm^{-1} .

#	(n,m) indices	d_i	d_o	ω_L^{exp}	ω_H^{exp}	$\Delta\omega_L^{(1)}$	$\Delta\omega_H^{(1)}$	$\Delta\omega_L^{(2)}$	$\Delta\omega_H^{(2)}$	$\Delta\omega_L^{(3)}$	$\Delta\omega_H^{(3)}$
1	(12,8)@(16,14)	1.37	2.04	133	186	3	0	4.1	3.7	-0.26	0.5
2	(13,9)@(24,7)	1.5	2.21	123	169	4	1	3.6	4.4	-0.3	0.5
3	(14,7)@(20,10)	1.45	2.07	127	170	-7	12	3.5	5.8	-0.2	0.3
4	(18,2)@(20,12)	1.49	2.19	122	167	6	4	3.3	5.6	-0.3	0.4
5	(22,11)@(27,17)	2.28	3.01	98	121	-2	13	4.2	-1.2	0.1	-0.2
6	(23,5)@(22,17)	2.03	2.65	113	154	-5	-9	5.8	-5.6	0.1	-1.3
7	(21,4)@(20,16)	1.82	2.45	111.5	154	4.5	0	4.3	4.2	-1.4	5.4

Surprisingly, model 1 (discrete theory) and model 2, that assumed clean and free of defects inner layers, show the biggest deviation from our experimental data. On the contrary, in the model 3, deviation was less than 0.5 cm^{-1} for some of the nanotubes. This means that both layers of a DWNT seem to be affected in the same way by the environment (independent of its exact nature).

Experimental data on the RBLMs of DWNT provide a unique possibility to compare different theories. We state that our experimental data are well described best by the 2D continuous membrane theory (model 3).

4.2 G-modes of DWNTs

Although the double-walled carbon nanotubes have been studied for more than one decade, the behavior of their high-frequency G-modes is still not completely clear. This was mainly due to the absence of experimental data on individual DWNTs. The macroscopic samples of double-walled tubes used for the studies so far gave only average information on the G-modes of ensemble of tubes. Measurements on index-identified individual nanotubes provide the unique possibility to study G-modes of DWNT in detail.

We remind that in chiral SWNT, two G-modes are Raman active in // // polarized spectrum, the so-called G- and G+ component. In metallic (semiconducting) SWNT, G- is assigned to LO (TO) mode and the G+ component is assigned to TO (LO) mode. For achiral tube, a single G-mode is active; the LO mode in zigzag SWNT and the TO mode in armchair SWNT. On the other hand, the line shape of the G-mode differs depending of the metallic or semiconducting character of the nanotube. For semiconducting SWNT, the line shape of LO and TO mode is narrow and symmetric. By contrast, in metallic SWNT, the line shape of LO mode is broad and asymmetric and the profile of the TO mode is narrow and symmetric.

We performed the analysis of the high-frequency part of Raman spectra of 11 individual DWNTs and tried to deduce some of general features. The results will be presented in two parts: in part (a), the behavior of G-modes in SC@SC DWNTs is detailed, and in part (b) the behavior of DWNTs containing metallic components (SC@M, M@SC or M@M) is briefly reported. In the last part we focus on the extreme sensitivity of metallic DWNTs on the environmental conditions, including the power impinging the sample.

4.2.1 Semiconducting@Semiconducting DWNTs (SC@SC).

In all the spectra measured on SC@SC DWNTs, the line shape of all the modes of the G-band range is narrow and symmetric (as expected from the SWNT results). By analyzing the high-frequency part of Raman spectra of SC@SC DWNTs we found two distinct behaviors of G-modes:

-Behavior 1: A clear shift of the G-mode frequencies of constituent layers in comparison with those of related individual single-walled nanotubes.

-Behavior 2: The spectrum of DWNT was just a simple sum of G-mode of corresponding SWNTs.

We now present and discuss these two behaviors in more details.

Behavior 1: The G-modes of DWNTs are shifted in comparison with G-modes of related SWNTs

Fig. 4.15 shows the G-band of the (13,9)@(24,7) DWNT measured at 458, 488, 514, 530, 567, 633, 647, 676, 710 and 740 nm. Such a wide variety of excitation wavelengths allowed us to

separate for the first time the response of the inner and outer layers of a DWNT. Fig. 4.16 illustrates this observation.

At 458 nm, both (13,9) and (24,7) nanotubes are in resonance with the incident radiation (see Fig. 4.15b, keep in mind that we need to downshift theoretical optical transitions of corresponding SWNTs by 100 meV). By fitting the spectra shown at Fig. 4.16 (center) with 3 Lorentzians we obtain the following frequencies: 1560, 1584 and 1592 cm^{-1} . At 514 nm, we observe only the response of the inner layer. The fit gives 1560 and 1584 cm^{-1} for the G-(TO) and G+(LO) components respectively (Fig. 4.16, top part). On the other hand, at 647 nm we observe a dominant component at 1592 cm^{-1} assigned to the G+(LO) mode of the outer layer (Fig. 4.16, bottom part).

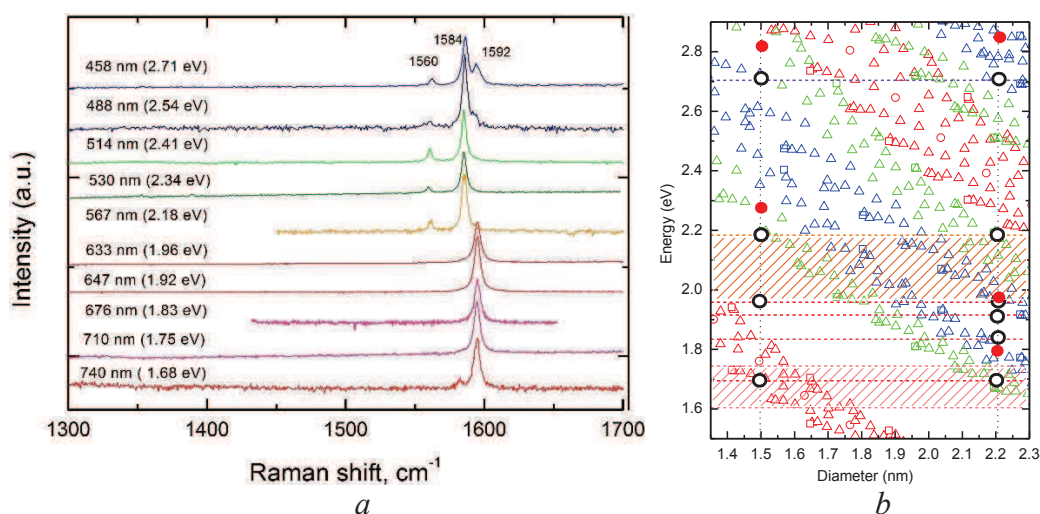


Fig. 4.15: G-band of the (13,9)@(24,7) DWNT measured at 10 excitation wavelengths: 458, 488, 514, 530, 567, 633, 647, 676, 710 and 740 nm.

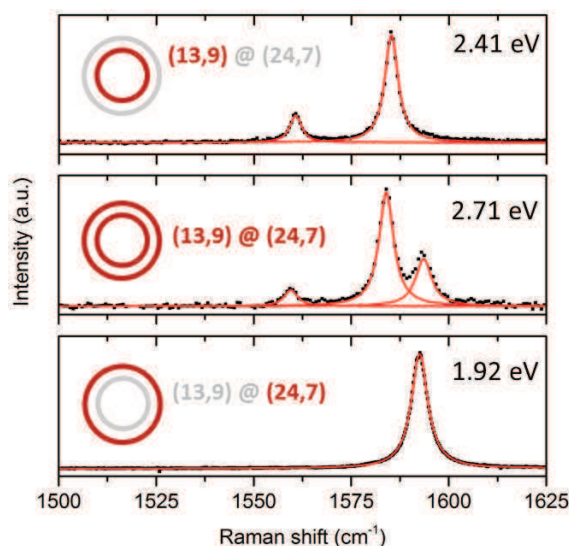


Fig. 4.16: A zoom of the G band of the (13,9)@(24,7) DWNT at 2.71 eV (458 nm), 2.41 eV (514 nm) and 1.92 eV (647 nm) showing the response of two layers simultaneously (in the center), of the inner tube (in the top) and of the outer tube (in the bottom). The spectra are fitted with Lorentzians.

Using the well-established diameter dependence of the G-mode frequency of SWNTs (see Chapter 3), we determine the expected frequencies of the individual (13,9) and (24,7) SWNTs: for (13,9) TO = 1569 cm⁻¹ and LO = 1591 cm⁻¹; for (24,7) TO = 1573 cm⁻¹ and LO = 1591 cm⁻¹. Consequently, we may definitely claim that, in (13,9)@(24,7) DWNT, the frequencies of the G modes of the inner layer are significantly shifted in comparison with G-modes of related individual SWNTs.

Behavior 2. G-band of the DWNT is a sum of G-mode of related SWNTs.

To illustrate the second type of behavior we again turn our attention to (12,8)@(16,14) DWNT. Figure 4.17 shows the G band measured on this DWNT at different laser excitation energies.

At 2.54 eV, where no RBLM is observed, a strong G band signal is detected because at this energy the nanotube is in resonance with the outgoing light scattered by the G-modes of the inner tube. The G- component is located around 1564.5 cm⁻¹ and the G+ component around 1590 cm⁻¹.

At 2.41 and 2.18 eV, the G band is composed of three components located at 1590, 1570, and 1564.5 cm⁻¹, the latter being very weak at 2.18 eV. Finally, at 1.92 eV the G⁺ component close to 1590 cm⁻¹ dominates the spectrum with a very small component around 1570 cm⁻¹. With respect to the G modes measured on semiconducting SWNTs, it is reasonable to assign the components at 1570 and 1564.5 cm⁻¹ to the TO modes of the outer and inner tube, respectively, and consider the G⁺ band as a simple superposition of the LO modes of both tubes.

These conclusions are based on the following considerations: (i) In the Figure 4.18 we directly compare the G-mode range of the DWNT with the one of the (12,8) and (15,14) SWNTs. The TO component of the (12,8) SWNT is located at 1563 cm⁻¹ and the TO mode of (15,14) is located around 1570 cm⁻¹. These frequencies are close to the G- components measured on the (12,8)@(16,14) DWNT. On the other hand, the diameter dependence of the TO phonon modes in semiconducting SWNTs is well-described theoretically (see, e.g., ref [15]). For individual SWNT with diameters ≈1.3 and ≈2.0 nm, the TO modes are predicted close to ≈1565 and ≈1573 cm⁻¹ respectively (close to the positions in (12,8)@(16,14) DWNT). (ii) For SWNTs with diameter ≥1.4 nm, the frequency of the LO mode is measured and predicted at about 1590 cm⁻¹, independently of the diameter. This explains why no splitting of the LO bands coming from the inner and the outer tube is observed in the investigated DWNT.

Then, taking the results of SWNTs as a reference, only slight or no significant shifts of the G

modes due to the interaction between the layers is measured in the (12,8)@(16,14) DWNT.

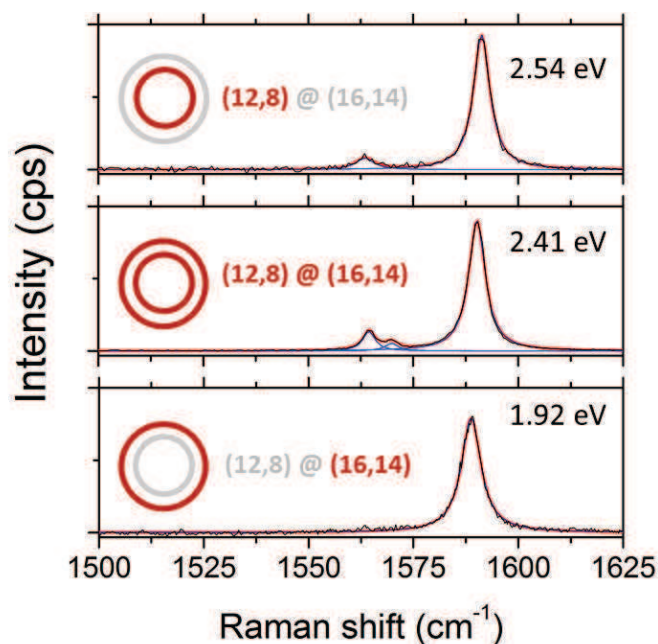


Figure 4.17: G band of the (12,8)@(16,14) DWNT measured at three excitation energies (from top to bottom: 2.54, 2.41 and 1.92 eV). The spectra are fitted with Lorentzians.

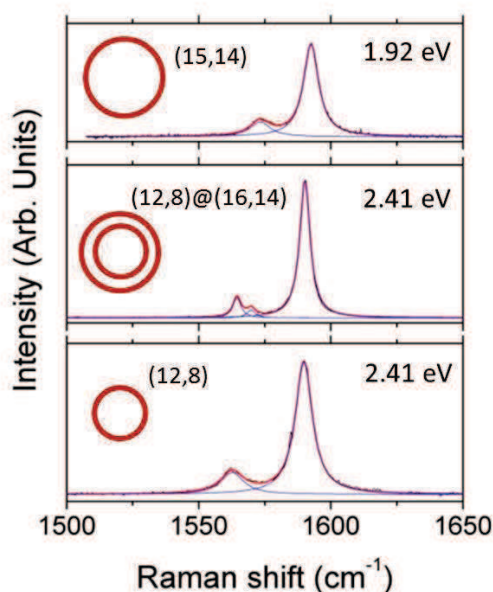


Figure 4.18: G-mode range of the Raman spectrum of (15,14) SWNT (top), (12,8)@(16,14) DWNT (middle) and (12,8) SWNT (bottom).

We propose an explanation of the two distinct behaviors of G-modes of DWNTs. Previously we mentioned that Liu et al. [12] studied the van der Waals interaction in DWNTs. On the basis of 13 double-walled nanotubes they managed to trace the effective pressure between the walls of as-

grown DWNTs as a function of the inter-tube separation. It was found that the negative pressure may reach gigapascals owing to variations in the tube–tube separation (Fig. 4.19).

First, keeping in mind that the inter-wall separation in the (13,9)@(24,7) tube equals 0.355 nm and using the data of Liu et al., we estimated the effective pressure to be around -1.2 GPa (see the blue line in the Fig. 4.19). We now want to find out, how this negative pressure could be at the origin of behavior of the G-modes observed in the (13,9)@(24,7) DWNT.

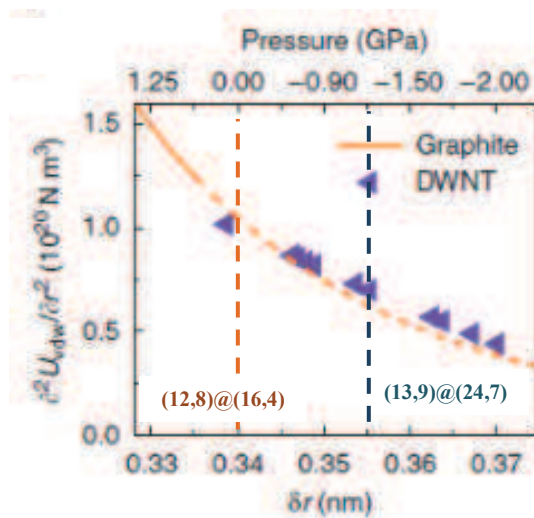


Fig 4.19: Derived unit-area force constant owing to tube–tube van der Waals interaction, ($\partial^2 U_{vdw}/\partial r^2$), for different inter-tube separation (triangles), and the comparison to results from high-pressure graphite measurements (line). The different inter-tube separation in DWNTs corresponds an effective pressure variation from 0.2 to - 2.0 GPa (top label) From [12].

It is well-known that the vibrational modes of carbon nanotubes depend on the hydrostatic pressure. For example, Lebedkin et al. [16] studied the pressure dependence of the Raman G-modes of HiPco nanotubes dispersed in water at different excitation wavelengths. They found that TO and LO modes of single-walled carbon nanotubes have 6.5-8 cm⁻¹/GPa dependence on the compressive stress (Fig.4.20).

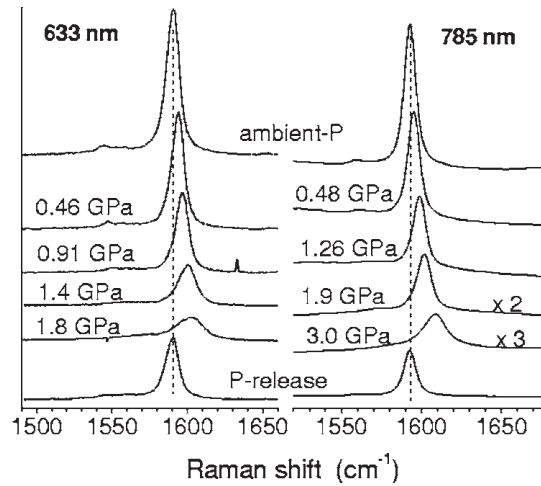


Fig. 4.20: The pressure dependence of the Raman G band of HiPco nanotubes dispersed in water - 1 wt.% sodium cholate and excited at 633 and 785 nm. For each excitation wavelength and sample, the pressure was increased in steps to the largest indicated value and then decreased. From [16].

Behavior 1: Assuming that the inner layer is affected by the stress, the extrapolation of this result in the negative pressure range predicts a downshift of about 8-9 cm⁻¹ of the TO and LO modes of the inner layer (for a negative pressure of -1.2 GPa) in (13,9)@(24,7) DWNT.

The TO and LO modes of (13,9) layer in the DWNTs are located at 1560 cm⁻¹ and 1584 cm⁻¹ respectively (see Fig. 4.15). We now compare these frequency to those predicted for isolated (13,9) SWNT. Fig. 4.21 shows the corresponding dependence of the G-modes on diameter in semiconducting SWNTs. This plot predicts the frequencies of the G- (TO) and G+ (LO) components of the (13,9) SWNT to be close to 1569 and 1591 cm⁻¹ respectively (d=1.5 nm, left blue line and blue circles in the Fig. 4.21). Comparing the experimental G-(TO) and G+(LO) component in (13,9)@(24,7) DWNT and this prediction for SWNT, we find a frequency shift of 7-9 cm⁻¹. This shift can be associated to the effect of the “negative” pressure on the G-mode frequencies of the inner tube.

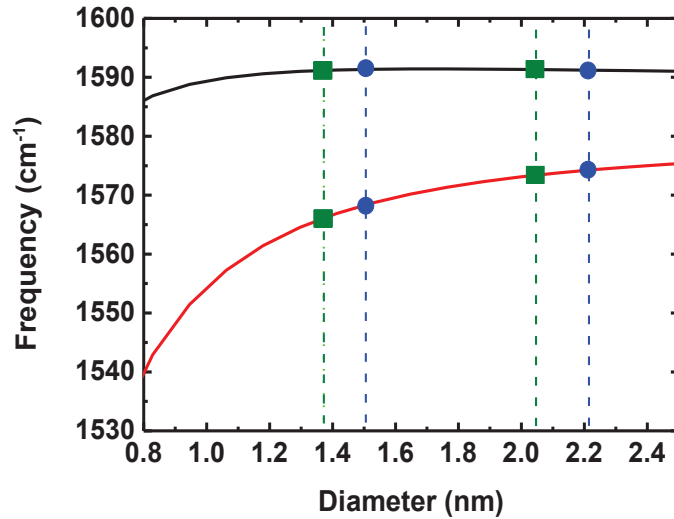


Fig 4.21: Frequency of the TO and LO modes as the function of the diameter of SWNT. The (13,9) and (24,7) SWNTs are shown by blue circles. The frequency of the TO (LO) mode for (13,9) tube is 1569 (1591) cm^{-1} . The frequency of the LO mode for (24,7) tube is 1591 cm^{-1} . The (12,8) and (16,4) SWNTs are illustrated by green squares. The frequency of the TO (LO) mode for (12,8) tube is 1565 (1591) cm^{-1} . The frequency of the TO (LO) mode for (16,4) tube is 1573 (1591) cm^{-1} .

Behavior 2: On the contrary, the interlayer distance in (12,8)@(16,4) DWNT is 0.34 nm. According to Fig. 4.19 (green line) this corresponds to a zero pressure inside double-walled nanotube. Consequently, we expect a slight or any significant shift of the TO and LO modes with respect to the same modes measured in the corresponding SWNTs. This conclusion is in good agreement with experimental data.

The comparison of these two behaviors is summarized in the Table 4.5 below.

Table 4.5. The comparison between two experimental behaviors of tangential modes of DWNTs.

Behavior	(n,m)	d,nm	Interwall distance δr , nm	Pressure [12], GPa	ω_{TO}^{exp}	ω_{LO}^{exp}	ω_{TO}^{SWNT}	ω_{LO}^{SWNT}	$\Delta\omega_{TO}$	$\Delta\omega_{LO}$	Pressure [16], GPa
1	(13,9)	1.5	0.355	-1.2	1560	1584	1569	1591	-9	-7	-1
	(24,7)	2.21			-	1592	-	1591	-	1	
2	(12,8)	1.37	0.34	0	1564.5	1590	1565	1591	0.5	1	~0
	(16,4)	2.04			1570	1590	1573	1591	-3	-1	

The experiments performed on seven SC@SC DWNT allows to confirm our previous statement regarding the dependence of the position of the LO and TO modes as a function of the interlayer distance or, in other words, as a function of the “positive/zero/negative” pressure.

1-All the DWNTs that have an interlayer distance larger than 0.34 show a downshift of the LO mode and TO mode of the inner tube (behavior 1).

Example 1. (22,11)@(27,17) DWNT, inter-layer distance = 0.365 nm

- The frequencies of isolated (22,11) and (27,17) are :
 (22,11) TO= 1574 cm⁻¹ and LO= 1591 cm⁻¹ ;
 (27,17) TO= 1575 cm⁻¹ and LO= 1591 cm⁻¹ .
- The frequencies of G-modes of (22,11)@(27,17) DWNT are: 1562, 1583 cm⁻¹ and 1592 cm⁻¹.
- The downshift of the LO and TO modes of the inner tube is close to 8 cm⁻¹ and 12 cm⁻¹ respectively.

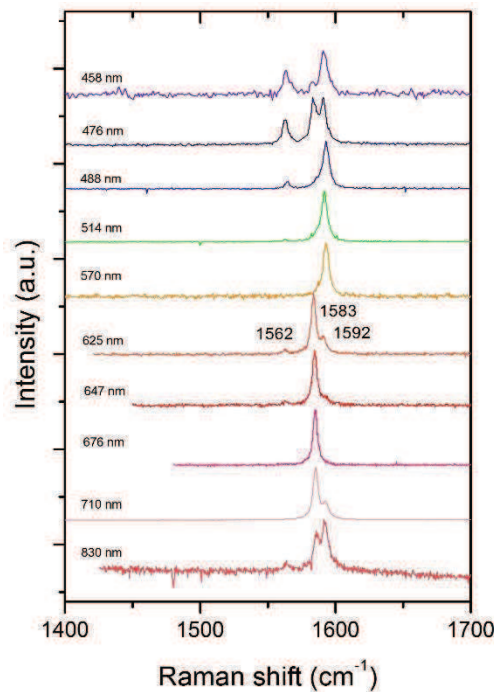


Fig. 4.22: High-frequency tangential modes of (22,11)@(27,17) DWNT measured in a wide range of excitation wavelengths.

Example 2. (18,2)@(20,12) DWNT, inter-layer distance = 0.35 nm.

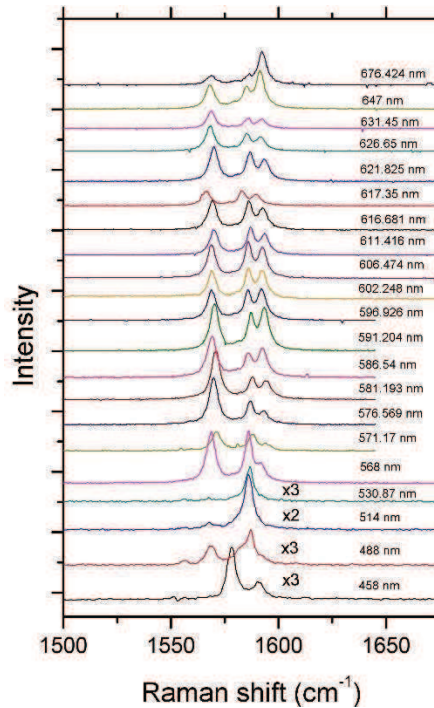


Fig. 4.23: High-frequency tangential modes of (18,2)@(20,12) DWNT measured in a wide range of excitation wavelengths.

- The frequencies of isolated (18,2) and (20,12) are :
 (18,2): TO= 1567 cm⁻¹ and LO=1591 cm⁻¹ ;
 (20,12): TO= 1572 cm⁻¹ and LO=1590 cm⁻¹ .
- The frequencies of G-modes of (18,2)@(20,12) are: 1562, 1583 cm⁻¹ and 1592 cm⁻¹.
- The downshift of the LO and TO modes of the inner tube is close to 8 cm⁻¹ and 5 cm⁻¹ respectively.

2-DWNTs that have an interlayer close to 0.34 nm do not show a downshift of the LO mode and TO mode of the inner tube.

We have only the (12,8)@(16,14) DWNT (Fig. 4.17, 4.18) to illustrate unambiguously this behaviour. Other DWNTs, which have the same behavior of the G-modes, are not unambiguously

index-identified. Strikingly, the DWNTs which display this behavior (in other words having a 0.34 nm inter layer distance) are very rare. The analysis of the DWNT investigated by Liu et al. leads to the same conclusion.

In conclusion, considering the negative pressure inside DWNT as the origin of the downshift of the LO and TO mode of the inner tube allows to understand the experimental behaviors measured in SC@SC DWNTs. It is interesting to emphasize that the measurement of a shift of the TO and LO modes, combined with ED data analysis, may help in the chiral-index assignment.

4.2.2 G-modes in Metallic in Semiconducting (M@SC), Semiconducting in Metallic (SC@M) and Metallic in Metallic (M@M) DWNTs.

In this part, we briefly report the dependence of the G-modes when a metallic layer is present. Similar to SWNTs, Raman spectra of SC@M, M@SC and M@M DWNTs always display a broad component that is assigned to the LO mode of the corresponding metallic tube. An example of such DWNT is shown in Figure. 4.24.

Unfortunately, the number of index-identified DWNTs with metallic tube inside the structure is small and, by contrast to SC@SC DWNTs, any generalization of the results is not possible.

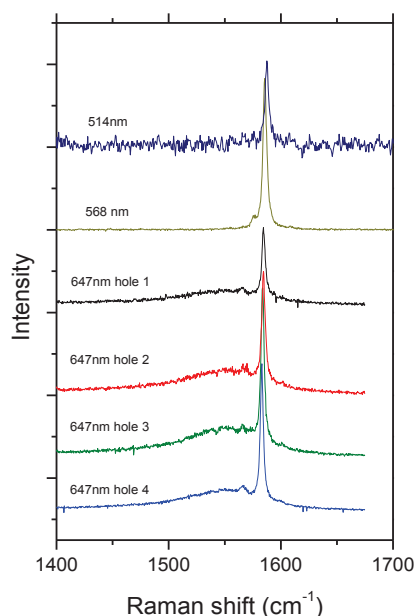
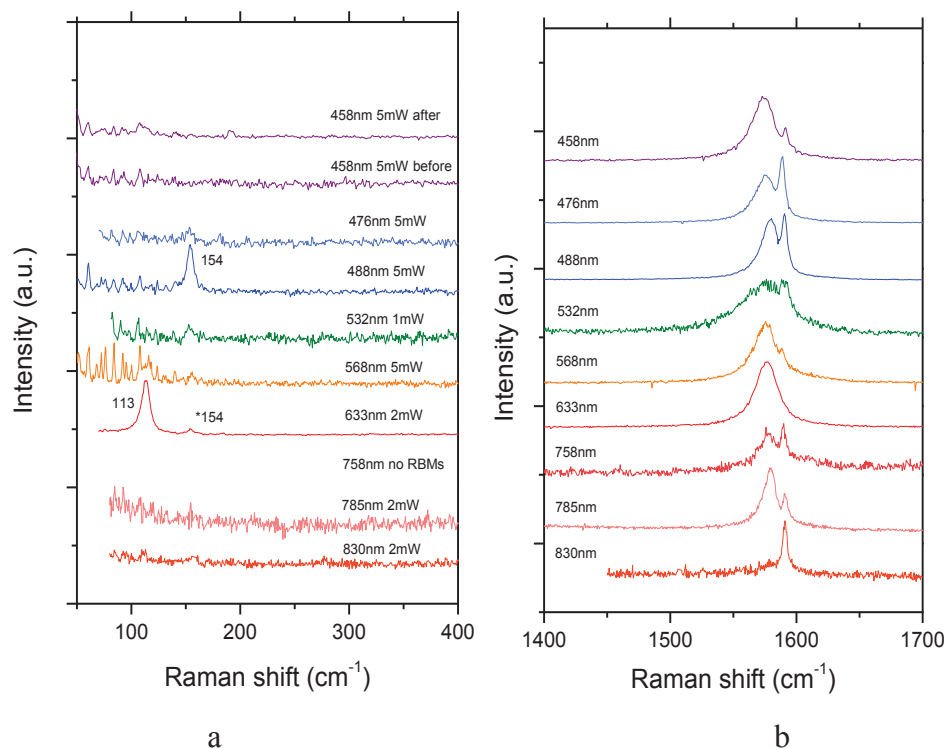


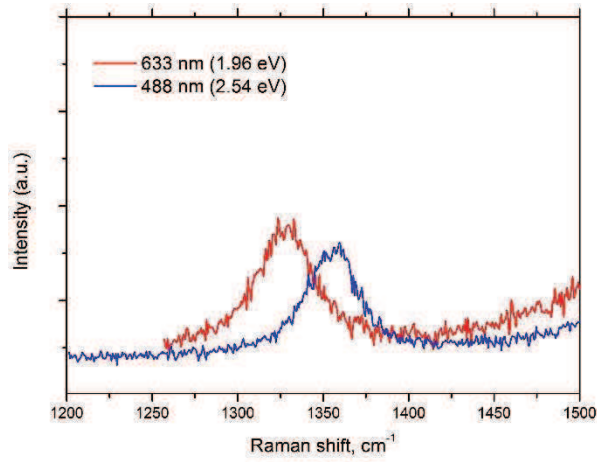
Figure 4.24: G-band of non-index identified DWNT with a metallic layer.

However, DWNTs with a metallic layer show a larger dependence on the environment and experimental conditions than the SC@SC DWNTs. Using results measured on DWNTs in which a metallic layer is involved, we present below an analysis of the sensitivity of such individual DWNT on the environmental effects.

4.3. Sensitivity of individual DWNTs to the environmental effects.

We illustrate this point from the precise analysis of the dependence of a non-index identified DWNT as a function of the incident power impinging the tube. The RBLMs and G-modes of the Raman spectra, measured in a broad range of excitation wavelengths, are reported in the Figure 4.25 (a,b). The outer tube is resonant at 1.96 eV and the inner tube at 2.54 eV. The low-frequency RBLM is located at 113 cm^{-1} and the high-frequency RBLM at 154 cm^{-1} . The relative large intensity of the D band in the spectra measured at these two energies suggests a large density of defects both on the outer and inner tubes (Fig. 4.25c). Finally, the profiles of the G-modes unambiguously state that at least one of the tubes is metallic. The profile of the Raman spectra confirms the outer tube to be a close zigzag. The LO component of the outer tube is located at 1573 cm^{-1} and the frequency of the G+ component of the inner tube is at 1592 cm^{-1} .





c

Fig. 4.25: (a) RBLM and (b) G band of the DWNT with a metallic layer measured at 9 excitation wavelengths: 458, 476, 488, 532, 568, 633, 758, 785, 830 nm and different incident power (c) Corresponding D-band measured at 488 and 633 nm.

In contrast with previous examples, the change of the profiles of the G-modes with the excitation energy are difficult to understand. The reason is supposed to be the effects of the environment, including the influence of the power impinging the tube.

This DWNT is long and lying across different holes of the grid. We measured Raman spectra at different holes and/or using different incident power. The figure 4.26 illustrates the main results. We compare the spectra measured at two holes at low incident power ($E_{\text{laser}}=2.54$ eV, $\lambda_L = 488$ nm): (i) the positions of the RBLMs are the same (Fig. 4.26 a). (ii) The profiles of the G-modes are different (Fig. 4.26 b).

On the other hand, an evolution of the profile of the G-band is observed under irradiation in the spectrum excited at 2.71 eV ($\lambda_L=458$ nm), (Fig. 4.27). By contrast, the RBLM frequency does not change. Increasing the incident power and/or irradiation time, the LO G-mode assigned with the metallic outer tube broadens and is slightly downshifted. Usually, a broad (and asymmetric) profile of LO mode in a metallic tube is assigned to a neutral state. In consequence, we understand the different profiles of figure 4.27 by considering that: (i) the as-grown tubes are doped (initial state), (ii) the level of doping is different from a hole to hole, and (iii) under irradiation, tubes go to their neutral state. These effects are more significant on metallic tubes than semi-conducting indicating a stronger sensitivity of the metallic tubes to the environmental conditions.

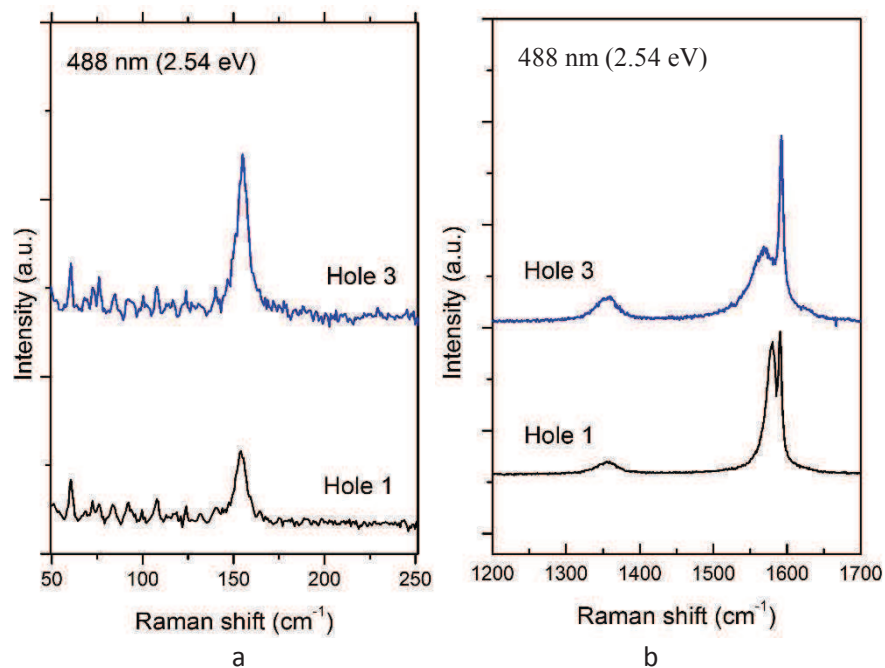


Fig. 4.26: (a) RBLM and (b) G band of the DWNT with a metallic layer measured at different holes (holes 1 and 3).

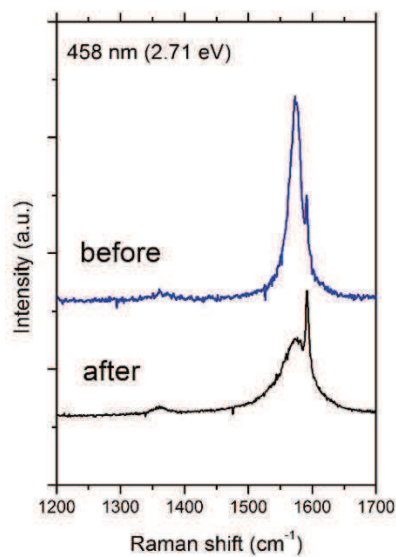


Fig. 4.27: The G-band of metallic DWNT before and after a long laser irradiation (600 s)

Summary

In the second part of Chapter 4 we have presented the analysis of the experimental studies of RBLMs of DWNTs by the group of Liu et al. [12]. We stated the agreements and discussed the discrepancies between our data and those of Ref [12].

Next, we applied the 2D continuous membrane theory of Rochal et al. [14] to the case of DWNTs and calculated the RBLMs frequencies of our individual DWNTs. The comparison between the discrete theory of Popov et al. [6] and the continuous theory of Rochal et al. was given.

The profile of the G-modes of individual index-identified DWNTs was reported and discussed. Particularly, by analyzing the high-frequency part of Raman spectra of SC@SC DWNTs, we found two distinct behaviors of the G-modes:

-Behavior 1: A clear shift of the G-mode frequencies of constituent layers in comparison with those of individual single-walled nanotubes.

-Behavior 2: The spectrum of DWNT was just a simple sum of G-mode of corresponding SWNTs.

These behaviors were explained in terms of “positive/negative” pressure effect inside individual DWNTs.

Finally, from the analysis of the dependence of the Raman spectra on the incident power impinging the tube, we argued the much higher sensitivity of metallic double-walled nanotubes to the environmental effects.

4.4 Understanding of Raman data measured on non-index identified DWNTs.

On the basis of these previous results, we can understand the data measured on non-identified DWNTs. Two examples are detailed below.

The RBLM range and G-mode region of Raman spectra measured on two individual non-index identified DWNTs of two different samples are displayed in Figures 4.28 and 4.29 (it must be emphasized that the DWNT nature of these nanotubes was established from HRTEM). The G-mode ranges of the Raman spectra for each DWNT unambiguously show that all the tubes are semiconducting. The diameter of each layer can be derived from their RBLM frequencies by using our model. Considering these diameters, the semi-conducting character of all the tubes and the laser energies used in each measurement, the presence of the two RBLMs in each spectrum can only be understood by considering a mechanical coupling between the layers.

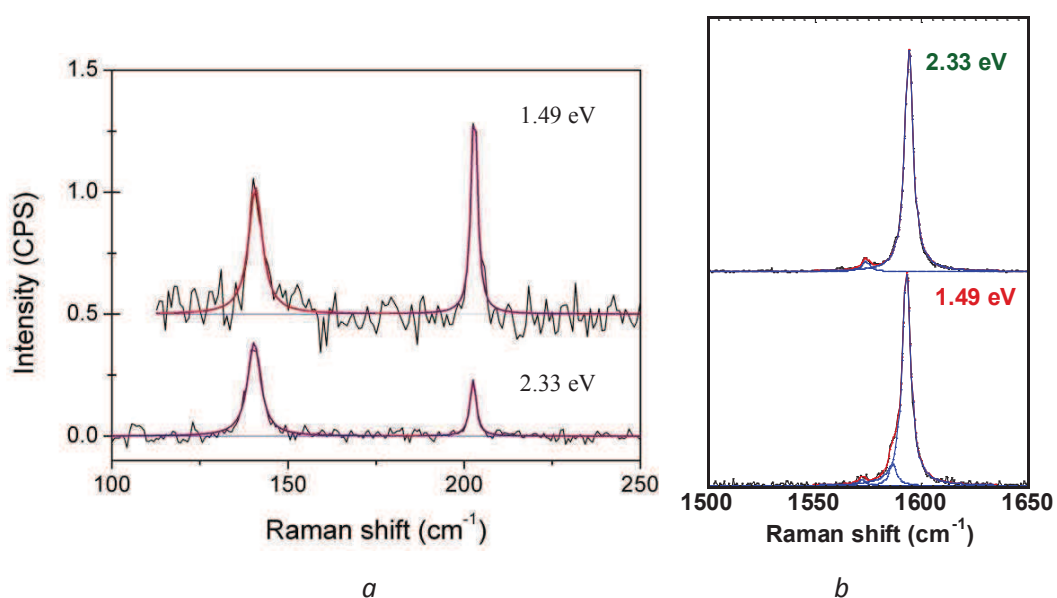


Fig. 4.28: (a) RBLM range and (b) high-frequency part of Raman spectra measured on an individual DWNT (the spectra are vertically shifted for clarity). Excitation energy E_L : 1.49 eV and 2.33 eV.

The outer and inner diameters of the first DWNT estimated from the RBLM frequencies (located at 140 cm⁻¹ and 202.5 cm⁻¹ respectively) are 1.90 nm for the outer tube and 1.22 nm for the inner tube.

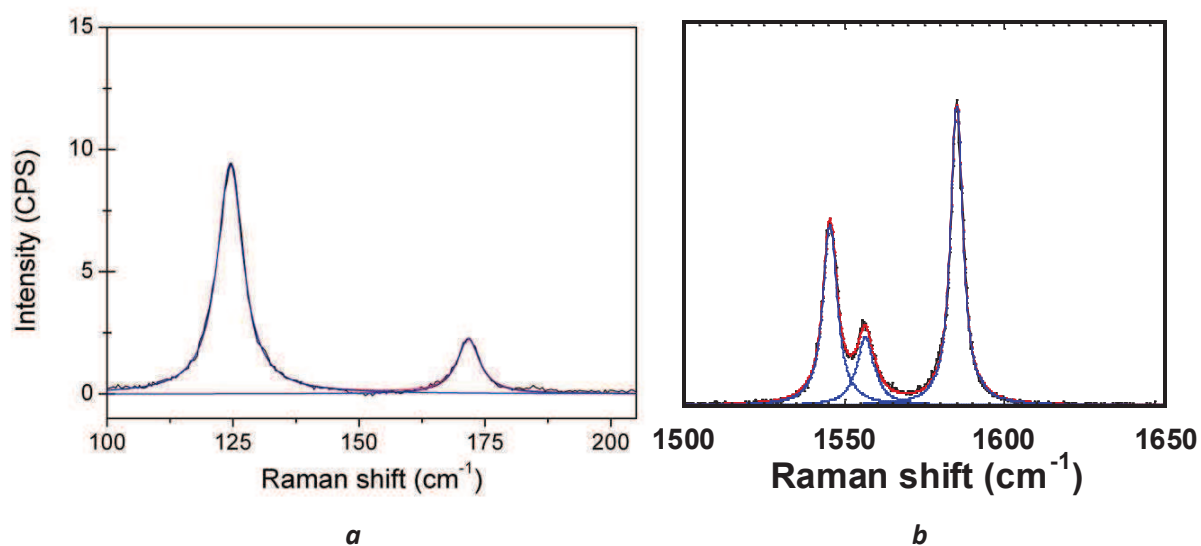


Figure 4.29: (a) RBLM range and (b) High-frequency part of Raman spectrum measured on a second individual DWCNT. Excitation energy, $E_L = 1.96$ eV.

The outer and inner diameters of the second DWNT estimated from the RBLM frequencies (located at 123 cm^{-1} and 170 cm^{-1} respectively) are 2.20 nm for the outer tube and 1.52 nm for the inner tube.

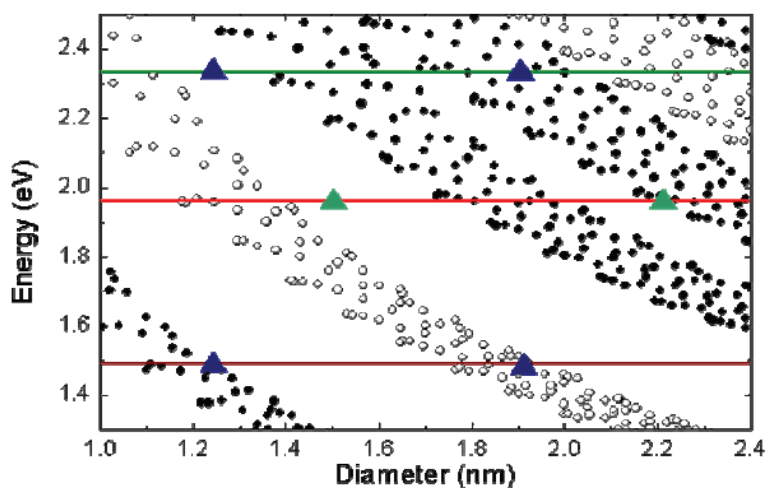


Fig. 4.30: Normalized Kataura plot used to determine the resonance conditions of RBLM. Open (black) symbols: transition energies for metallic (semiconducting) SWNTs. Solid blue triangles represent the energy transitions of the first DWNT. Solid green triangles are the energy transitions of the second DWNT.

For the first DWNT: the presence of the two RBLMs at each excitation wavelength suggests that the resonance energies are close to 2.33 eV and 1.49 eV. Regarding the semi conducting

character of the inner and outer tubes, the Kataura plot leads to the following conclusion: (i) the outer tube is resonant at 2.33 eV and the inner tube at 1.49 eV. (ii) the outer and inner layer are coupled.

For the second DWNT: the presence of the two RBLMs in the spectrum excited at 1.96 eV is totally understood by considering that only the semiconducting inner tube is in resonance at this excitation energy and the both tubes are coupled.

In conclusion, all these results can only be understood by considering a mechanical coupling between the two layers as the origin of the observation of two RBLMs whenever only one of the two layers is in resonance.

4.5. Optical transitions of individual free-standing DWNTs from the measurements of the excitation profile of the RBM and G-modes.

In the framework of this thesis we have measured, for the first time to the best of our knowledge, the resonance profiles of several individual free-standing DWNTs. In order to illustrate these results, we focus on the profiles of RBM and G-modes for such double-walled nanotube, namely (13,9)@(24,7) (see Fig. 4.31 a,b).

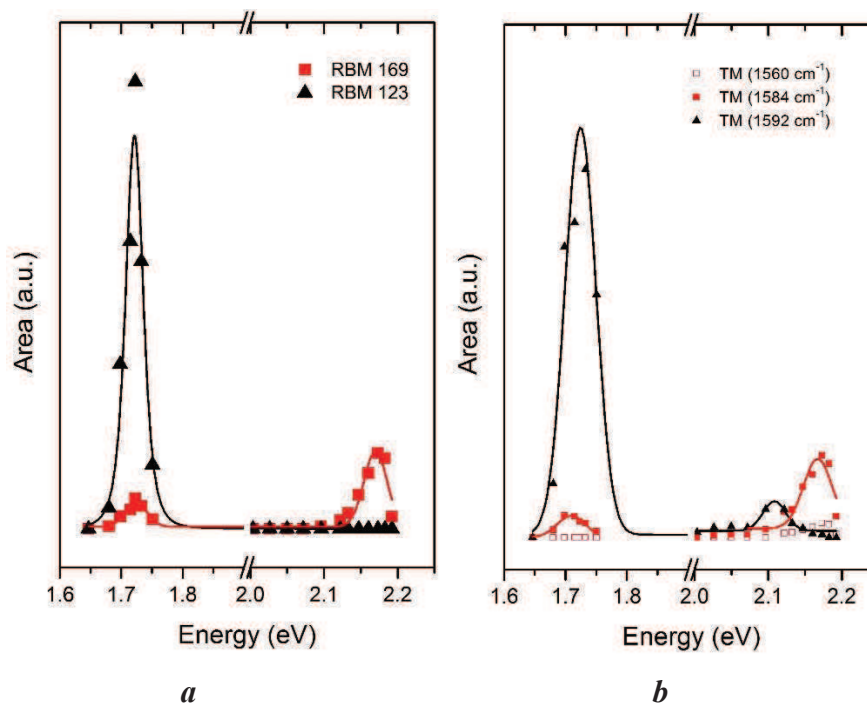


Fig. 4.31: (a) RBM and (b) G-modes resonance profiles for the (13,9)@(24,7) DWNT.

We fitted the data from Figure 4.31 to determine the energies of the optical transitions. The fit was done using the following expression, which is usually used in the literature:

$$I(E_{Laser}) \propto \frac{1}{\left[(E_{laser} - E_{ii})^2 + \frac{\Gamma^2}{4} \right] \left[(E_{laser} - E_{ii} + \hbar\omega_{phonon})^2 + \frac{\Gamma^2}{4} \right]}$$

where E_{ii} is a transition energy, Γ is width of the resonance window (related to the lifetime of the excited state) and $\hbar\omega_{phonon}$ is phonon energy involved the scattering process.

We found that $S_{33} = 1.71$ eV for the (24,7) and $S_{33} = 2.17$ eV for the (13,9) carbon nanotubes. Moreover, the comparison between the experimental transition energies and theoretical ones [9, 17] is given in the Table 3.7. It is clear, that the different values of S_{33} obtained in the two theoretical models (normalized on experimental data) for the outer tube are significantly different (it differs by 88 meV). The experimental value is close to the one calculated in Ref. [17]. For the inner (13,9) tube, both Ref [9,17] give values that are upshifted by 100 meV from the experimental data. This deviation is probably due to the shielding effect of inner tube by the outer. This difference in energy has been qualitatively discussed in the previous section. From the measurement of the excitation profile we have a quantitative determination of the optical transitions of this DWNT.

Table 3.7. Comparison between experimental and theoretical data

	(13,9)	(13,9) SWNT		(24,7)	(24,7) SWNT	
	DWNT Exp.	Ref [9]	Ref [17]	DWNT Exp.	Ref [9]	Ref [17]
S_{33} (eV)	2.17	2.274	2.265	1.71	1.799	1.711

The mechanical coupling between the outer and inner layers is also directly evidenced from the excitation profile of the in-phase RBLM around 1.7 eV. The out-of-phase RBLM intensity follows the resonantly excited in-phase RBLM. We note, however, that the integrated area ratio of A_{in-ph}/A_{out-ph} is close to 16.

Finally, Fig. 4.31 also confirms the assignment of the TO and LO G-modes to the corresponding RBLMs (see Fig. 4.7). The component of the G-band at 1592 cm^{-1} is at resonance at the same energy as the in-phase RBLM 123 cm^{-1} , and, in consequence, it is assigned to the LO G-mode of the outer tube. On the other hand, the maximum of the excitation profile of the 1584 and 1560 cm^{-1} G-modes coincides with the resonant energy of the out-of-phase RBLM at 169 cm^{-1} . We thus conclude that the LO and TO of the inner layer have 1584 and 1560 cm^{-1} , respectively.

4.6. Conclusion

In this chapter we have presented the Raman spectroscopy study of double-walled nanotubes (DWNTs) as the ideal example of the complex nanosystem that is still simple enough to allow us to investigate the coupling between the layers on the properties of carbon nanotubes. We showed that the complementarity of the information provided, on the one hand from TEM and electron diffraction and on the other hand from Raman experiments, is essential to evidence different interactions inside individual DWNTs.

We then presented a detailed Raman study of individual suspended DWNTs. The independent structural identification of the investigated DWNT allowed us to compare the Raman results to previous experimental data and theoretical predictions. We showed that the Raman features obtained at different excitation energies of 11 DWNTs can only be understood in a coherent way by considering the coupling between the two concentric layers of the DWNTs. This coupling plays a major role for the conditions of observation of the modes in a Raman spectrum excited at a given laser energy as well as for the frequencies of the in-phase and out-of-phase RBLMs. In terms of characterization, we can conclude that the identification of the indexes of the layers in a DWNT from the Raman spectra should be done by considering a possible mechanical coupling between the layers. A key parameter for the understanding of the position of the RBLM and to explain the shift of the G-modes, is the inter-wall distance Δ . Depending on this distance, the inner tube experiences a negative pressure for Δ larger 0.34, no pressure for Δ close to 0.34 nm and a positive pressure for Δ smaller than 0.34.

We also showed that van der Waals interaction, usually treated as a weak perturbation, can actually produce quantum phenomena in coupled nanostructures that need to be considered in order to correctly understand their vibrational and optical properties.

Reference of Chapter 4:

1. F.Villalpando-Paez, H. Son, D. Nezich, Y.P. Hsieh, J. Kong, Y.A. Kim, D. Shimamoto, H. Muramatsu, T. Hayashi, M. Endo, M. Terrones, and M.S. Dresselhaus, *Nano Lett.* 8 (2008), pp. 3879–3886.
2. D.I. Levshov, Yu. I.Yuzyuk, T.X. Than, R. Arenal, V.N. Popov, R. Parret, M. Paillet, V. Jourdain, A.A. Zahab, T. Michel, J.-L. Sauvajol, Experimental Evidence of a Mechanical Coupling between Layers in an Individual Double-Walled Carbon Nanotube, *Nanoletters*, 11, 4800 – 4804, 2011
3. T.X. Tinh, V. C. Nguyen, V. Jourdain, M. Paillet, D.-Y. Kim, J.-L. Sauvajol, T. Ngo, N.M. Phan, *J. Exp. Nanosci.* 2011, 6, 1–10.
4. K. Liu, W. Wang, M. Wu, F. Xiao, X. Hong, S. Aloni, X. Bai, E. Wang, and F. Wang, Intrinsic radial breathing vibrations in suspended single-walled carbon nanotubes, *Phys. Rev. B* 83, 113404 (2011).
5. J. C. Meyer, M. Paillet, T. Michel, A. Moreac, A. Neumann, G. S. Duesberg, S. Roth and J.-L. Sauvajol, Raman Modes of Index-Identified Freestanding Single-Walled Carbon Nanotubes, *Phys. Rev. Lett.* 95, 2005, 217401.
6. V. N. Popov, L. Henrard, Breathing-like phonon modes of multiwalled carbon nanotubes, *Phys. Rev. B* 65, 235415 (2002).
7. V. Popov et al (private communication).
8. A. Rahmani, J.-L. Sauvajol, J. Cambedouzou, C. Benoit, Raman-active modes in finite and infinite double-walled carbon nanotubes, *Phys.Rev. B* 2005, 71, 125402.
9. V. N. Popov and L. Henrard, Comparative study of the optical properties of single-walled carbon nanotubes within orthogonal and nonorthogonal tight-binding models, *Phys. Rev. B* 70, 115407 (2004).
10. T. Hertel, A. Hagen, V. Talalaev, K. Arnold, F. Hennrich, M. Kappes, S. Rosenthal, J. McBride, H. Ulbricht, E. Flahaut, Spectroscopy of single- and double-wall carbon nanotubes in different environments, *Nano Lett.* 2005, 5 (3), 511–514.
11. A. Débarre, M. Kobylko, A. M. Bonnot, A. Richard, V. N. Popov, L. Henrard, and M. Kociak, Electronic and Mechanical Coupling of Carbon Nanotubes: A Tunable Resonant Raman Study of Systems with Known Structures, *Phys. Rev. Lett.* 101, 197403 (2008).
12. K. Liu, X. Hong, M. Wu, F. Xiao, W. Wang, X. Bai, J. W. Ager, S. Aloni, A. Zettl, E. Wang & Feng Wang, Quantum-coupled radial-breathing oscillations in double-walled carbon nanotubes, *Nat. Commun.* 4, 1375 (2013).

13. R. Pfeiffer, F. Simon, H. Kuzmany, V.N. Popov, V. Zolyomi, and J. Kurti, Tube–tube interaction in double-wall carbon nanotubes, *Phys. Stat. Solidi B* 243(13) (2006), pp. 3268–3272.
14. S.B. Rochal, V.L. Lorman, Yu.I. Yuzyuk, Two-dimensional elasticity determines the low-frequency dynamics of single- and double-walled carbon nanotubes *Phys. Rev. B* 88, 235435 (2013).
15. V. Popov, P. Lambin, Radius and chirality dependence of the radial breathing mode and the G-band phonon modes of single-walled carbon nanotubes, *Phys. Rev. B* **73**, (2006) 085407.
16. S. Lebedkin, K. Arnold, O. Kiowski, F. Hennrich, and M. M. Kappes, Raman study of individually dispersed single-walled carbon nanotubes under pressure, *Phys. Rev. B* 73, 094109 (2006).
17. K. Liu, J. Deslippe, F. Xiao, R. B. Capaz, X. Hong, S. Aloni, A. Zettl, W. Wang, X. Bai, S. G. Louie, E. Wang and F. Wang, An atlas of carbon nanotube optical transitions, *Nature Nanotechnology* 7, 312 (2012).

Chapter 5

Combination of Electron Diffraction and Raman spectroscopy for the index assignment of carbon nanotubes

5.1 Introduction

The experimental procedure for the study of individual single- and multi-walled carbon nanotubes is based on the combination of two techniques: Resonant Raman spectroscopy and electron diffraction. It is worth reminding that these two techniques taken separately are widely used for the (n,m) index assignment of the carbon nanotubes. In this chapter we will consider in more details the complementarities between RRS and ED in order to propose an improved approach for the index assignment of CNTs. In particular, we will show that Resonant Raman spectroscopy offers several criteria which greatly facilitate the (n,m) index assignment of SWNTs and MWNTs and helps to eliminate possible ambiguities that could exist if we consider only ED data.

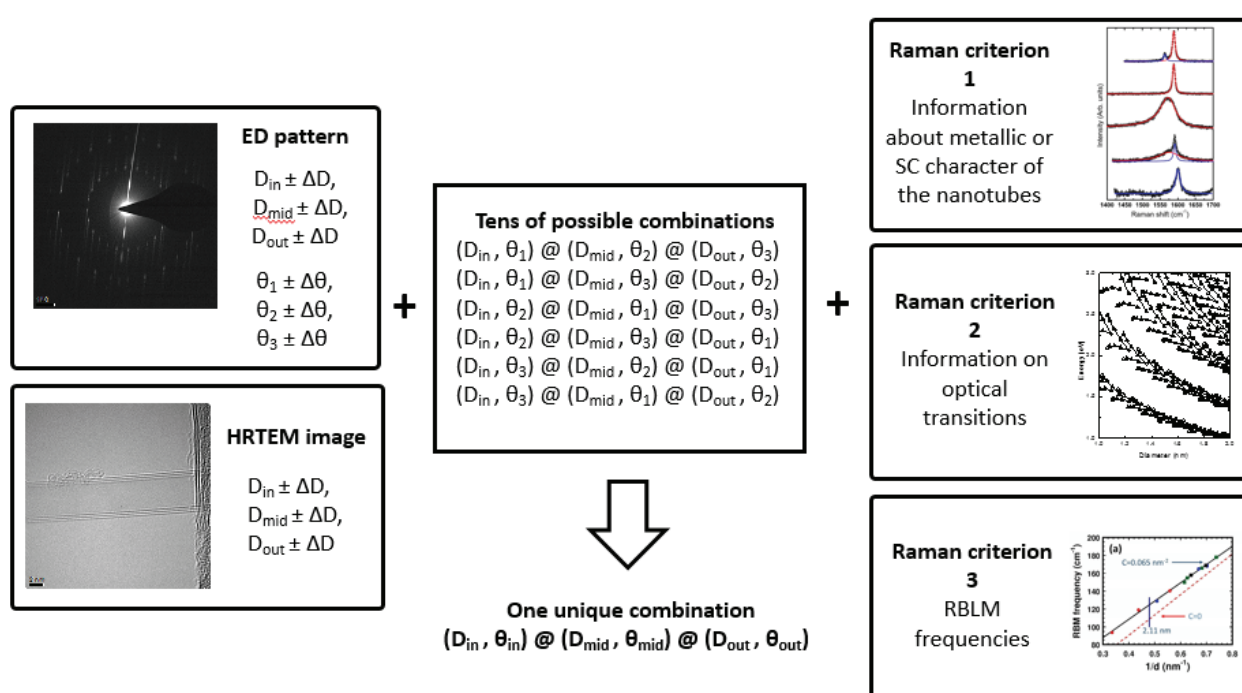


Fig. 5.1: Combination of ED, HRTEM and Raman spectroscopy for (n,m) index-assignment of multi-walled carbon nanotubes

This approach is illustrated in the Figure 5.1. HRTEM unambiguously identifies the nature of the CNT under consideration: SWNT, DWNT, TWNT, etc. ED pattern analysis provides with a good accuracy ($\pm 0.2^\circ$) the chiral angles of all nanotubes and their diameter ranges (usually with $\Delta d = 10\%$ of the diameter value). On this basis, a list of possible indices is proposed. Then according to Raman data the different candidates are sorted to ideally obtain the most likely CNT structure in agreement with all the experimental data.

This chapter is organized as follows: first, we will present the development of the software that allows the combination of all the experimental results for a given CNT with a database including structural and electronic characteristics. Then we will describe the complementarities of RRS and ED through the examples of a SWNT and a TWNT. For the latter case, we will show that our approach combining RRS and ED is particularly relevant.

5.2 Presentation of our identification procedure and of an adapted software

The reason why we developed a procedure and adapted software is clear if we consider the basic algorithm for the index-assignment of a TWNT. At the first step, the software calculates all possible (n,m) indices from the knowledge of diameters and chiral angles derived from HRTEM and ED (within experimental errors). Note, that except for the case of SWNTs, it is generally difficult (or impossible) to determine unambiguously what chiral angle correspond to what layer of the MWNT, so all geometrical combinations need to be considered. Secondly, we find TWNT combinations by taking only the nanotubes that coincide with the possible interlayer distances in the MWNT (adjustable parameter in a reasonable range). For TWNTs, these lead to six possible geometrical combinations:

$$(d_{in}, \theta_1) @ (d_{mid}, \theta_2) @ (d_{out}, \theta_3)$$

$$(d_{in}, \theta_1) @ (d_{mid}, \theta_3) @ (d_{out}, \theta_2)$$

$$(d_{in}, \theta_2) @ (d_{mid}, \theta_1) @ (d_{out}, \theta_3)$$

$$(d_{in}, \theta_2) @ (d_{mid}, \theta_3) @ (d_{out}, \theta_1)$$

$$(d_{in}, \theta_3) @ (d_{mid}, \theta_2) @ (d_{out}, \theta_1)$$

$$(d_{in}, \theta_3) @ (d_{mid}, \theta_1) @ (d_{out}, \theta_2)$$

Depending on the experimental error each combination may have tens of TWNTs. The situation becomes more complicated when increasing the diameter of constituent layers, as more and more nanotubes may appear within the interval of the experimental error. It is thus almost impossible to deduce the (n,m) indices solely from ED and HRTEM data. At this point electronic and vibrational information provided by RRS data will play a crucial role.

An image of the interface of the software is given in Figure 5.2, divided in 4 different panels. Using structural formulas for single-walled carbon nanotubes (see Chapter 1) we form a database of SWNTs containing their diameters, chiral angles, type, radial breathing modes

frequencies (calculated from two relations $\omega_{\text{RBM}} (\text{cm}^{-1}) = 228/d (\text{nm})$ and $\omega_{\text{RBM}} (\text{cm}^{-1}) = 204/d (\text{nm}) + 27$), radial-breathing like frequencies (for MWNTs) and optical transition energies for every nanotube with diameter up to 7 nm. Moreover, in the code we incorporated SWNT's optical transitions data calculated by Popov et al. [1] for every nanotube up to 2.5 nm. In addition to cross-check this information and also to include nanotubes bigger than 2.5 nm we used the results of Liu et al [2].

Structural parameters with their experimental uncertainties (e.g. diameters, chiral angles and intertube distance) obtained from ED or HRTEM are entered in the upper left part of the interface (Figure 5.2 panel 1). On the basis of these ED data, the software calculates all the possible (n,m) combinations for the given SWNT or MWNT. The list of all combinations is shown in the panel 2 (upper right part of Figure 5.2).

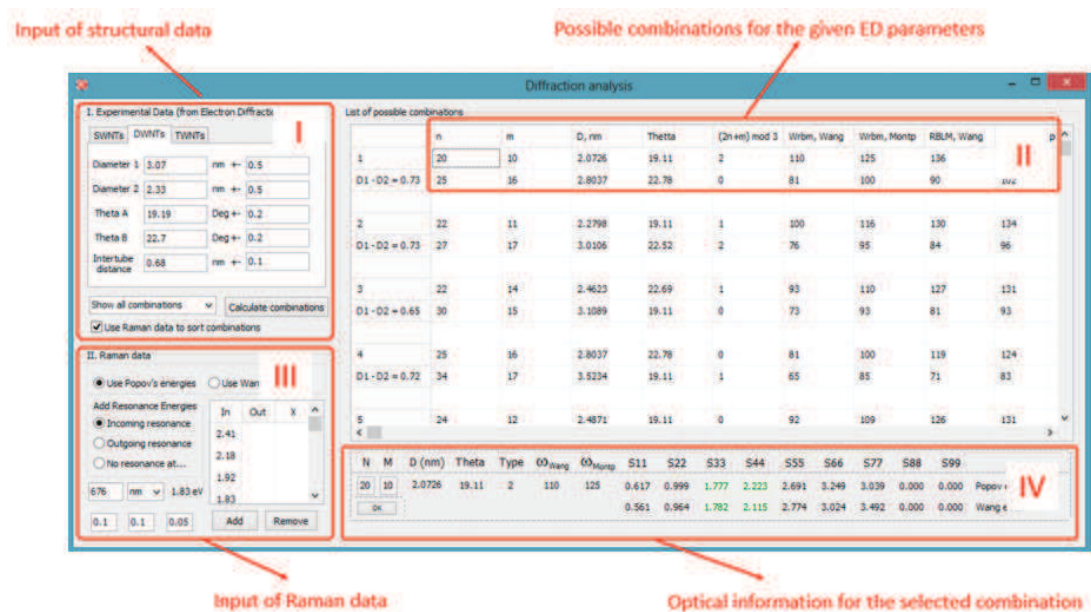


Fig. 5.2: The software for (n,m) index assignment of single- and multi-walled carbon nanotubes on the basis of ED and Raman data.

At this stage we may apply additional criteria for the (n,m) index-assignment. For example, **the first Raman criterion** that may reduce significantly the number of possible combinations is to consider the shape of the G band. As explained previously, the latter strongly depends, first, on the chiral or achiral type of tube and, secondly, on metallic or semiconducting character of the tube. **The second Raman criterion** consists in comparison of the experimental resonant frequencies of individual nanotubes to the theoretical ones. We assume that the laser excitation energy matches an electronic resonance of the system as soon as at least one low frequency mode (RBM or RBLM) is

detected. These two criteria can be included for a given nanotube in the lower left part of the interface, (Figure 5.2, panel 3). It is also possible for each candidate to have an easy view of the different theoretical transition energies in the panel 4. A color code indicate the resonances involved or not in the experiments from the input in panel 3. Finally, **the third Raman criterion** is to compare the experimental RBM or RBLM frequencies to those calculated from the models of Popov et al [3] and Rochal et al [4] (panel 2). The tubes with the largest deviation from the theory may be discarded.

We emphasize however that the Raman criteria may be applied in a free manner (not in the order of presentation), as that is shown in the example below.

5.3 Combination of RRS and ED for the index assignment of a SWNT

Fig. 5.3 shows an individual SWNT deposited on a TEM grid by CCVD method. We measured HRTEM and ED data at several holes on the sample (see Fig. 5.3a). Data from different holes appeared to be identical which indicated the homogeneous character of the nanotube.

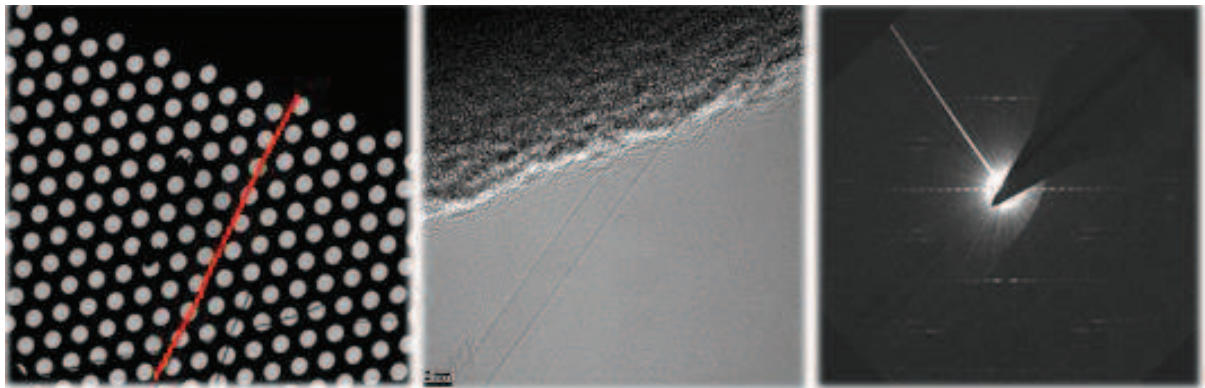


Fig. 5.3: (a) TEM, (b) HRTEM and (c) ED pattern of the individual single-walled carbon nanotube.

Electron diffraction and HRTEM data treatment

HRTEM image presented in the Fig. 5.3b proves that the nanotube is indeed individual and gives an evaluation of the tube diameter about:

$$d_{\text{HRTEM}} = 2.25 \pm 0.25 \text{ nm}$$

Next, we analyzed the ED pattern (Fig. 5.3c) as explained in the Chapter 2 and got the following values of the chiral angle and tube diameter:

$$d_{\text{ED}} = 2.4 \pm 0.2 \text{ nm}$$

$$\theta_{ED} = (3.4 \pm 0.2)^\circ$$

At this stage we may calculate different (n,m) indices based exclusively on ED data. To show the efficiency of our method we deliberately extend the range of the experimental error for diameter and chiral angle

$$d = 2.3 \pm 0.3 \text{ nm}$$

$$\theta = (3.4 \pm 0.3)^\circ$$

For these values of structural parameters, we obtain six possible (n,m) indices:

Table 5.1. List of the (n,m) indices for the individual SWNT in question, derived from ED patterns and HRTEM images analysis.

#	(n,m)	d (nm)	Θ (°)	Type
1	(26,2)	2.119	3.67	0
2	(27,2)	2.198	3.54	2
3	(28,2)	2.276	3.42	1
4	(29,2)	2.354	3.3	0
5	(30,2)	2.432	3.2	2
6	(31,2)	2.5104	3.1	1

Raman criterion 1. Metallic or semiconducting

We now apply the first Raman criterion, which concerns the electronic character of the nanotube under consideration. Fig. 5.4a shows the Raman spectra of this individual SWNT measured at 530.5 and 514 nm. A fit of the G-band obtained at 530 nm is presented in the Fig. 5.4b. The presence of a broad component at 1570 cm^{-1} associated to a weak component at 1591 cm^{-1} indicates that this nanotube is a chiral (close zigzag) metallic SWNT.

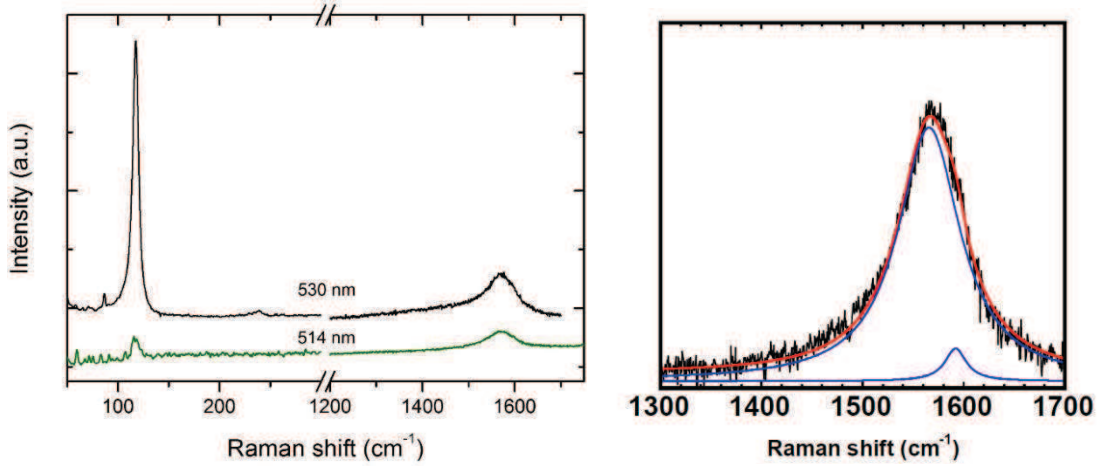


Fig. 5.4: (a) Raman spectra of the given individual SWNT measured at 514 and 530 nm; (b) G-band of the SWNT at 530 nm. The frequency of the broad component is 1570 cm^{-1} .

According to the Table 5.1, this information reduces the number of possible combination to 2, leaving only metallic (26,2) and (29,2) nanotubes. To choose between these two SWNTs we apply the second Raman criterion.

Raman criterion 2. RBM frequencies

We now apply the second Raman criterion and compare the experimental ω_{RBM} with those calculated from relation $\omega = 204/d + 27$ (this relation was experimentally established for our SWNTs). For the diameters of 2.12 ((26,2)) and 2.35 ((29,2)) nm we predict $\omega_{\text{RBM}} = 123$ and 114 cm^{-1} respectively (see Table 5.2).

Table 5.2. Experimental and calculated radial breathing mode frequencies of the individual SWNT.

#	(n,m)	d (nm)	$204/d+27 \text{ (cm}^{-1}\text{)}$	ω_{exp}
1	(26,2)	2.119	123	119
2	(29,2)	2.354	114	

Both calculated ω_{RBM} are shifted by 4-5 cm^{-1} from the experimental data, so we cannot discern between the two candidates using only the 2nd criterion.

Raman criterion 3. Optical transitions

We now show that the information on the optical transition may determine the (n,m) indices of the nanotube in question. Table 5.3 summarize the electronic transition energies calculated

within two models of Popov et al [1] and Liu et al [2] for the (26,2) and (29,2) nanotubes. We note that there exist certain discrepancies between two models, especially for M₂₂ and M₃₃ optical transitions.

Table 5.3. Optical transition energies for a (26,2) and (29,2) nanotubes calculated within the models of Ref [1,2].

Transition energies	(26,2)		(29,2)	
	Ref [1], eV	Ref [2], eV	Ref [1], eV	Ref [2], eV
M _{11L}	1.296	1.386	1.204	1.267
M _{11H}	1.388	1.389	1.282	1.269
M _{22L}	2.301	2.677	2.137	2.439
M _{22H}	2.639	2.690	2.414	2.449
M _{33L}	3.080	3.929	2.867	3.567
M _{33H}	3.746	3.957	3.469	3.588
M _{44L}	3.374	-	3.067	-

We searched for the resonant transitions of the given individual SWNT at several wavelengths in the visible range, namely at 458, 476, 488, 514, 530, 580-612 and 633-676 nm. The results are summarized in Table 5.4. Briefly, we found incident resonant responses only at 514 and 530 nm. The latter was much more intensive (see Fig. 5.4a), which indicates that this excitation energy is closer to the optical transition energy in the SWNT. We note that no sign of the outgoing resonance, namely the presence of only the G-band in the spectra, was observed.

Table 5.4. Comparison of the experimental and theoretical data. In our experiment we observed only incident resonances. At all excitation frequencies there was no sign of the outgoing resonance, namely the presence of only the G-band in the spectra.

RRS data			(26,2)		(29,2)	
λ , nm	Excitation energy, eV	Resonance	Ref [1], eV	Ref [2], eV	Ref [1], eV	Ref [2], eV
633-676	1.83-1.96	No	-	-	-	-
580-612	2.03-2.14	No	-	-	2.137	-
530	2.34	Incident (High I)	2.301	-	-	-
514	2.41	Incident (Low I)	-	-	2.414	2.439 2.449
488	2.54	No	-	-	-	-
476	2.61	No	2.639	2.677	-	-
458	2.71	No	-	2.690	2.867	-

The data of the Table 5.4 is illustrated in the Fig. 5.5 in a more intuitive way. First, we see that the transition energies of the (26,2) nanotube calculated within the model of Liu et al (green dots) are not in good agreement with experimental data. Moreover M_{22H} transition from Popov's model (red dots) is not seen at blue frequencies (458 and 476 nm). On the contrary the transition energies of the (29,2) tube calculated with the Ref [2] have much better agreement.

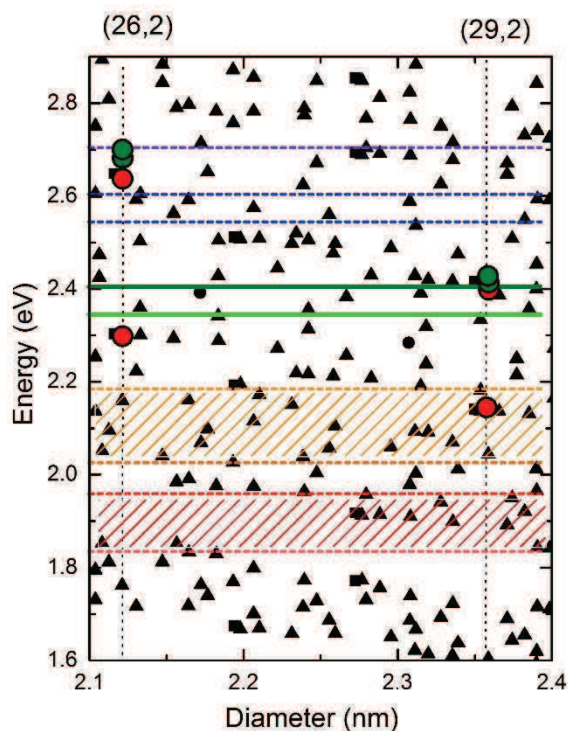


Fig. 5.5: A Kataura plot for (26,2) and (29,2) nanotubes calculated within the model of Popov et al [1] and corrected for many-body interactions. The optical transitions for the nanotubes are illustrated by red dots. On the same plot we display the optical energies calculated within the model of Liu et al [2] (green dot). Horizontal lines show the experimental excitation energies used in this work. A two dashed box between 1.8 and 2.2 eV indicate the measurements made with continuous lasers (see Table 5.4 for the summary).

Finally, we conclude that the nanotube in question is a (29,2) metallic SWNT.

5.4 Combination of RRS and ED for the index assignment of a TWNT

The importance of the RRS data is even more evident when considering an indexation of triple-walled carbon nanotubes. We present below an individual suspended TWNT produced by chemical vapor deposition method (see Chapter 2). HRTEM and ED measurements were made at

the multiple areas on the nanotube (see Fig. 5.6 a,b,c). Then Raman signal was searched in the same areas in a wide range of laser excitation wavelengths: 458, 488, 514, 530, 568-633, 647 and 676 nm.

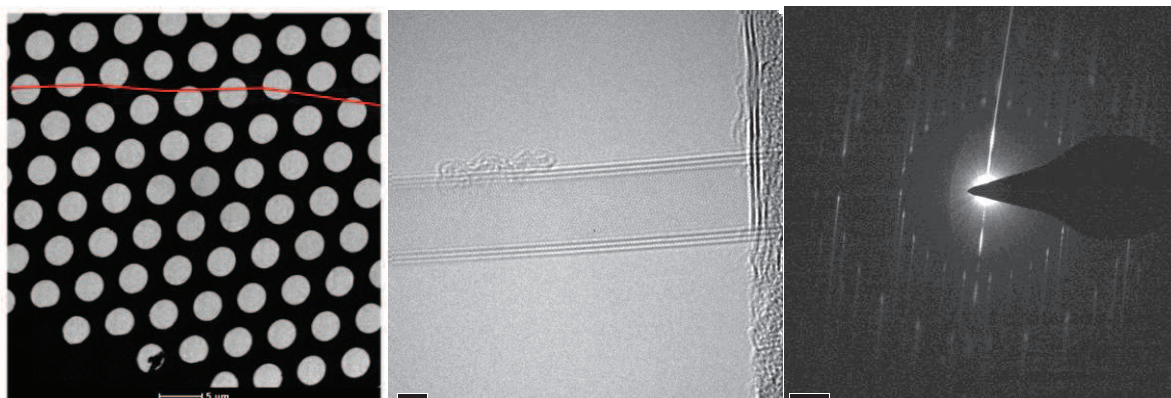


Fig. 5.6: (a) TEM and (b) HRTEM micrographs and (c) the ED pattern of an individual triple-walled carbon nanotube.

Electron diffraction data treatment

HRTEM image and ED pattern of the studied triple-walled carbon nanotube are presented in the Fig. 5.6 b,c. Interestingly, from electron diffraction we found that two chiral angles among the constituent layers are identical. This fact complicates the assignment as we need to perform the procedure two times: first for $\theta_1 = \theta_3$, θ_2 and then for θ_1 , $\theta_2 = \theta_3$ increasing the number of possible nanotubes. The chiral angles have the following values:

$$\theta_1 = (21.35 \pm 0.2)^\circ$$

$$\theta_2 = (7.1 \pm 0.2)^\circ$$

Unfortunately it was impossible to extract diameters from ED patterns, as the equatorial line oscillations in this case are not so simple to analyze and do not give the direct information on the dimensions of the constituent layers. We thus measured the diameters from HRTEM images, and then consider a higher uncertainty for these real space image parameters compared to ED-derived diameters:

$$d_{in} = 4.5 \pm 0.5 \text{ nm}$$

$$d_{mid} = 5.2 \pm 0.5 \text{ nm}$$

$$d_{out} = 5.8 \pm 0.5 \text{ nm}$$

We now are able to input the structural parameters in the developed software and get a list of possible (n,m) indices of this TWNT. Twelve combinations are possible:

For $\theta_1 = \theta_3 = (21.35 \pm 0.2)^\circ$, $\theta_2 = (7.1 \pm 0.2)^\circ$:

1. (38,22)@(57,9)@(51,30),
2. (39,23)@(58,9)@(51,30),
3. (39,23)@(58,9)@(52,30),
4. (50,8)@(46,27)@(52,30),
5. (51,8)@(46,27)@(52,30),
6. (57,9)@(51,30)@(57,33),
7. (58,9)@(51,30)@(57,33),
8. (58,9)@(52,30)@(58,34),

And for $\theta_1 = \theta_3 = (7.1 \pm 0.2)^\circ$, $\theta_2 = (21.35 \pm 0.2)^\circ$:

9. (50,8)@(58,9)@(51,30),
10. (50,8)@(58,9)@(52,30),
11. (50,8)@(59,9)@(52,30),
12. (51,8)@(59,9)@(52,30).

Raman criterion 1. Metallic or semiconducting

Fig. 5.7 shows the Raman spectra of the individual TWNT measured at five excitation wavelengths: 488, 514, 568, 647 and 676 nm.

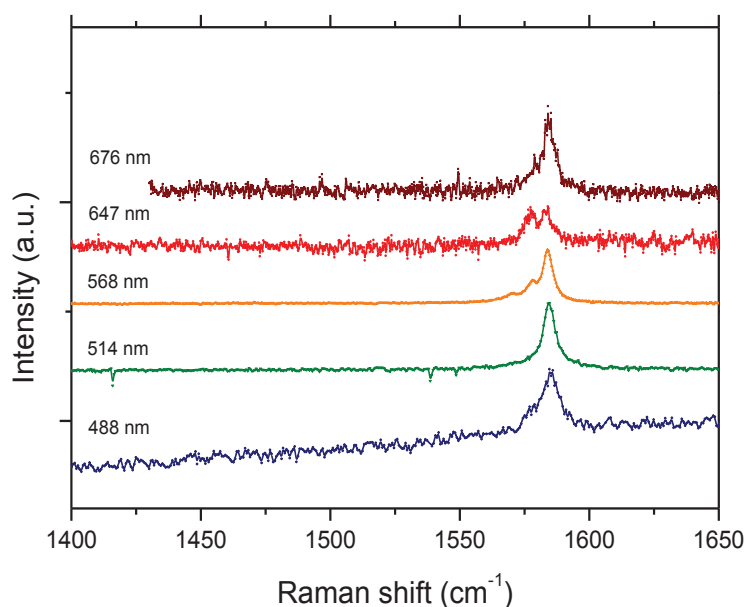


Fig. 5.7: High frequency part of the Raman spectra obtained on an individual TWNT (excitation wavelengths are indicated in the figure).

The spectra measured at 647, 568 and 514 nm are detailed in Fig. 5.8. The G-band was fitted with Lorentzians following standard procedures. The absence of a broad component in the G-band indicates that the layers of the TWNT should have a semiconducting character. Due to the broad range of excitation wavelengths, it is more likely that all the constituent layers were in resonance during the experiment.

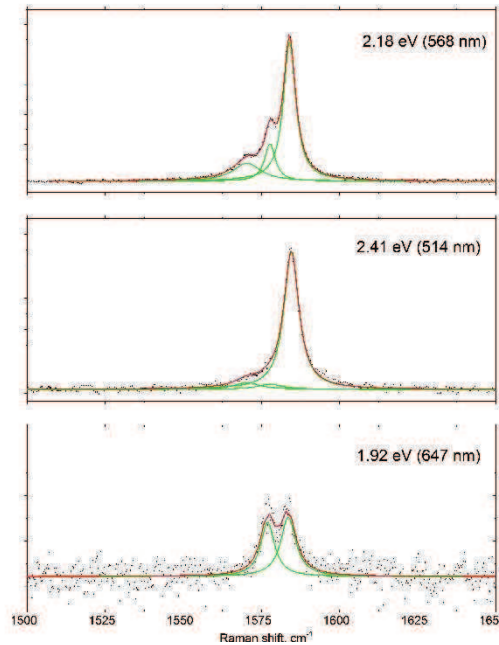


Fig. 5.8: G-band of the investigated triple-walled nanotubes measured at 514, 568 and 647 nm.

If we use the information about the electronic type of the layers, namely none of these layers are metals, for the given TWNT the number of combinations reduces to 3:

For $\theta_1 = \theta_3 = 21.35 \pm 0.2$, $\theta_2 = 7.13 \pm 0.2$:

1. (39,23)@(58,9)@(52,30),
2. (51,8)@(46,27)@(52,30),

And for $\theta_1 = \theta_3 = 7.13 \pm 0.2$, $\theta_2 = 21.35 \pm 0.2$:

3. (51,8)@(59,9)@(52,30).

Raman criteria 2 (Optical transitions) and 3 (RBLM frequencies)

The low-frequency part of Raman spectra of this individual TWNT, measured at 514, 568, 647 and 676 nm, are shown in the Fig. 5.9a. We observe three radial breathing-like frequencies at

60, 84 and 107 cm^{-1} . The RBLM lines have a very low-intensity, certainly due to the big diameter of the constituent layers.

To be sure that these lines really correspond to TWNT and are not some parasite peaks we performed the measurement of resonance profile in the range 568-633 nm. The corresponding data are presented in the Fig. 5.9b.

The evolution of the three peaks observed previously with changing the excitation wavelengths clearly indicates that these lines are real and correspond to the RBLM of the different layers of TWNT.

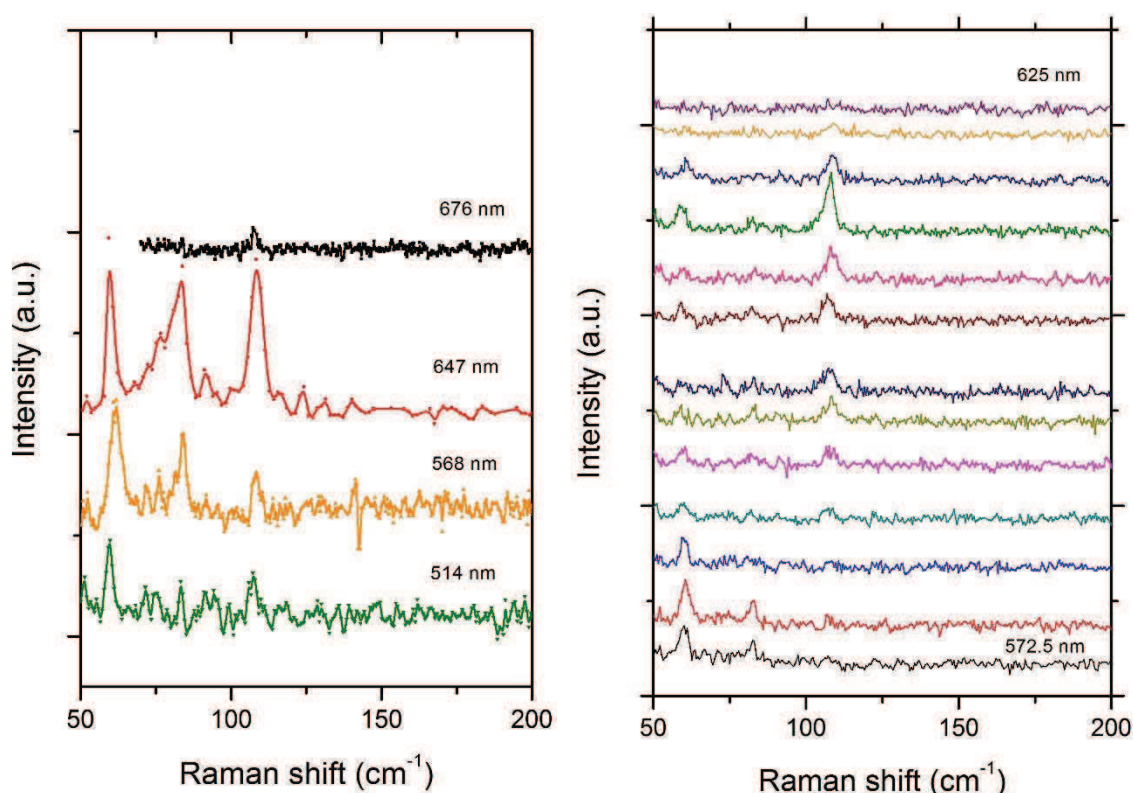


Fig. 5.9: Low-frequency part of Raman spectra for a TWNT. Spectra in the left panel are obtained using discrete laser energies indicated in the figure. Right panel: excitation profile by varying excitation energy in the range [572-625] nm by steps of 10 nm.

From Fig. 5.9 we may deduce the following incident resonant frequencies close to: 2.41 eV (514 nm), 2.18 eV (568 nm), 1.92 eV (647 nm) and 1.83 eV (676 nm). The strongest resonances are at 2.18 and 1.92 eV. Though we see three RBLM peaks at 647 nm it is not clear a-priori if they are due to the mechanical coupling between the layers or all three layers are in resonance at this excitation energy. We thus need to proceed with caution.

In our code the optical transitions energies from Ref [1,2] are automatically calculated for every nanotubes at the generation of the database. So we only need to enter the observed resonant frequencies for the given TWNT and the code will sort the combinations by the number of matches:

1. **(51,8)@(46,27)@(52,30),**
2. (39,23)@(58,9)@(52,30),
3. (51,8)@(59,9)@(52,30).

The most probable combination is (51,8)@(46,27)@(52,30) inter tube distances $\Delta_1 = 0.335$ nm (internal-intermediate), $\Delta_2 = 0.31$ nm (intermediate-external). However we deliberately do not exclude the other tubes keeping in mind that the triple-walled carbon nanotubes are not fully studied and we cannot unambiguously predict the behaviour of their optical transitions (for example, the role of inter tube interactions is not yet clear).

Another effect is worth noting. Considering the most probable assignment on this TWNT as (51,8)@(46,27)@(52,30), we find a disagreement between the theoretical calculations of radial breathing-like mode frequencies of TWNTs with the experimental ones [3,4]. Popov et al [3] calculated these frequencies for a TWNT in which all the tubes are armchair tubes. For a triple-walled nanotube with an outer diameter $d_{\text{out}} = 5.8$ nm and an inter-layer distance $\Delta = 0.34$ nm, the calculation predicts

$$\omega_1 = 45 \text{ cm}^{-1} \quad \omega_2 = 78 \text{ cm}^{-1} \quad \omega_3 = 115 \text{ cm}^{-1}$$

in a poor agreement with the observed RBLMs located near of 60, 84 and 107 cm^{-1} , especially for the lowest-frequency component. For the moment, we do not have a clear explanation of these discrepancies. Additional experiments and modelizations are required in order to solve this problem.

5.5 Conclusion

In this chapter we discussed the complementarity of electron diffraction and resonant Raman spectroscopy for chiral-index assignment of individual carbon nanotubes. Two examples of a single- and a triple-walled nanotube were presented. We argued that the index-assignment based on only ED data lead to ambiguous results even in the case of SWNT. For TWNTs the situation became worse due to the greater number of possible combinations.

Moreover, even having structural parameters (e.g. diameters and chiral angles) and RRS data for a given nanotube, the search and the sorting of its possible (n,m) indices were quite

laborious and time-consuming. To automate this procedure we wrote a code that performs a search of the possible combinations based on electron diffraction and then eliminates and sorts the indices by Raman data.

We argue that that the approach developed greatly facilitate an index-assignment procedure and makes it easier to find chiral indices of multi-walled nanotubes.

References of chapter 5:

1. V. N. Popov and L. Henrard, Comparative study of the optical properties of single-walled carbon nanotubes within orthogonal and nonorthogonal tight-binding models, *Phys. Rev. B* 70, 115407 (2004).
2. K. Liu, J. Deslippe, F. Xiao, R. B. Capaz, X. Hong, S. Aloni, A. Zettl, W. Wang, X. Bai, S. G. Louie, E. Wang and F. Wang, An atlas of carbon nanotube optical transitions, *Nature Nanotechnology* 7, 312 (2012).
3. V. N. Popov, L. Henrard, Breathing-like phonon modes of multiwalled carbon nanotubes, *Phys. Rev. B* 65, 235415 (2002).
4. S.B. Rochal, V.L. Lorman, Yu.I. Yuzyuk, Two-dimensional elasticity determines the low-frequency dynamics of single- and double-walled carbon nanotubes *Phys. Rev. B* 88, 235435 (2013).

General conclusions

The understanding of the Raman responses of single-walled and multi-walled carbon nanotubes was the objective of this work. We have privileged a systematic approach that consists in combining on the same single nano-object spectroscopic investigations and electronic microscopy, including electron diffraction. Several important and original experimental results were derived, especially concerning few-layered nanotubes that were poorly studied in the literature, at least in their individual form. As measurements were performed on the systems that are the closest to the ideal, we were able to compare our experimental findings with theoretical models.

In the first chapter we briefly reviewed the main general properties of carbon nanotubes. Nowadays a huge number of reference books are available on this topic. In this chapter, we focused on the main concepts necessary for the understanding of our results by the reader.

In chapter 2 we have presented the different steps prior to the spectroscopic investigations of the samples including the synthesis, the localization and structural analysis of samples of individual single- and multi-walled carbon nanotube. A review of the different methods for the atomic structure identification of carbon nanotubes by electron diffraction (ED) was presented. Applications of these methods to the (n,m)-assignment of single-, double- and triple-walled nanotubes were reported. It was highlighted that for multi-walled tubes an unambiguous index assignment based exclusively on ED and High Resolution Transmission Microscopy (HRTEM) data cannot be proposed in several cases.

Results concerning the main Raman active modes (RBM and G-modes) of the individual single-walled carbon nanotubes were presented in the chapter 3. The present contribution completes previous investigations performed in the Montpellier group since 2005. In particular, one objective was to acquire a new set of data on samples synthesized by an improved protocol in order to derive the intrinsic experimental relationship between RBM frequency and the tube diameter. Nevertheless, the new experimental data do not fit the expected $228/d$ relationship. We propose possible explanations of the observed deviation. The role played by amorphous carbon adsorbed around the tubes and the effect of substrate were identified as the possible main experimental parameters to explain our measurements.

In order to quantify the origins of deviations, we propose a comparison between our experimental data and calculations performed by Rochal and co-workers in the framework of elasticity theory. From an experimental aspect we suggest to perform experiments in a controlled oxidative atmosphere to check if it is possible to observe a variation of the RBM frequency upon elimination of amorphous carbon.

Raman resonance profiles (including RBM and G-modes) performed on free-standing SWNTs with tunable lasers are reported. These experimental resonance energies improve our knowledge of the optical properties of SWNTs. Finally, we proposed an analysis of Raman spectra of an identified inhomogeneous dimer (bundle of two different SWNTs). The main striking result is the significant coupling between the tubes which is evidenced for the first time to the best of our knowledge from the shift of the G-modes.

Special attention was given to DWNTs in Chapter 4. DWNT is an ideal system to investigate interaction between concentric layers and their consequences on the vibrational and optical properties. The independent structural identification of the investigated DWNT allowed us to compare the Raman results to theoretical predictions. We would like to emphasize that the combined approach Raman-ED applied to single DWNTs has permitted to evidence unambiguously specific features that can never be derived from ensemble measurements. We showed that the mechanical coupling between the two concentric layers plays a major role in the conditions of the observation of the modes in a Raman spectrum. The low frequency range was understood in agreement with theoretical models in terms of collective in-phase and out-of-phase Radial Breathing Like Modes (RBLMs). In consequence, any relation $\omega_{\text{RBM}}(d)$ established for SWNTs does not work to derive the diameters of the layers from the RBLMs frequencies. Concerning the RBLM phonon properties, new calculations in the framework of elasticity theory have been developed (adapted from the model developed for SWNT).

The attribution of the different components in the G-modes have been proposed and supported by the examination of resonance conditions. A key parameter for the position of the G-modes, is the inter-wall distance Δ . To understand our results we propose that the inner tube experiences i) a negative pressure for $\Delta > 0.34$ nm leading to a shift of the LO and TO G-modes and ii) no pressure for $\Delta \approx 0.34$ nm, leading to the G band as the sum of the G-modes of each layer. The present results suggest revisiting the Raman spectra performed on some ensembles of DWNTs.

For the first time excitation profiles of RBLM and G-modes have been measured on individual suspended index-identified DWNTs. Such experiments allow to measure the transition energies of each layers and thus to precise resonance chart in DWNTs. In perspective, a more complete series of data will have to be collected. These data will give important insight on the optical and electronic properties of DWNTs.

Finally, in chapter 5 we discussed the complementarity of electron diffraction and resonant Raman spectroscopy for chiral-index assignment of individual carbon nanotubes. Two examples of

a single- and a triple-walled carbon nanotubes were presented. The index-assignment based on only ED data can lead to ambiguous results, especially in the case of large diameter SWNTs, and Raman features allow to discriminate between different (n,m) possibilities. For TWNTs the situation is worse due to the greater number of possible combinations. For single-, double- and triple-walled carbon nanotubes an improved procedure implemented in dedicated software permit to overcome these difficulties.

In conclusion, this work definitively states that the knowledge of Raman features and transition energies (extracted from resonance profiles) on well-identified carbon nanotubes are essential to probe the different layers and their interaction in multi-walled carbon nanotubes.